UNIVERSITÀ
DEGLI STUDI
DI BRESCIA

DOTTORATO DI RICERCA IN INGEGNERIA MECCANICA E INDUSTRIALE

CICLO XXXIV

Settore scientifico disciplinare
ING-IND/14

STUDY OF A NEW TARGET-ION SOURCE UNIT AND BEAM LINE FOR AN ENERGY AND POWER UPGRADE OF THE SPES PROJECT AT INFN LNL

DOTTORANDA: Lisa Centofante

RELATORE: Prof. Aldo Zenoni

CORRELATORI: Prof. Giovanni Meneghetti
Dott. Alberto Monetti

COORDINATORE: Prof.ssa Depero Laura Eleonora

TUTOR: Prof. Pagano Davide

CO-TUTOR: Prof. Bonomi Germano

A Luca,

Alla mia famiglia

RIASSUNTO

Dagli inizi del ventesimo secolo, la fisica nucleare ha esplorato il comportamento e la stabilità dei nuclei, affrontando via via nuove sfide scientifiche e tecnologiche. Lo sviluppo di tali ricerche ha richiesto il supporto di apparecchiature sempre più sofisticate e complesse. Nel corso degli anni, attraverso lo sviluppo e l'attività di numerosi centri di ricerca, l'Europa ha assunto un ruolo di leadership nel campo della ricerca nucleare e sta ora promuovendo il progetto EURISOL, volto alla realizzazione di una nuova macchina per la produzione di fasci di ioni radioattivi che permetterà di investigare con una ampiezza e dettaglio senza precedenti il comportamento dei nuclei più instabili, chiamati nuclei esotici. All'interno di questo programma di ampio respiro partecipa attivamente anche l'Istituto Nazionale di Fisica Nucleare (INFN), con il progetto SPES (*Selective Production of Exotic Species*), presso i Laboratori Nazionali di Legnaro. Tale progetto prevede la costruzione di una macchina per la produzione di fasci di ioni radioattivi ricchi di neutroni di elevata intensità e qualità utilizzando il metodo di produzione cosiddetto ISOL (Isotope Separation On Line). Il progetto italiano, assieme ad altri progetti europei attualmente in fase di costruzione o perfezionamento quali ISOLDE (CERN), SPIRAL-2 (Francia), e ISOL@MYRRHA (Belgio), costituisce un passaggio intermedio verso la realizzazione di EURISOL. SPES è un progetto nazionale finanziato interamente dall'Istituto Nazionale di Fisica Nucleare, e per questo completamente italiano. Rispetto agli altri progetti europei, consentirà di lavorare con fasci primari di protoni a maggiore intensità, permettendo così di ottenere isotopi esotici più distanti dalla valle di stabilità e, per questo motivo, più difficili da formare e attualmente meno conosciuti. Nella prima fase del progetto si utilizzerà un sistema linea di fascio primario-camera target progettato per operare con un fascio di protoni da 40 MeV di energia a 200 μA di intensità. Il ciclotrone utilizzato è però in grado di raggiungere un'energia massima di 70 MeV e di produrre una intensità di fascio di 300 μA. L'apparato attualmente progettato e costruito ha spinto le prestazioni dei singoli componenti, dei materiali costituenti e del sistema complessivo fino al proprio limite ingegneristico. L'innalzamento del valore dell'energia del fascio primario al massimo valore possibile per il ciclotrone impone quindi una revisione completa della struttura, dei componenti e dei materiali costituenti, sia del sistema camera target sia della linea di fascio primario. L'obiettivo è ambizioso e costituisce una sfida tecnologica molto significativa, anche per la diversità e complessità degli aspetti da considerare. Tuttavia, con il raggiungimento di tale obiettivo, si otterrebbe un incremento significativo delle prestazioni del sistema in termini di intensità e purezza dei fasci di ioni radioattivi prodotti, utilizzando essenzialmente lo stesso impianto generale della macchina attualmente disponibile e già completamente finanziato, quindi con notevole economia nell'utilizzo delle risorse. Con il suo completamento alle prestazioni più elevate, il progetto SPES costituirebbe, inoltre, un modello esemplare della costruzione di macchine per produzione e studio di fasci di ioni radioattivi di alte prestazioni in un laboratorio nazionale di Fisica Nucleare, non dotato

generalmente delle grandi macchine acceleratrici, e delle corrispondenti grandi risorse economiche, dei grandi laboratori internazionali come il CERN.

In quest’ottica si inserisce il presente lavoro di tesi. Il previsto incremento di energia e intensità del fascio primario di SPES, rende necessaria la riprogettazione di alcuni dei principali elementi dell’attuale linea a disposizione, giunta ormai al limite delle prestazioni. Si coglie tuttavia l’occasione per sviluppare e raccogliere una serie di esperienze sul piano tecnico metodologico in grado di fornire delle linee guida generali che permettano, per una macchina di produzione di ioni radioattivi con metodo ISOL, uno sviluppo guidato della linea di fascio primario e dei suoi componenti per le prestazioni più elevate raggiungibili attualmente con i ciclotroni. In questo modo la ricerca progettuale, al di là degli aspetti strettamente relativi al Progetto SPES, si arricchisce di un interesse metodologico che può trovare ampie applicazioni anche in contesti diversi della ricerca nucleare sperimentale.

CONTENTS

LIST OF ABBREVIATIONS

INFN	Italian National Institute for Nuclear Physics
ISOL	Isotope Separation On Line
LNL	National Laboratories of Legnaro
PIS	Plasma Ion Source
PPB	Primary Proton Beam
RIB	Radioactive Ion Beam
RILIS	Resonance Ionization Laser Ion Source
SIS	Surface Ion Source
SPES	Selective Production of Exotic Species
TIS	Target & Ion Source

INTRODUCTION

The current knowledge of unstable nuclei, called exotic nuclei, is still very limited. Their study is really important in order to better understand their structure and the forces that determine the properties of these nuclei. In order to explore ever-more exotic species, European nuclear physicists have built several large-scale facilities in various countries of the European Union. The realization of new radioactive ion beam facilities and the upgrade of existing ones has been recognized as an absolute priority by the nuclear physics community worldwide, a priority triggered by the need of accessing reliable information on nuclei far from stability. Several facilities are now in construction or in upgrade in Europe. These facilities, such as ISOLDE, SPIRAL-2, SPES and ISOL@MYRRHA, can be considered as intermediate step towards EURISOL, the project aimed at the construction of the "next generation" European ISOL (Isotope Separation On Line) radioactive ion beam facility. In particular, SPES (Selective Production of Exotic Species), currently in an advanced construction phase at the National Laboratories of Legnaro, is the only national project fully founded by the Italian National Institute for Nuclear Physics (INFN), and for this reason entirely Italian. The SPES facility will produce neutron rich nuclei to use for forefront research in the fields of Fundamental Physics and Interdisciplinary Physics. Working with high intensity beams, it will be possible to produce more unstable nuclei, for this reason more difficult to produce and less studied. In the first stage of the project, a 40 MeV and 200 μA beam line will be used, but the commercial cyclotron used as primary source is able to reach a maximum energy of 70 MeV and an intensity of 300 μA. A gradual energy and power upgrade of the present set up is therefore foreseen, in order to exploit the full performance of the cyclotron. This will involve an accurate analysis of the new operating conditions and imposes a complete revision of the structure, of the components and of the materials used. However, reaching this goal, a significant increase in performance will be possible, using the same basic plant already available and, therefore, with a significant cost savings.

The work presented in this thesis is devoted to the study of a new target – ion source unit and of some important devices of the proton beam line, in view of the planned energy upgrade up to 70 MeV. In particular, Chapter 1 provides a general overview of the SPES project and its scientific context. In Chapter 2, the design phase of a new target and collimator system is presented, together with the experimental tests performed at the National Laboratories of Legnaro to validate the design. Chapter 3 describes the design of three important devices of the SPES line: the Collimators, the Faraday Cup and the Target Window. In Chapter 4, high temperature experimental tests performed on graphite are presented. These tests are of fundamental importance to validate the previous designs, since graphite has been chosen as design material for all the devices. Finally, in Chapter 5, a mapping of the elements installed inside the SPES bunker is performed. Critical aspects related to the maintenance operations of the current procedures are highlighted and possible human-centered redesign solutions are proposed. General design guidelines for maintainability are then proposed.

CHAPTER 1

The SPES Project

1.1 Introduction

All atomic nuclei contain positively charged particles called protons and electrically neutral particles called neutrons. Together, protons and neutrons in an atom account for nearly all of its mass, but only a tiny fraction of its volume. The nucleus is in fact surrounded by a cloud of electrons, light negatively charged particles. The number of electrons is equal to the number of protons in a neutral atom. Because neutrons are electrically neutral, they do not contribute to an atom's overall charge. The identity of an element is determined by the number of protons in its nucleus. The number of protons in an atomic nucleus is also known as the atomic number, for which the symbol Z is used. The sum of protons and neutrons is the atomic mass number (A). Collectively, protons and neutrons are known as nucleons. All the known elements are arranged in order of increasing atomic number in the periodic table. However, atoms of a given element are not all identical: they have the same number of electrons and protons but may have different numbers of neutrons inside the nucleus. Atoms of an element differing from each other only in the number of neutrons are called *isotopes* of the element. Although most of the elements occurring in nature are stable, a few, such as uranium, thorium and radium, are made up entirely of unstable nuclides, where the unstable nuclide eventually transmutes into a nucleus of a different element while emitting charged ionizing radiations. Several other elements, such as potassium, tin, platinum, consist of a mixture of stable and slightly unstable nuclides. The naturally occurring unstable isotopes are called *natural radioactive isotopes*; unstable isotopes created artificially are called *artificial radioactive isotopes*.

The chart of nuclides (Figure 1.1) is a two-dimensional graph plotting the isotopes of the different elements, in which one axis represents the number of neutrons (N) and the other one represents the number of protons (Z) in the atomic nucleus. Each point plotted in the graph represents a nuclide. This way of ordering nuclides offers a greater insight into the characteristics of isotopes than the periodic table, which shows only the elements and not their isotopes. The stable nuclei are characterized by balanced combinations of protons and neutrons. In the chart of nuclides, they are positioned in the "valley of stability", in black squares in Figure 1.1.

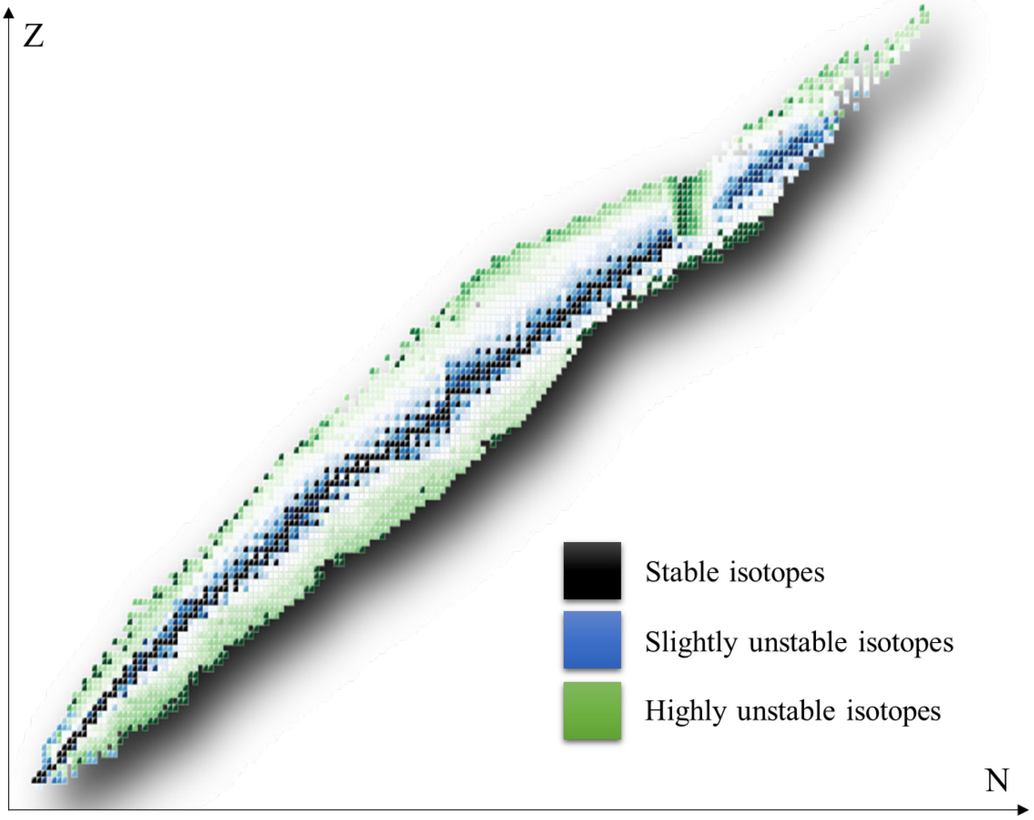

Figure 1.1 The chart of nuclides.

All the nuclides outside the stability valley are unstable, or radioactive. This means that the nucleus transforms, emitting radiations during or immediately after this transmutation. The rate of radiation emission for a given isotope is called *activity* and depends on the total number of unstable atoms present, while the kind of radiation depends on the isotope concerned. As more and more of the original unstable atoms transmute, the emission rate decreases. The time in which one-half of any starting number of unstable atoms decays is called *half-life* ($t_{1/2}$). The resulting elements or isotopes are called *decay products* and, in some cases, they are themselves radioactive. The activity of a radioisotopes, defined as its rate of decay, is always a constant fraction of the total number of unstable atoms present, and it is expressed by the fundamental law of radioactive decay:

$$\frac{dN}{dt} = -\lambda N \tag{1.1}$$

where N is the number of unstable nuclei present at time t, and λ is defined as the *probability of decay* per second for the isotope. The probability of decay and the half-life are connected by the following relation:

$$t_{1/2} = \frac{ln2}{\lambda} \tag{1.2}$$

There are three principal types of emissions from decaying radioisotopes, α β and γ:

- α radiation – An α particle is identical to the ordinary helium nucleus. It contains two neutrons and two protons. Alpha particles usually move at about one-tenth the speed of light and can be stopped by an aluminum foil of 0.05 mm thickness. Any nucleus that emits an α particle loses two protons and two neutrons. Its atomic number decreases by 2 units and its mass number decreases by 4 units.
- β radiation – β particles are electrons and usually move at very nearly the speed of light; they can have either a positive (positron) or a negative (electron) charge. If the β particle emitted is a positron, then a proton in the nucleus becomes a neutron. The atomic number decreases by 1, but the mass number remains unchanged. If the β particle emitted is an electron, a neutron in the nucleus becomes a proton. The atomic number increases by 1, but again the mass number is unchanged.
- γ rays– They are photons of electromagnetic energy that originate by transitions in the nucleus. When the nucleus emits a γ ray, the only change is to a less energetic form of the same isotope.

The current knowledge of highly unstable nuclei, called *exotic nuclei*, is still very limited. The study of these nuclei, lying very far from the valley of stability, is really important in order to better understand their structure and the forces that determine their properties.

1.2 The ISOL technique

There are numerous topics that can be tackled and deeply understood by studying the exotic nuclei. They are broadly used for studies in astrophysics, nuclear physics and materials science, but they are also exploited in biomedicine to produce innovative radionuclides for diagnostic and therapy. It is therefore necessary to build facilities able to create and study these exotic nuclei. This requires big accelerators by means of which nucleon or nucleus beams are forced to collide against a fixed target. The impact triggers a reaction that generates new nuclear clusters, most of them composed of exotic species.

The international community of nuclear physics has recognized as a priority the construction of new facilities aimed at producing radioactive ion beams with improved features, as well as the upgrade of the existing ones. A large common European project foresees the collaboration of many European nuclear physicists in planning the construction of an ultimate Radioactive Ion Beam (RIB) facility called EURISOL, based on the Isotope Separation On-Line (ISOL) method. The main elements of this technique are:

- The primary accelerator;
- The Target-Ion Source Unit (TIS-Unit);
- The mass separator;
- The post accelerator.

The primary beam, produced by an accelerator, interacts with a Target-Ion Source Unit, where a large variety of radioactive isotopes are produced by means of nuclear reactions. The isotopes are subsequently extracted and ionized by an ion source. After extraction, the species are mass separated and accelerated to the required energy. The aim of ISOL systems is the production of beams of exotic nuclei that are abundant, pure, and of good ion optical quality, leading to high intensity and high-quality beams. There are already a number of ISOL facilities around the world currently producing RIBs, such as the ISOLDE facility at CERN (Switzerland) and the ISAC facility at TRIUMF (Canada), each of them delivering more than 2800 h per year of exotic beams to experiments [1]. It is the consequential demand that motivates the construction of new facilities all over the world, such as ARIEL-TRIUMF (CANADA) [2], HIE-ISOLDE-CERN (Switzerland) [3], SPIRAL 2-GANIL (France) [4], RISP-IBS (Korea) [5] and SPES-INFN (Italy) [6].

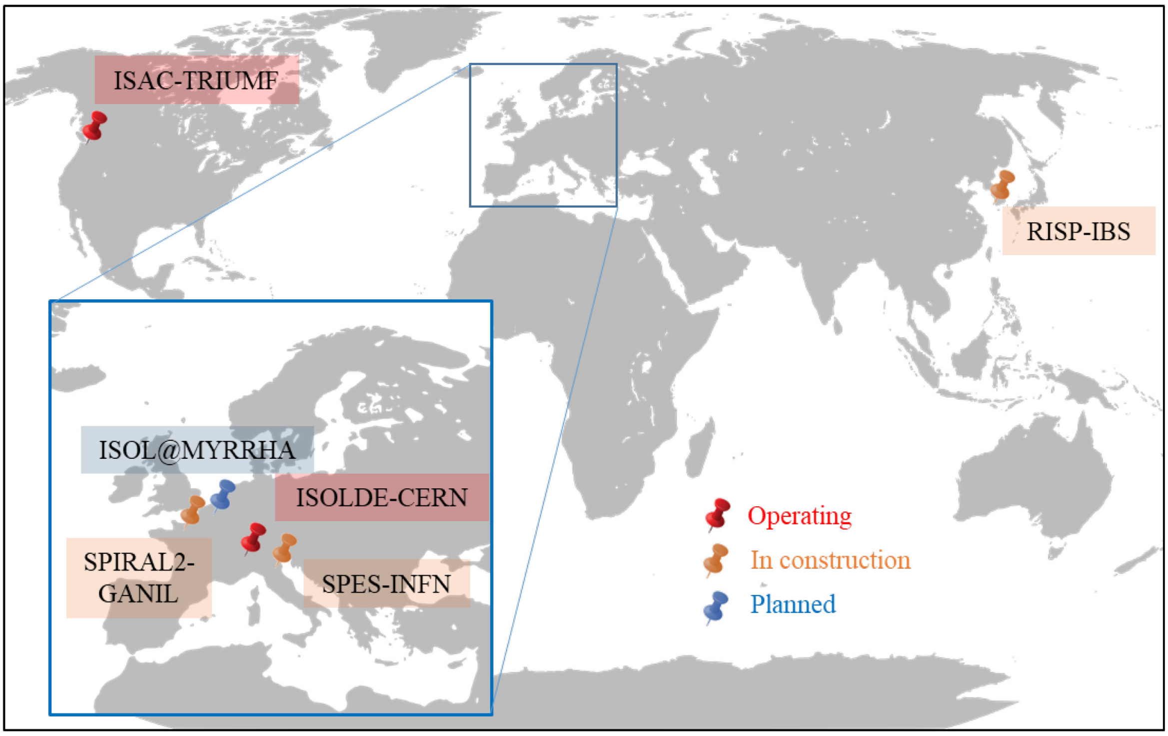

Figure 1.2 A map of some of the exiting, in construction and planned ISOL facilities in the world.

ISOLDE-CERN is characterized by high beam energy (1400 MeV) but low beam power (2.8 kW), while ISAC-TRIUMF operates with medium beam energy (480 MeV) and high power (48 kW).

SPES, the only national project fully founded by the Italian National Institute for Nuclear Physics (INFN), and for this reason entirely Italian, will work with low beam energy (40 MeV) and medium power (8 kW). It will allow higher intensity pure beams with respect to the other facilities to be obtained.

1.3 The ISOL facility at LNL: the SPES Project

SPES (Selective Production of Exotic Species) will be mainly focused to the technical challenges associated to a high intensity proton beam, generated by a commercial cyclotron as primary source. With respect to the other current European facilities, this project will work with higher intensity beams: it will be therefore possible to produce more unstable isotopes in sizable quantities, for this reason harder to produce and less studied. The considerable founds devoted to the project are a proof of its importance for the entire scientific community, both national and international.

The SPES goal is the production of radioactive neutron-rich isotopes in high quantities and purity, by means of nuclear fission induced in a Uranium Carbide (UC_x) target. The proton beam, accelerated by a cyclotron, travels along the primary beam line and, after entering the SPES bunker, impinges the UC_x target, housed in an opportunely designed vacuum chamber (the *target chamber*) installed in the SPES *Front-End,* described in Section 1.4. There, the exotic species are produced, ionized, accelerated at low energies and selected. The so formed radioactive ion beam is then delivered either to the low energy experimental halls or to post acceleration sectors (see Figure 1.3).

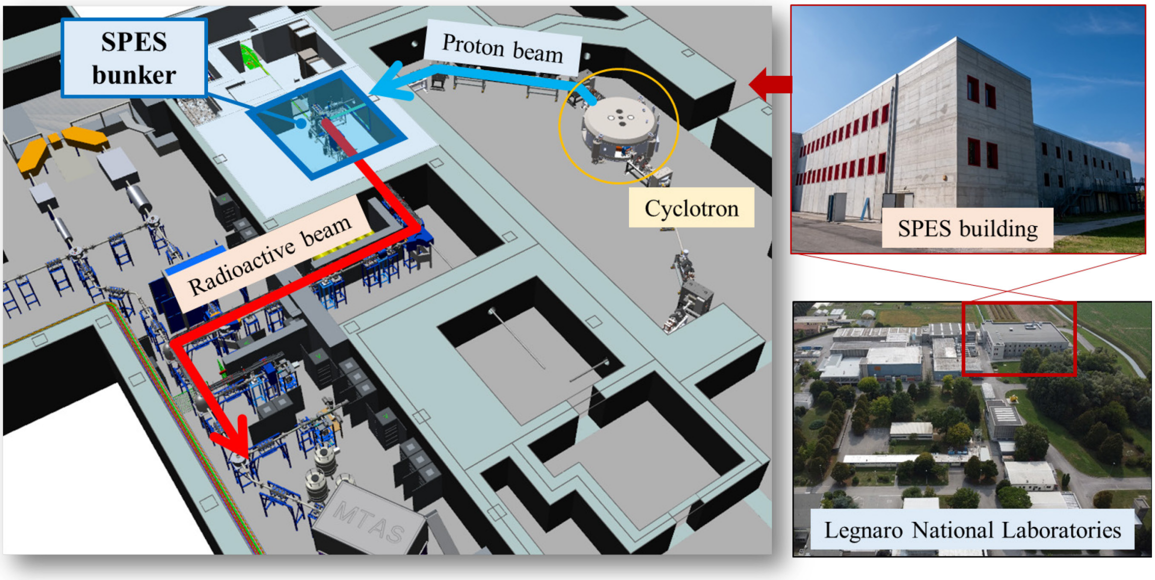

Figure 1.3 SPES project structure layout.

As first step, a 40 MeV proton beam will be used. However, the installed cyclotron is able to work with a maximum energy of 70 MeV and an intensity of 750 μA. For this reason, during the project time development, the energy and the intensity of the beam will be gradually increased to the cyclotron maximum limits. The system currently designed and built has pushed the component performance, the materials and the entire structure to their engineering limits. The planned increase in energy will therefore require a complete review of the system, of the components and the materials, both in the TIS-Unit and in the proton beam line, leading to a new setup called SPES-2. The goal is ambitious and represents a significant technological challenge, owing to the diversity and complexity of the aspects to be considered. However, in achieving the goal of this project, a significant increase of the performances would be gained, in terms of intensity and purity of radioactive isotopes produced, using the same general plant already available and completely founded, with significant savings. In this way, the SPES project would also represent the benchmark for other high-performance facilities designed for the production and study of radioactive ion beams in a National Laboratory of Nuclear Physics, usually lacking in big accelerators and financial resources, compared to big international laboratories.

1.3.1 Applications

The SPES project is devoted to basic research in nuclear physics and astrophysics, as well as to interdisciplinary applications, from the production of radionuclides of medical interest to the generation of neutrons for material studies, nuclear technologies and medicine.

Nuclear physics – The present physical models of the nuclear structure are based on the characteristics of nuclei very close to the stability valley. However, these models can hardly be validated in the neutron-rich region of the nuclide chart. Experiments with radioactive beams can provide more information to confirm or modify some aspects of the current nuclear structure models, improving the understanding of nuclear fundamental interactions.

Nuclear astrophysics – Measurements with radioactive beams can provide fundamental data for a better comprehension of the stellar evolution and the elemental abundance in the Universe. New evidence is providing new data in the abundance distribution inside and outside the solar system. All these recent findings are posing new challenges in theoretical modelling of the chemical evolution of the Universe. At present, the calculation models fail in reproducing some aspects of the observed abundance pattern. In this respect, the SPES project will provide an important contribution to the large experimental and theoretical efforts to the field of nuclear astrophysics. The SPES intense radioactive beams will open new possibilities for measuring basic nuclear physics quantities related to the chemical evolution of the Universe and will also shed light on processes like Supernovae explosions.

Nuclear medicine – Nowadays, nuclear medicine is a fundamental branch of medicine. One of the most studied sector of nuclear medicine concerns radiopharmaceuticals, used in diagnostics and therapy of cancer diseases and other pathologies. Radiopharmaceuticals are medicines that deliver a defined dose of radiation to a target tissue for therapeutic or diagnostic procedures. For example, particle emissions capable of inducing cell death, such as α and β^- emissions, are used in cancer therapy. High-penetrating radiation, such as γ emission, is mainly used for the early diagnosis of tumours and inflammatory diseases [7].

At the INFN National Laboratories of Legnaro, the ISOLPHARM project will exploit the radioactive beam produced in the SPES facility to obtain pure isotopic beams without contaminants. It will be then possible to collect radionuclides of interest upon a substrate at the end of the experimental line. The steps that lead to radiopharmaceuticals production are shown in Figure 1.4.

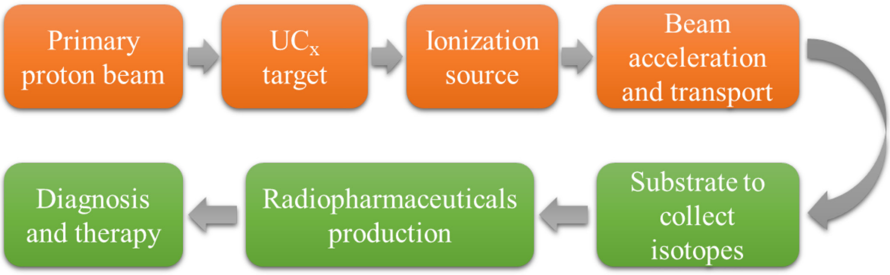

Figure 1.4 Steps in radionuclide and radiopharmaceutical production.

The ISOLPHARM method will allow a great variety of medically relevant nuclides to be produced, both never studied ones (^{111}Ag) and nuclides hardly obtainable with traditional techniques. All of them will be characterized by high purity and specific activity, fundamental aspects to determine the diagnostic or therapeutic efficacy of the radiopharmaceutical.

1.4 The SPES bunker

Currently, the SPES facility is in an advanced construction phase at the National Laboratories of Legnaro. In the SPES building, at the underground floor, following the cyclotron hall for the production of the primary beam, a shielded production bunker with the Front-End beam lines can be found. The proton beam enters the bunker through a beam pipe coming directly from the cyclotron. Three different main assemblies can be found inside the bunker, constituting the SPES Front-End, as shown in Figure 1.5:

- The Protonic beam line
- The Target-Ion Source Unit (TIS)
- The Radioactive beam line

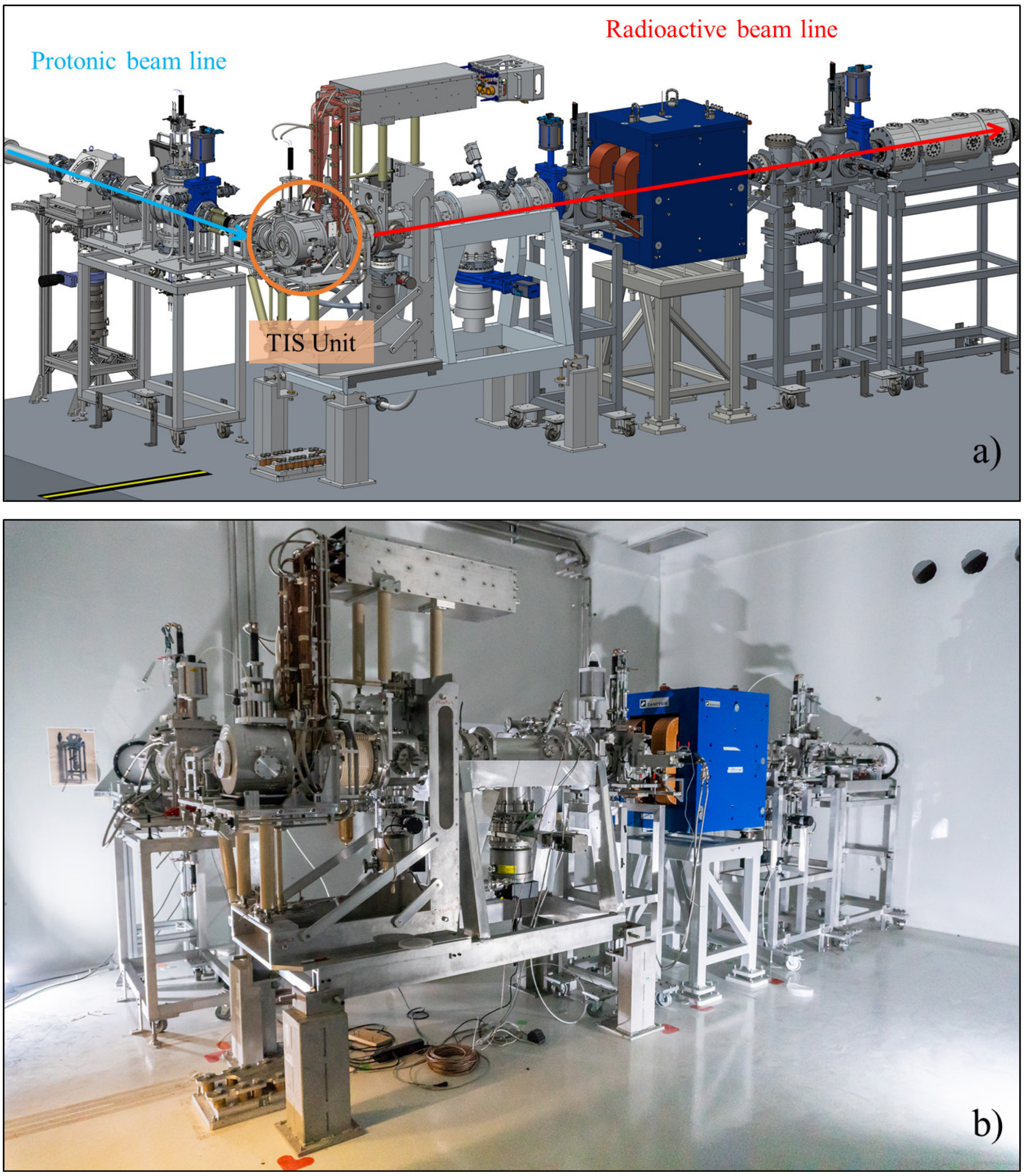

Figure 1.5 The CAD model (a) and a picture (b) of the Front-End installed inside the SPES bunker.

1.4.1 The Proton Beam Line

Several devices are placed along the proton beam line, to control the beam characteristics, before the beam impinges the target. The main components of the proton beam line are:

- The Collimators: they are constituted of four coaxial graphite rings. The collimators are used to prevent and detect beam misalignment and are essential to determine the proton beam size. Moreover, as better explained in Sec. 3.2, they are used to absorb a certain percentage of protons in the beam external halo, avoiding that this part of the beam impinges other elements of the beam line.

- The Beam Profiler: It is a device able to measure the profile of the beam. It is constituted by a horizontal and a vertical grid of insulated wires. By counting the particles impinging in each wire it is possible to obtain the beam profile.
- The Faraday Cup: It is a device that monitors the beam intensity. It is essentially an insulated cup, typically in graphite or copper, that intercepts and completely stops the beam. Here the beam current is deposited and, thanks to electrical connections to an ammeter, it can be measured.

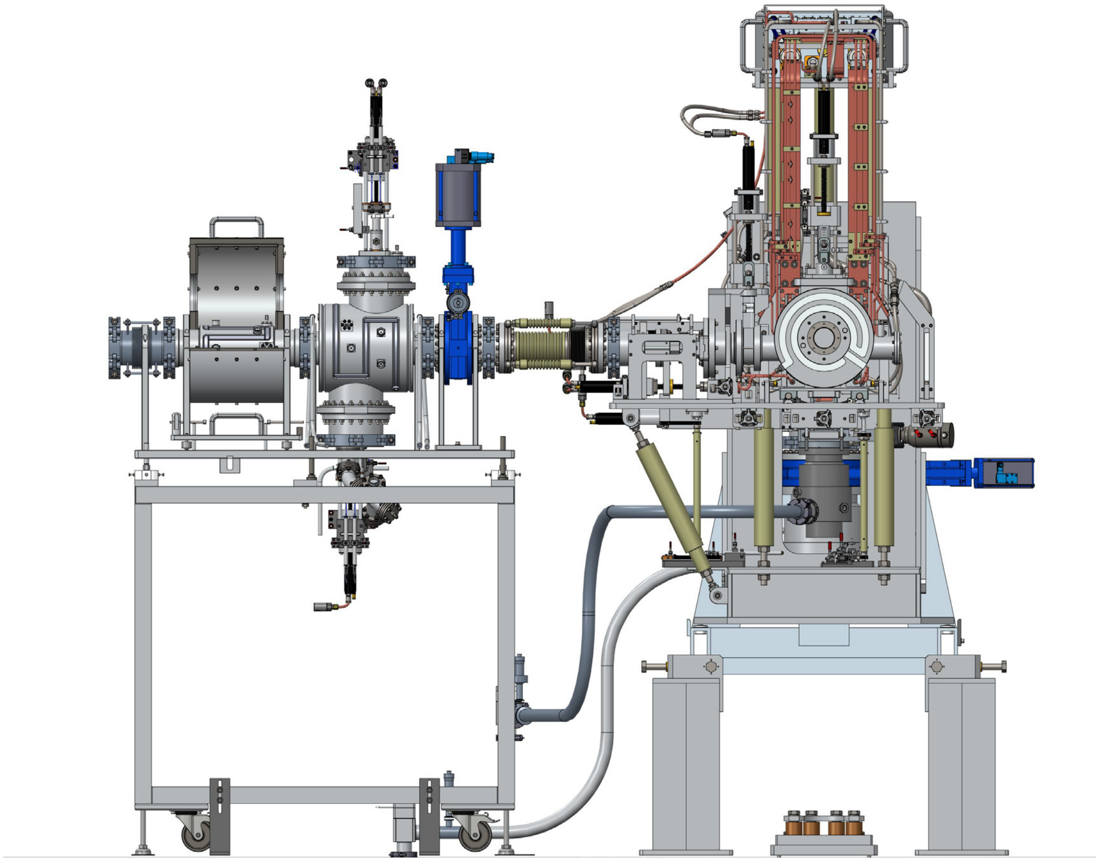

Figure 1.6 The devices of the protonic beam line.

1.4.2 The Target and the Ion Source

The Target-Ion Source Unit (TIS Unit) is the core of the facility: here, the radioactive nuclei are produced by the interaction of the proton beam with an Uranium Carbide target. As better explained in the next sections, the newness of the SPES target lies on its special design consisting in several coaxial separated Uranium Carbide thin discs. This configuration allows the deposited beam power to be efficaciously dissipated by radiation exchange, increasing the heat exchange surface. Once formed, the reaction products are extracted from the discs by thermal processes, by keeping the target at high temperature (more than 2000°C) in high vacuum (10^{-6} mbar). Through the transfer line, they are then transported from the production target to the ion source by effusion, and ionized 1+ by an ion source. Different configurations of the Target-Ion Source can be used in operations, each of them requiring proper beam characteristics.

The proton beam - The distribution of particles inside the beam is commonly modeled as a bi-dimensional Gaussian distribution. When the beam is centered with respect to the disc axis, as shown in Figure 1.7, it can be described by Eq. 1.3:

$$f(x,y) = \frac{1}{2\pi\sigma^2} \cdot e^{\frac{x^2-y^2}{2\sigma^2}} \tag{1.3}$$

where x and y are the spatial coordinates and σ is the proton beam mean square deviation (or RMS radius), assumed identical in x and y.

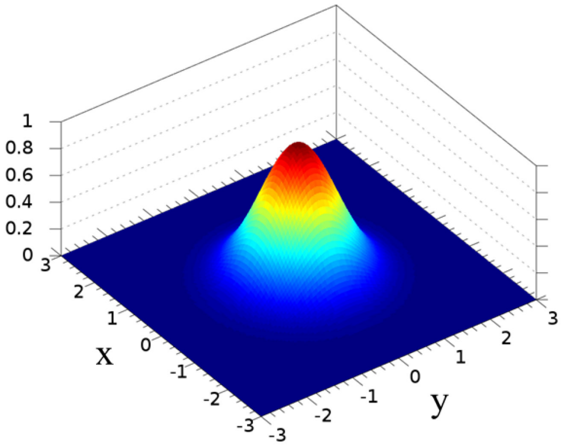

Figure 1.7 Example of a Gaussian distribution used to model a centered proton beam.

The beam axis can also be rotated, or *wobbled*, around the disc axis. This allows the beam power to be spread in the disc surface, leading to a decrease of the temperature difference between the center and the edge of the disc and, consequently, to lower stresses [8]. In this case the particle distribution of the beam can be described by Eq 1.4:

$$f(x,y) = \frac{1}{2\pi\sigma^2} \cdot e^{-\frac{\left((x-r_w\cdot\cos(\omega t))^2+(y-r_w\cdot\sin(\omega t))^2\right)}{2\sigma^2}} \tag{1.4}$$

where r_w is the wobbler radius and ω is its angular frequency.

The beam characteristics are therefore defined by:

- The RMS radius
- The wobbling radius, r_w

The target – When the facility will be fully operative, the radioactive species will be produced by the interaction of a 40 MeV proton beam with an Uranium Carbide target, with currents up to 200 μA. The target is composed of seven discs, with 40 mm diameter and 0.8 mm thickness, and a density of about 4 g/cm^3, for a total target thickness of about 2.3 g/cm^2. The discs will be housed in a cylindrical graphite box that is placed inside a tantalum heater. It is indeed important to reduce the temperature gradient, avoiding thermal variations that would be dangerous for the structural integrity of the discs. This particular layout, shown in Figure 1.8, aims to efficiently dissipate the 8 kW total power deposited in the discs during irradiation. For this target, called *high power target,* a wobbled beam characterized by an RMS radius equals to 7 mm and a wobbler radius equals to 11 mm is foreseen. This system will produce a rate of about 10^{13} fissions per second.

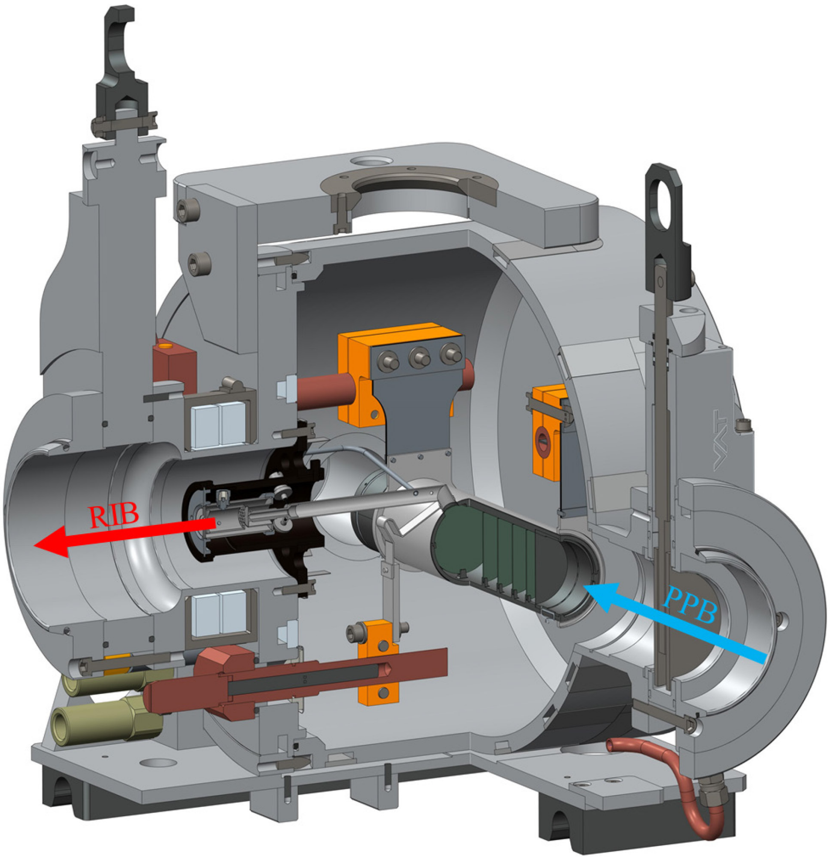

Figure 1.8 Section of the CAD model of the target chamber with the 40 MeV high power target and the Plasma Ion Source.

However, different target configurations are available: in the first stage of the project, for example, a lower beam power (~800 W) and a smaller target will be used, for safety reasons. This *low power* target is characterized by smaller discs, with 13 mm diameter, and will work with different beam characteristics. In particular, a centered beam with RMS radius equal to 5 mm will be used. Moreover, during the project development, the energy of the beam will be gradually increased up to 70 MeV (SPES-2). As better explained in Chapter 2, this upgrade leads to higher temperatures and stresses in the discs. Different targets will be therefore used with a 70 MeV proton beam energy. The different SPES target configurations and the related beam characteristics are summarized in Figure 1.9.

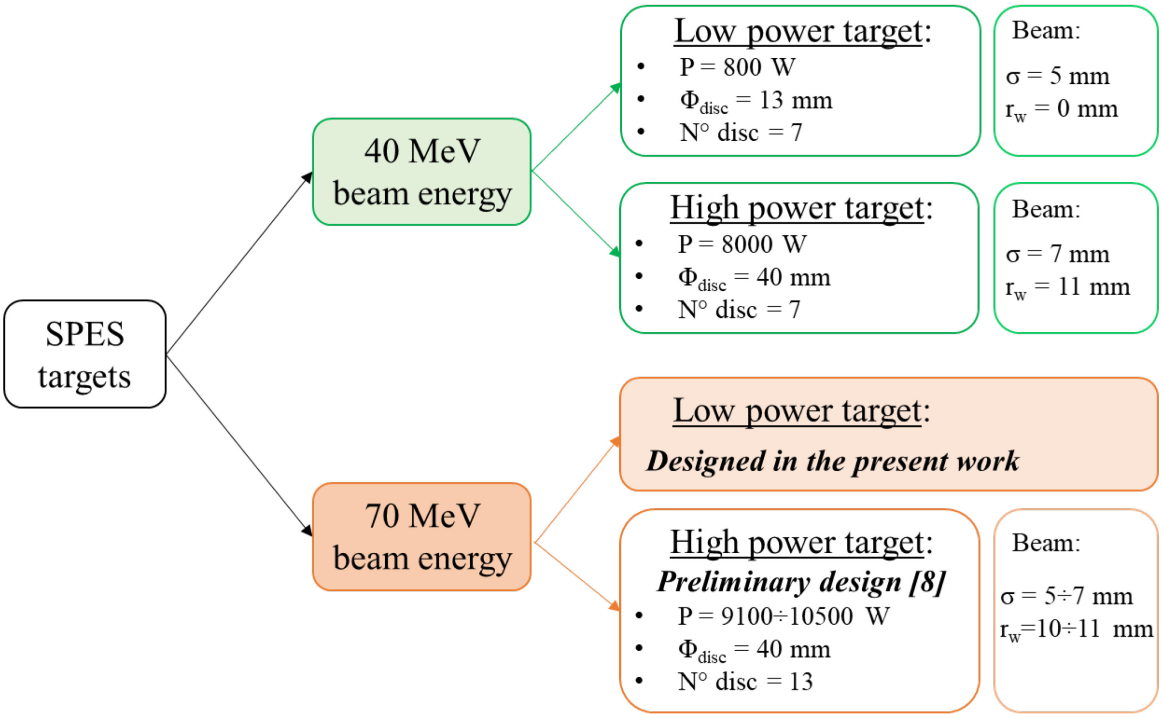

Figure 1.9 SPES target configurations and related beam characteristics.

The ion source – Three different ion sources can be used depending on the required radioactive beam: the SPES Surface Ionization Source (SIS) [9], the SPES Plasma Ionization Source (PIS) [10], or the Resonance Ionization Laser Ion Source (RILIS) [11]. In the SIS, the surface ionization mechanism is applied in a tantalum hot cavity: it is very effective for low ionization potential elements such as alkali or alkaline-earth metals. The RILIS system is structurally identical to a hot cavity ion source, but the atoms are continuously irradiated with laser pulses while kept in the gaseous phase in the cavity. The laser-induced ionization is highly selective for a wide range of elements, resulting in isobarically and isomerically pure beams, except for the surface ionized ions. In the SPIS, electron impact ionization is used to ionize the atoms that are present in the gas phase inside the ion source: this method is indicated for high ionization potential elements, but it is not very selective.

1.4.3 The Radioactive Beam Line

Downstream the Target-Ion Source unit, several devices are needed to extract, separate and transport the radioactive ion beam downstream the target. In particular, four main elements are responsible for the beam transport:

- The ion extraction electrode: it provides the first step of acceleration to the radioactive beam. When the experimental setup is ready to produce radioactive ions, it is moved close to the ion source at a distance of about 60 mm. The electric field due to the potential difference allows the positive ions from the source (at high voltage) to be accelerated to the ion extraction electrode (to the ground).
- The deflectors (or steerers): they are essentially composed of two plates, with an opportune shape, maintained at a certain potential. Usually, one of the electrodes is at a negative potential, while the other one is set at a positive potential. In this way, they are used to correct beam misalignments by creating a constant electric field.
- The triplets: They are composed of three quadrupoles and are used to control the beam size along the beam line.
- The Wien Filter: it is a velocity separator, used in the SPES bunker as mass separator.

Together with these transport devices, two diagnostic boxes are installed in the radioactive line, to control the beam properties. Both are provided by a Faraday Cup and a Beam Profiler.

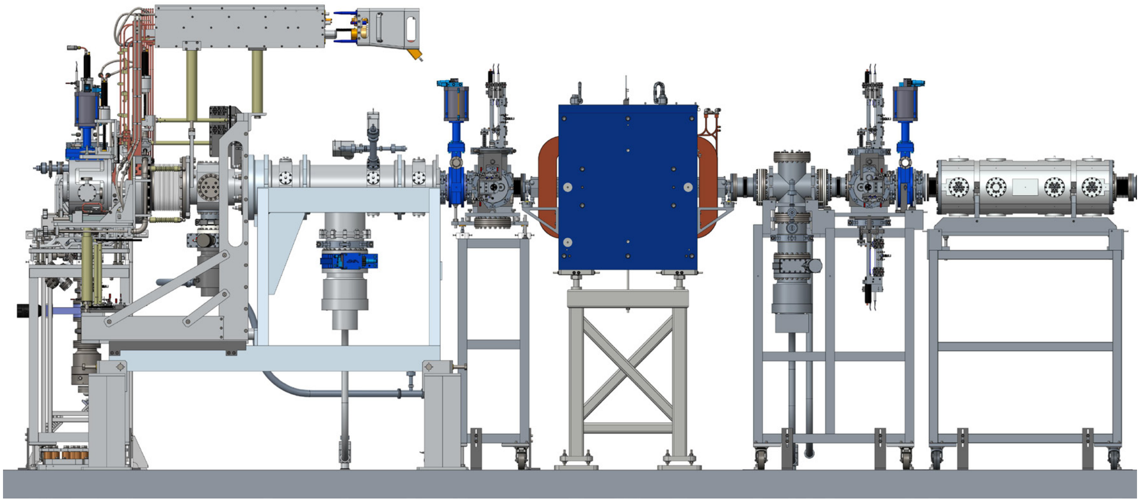

Figure 1.10 The devices of the radioactive beam line.

CHAPTER 2

The Target-Ion Source Unit upgrade

2.1 Introduction

The present SPES line has been designed for a 200 μA and 40 MeV proton beam. However, the commercial cyclotron used as primary source can reach a maximum energy of 70 MeV and an intensity of 750 μA. An upgrade of the present SPES line to the cyclotron intrinsic limits would increase the productivity of the Target-Ion Source system and would allow the production of new types of radioisotopes to be achieved. In fact, the range and the amount of produced nuclides increase with the primary beam energy. However, the number of side channel reactions increases as the energy increases, and unwanted radionuclides can also be produced. Moreover, the upgrade would lead to higher temperatures and stresses for the components intercepting the beam, and to a larger activation of the structural materials. To find the optimum design for the Target-Ion Source unit, the correlations between all these factors has to be considered.

In Section 2.2 of the present chapter some physics considerations related to the energy upgrade are presented. In particular, the influence of the beam energy in the productivity of the target and in different properties of the beam are analyzed. In Section 2.3, the design of the 70 MeV l*ow power* target (see Sec. 1.4.2) is presented, while in Section 2.4 a new collimator for the target is studied. Finally, in Section 2.5, experimental tests carried out at National Laboratories of Legnaro on the new designed target and collimator are described.

2.2 Physics considerations

2.2.1 Interaction of charged particles with matter [12] [13]

As a charged particle moves through a surrounding medium, it interacts through ionization, scattering and various types of radiative losses. The four main modes of interaction occurring are:

- Inelastic collisions of the particles with the atomic electrons of the surrounding medium. In this case, the electrons are promoted to a higher energy level (excitation) or an unbound state (ionization). If ionization occurs, the ions and electrons recombine to form an excited neutral atom or molecule. The excited atom must transfer the excess energy to the surrounding molecules: this is the primary energy loss mechanism for the charged particle beam and the major source of heat release in the target material.

- Inelastic collisions of the particles with the nuclei of the target material. In this case, the charged particle is deflected by an amount depending on the proximity of the encounter and the charges involved. In some of these deflections, a quantum of energy is lost from radiation (bremsstrahlung) and a corresponding amount of kinetic energy is lost from the colliding pair. The total bremsstrahlung intensity varies inversely with the square of the mass of the charged particle, so it is not usually important for protons or massive particles.
- Elastic collisions of the particles with the nuclei of the target material. In an elastic collision, the incident particle is deflected but neither emitted radiation nor excitation of the target nucleus result. The only kinetic energy loss is due to the conservation of momentum by the deflection of the particle. This process, common for electrons, is less probable for havier charged particles.
- Elastic collisions of the particles with the atomic electrons of the surrounding medium. This process occurs at low energy when the charged particle does not transfer enough energy to the atomic electron to promote it to the lowest excited state energy level.

The charged particle loses energy as a result of all four of these processes as it moves through the target material. The type of collisions and the exact path of an individual particle cannot be predicted but the overall behavior of the beam can be predicted with high accuracy and reliability.

Stopping power – The average loss of kinetic energy of a charged particle per unit length due to the interaction with matter is called the *stopping power*. It is defined as:

$$S(E) = -\frac{dE}{dx} \qquad 2.1$$

Where E is the particle energy (MeV) and x is the travelled distance (cm). The exact calculation of the stopping power is complex but, assuming that the particle is massive in comparison with the electrons, for non-relativistic and not too slow particles, a reasonable approximation may be obtained from the so-called *Bethe Bloch* formula as:

$$-\frac{dE}{dx} = \frac{4\pi z^2 e^4 NZ}{m_0 V^2 A} \ln\left(\frac{2m_0 V^2}{I}\right) \qquad 2.2$$

where z is the particle atomic number (amu), Z is the absorber atomic number (amu), e is the electronic charge, m_0 is the rest mass of the electron (MeV), A is the atomic mass number of the absorber (amu), V is the particle velocity (cm/s), N is Avogadro’s number and I is the ionization potential of the absorber (eV). The integration of this function along the particle path gives the energy deposition of the beam particles in the target material.

Range and projected range – As seen, the charged particle loses energy by means of both nuclear and electronic interactions with the surrounding medium. The former interaction consists of individual elastic collisions between the ion and the nuclei, whereas the electronic interactions can be viewed as a continuous viscous drag phenomenon between the charged particle and the electrons surrounding the target nuclei. When the nuclear contribution to the stopping process dominates, this is reflected in the ion trajectories as the ion comes to rest within the solid. As shown in the schematic representation of Figure 2.1, the charged particle does not travel to its resting place in a straight path due to collisions with target atoms. The actual integrated distance traveled by the ion is called *range*, R. The ion's net penetration into the material, measured along the vector of the ion's incident trajectory is called the *projected range,* R_P.

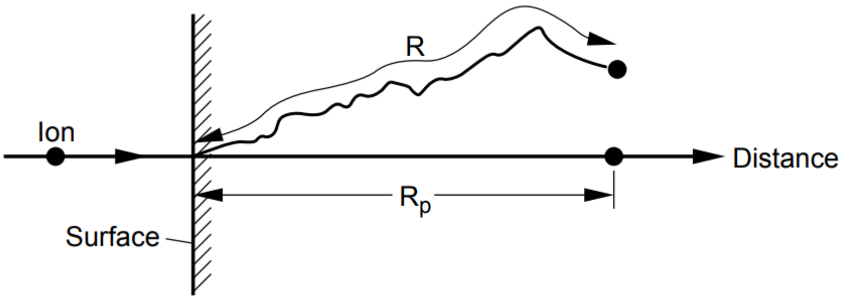

Figure 2.1 A charged particle incident on a target material penetrates with a total path length R, which gives a projected range R_p*, along the direction parallel to that of the incident ion* [13].

The *range* of a charged particle through the absorber medium is simply the integral of the energy loss equation:

$$R = \int_{0}^{E_{max}} \frac{1}{S(E)} dE \tag{2.3}$$

where $S(E)$ is the stopping power at energy E. Because the stopping of an ion is a random process, the collision sequence, the ion deflection and the ion's total path length vary randomly from ion to ion. Hence, all ions of a given type and incident energy do not necessarily have the same range. Instead, a statistically broad distribution in the depths to which ions penetrate would be observed. This phenomenon is referred as *energy straggling:* the distribution in projected ranges is referred to as the *range straggling*, with the most probable projected range referred as the *mean projected range.*

Both the stopping power and the projected range depend on the particle energy, as shown for a Uranium Carbide target, in Figure 2.2. Protons of higher energies present lower stopping power and release lower energy in the target per unit length. On the contrary, a higher deposition of energy occurs when protons have lower energies, at the end of their trajectory. Moreover, during penetration inside the target material, the beam particles are subject to **scattering.** The scattering is a change in the direction of motion of a particle because of a collision with another particle. If the beam is completely stopped inside the target, the higher the energy of the beam, the higher is the scattering inside the target block: a larger number of collisions will in fact take place before the particle stops.

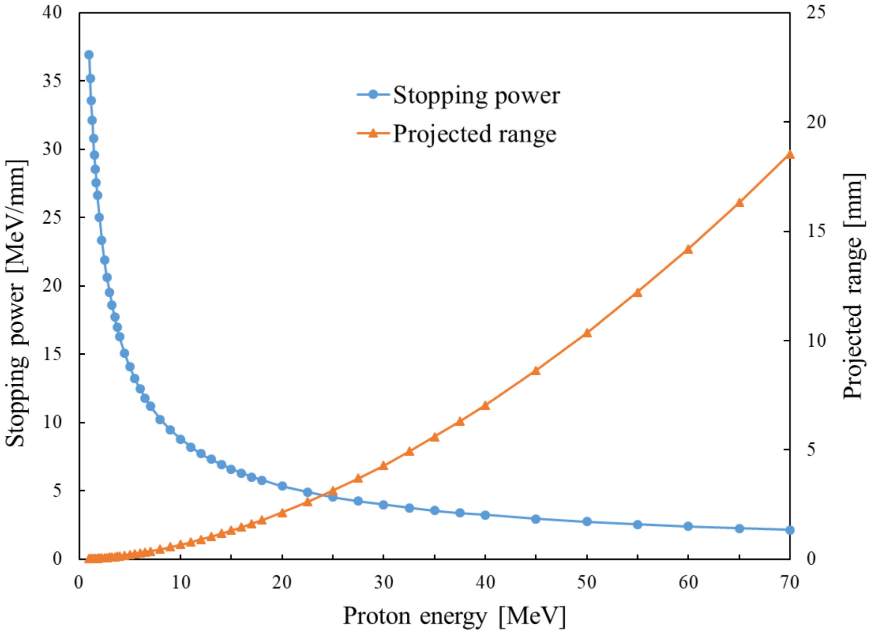

Figure 2.2 Stopping power and projected range for different proton energies in a Uranium Carbide UC_4 *target.*

2.2.2 Target productivity

The productivity of an ISOL target, expressed in terms of intensity of the reaction products synthesized in the target, depends on several factors, including the reaction cross section as a function of the incoming particle energy, the thickness of the target in terms of nuclei per cm^2, and the flux of the incoming particles. The rate of production is given by [14]:

$$I_{production} = \sigma(E) \cdot N_{target} \cdot \Phi \qquad 2.4$$

where σ is the reaction cross section (cm^2), E is the incoming particle energy, N_{target} is the number of target atoms per surface area (cm^{-2}) and Φ the primary beam intensity (particle/s). However, the final intensity of the secondary beam will be reduced due to different loss processes involved. When the radioactive species are generated inside the target, they start to diffuse with a velocity and a direction related to the target microstructure and temperature. At the same time, the radioactive nuclides are subject to radioactive decay, each one with a specific mean lifetime. When the produced species reach the surface of the target, they start moving inside the surrounding empty volume, until they reach the ion source by an effusion process. All the processes occurring from the isotopes generation to their effective use are characterized by different losses of efficiency. The final intensity of the secondary beam can therefore be expressed as:

$$I = I_{production} \cdot \varepsilon = \sigma(E) \cdot N_{target} \cdot \Phi \cdot \varepsilon \qquad 2.5$$

where ε represents the efficiency of the whole process and is the product of a series of partial efficiencies. One of these efficiencies is related to the delay time and expresses the relative amount of isotopes that survive the time elapsed from their production to their extraction from the ion source, in spite of their radioactive decay. This time is often referred as **release time** and it is determined by the diffusion from the target material, the desorption from the material surface and the effusion to the ion source exit hole [14].

The SPES production targets are composed by discs made of Uranium Carbide, commonly referred to as UC_X. This notation indicates that it is composed of different phases: uranium dicarbide (UC_2), graphite (C) and a minor amount of uranium monocarbide (UC) [15][16][17]. The main characteristics of the Uranium Carbide used in the SPES targets are summarized in Table 2.1.

Table 2.1 Main characteristics for the Uranium Carbide used for the SPES target [18][19].

Property	**Value**
Thermal conductivity	8 W/mK
Emissivity	0.85
Density	4 g/cm^3
Thermal expansion coefficient	$12.4 \cdot 10^{-6}$ °C^{-1}
Elastic modulus	176 GPa
Poisson’s ratio	0.269
Maximum stress	200 MPa
Maximum temperature	2300°C

Figure 2.3 shows the cross section (σ) of the proton-induced fission in ^{238}U in an energy range up to 80 MeV. The cross section is an energy dependent quantity and expresses the probability of interaction between particles. It represents the hypothetical area around the target particle: if a particle of the beam crosses this surface, an interaction can take place. As shown, for particle energies below 15-20 MeV the cross section rapidly decreases: it is, therefore, unlikely that fission reactions take place below these energies.

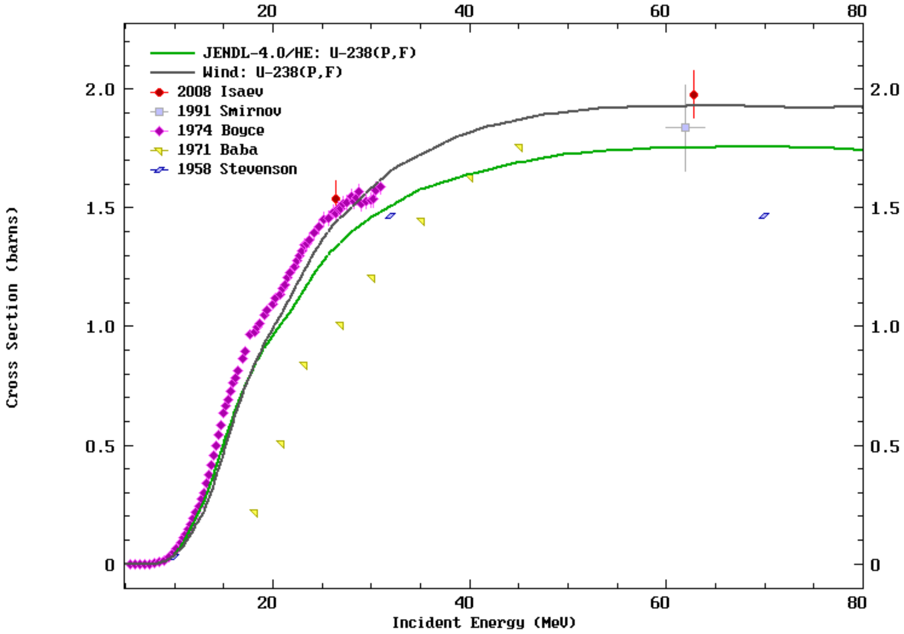

Figure 2.3 Evaluated (solid lines) and experimental (scatter plots) cross sections of the proton-induced fission in ^{238}*U, taken from ENDF* [20] *and EXFOR* [21] *databases respectively.*

By analyzing the stopping power curve shown in Figure 2.2, it is possible to calculate in first approximation the necessary target thickness for letting the beam exit with an energy of about 15 MeV. With a 40 MeV proton beam energy, a thickness of about 7 mm is calculated while with 70 MeV a thickness of about 17 mm is found. In fact, starting from the initial energy of the beam, it is possible to obtain for each millimeter thickness the deposited energy from the stopping power curve (see Section 2.3.2). It is therefore possible to compare the mass yield spectrum calculated with the Monte Carlo FLUKA simulation code [22][23] in the two cases, as shown in Figure 2.4. Moreover, in Figure 2.5, the comparison between the isotope productions is presented. These results are obtained for 1 μA beam current reaching the target material. With a beam energy of 70 MeV, a significant increase in the production yield can be observed, together with the production of new species of isotopes.

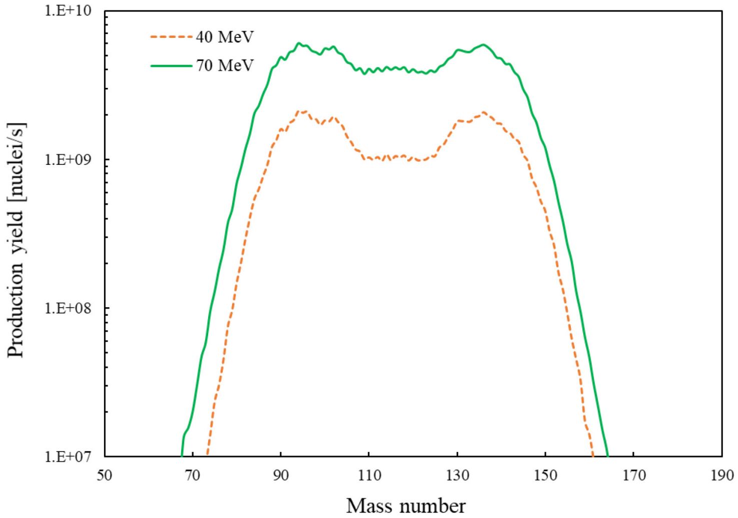

Figure 2.4 Comparison of the mass yield spectrum due to the proton beam interactions, with a 40 MeV target (thickness 7 mm) and a 70 MeV target (thickness 17 mm), for 1 µA current reaching the target.

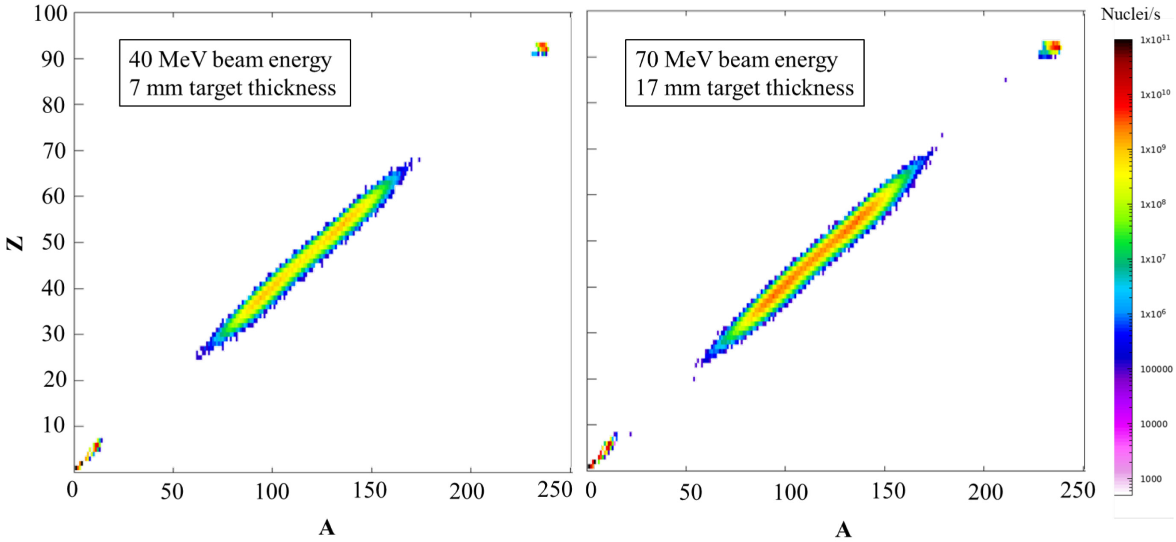

Figure 2.5 Comparison of the isotope production due to the proton beam interactions, with a 40 MeV target (thickness 7 mm) and a 70 MeV target (thickness 17 mm), for 1 µA current reaching the target.

2.3 The 70 MeV target

The target is the real core of the entire ISOL facility since, by the interaction between the primary beam and its nuclei, the radioactive species of interest are created. The design of an ISOL target implies three main issues:

- In-target fission rate;
- Release time;
- Temperature of the target.

These issues are someway conflicting. The target should be as thick as possible in order to maximize the fission rate. The release time should be as short as possible to minimize the losses caused by the decay of the isotopes, but this requires, on the contrary, a small size of the target to reduce the lengths of the isotope paths. However, a small size could lead to extreme temperatures, due to the reduced radiant cooling, and consequently to the melt down of the target. Besides, high temperatures increase the thermal velocity of the isotopes, leading to the reduction of the release time [24].

2.3.1 Boundary conditions

In order to reduce the degrees of freedom in the design of the SPES 70 MeV UC_x low power target, the external dimension of the SPES 40 MeV SiC low power target is maintained, so as the same heater configuration. The main geometrical constraints are summarized as follows:

- Discs: 13 mm diameter
- Tantalum heater: 110 mm length, 20 mm inner diameter, 0.5 mm thickness
- Graphite box: 70 mm length, 16 mm inner diameter, 0.8 mm thickness

Concerning the proton beam, an energy of 70 MeV is set and a centered beam without wobbler is foreseen. The beam shape is assumed to be Gaussian, as presented in Section 1.4.2.

2.3.2 Definition of the main parameters

Once the external dimensions are set, four main parameters have to be defined: the thickness and number of the discs, the power and size of the beam. These factors influence the target performance in terms of number of fissions, release time, maximum temperatures and mechanical stresses in the discs.

As shown in Section 1.4.2, the beam size is defined by the Gaussian standard deviation, or RMS radius. Initially an RMS radius equal to 4 mm is chosen. As shown in Section 2.2.1, in fact, an higher beam energy leads to higher straggling and scattering of the protons, decreasing the isotope production and the power deposition in the last discs [8]. With the aim to mitigate these effects, a smaller size of the beam, with respect to the 40 MeV centred beam, is chosen. However, a comparison with an RMS beam radius equal to 5 mm will be also presented in Section 2.3.5.

The maximum beam power will be determined in the following section by means of thermal and structural simulations. The power *P* deposited in the target is obtained as:

$$P = E \cdot I_{target} \quad [W] \tag{2.6}$$

where E is the beam energy [MeV/q] and I_{target} is the beam current reaching the target [μA]. In fact, not all the beam particles will reach the target, due to beam intensity loss along the beam line. A higher current should therefore be provided by the cyclotron. Assuming a Gaussian distribution of the beam, as shown in Section 1.4.2, it is possible to calculate the percentage of the beam reaching the target as:

$$\int_{\theta_0}^{\theta_f} \int_{r0}^{rf} \frac{1}{2\pi\sigma^2} \cdot e^{\frac{-\rho^2}{2\sigma^2}} \cdot \rho d\rho d\theta \tag{2.7}$$

$$\int_{r0}^{rf} \frac{1}{\sigma^2} \cdot e^{\frac{-\rho^2}{2\sigma^2}} \cdot \rho d\rho = \int_{0}^{r_d} \frac{1}{\sigma^2} \cdot e^{\frac{-\rho^2}{2\sigma^2}} \cdot \rho d\rho \tag{2.8}$$

$$1 - e^{-\frac{r_d^2}{2\sigma^2}} \tag{2.9}$$

With a disc radius equal to 6.5 mm and an RMS radius of the beam equal to 4 mm, about 73.3% of the particle will reach the target block, while with an RMS equal to 5 mm a percentage of 57% is obtained. In the next Sections, with *proton beam current* the current reaching the target is meant.

A thickness of 1 mm is chosen for the discs. Release studies performed by Corradetti [25] during on-line tests at the HRIBF facility of the Oak Ridge National Laboratory showed the production of several tens of radioactive isotopes with a target composed by 7 discs of 1 mm thickness. A higher thickness could increase the release time causing a loss of efficiency in the production of the most exotic species.

Concerning the number of discs, the projected range of a 70 MeV proton beam in a uranium carbide target is first calculated with SRIM [26], as shown in Section 2.2.1. At least 20 mm are required to fully stop the beam. Once the disc thickness is set at 1 mm, a first simulation with the FLUKA Monte Carlo code [22][23] is implemented with 20 discs. The normalized cumulative number of fissions is then estimated, as shown in Figure 2.6. It is evident that almost the entire amount of fissions is obtained for beam energies between 20 and 70 MeV. This is also in accordance with the uranium cross section, as shown in Figure 2.3.

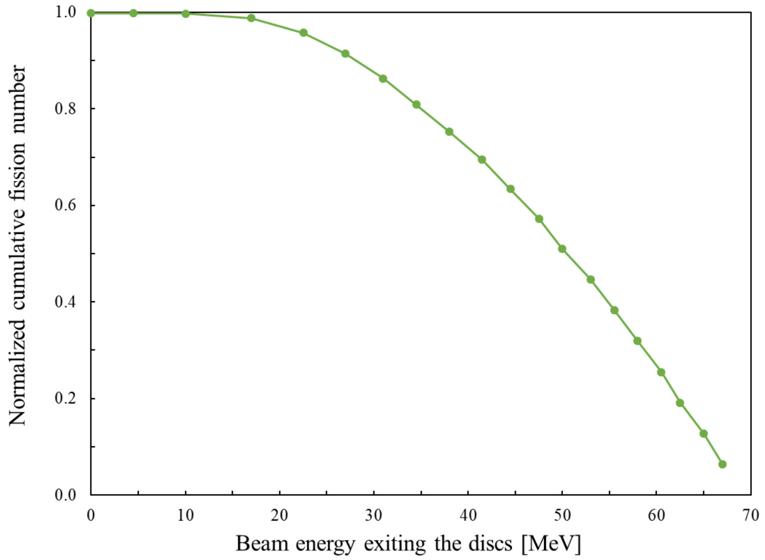

Figure 2.6 Normalize cumulative number of fissions for a 70 MeV proton beam impinging in a uranium carbide target with 20 discs (1 mm thickness).

The number of discs necessary to obtain an average exit energy of 20 MeV can be deduced in Figure 2.7, and is equal to 17. In fact, for a 70 MeV initial energy, about 2.1 MeV are deposited in the first disc of 1 mm thickness. Therefore, after the first disc, the beam will exit with an average energy of about 67.9 MeV, being the latter the initial energy for the next disc. Since the initial average energy of the entering beam is lower, a higher energy of about 2.3 MeV will be deposited in the second disc, and so on. In the 17th disc, the beam will enter with an average initial energy of about 23.6 MeV and an energy deposition of about 5 MeV will occur, leading to an average exit energy of about 18.7 MeV. Downstream the target, graphite dumps will be used to completely stop the beam. Taking into account the available length inside the graphite box and setting the number of discs to 17, a distance between each disc of 1 mm is chosen. A higher distance could in fact lead to a higher beam transverse spread on the target discs and, consequently, to the loss of beam current to the graphite box.

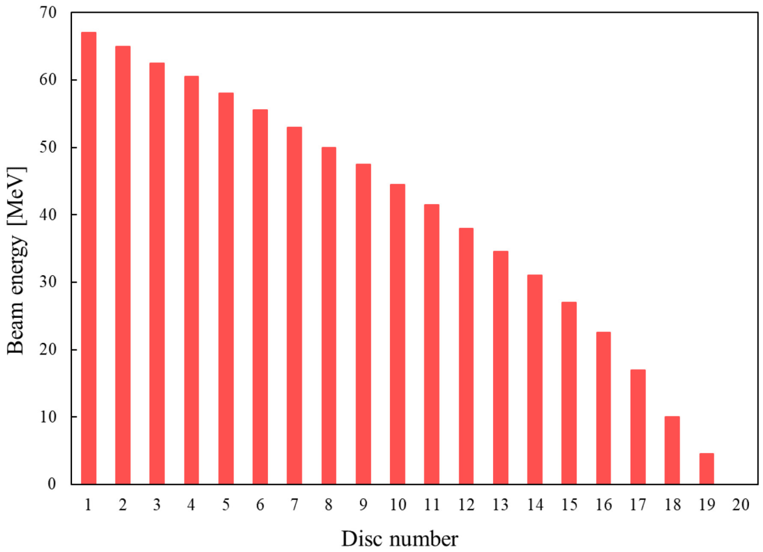

Figure 2.7 Average beam energy at the exit of each Uranium Carbide disc of the target, for an initial beam energy of 70 MeV and for discs thicknesses of 1 mm.

2.3.3 2D Thermal and structural simulations

During the dimensioning process, the power deposition is calculated by means of the FLUKA Monte Carlo simulation code. A detailed analysis aimed at validating the reliability of this code was already presented in previous works [19]. In the present simulation, a 70 MeV proton beam with RMS radius of 4 mm impinges on the target assembly composed of 17 uranium carbide discs, a graphite box, three graphite windows, three graphite dumps and the relative spacers, as show in Figure 2.8.

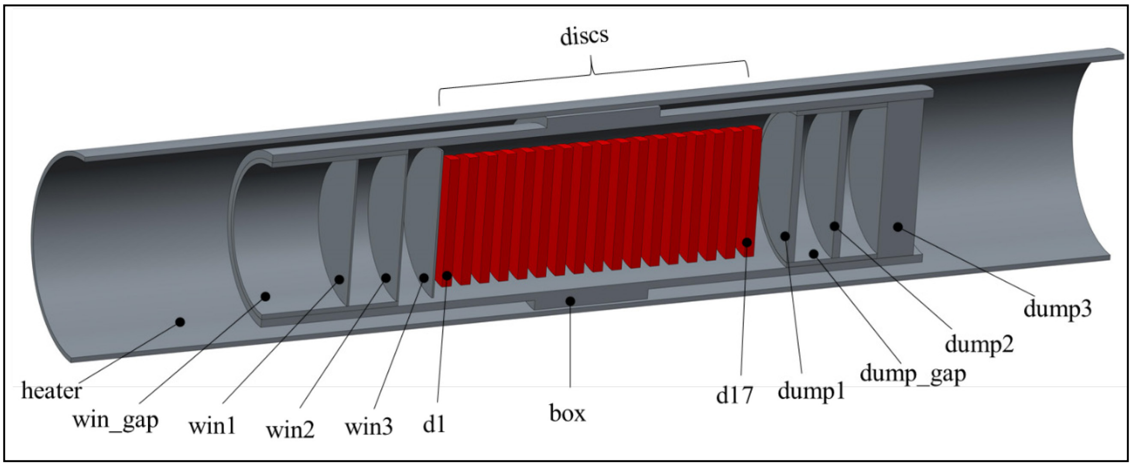

Figure 2.8 Components of the target assembly implemented in the simulations.

A collimator with an exit diameter of 13 mm, equal to the diameter of the target discs, is also simulated in order to shape the beam. A regular spatial mesh is defined and the power deposition distribution is calculated for each component.

Thermal-structural simulations are then implemented in ANSYS Mechanical [27]: the power deposition calculated with FLUKA is applied as body load to calculate the thermal distribution, and the thermal distribution is given as boundary condition for stress analysis on the discs. Initially, a simplified axisymmetric geometry of the target is used. This allowed faster bi-dimensional simulations in the first stage of the dimensioning process to be performed. Only the heather tube is simulated, without the tantalum wings and the copper connectors. Moreover, a constant heat power generation is imposed in the tube, instead of a current flow. No contact is foreseen between the heater, the box, the discs, the windows and the dumps, considering radiating energy as the only heat transfer method. To complete the geometry, the chamber is introduced, fixing its temperature at 50°C. However, as shown in [8], this value does not affect the temperature of the target block, being the chamber sufficiently large. The final bi-dimensional model is shown in Figure 2.9.

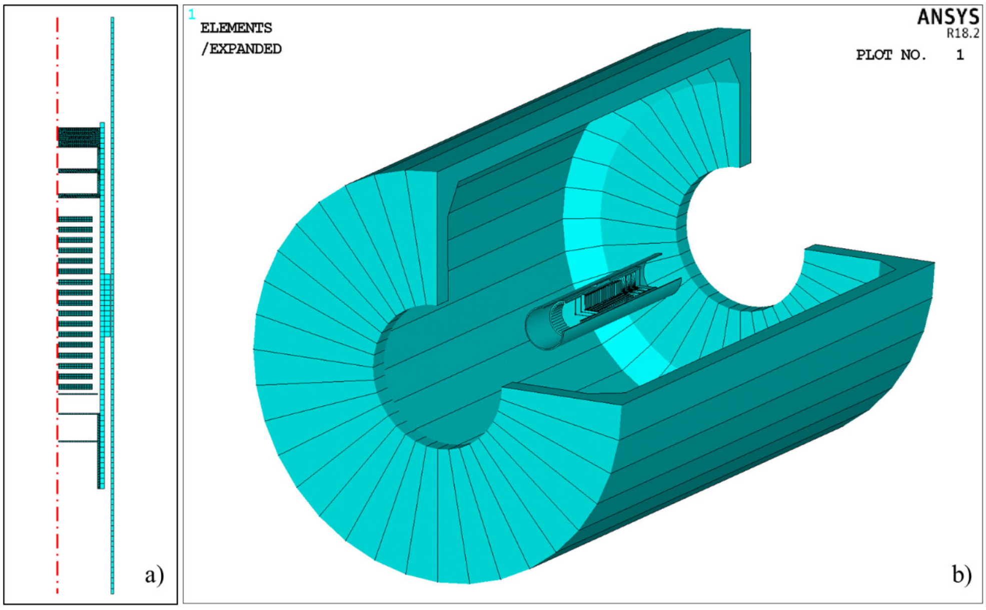

Figure 2.9 Bi-dimensional model implemented in ANSYS (a) and its axisymmetric expansion (b).

Heating is obtained by beam power deposition and by Joule effect in the heater tantalum tube. The only constraints on the available heater power regard the maximum current and the potential difference provided by the power supply. In particular, the current must not exceed 1300 A and the potential difference must be lower than 13 V. Assuming a maximum heater power of 3000 W, the constraints are verified as follows. The electric resistance *R* of the tantalum tube is calculated as:

$$R = \frac{\rho L}{A} = 8.3 \cdot 10^{-7} \Omega m \cdot \frac{0.11\, m}{\pi \cdot (0.0105^2 - 0.01^2)} = 2.835 \cdot 10^{-3}\, \Omega \qquad 2.10$$

where ρ is the tantalum electrical resistivity (at about 1800°C), L is the heater length and A is the heater's cross-sectional area. With a heater power of 3000 W, the requested current *I* results:

$$I = \sqrt{\frac{P}{R}} = \sqrt{\frac{3000\ W}{2.835 \cdot 10^{-3}\ \Omega}} \cong 1030\ A \quad < \mathbf{1300\ A} \tag{2.11}$$

where P is the heater power and R is the electrical resistance. The corresponding potential difference ΔV is then calculated as:

$$\Delta V = I \cdot R = 1030\ A \cdot 2.835 \cdot 10^{-3}\ \Omega = 2.92\ V < \mathbf{13\ V} \tag{2.12}$$

Therefore, both constraints are respected with a heater power of 3000 W.

Before starting the analysis, a sensibility study on the V2DOPT ANSYS command is performed. This command allows the axisymmetric view factor calculation options to be specified. In radiative heat transfer, the view factor F_{ij} is defined as the fraction of total radiant energy leaving surface *i* that arrives on surface *j*. With V2DOPT it is possible to define the number of zones for the view factor calculation [28]. Different results are obtained with different number of divisions. In order to set the proper V2DOPT value, several bi-dimensional simulations with different number of divisions are compared with a similar three-dimensional model. An arbitrary value of the proton beam current equal to 8.5 μA and of the heater power equal to 1200 W are fixed, since the only aim of the comparison is to set the proper V2DOPT value. In Figure 2.10 the comparison of the temperatures reached in the main components of the target is reported. By evaluating the results, a value of 300 divisions is chosen: with this value, in fact, equal or higher temperatures with respect to the 3D model are obtained.

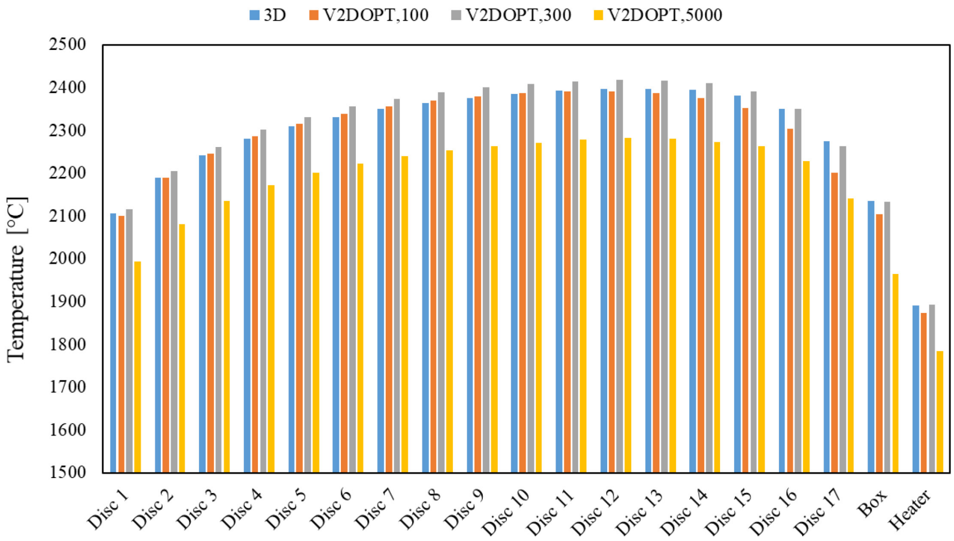

Figure 2.10 Sensitivity analysis on the V2DOPT parameter for the bi-dimensional axisymmetric model with respect to the three-dimensional model.

It is important to remark that, also in the three-dimensional model, options for the view factors calculation are defined, by means of the HEMIOPT ANSYS command. However, the correct settings have been already verified in previous studies through comparison with experimental data [29].

Since both the beam current and the heater power must be determined, parametric simulations are implemented, by varying the heater power between 0 and 3000 W, with steps of 300 W, and the beam current between 4.5 μA and 9 μA, with steps of 0.5 μA. For each combination, the maximum discs' temperature and stress are analyzed. Setting for uranium carbide a maximum temperature of about 2300°C and a maximum stress of 200 MPa, the eligible combinations are highlighted, as shown in Figure 2.11. It is important to remark that the Von Mises stresses are considered in the structural analysis, as already done in previous studies [8][18]. However, the behavior of the uranium carbide is not well known for the working temperatures of the SPES targets. For this reason, also the principal stresses are checked during the analysis.

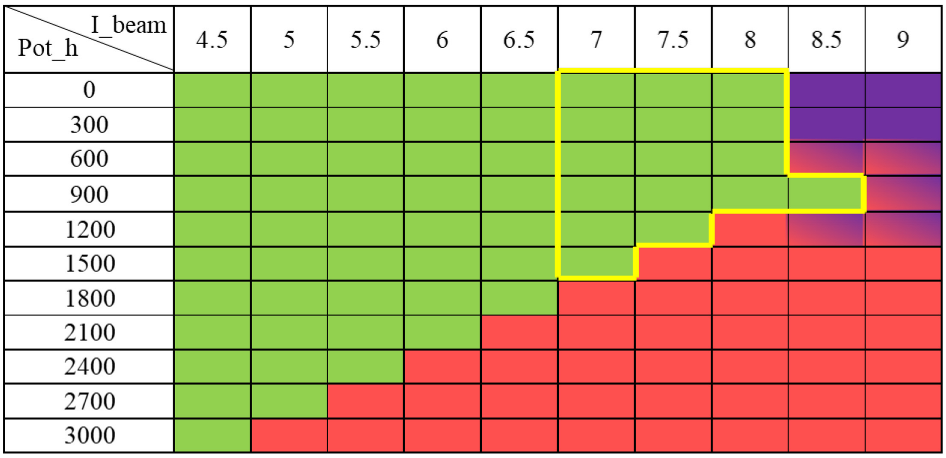

Pot_h \ I_beam	4.5	5	5.5	6	6.5	7	7.5	8	8.5	9
0	🟩	🟩	🟩	🟩	🟩	🟩	🟩	🟩	🟪	🟪
300	🟩	🟩	🟩	🟩	🟩	🟩	🟩	🟩	🟪	🟪
600	🟩	🟩	🟩	🟩	🟩	🟩	🟩	🟩	🟥🟪	🟥🟪
900	🟩	🟩	🟩	🟩	🟩	🟩	🟩	🟩	🟩	🟥🟪
1200	🟩	🟩	🟩	🟩	🟩	🟩	🟩	🟥	🟥🟪	🟥🟪
1500	🟩	🟩	🟩	🟩	🟩	🟩	🟥	🟥	🟥	🟥
1800	🟩	🟩	🟩	🟩	🟩	🟥	🟥	🟥	🟥	🟥
2100	🟩	🟩	🟩	🟩	🟥	🟥	🟥	🟥	🟥	🟥
2400	🟩	🟩	🟩	🟥	🟥	🟥	🟥	🟥	🟥	🟥
2700	🟩	🟩	🟥	🟥	🟥	🟥	🟥	🟥	🟥	🟥
3000	🟩	🟥	🟥	🟥	🟥	🟥	🟥	🟥	🟥	🟥

Figure 2.11 Schematic results of the preliminary dimensioning simulations, by varying the heater power (Pot_h, in W) and the beam current (I_beam, in μA). The eligible combinations are shown in green; in purple the not acceptable combinations due to excessive stresses; in red the not acceptable combinations due to excessive temperature. In yellow, the analyzed combinations are highlighted.

In Figure 2.12 the maximum beam current and the corresponding maximum temperature reached in the hottest disc are shown, as a function of the heater power. As can be seen, up to 600 W the heater power allows an increase of the maximum beam current by reducing the temperature gradient in the discs, and consequently the stresses. However, for higher heater power, the beam current must be decreased to prevent the maximum temperature for uranium carbide to be overcome.

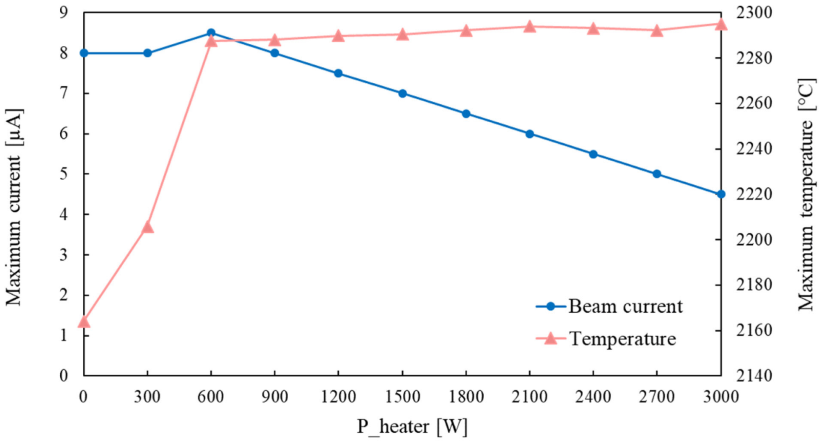

Figure 2.12 The maximum beam current and the corresponding maximum temperature reached in the hottest disc, by varying the heater power.

In Table 2.2, the temperatures and the stresses for the most interesting combinations are reported. In particular: T_{max} represents the maximum temperature reached in the hottest disc; T_{min} the minimum temperature reached in the coldest disc; ΔT is the difference between the previous values; σ_{VM} is the maximum Von Mises stress; *Number of fissions* represents the number of fissions obtained at the corresponding beam current.

Table 2.2 Maximum temperatures and stresses in the discs by varying the beam current and the heater power, for a RMS radius of 4 mm.

I_beam [µA]	***Pot_h [W]***	***T max [°C]***	***T min [°C]***	***ΔT***	***σ_{VM} [MPa]***	***Number of fissions***
7.0	0	2073	1664	409	160	9.75E+11
7.0	300	2122	1728	394	156	9.75E+11
7.0	600	2169	1790	380	153	9.75E+11
7.0	900	2214	1847	367	150	9.75E+11
7.0	1200	2253	1896	357	148	9.75E+11
7.0	1500	2291	1943	347	145	9.75E+11
7.5	0	2120	1695	425	169	1.04E+12
7.5	300	2164	1755	409	165	1.04E+12
7.5	600	2211	1815	396	162	1.04E+12
7.5	900	2252	1869	383	159	1.04E+12
7.5	1200	2290	1917	373	156	1.04E+12
8.0	0	2164	1724	440	178	1.11E+12
8.0	300	2206	1781	425	174	1.11E+12
8.0	600	2249	1838	411	171	1.11E+12
8.0	900	2288	1889	399	168	1.11E+12
8.5	600	2288	1861	426	180	1.18E+12

In order to choose the best combination, it is important to remark that:

- Increasing the beam current, the number of fissions increases;

- A temperature of about 2000°C must be guaranteed in the target assembly, in order to enhance the radioactive isotopes extraction;
- Given the uncertainties about the maximum temperature and stress for uranium carbide, a safety factor should be considered. Further experimental tests on the material's properties could lead to a different choice.

With this is mind, a beam current of 7.5 μA and a heater power of 900 W are chosen. With these values, a reasonable number of fissions of about $1.04 \cdot 10^{12}$ is obtained, but safer maximum temperature and stress are guaranteed with respect to a higher beam current. In Figure 2.13 the power density radial distributions for some discs are presented. As expected, the last disc is subject to a higher power deposition. In Figure 2.14, the power deposition and the corresponding temperature distribution obtained with ANSYS are presented for the 17 discs.

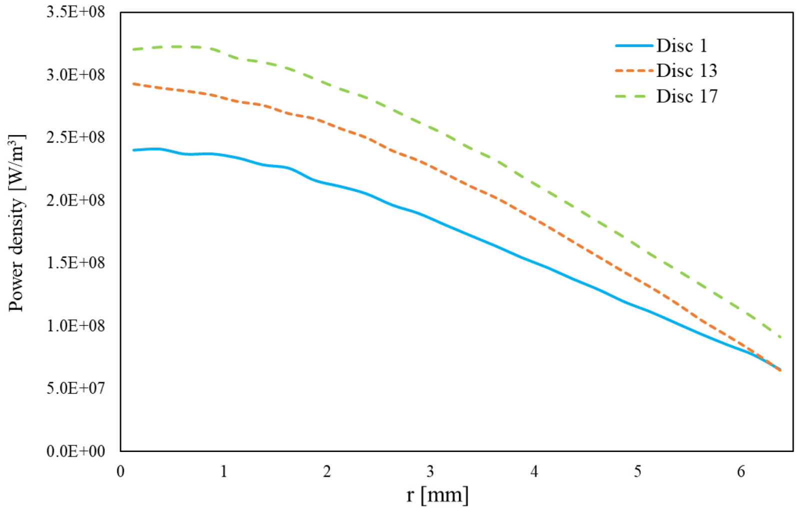

Figure 2.13 Power density radial distributions for some UCx disc, for 7.5 μA beam current.

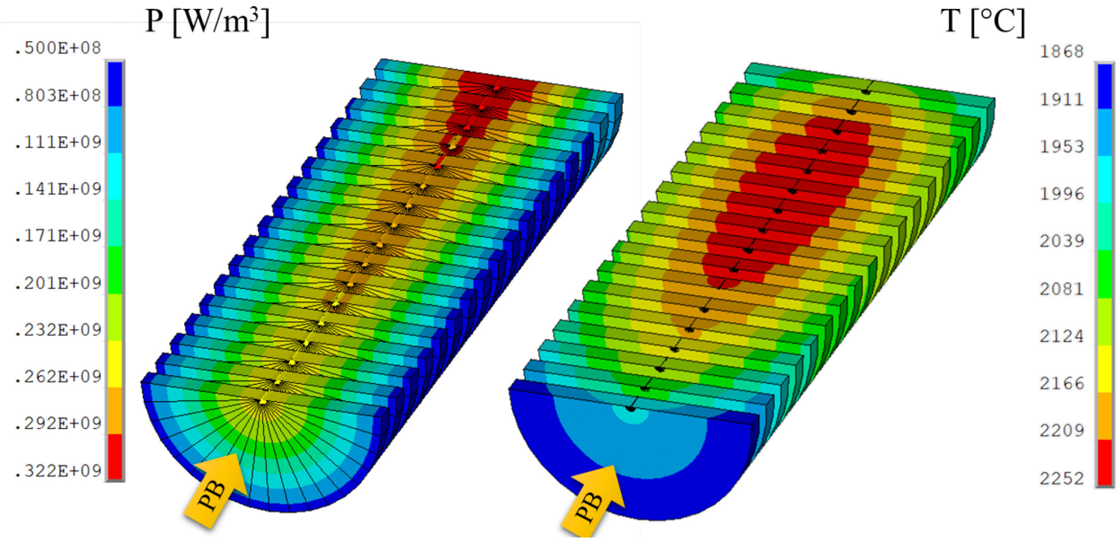

Figure 2.14 Power deposition and temperature distribution in the uranium carbide discs, with 7.5 μA beam current and 900 W heater power, obtained with the simplified axisymmetric 2D model.

The maximum, the mean and the minimum temperatures reached in each disc are shown in Figure 2.15, while in Figure 2.16 the maximum Von Mises stresses and the corresponding temperature differences are reported. A close correlation between these two values can be noted.

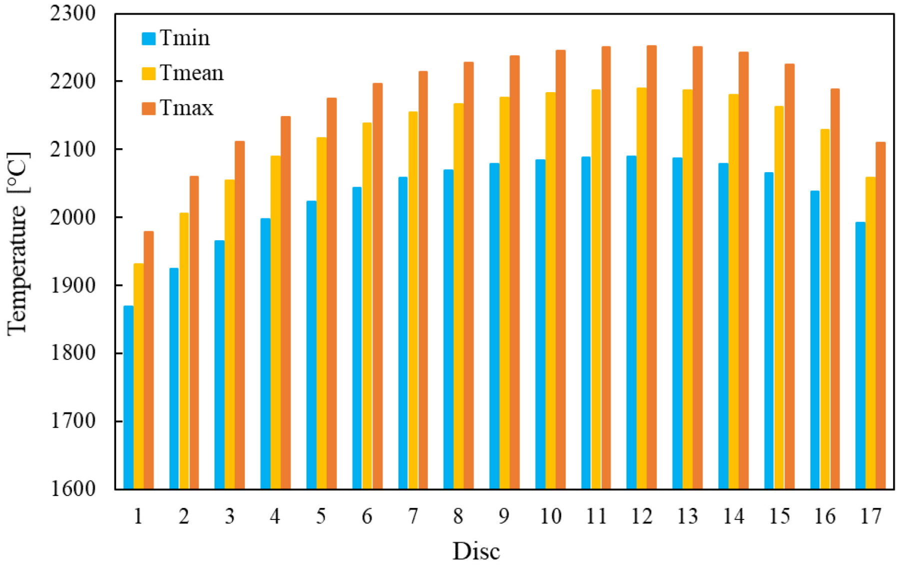

Figure 2.15 Minimum (T_{min}), mean (T_{mean}) and maximum (T_{max}) temperature reached in each disc with 7.5 μA beam current and 900 W heater power, obtained with the simplified axisymmetric 2D model.

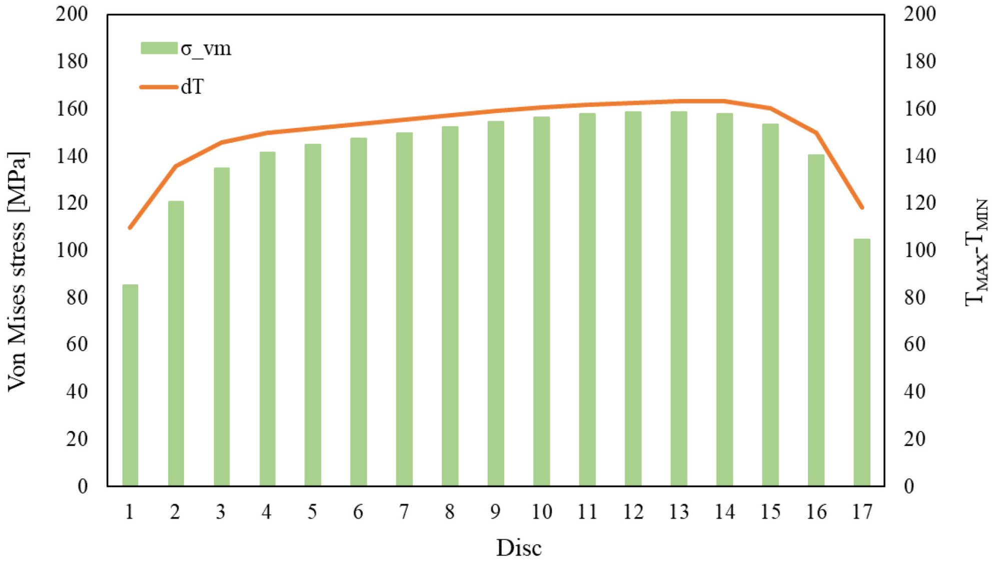

Figure 2.16 Maximum Von Mises stresses (σ_vm) reached in each disc and relative temperature difference (dT), with 7.5 μA beam current and 900 W heater power, obtained with the simplified axisymmetric 2D model.

Finally, in Table 2.3, the power deposition and the maximum temperature for each target assembly component are reported. Considering a maximum operating temperature of 2200°C for tantalum and 2500°C for graphite, it can be noted that a critical temperature is not reached in any component.

Table 2.3 Power, temperature and maximum stress for the uranium carbide discs and the other components of the target, with 7.5 µA beam current and 900 W heater power, obtained with the simplified axisymmetric 2D model.

Component	***Material***	***P [W]***	***T_{MAX} [°C]***	***σ_{VM} [MPa]***	***N°fission***
Disc 1	UCx	18.2	1978	85	$6.9\cdot10^{10}$
Disc 2	UCx	18.5	2060	121	$6.9\cdot10^{10}$
Disc 3	UCx	18.7	2111	135	$6.9\cdot10^{10}$
Disc 4	UCx	19.0	2148	141	$6.9\cdot10^{10}$
Disc 5	UCx	19.2	2175	145	$6.9\cdot10^{10}$
Disc 6	UCx	19.5	2197	147	$7.0\cdot10^{10}$
Disc 7	UCx	19.7	2214	150	$6.8\cdot10^{10}$
Disc 8	UCx	20.0	2227	152	$6.8\cdot10^{10}$
Disc 9	UCx	20.2	2237	155	$6.7\cdot10^{10}$
Disc 10	UCx	20.5	2245	156	$6.5\cdot10^{10}$
Disc 11	UCx	20.8	2250	158	$6.3\cdot10^{10}$
Disc 12	UCx	21.2	2252	159	$6.0\cdot10^{10}$
Disc 13	UCx	21.6	2250	159	$5.7\cdot10^{10}$
Disc 14	UCx	22.1	2243	158	$5.4\cdot10^{10}$
Disc 15	UCx	22.8	2225	153	$4.9\cdot10^{10}$
Disc 16	UCx	23.8	2188	140	$4.2\cdot10^{10}$
Disc 17	UCx	25.4	2110	105	$3.5\cdot10^{10}$
Heater	Tantalum	39.3	1758		
Box	Graphite	30.5	1993		
Window 1	Graphite	2.5	1529		
Window 2	Graphite	2.5	1681		
Window 3	Graphite	2.5	1820		
Dump 1	Graphite	19.1	1951		
Dump 2	Graphite	20.0	1858		
Dump 3	Graphite	52.6	1725		
Win_gap	Graphite	0.1	1595		
Dump_gap	Graphite	18.1	1901		

The higher number of fissions is obtained in the first discs, even though the maximum power is deposited in the last ones. However, the highest temperatures are registered around the 12th and 14th discs, so as the maximum stresses. This is due to the different cooling by radiation of the external discs with respect to the internal ones. The radial, circumferential, axial stress components, Von Mises stress and first principal stress in the middle plane of the 12th disc are shown in Figure 2.17. All the stress components in the most critical disc are lower than the fracture stress value of uranium carbide, equal to 200 MPa. It is important to remark, as explained in [29], that this fracture value is referred to a temperature of 1300°C. However, even though a decrease of this value is expected at higher temperature, the expected plasticity of uranium carbide should help to attenuate the stress state.

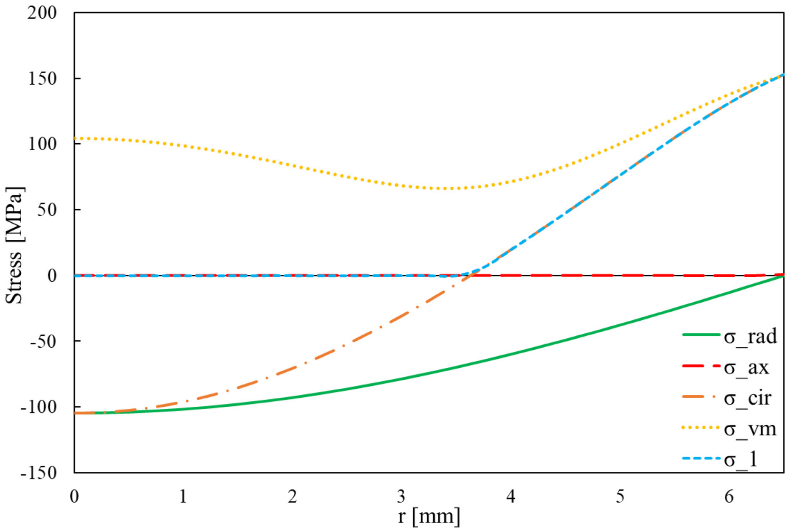

Figure 2.17 Radial (σ_rad), axial (σ_ax), circumferential (σ_cir) stress components, Von Mises (σ_vm) and first principal (σ_1) stress in the middle plane of the 12th disc, with 7.5 µA beam current and 900 W heater power, obtained with the simplified axisymmetric 2D model.

In the adopted model no Ion Source has been simulated. Actually, during operation, also the Ion Source is heated by Joule effect, to guarantee a temperature of about 2000°C of the transfer line in order to allow for the isotope effusion. However, the average temperature of the discs caused by the beam power deposition is higher than 2000°C. No significant influence of the ion source is therefore expected on the discs' maximum temperatures and stresses.

2.3.4 3D Thermal and structural simulations

In order to study in detail the behavior of the target block and to validate the assumptions of the bi-dimensional simulations, a new three-dimensional model is developed, as shown in Figure 2.18. A beam current of 7.5 µA and a heater power of 900 W are assumed. With respect to the simplified bi-dimensional axisymmetric model, a current flow is imposed through the copper clamps. In particular, a constraint of 0 V is assigned to one of the copper clamps, whereas an electric current is forced in the other one. A perfect electrical and thermal contact is considered between the tantalum support and the copper clamps. Natural convection is applied to the external surface of the chamber, while forced convection is applied to the surfaces of the chamber's cooling circuit. Also in this case, the power deposition obtained with FLUKA is imposed as input for the thermal structural simulation with ANSYS. In Figure 2.19 the comparison of the maximum temperatures reached in each component between the simplified bi-dimensional and the three-dimensional model are reported, while in Figure 2.20 the comparison of the maximum Von Mises stresses can be observed.

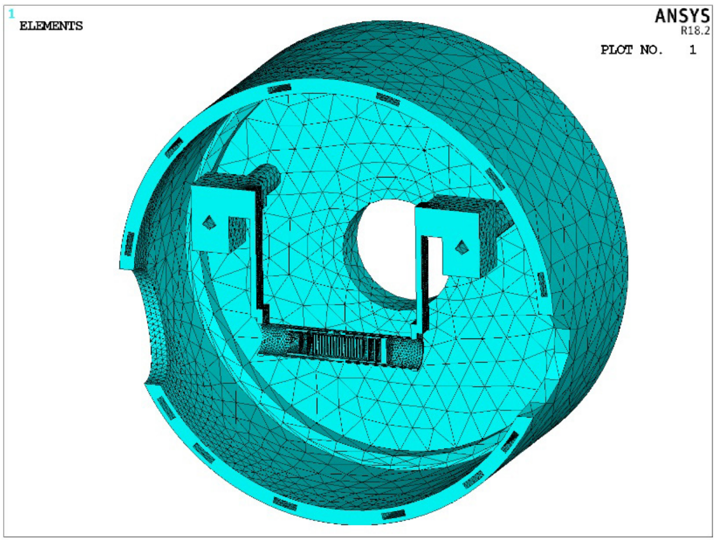

Figure 2.18 Section view of the 3D model used to simulate the thermal-electrical behavior of the target heating.

A slight decrease of the maximum temperatures in the central discs can be observed in the three-dimensional model. This is probably due to the holes in the cylinders of the heater and the box at the point of the connection with the transfer line, as shown in Figure 2.21. Also in the three-dimensional model, in fact, the ion source is not simulated. As previously said, its presence does not increase the maximum temperature of the discs, but it seems that its absence leads to a cooling of the central part of the target block. As a consequence, a higher temperature difference in the central discs leads to higher stresses. The maximum difference between the Von Mises stresses, observed in the 4th disc, is equal to 8%. However, also in this case, the stresses do not exceed the fracture value of 200 MPa.

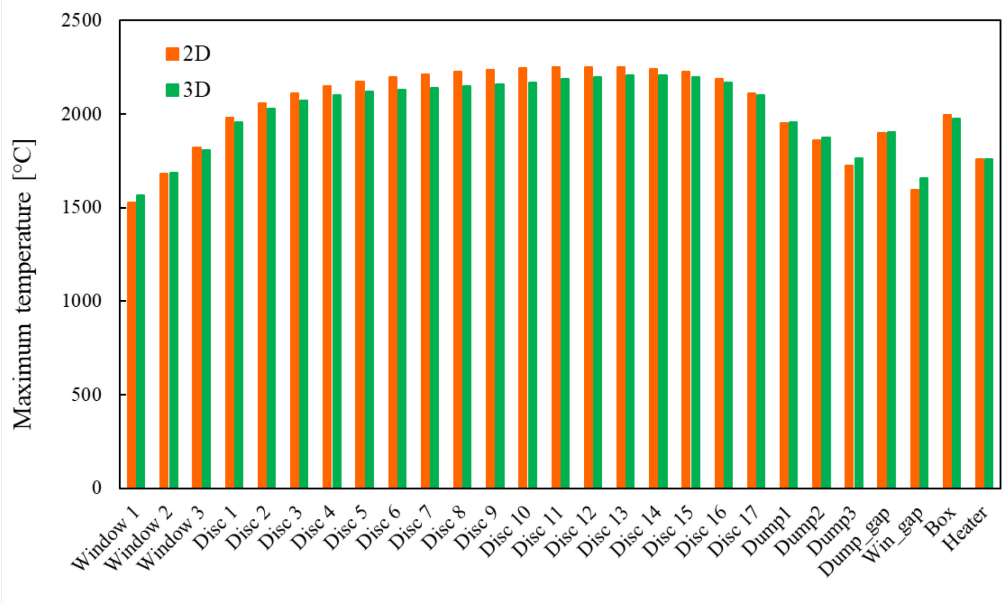

Figure 2.19 Comparison of the maximum temperatures of the components, between the simplified axisymmetric 2D model and the complete 3D model.

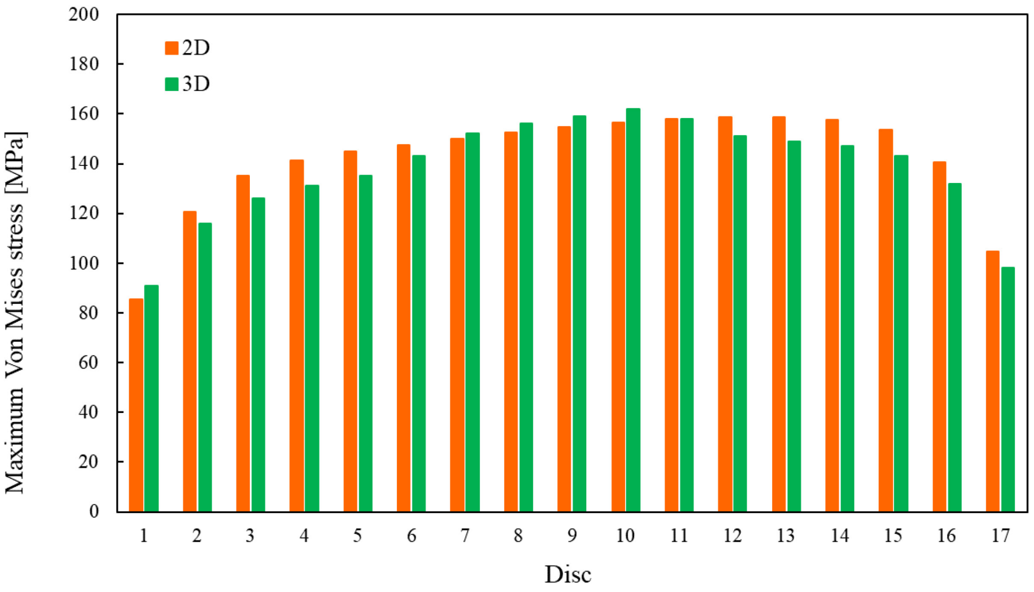

Figure 2.20 Comparison of the maximum Von Mises stresses on the uranium carbide discs, between the simplified axisymmetric 2D model and the complete 3D model.

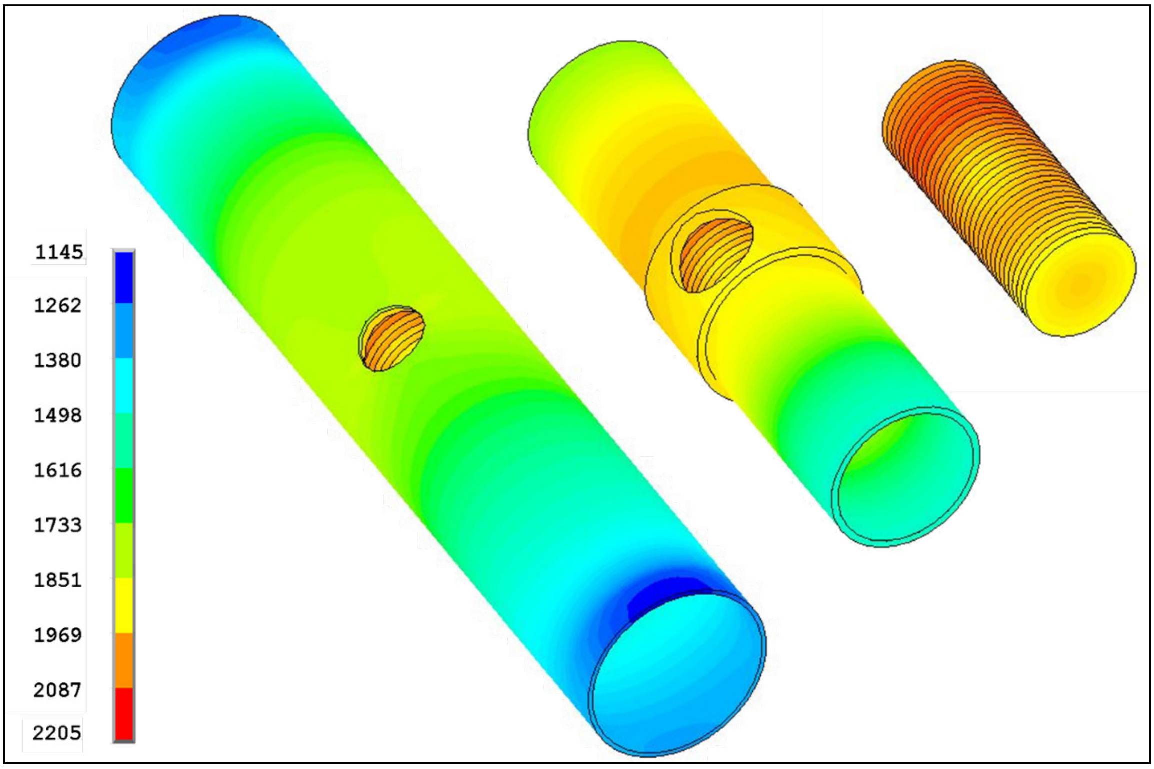

Figure 2.21 Cooling effect of the transfer line hole in the heater, the box and the discs, respectively. Temperature are expressed in [°C].

In Figure 2.22, the comparison of the temperature distributions along the radius of the 14th and 17th discs are shown: a cooling of the central discs in the three-dimensional model seems confirmed, while the temperature distributions in the 17th disc, far from the transfer line's hole, are very similar.

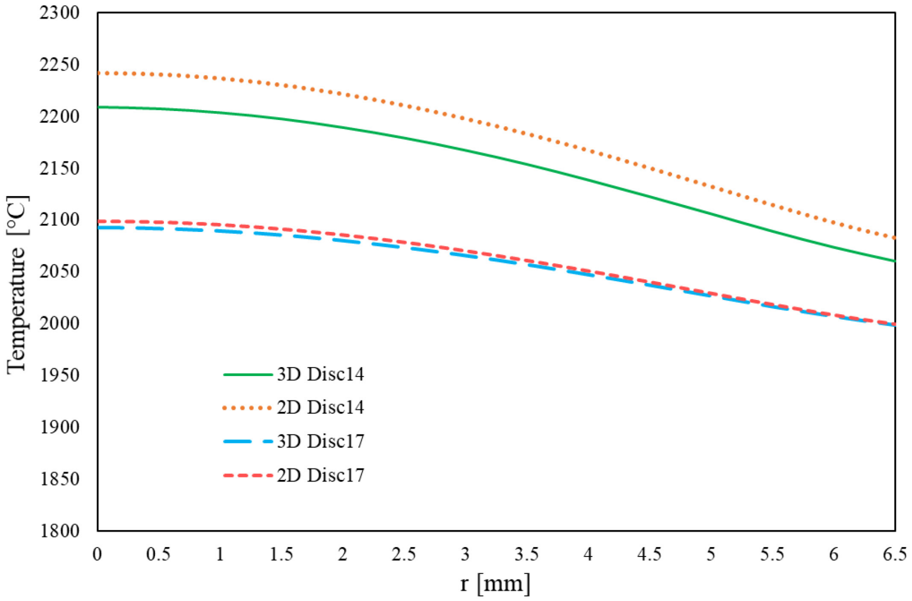

Figure 2.22 Comparison of the radial temperature distribution for the 14th and the 17th discs, between the simplified axisymmetric 2D model and the complete 3D model.

Particular attention is paid to the heater tube, in order to evaluate the importance of simulating a current flow instead of a power generation along the tantalum tube. In Figure 2.23 the temperature distribution along its length is shown, in different positions of the heater.

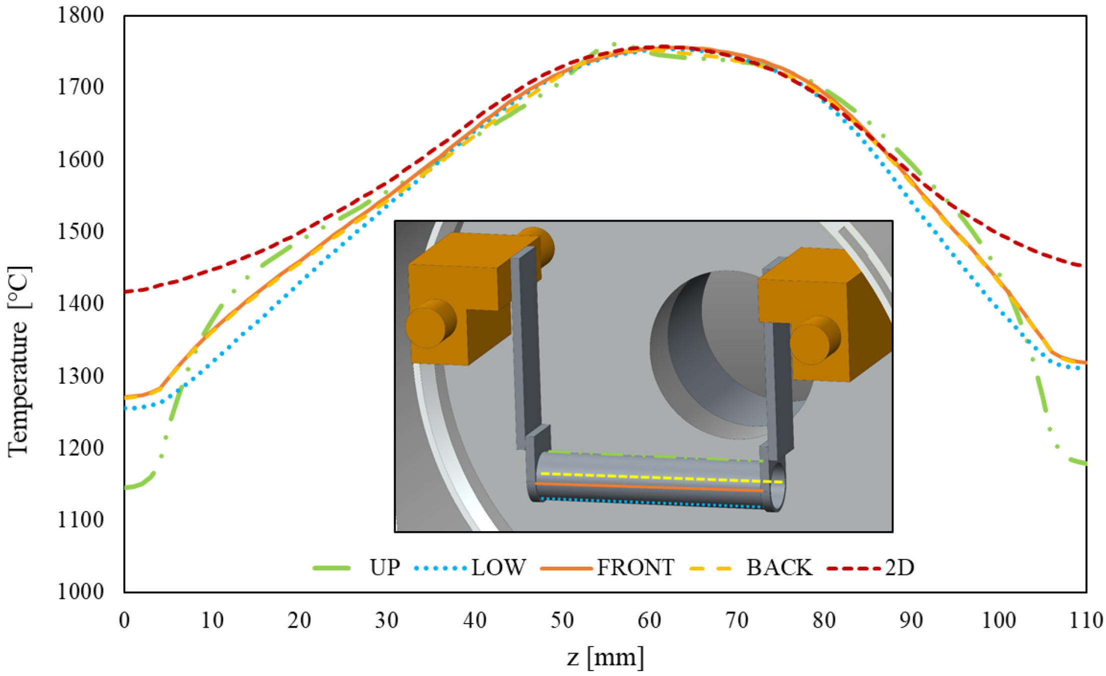

Figure 2.23 Comparison of the longitudinal temperature distribution on the heater tube, between the simplified axisymmetric 2D model and different positions of the complete 3D model.

As shown in Figure 2.23, no particular differences can be observed in the central part of the heater, where the discs are located. On the other hand, in the upper zones near the tantalum wings, a lower temperature is reached due to the cooling of the copper clamps. However, a higher current flow in the upper part of the tube leads to higher temperatures moving away from the wings.

2.3.5 Preliminary simulations with a different beam size

Once validated the bi-dimensional simulations, as seen in Section 2.3.4, it is possible to perform a preliminary study with a different beam size, choosing an RMS radius equal to 5 mm. The power deposition is calculated with the FLUKA Monte Carlo simulation code and thermal-structural parametric simulations are implemented in ANSYS, by varying the heater power and the beam current. Set a maximum temperature of 2300°C and a maximum stress of 200 MPa, the eligible combinations are presented in Figure 2.24 and Table 2.4. As shown, the only constraint is represented by an excessive temperature: no combination of heater power and beam current leads in fact to excessive stresses. This is in line with expectations, since a bigger size of the beam allows lower temperature difference between the center and the edge of the discs to be obtained. Moreover, if on the one hand, with the same current a lower number of fissions is expected with a bigger size of the beam, on the other, a higher current should be eligible before reaching the limit temperature of uranium carbide.

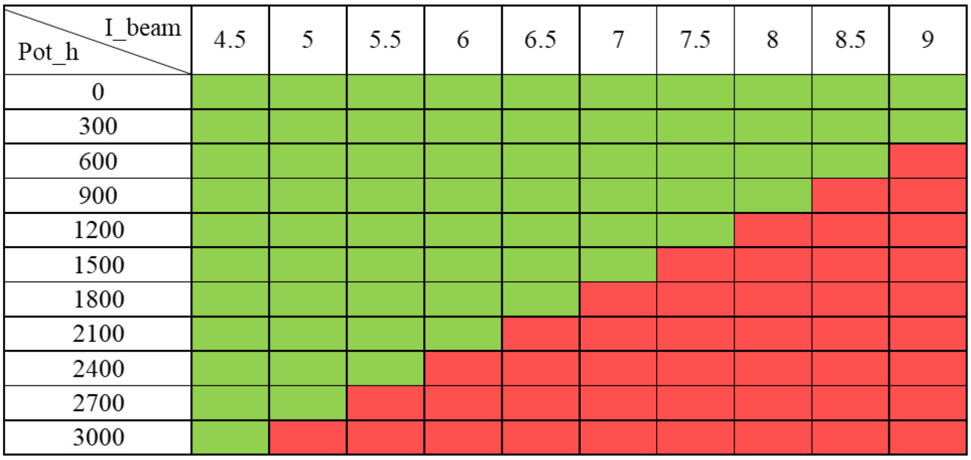

I_beam Pot_h	4.5	5	5.5	6	6.5	7	7.5	8	8.5	9
0	🟩	🟩	🟩	🟩	🟩	🟩	🟩	🟩	🟩	🟩
300	🟩	🟩	🟩	🟩	🟩	🟩	🟩	🟩	🟩	🟩
600	🟩	🟩	🟩	🟩	🟩	🟩	🟩	🟩	🟩	🟥
900	🟩	🟩	🟩	🟩	🟩	🟩	🟩	🟩	🟥	🟥
1200	🟩	🟩	🟩	🟩	🟩	🟩	🟩	🟥	🟥	🟥
1500	🟩	🟩	🟩	🟩	🟩	🟩	🟥	🟥	🟥	🟥
1800	🟩	🟩	🟩	🟩	🟩	🟥	🟥	🟥	🟥	🟥
2100	🟩	🟩	🟩	🟩	🟥	🟥	🟥	🟥	🟥	🟥
2400	🟩	🟩	🟩	🟥	🟥	🟥	🟥	🟥	🟥	🟥
2700	🟩	🟩	🟥	🟥	🟥	🟥	🟥	🟥	🟥	🟥
3000	🟩	🟥	🟥	🟥	🟥	🟥	🟥	🟥	🟥	🟥

Figure 2.24 Schematic results of the preliminary dimensioning simulations, by varying the heater power (Pot_h, in W) and the beam current (I_beam, in μA). The eligible combinations are shown in green, in red the not acceptable combinations due to excessive temperature.

Table 2.4 Maximum temperatures and stresses in the discs by varying the beam current and the heater power, for an RMS radius of 5 mm.

I_beam [μA]	**Pot_h [W]**	**T max [°C]**	**T min [°C]**	**dT**	**σ_{VM} [MPa]**	**Number of fissions**
7.0	0	2055	1667	388	151	9.54E+11
7.0	300	2105	1731	374	148	9.54E+11
7.0	600	2154	1793	360	145	9.54E+11
7.0	900	2197	1848	348	142	9.54E+11
7.0	1200	2239	1900	339	140	9.54E+11
7.0	1500	2276	1946	330	137	9.54E+11
7.5	0	2100	1697	403	160	1.02E+12
7.5	300	2147	1759	389	156	1.02E+12
7.5	600	2194	1818	375	154	1.02E+12
7.5	900	2236	1872	364	151	1.02E+12
7.5	1200	2273	1920	353	148	1.02E+12
8.0	0	2145	1727	418	168	1.09E+12
8.0	300	2187	1784	403	165	1.09E+12
8.0	600	2231	1841	390	162	1.09E+12
8.0	900	2271	1893	378	159	1.09E+12
8.5	0	2185	1754	432	176	1.16E+12
8.5	300	2227	1810	417	173	1.16E+12
8.5	600	2269	1865	404	170	1.16E+12
9.0	0	2226	1781	445	185	1.23E+12
9.0	300	2264	1833	431	181	1.23E+12

However, a higher power deposition in the box and in the heater should also be expected. For example, considering the limitations presented in Section 2.3.3, the combination with 8 μA beam current and 600 W heater power could be chosen. As shown in Figure 2.25, significant differences can be appreciated between the power deposited in the heater and the box in the two cases. Anyway, further analyses are necessary for a comprehensive comparison between the two cases, considering also the particle straggling inside the target chamber.

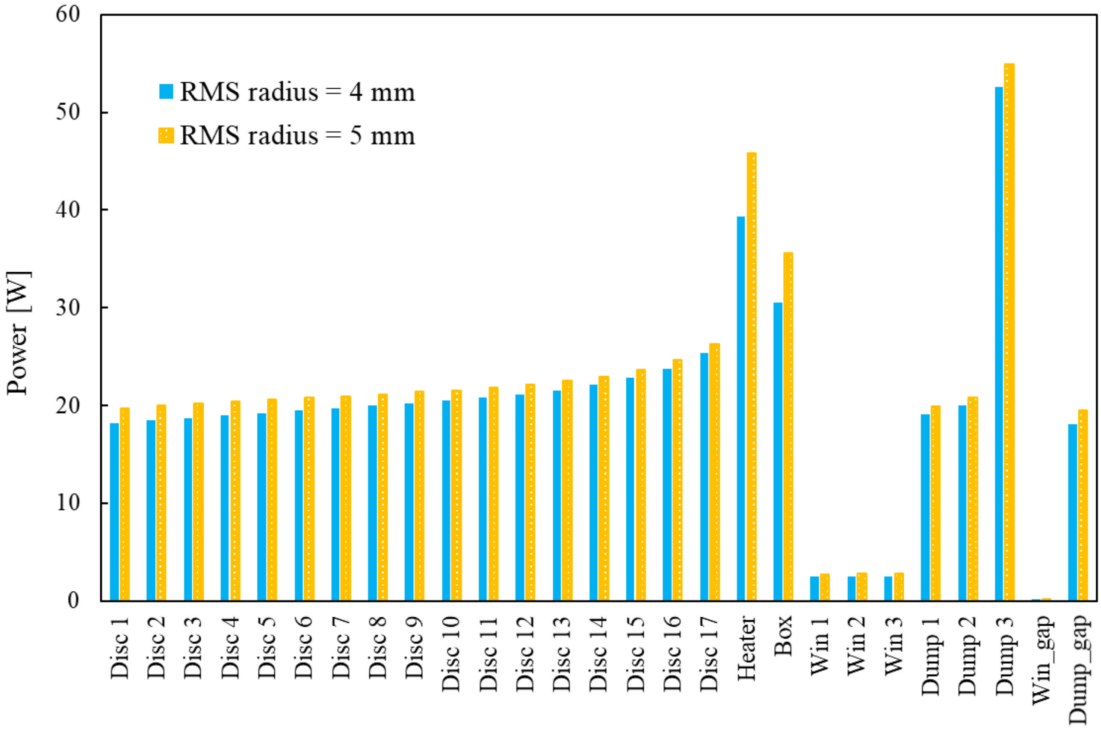

Figure 2.25 Comparison between the power deposition on the target components for a proton beam with 7.5 μA current and 4mm RMS radius (σ=4mm) and for a proton beam with 8 μA current and 5 mm RMS (σ=5 mm).

2.4 The collimator inside the target chamber

In the previous Sections, only the target block was studied, assuming a centered proton beam shaped by a collimator with an exit diameter of 13 mm, equal to the discs' diameter. In this Section the design of a new collimator housed inside the target chamber is presented. This device prevents the beam scattering on the surfaces surrounding the target assembly: this phenomenon would in fact lead to an excessive temperature of the aluminum target chamber. The collimator narrows the beam, in order to force the beam size into the target. For this reason, it has to be placed as close as possible to the target. The study presented in the next sections takes into account the thermal electric behavior of the component and its influence on the target's temperature and stresses.

2.4.1 Boundary conditions and preliminary design

During the design phase, several conditions must be fulfilled. Firstly, the collimator should be used with both a 40 MeV and a 70 MeV proton beam energy. At this purpose, a thickness able to completely stop the beam in both cases must be guaranteed. Secondly, the component must be housed inside the target chamber, far from the protonic VAT valve of the chamber. A significant power deposition in the collimator is in fact foreseen, which would cause its heating. The damage of the EPDM O-ring of the VAT valve must be avoided. Moreover, a material with a good thermal conductivity and high resistance at high temperature must be chosen for the design. Finally, the collimator should permit operations also in case of target misalignment and therefore an exit diameter bigger than the discs' diameter must be foreseen.

Considering all these constraints, a graphite collimator is designed. With this material, a thickness of at least 30 mm is requested to fully stop a 70 MeV proton beam. Considering the temperature distribution in the tantalum supports and their possible expansion during heating, a target misalignment of about 1 mm is estimated: an exit diameter of the collimator equal to 16 mm is therefore chosen. The resulting design is presented in Figure 2.26.

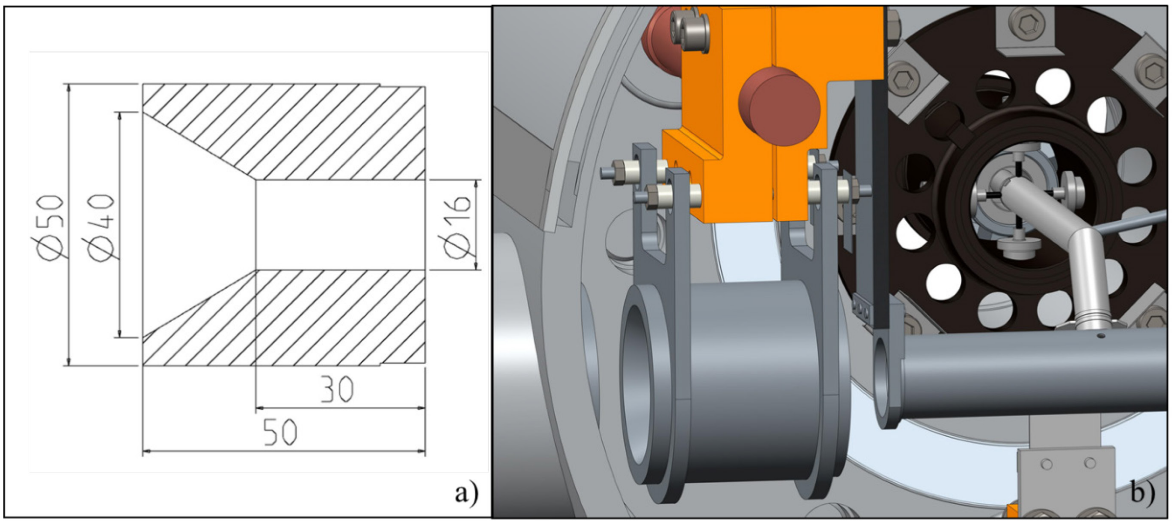

Figure 2.26 Section of the collimator and its possible positioning inside the target chamber.

It is important to remark that a higher exit diameter of the collimator leads to higher power deposition in the box and in the heater. Moreover, a higher number of protons can exit the target, not impinging in the uranium carbide discs. All these aspects are taken into account in the next sections. To check the behavior of the whole assembly, also the Plasma Ion Source is simulated.

2.4.2 Thermal study of the collimator

The 3D model of the target block, the collimator, the Plasma Ion Source and the surrounding vacuum chamber is reported in Figure 2.27. A simplified model is implemented in CREO Parametrics [30] and imported in ANSYS Mechanical [27] in order to carry out the thermal-electrical analysis (Figure 2.28).

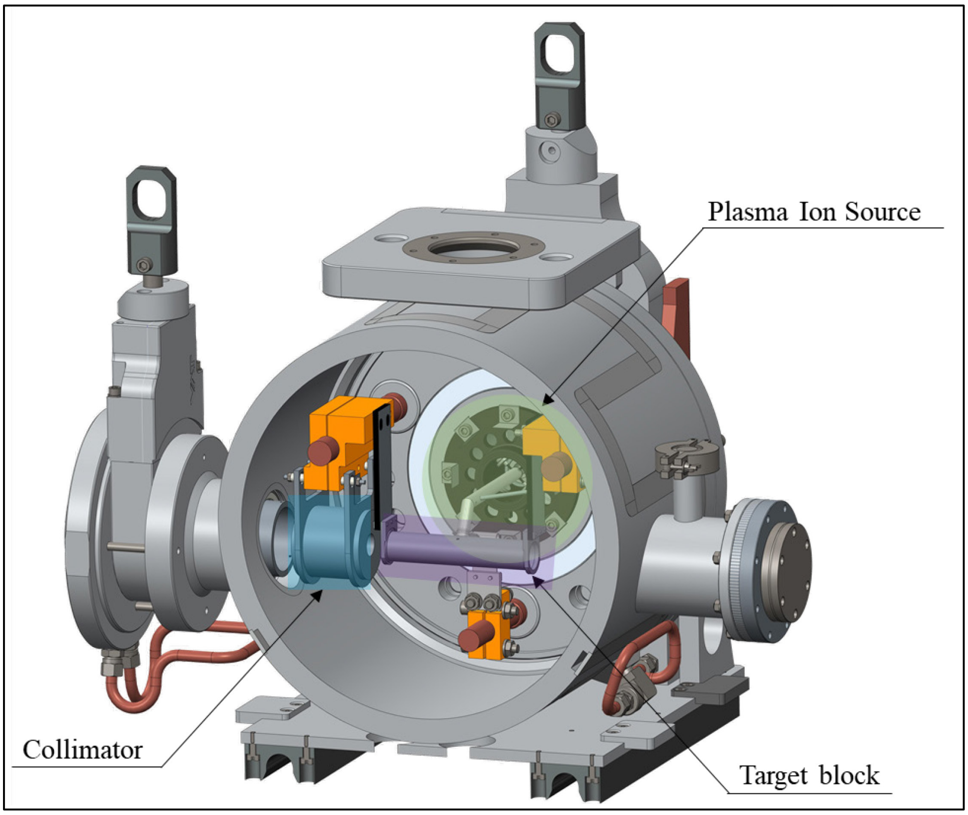

Figure 2.27 3D model of the assembly used during the pre-commissioning tests.

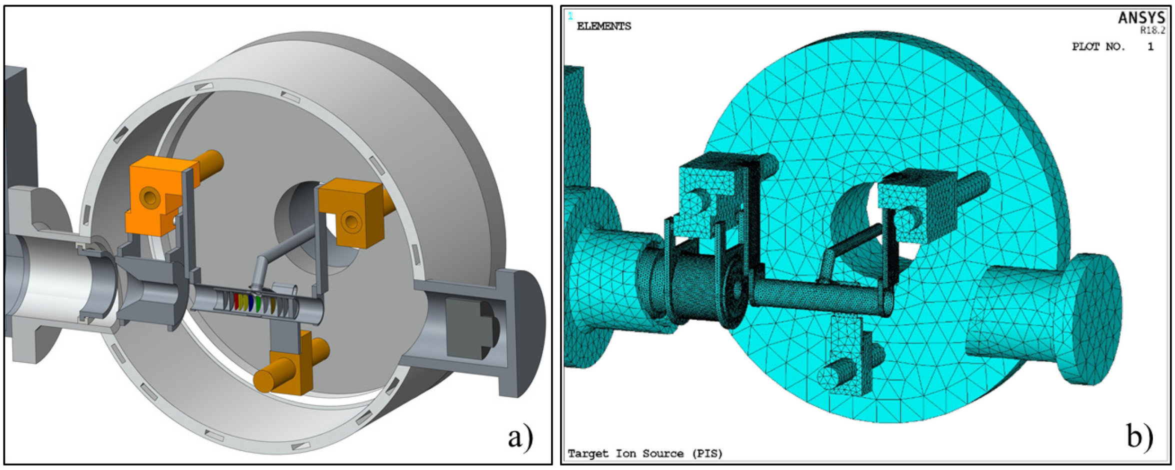

Figure 2.28 The simplified 3D model (a) implemented in ANSYS (b)

The same thermal loads and boundary conditions used in the previous Sections are imposed. In particular, a proton beam with an energy of 70 MeV, a current of 7.5 μA and an RMS radius equal to 4 mm is simulated. For the electrical loads, as shown in Figure 2.29, two different circuits are implemented. The first one, the target circuit, foresees two equal and opposite current loads in the upper clamps (in green in Figure 2.29). In the second one, the Plasma Ion Source (PIS) circuit, a current load is imposed in the lower clamp while a grounding constraint (0 V) is introduced at the end of the transfer line (in blue in Figure 2.29). In particular, for the PIS circuit, a current equal to

400 A is requested, in order to reach about 2000°C in the transfer line, necessary for its operation. For the target circuit a current of about 564 A is foreseen, to obtain a power of 900 W in the heater.

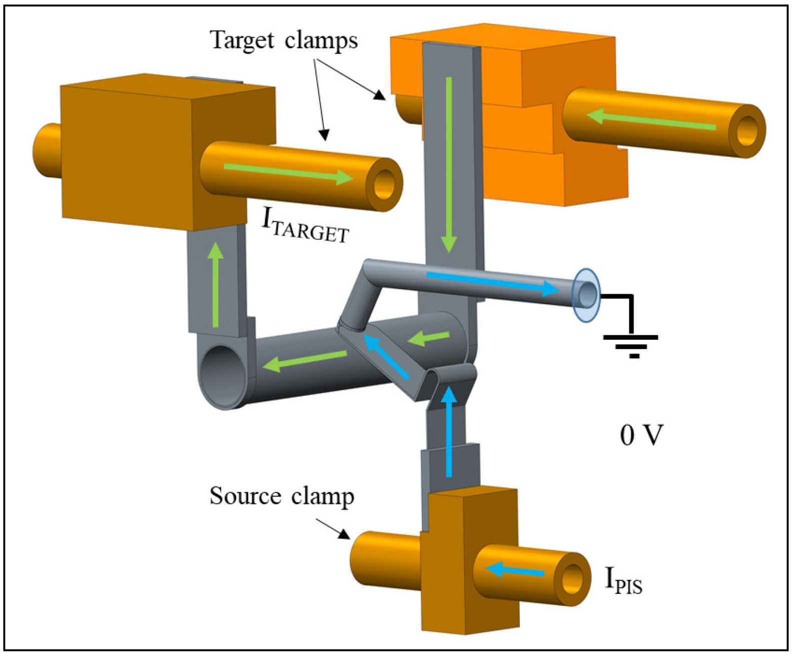

Figure 2.29 The target and the Ion Source electrical circuits, implemented in the thermal-electrical simulations.

The collimator's power deposition and temperature distribution are presented in Figure 2.30. As shown, no critical temperatures are reached: the maximum temperature of 610 °C is in fact far from the limit value for graphite, above 2000°C.

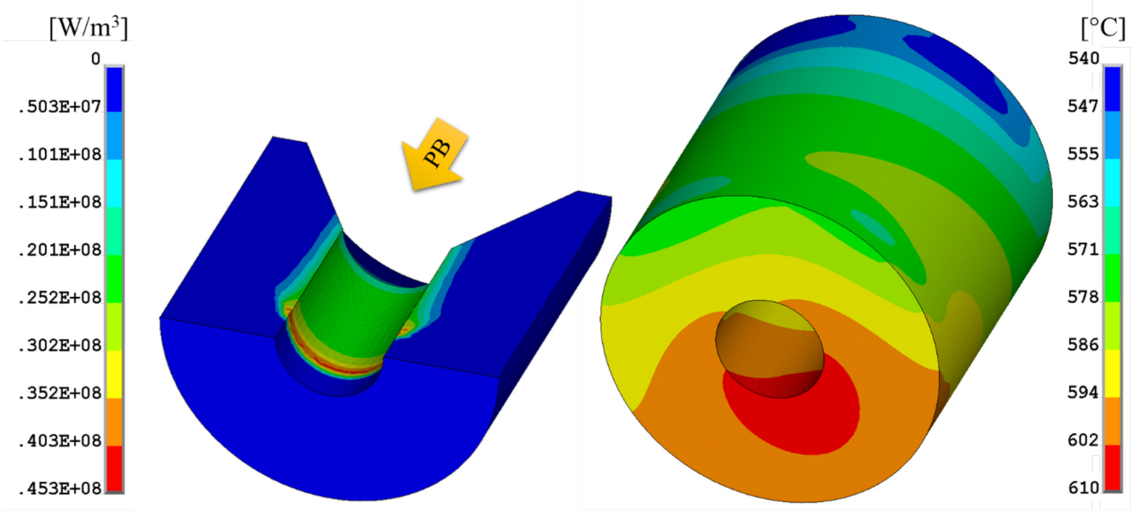

Figure 2.30 Collimator's power deposition (a) and temperature distribution (b).

In order to check the influence of the new collimator on the target block, the power deposition on different components of the assembly is shown in Figure 2.31. However, even if the deposition on the heater, the box and the last dump increases, a difference between the total power deposition in the two cases can be noted. This can be explained by looking at the proton fluxes shown in

Figure 2.32. With the new collimator, a bigger beam reaches the target. The beam external particles not intercepting the discs, that in the previous configuration were stopped in the collimator, are now able to reach the final dumps of the target assembly. However, the dumps are not enough thick to stop them. As a consequence, a portion of the beam not impinging neither the collimator nor the uranium carbide discs is able to exit the target assembly.

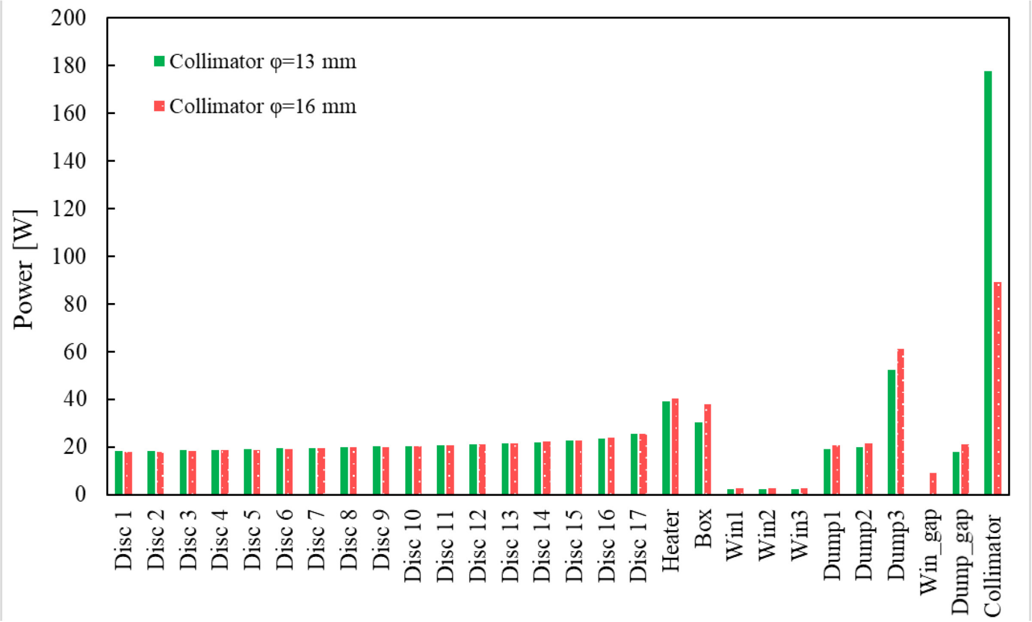

Figure 2.31 Comparison of the component's power deposition between the old collimator (exit diameter φ=13 mm) and the new collimator (exit diameter φ=16 mm).

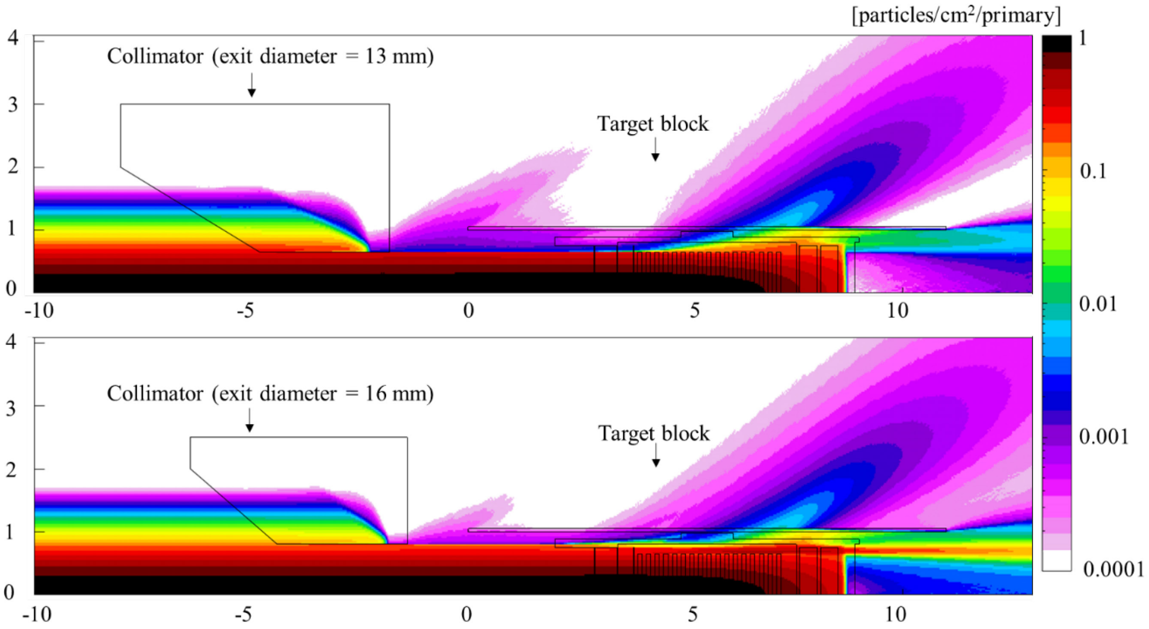

Figure 2.32 Proton flux mesh calculated with the FLUKA Monte Carlo code [22][23] *inside the target chamber by varying the collimator's exit diameter.*

In order to avoid this problem, a modification is proposed for the target block. In particular, the windows' and dumps' spacers are enlarged to stop the particles not impinging the uranium carbide discs. The inner diameter of the window's spacer is reduced up to 13 mm while the dumps' spacer is reduced up to 12 mm inner diameter. The proton flux mesh with the new target configuration is shown in Figure 2.33. It can be seen how, with this new configuration, the portion of the beam not impinging neither the collimator nor the uranium carbide discs is now stopped by the graphite spacers. With a new thermal-structural analysis implemented in ANSYS, no significant variations of the components' temperatures are highlighted.

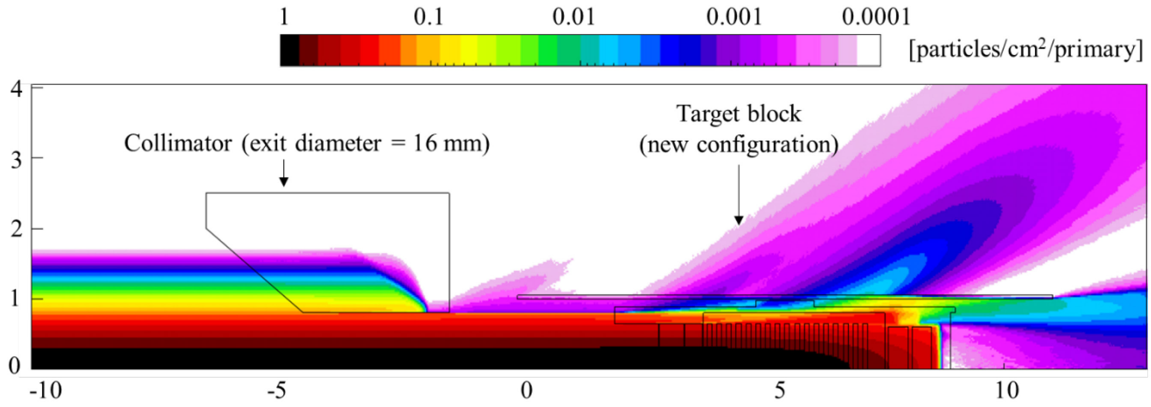

Figure 2.33 Proton flux mesh calculated with FLUKA for the new target configuration.

2.4.3 Potential distribution of the collimator

The beam current dropped in the collimator can be read by an ammeter, in order monitor the beam size and position, and to evaluate the current impinging in the target. For this reason, it is essential to suppress the emission of secondary electrons which are ejected when a particle with enough energy strikes a conductive surface. Using an electrode at a negative potential, the electrons emitted can be pushed back to the collimator. For a suppressor voltage of about -90 V almost all the electrons are shielded.

A simulation of the potential distribution is carried out to properly design the suppressor and assure the minimum potential shield to suppress the secondary electrons. An axisymmetric geometry is implemented and a potential of -1 V is applied in the suppressor, as shown in Figure 2.34. A suppression efficiency of about 0.3 is found at the entrance of the collimator: assuming a potential suppression of -300 V, a shielding potential of -90 V is ensured.

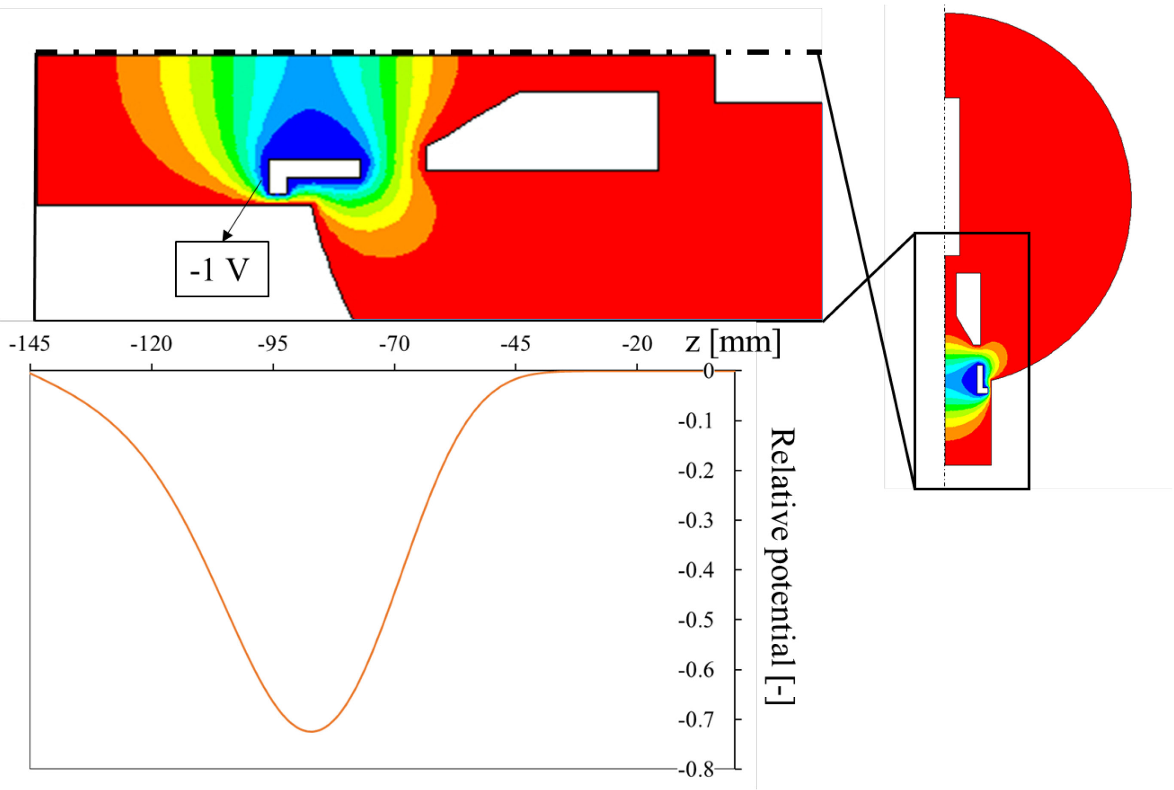

Figure 2.34 Potential distribution near the collimator's entrance.

2.5 Experimental tests at LNL

Off-line pre-commissioning tests have been planned at the National Laboratories of Legnaro of the National Institute for Nuclear Physics (LNL-INFN). In an off-line test, the target is heated only by Joule effect, created by electrical current flowing: therefore, no beam power is deposited. The SPES 40 MeV low power target is used for the test. As explained in Section 2.3.1, the relative dimensions of the SPES 40 MeV low power target have been maintained during the design of the SPES 70 MeV low power target. Similar temperatures are therefore expected on the heater and on the external graphite elements (first window and final dump), where the temperature measurements are carried out.

Silicon carbide discs are chosen for the tests. As a matter of fact, this material will be used for the first beam production: its relatively low activation after irradiation reduces the radioprotection issues and does not require any special permission. A commercial SiC material, the Hexoloy SA, is chosen, supplied by Saint-Gobain [31]. This material has been already characterized in detail in previous studies: its main characteristics are summarized in Table 2.5.

Table 2.5. Main characteristics for the Silicon Carbide Hexoloy SA used in the SPES target.

Property	Average value	Reference
Thermal conductivity	$30\ W/mK$	[32]
Emissivity	0.85	[33]
Bulk density	$3.18\ g/cm^3$	[33]
Melting point	$2300\ °C$	[32]
Maximum operating temperature	$1800\ °C$	[8]

The target configuration coupled with the Plasma Ion Source (see Section 1.4.2) is chosen. The collimator designed in Section 2.3 is also tested. Thermal-electrical simulations are implemented (Section 2.5.1) in order to evaluate the temperatures reached during the tests: the comparison with the experimental measurements is presented in Section 2.5.3.

2.5.1 Thermal-electric simulations

Thermal electrical simulations are implemented in order to recreate the real test conditions. Similar models and loads as shown in the previous sections are maintained but no proton beam deposition is implemented. In a first stage, only the Ion source load is imposed, by raising the PIS current with steps of 25 A and then keeping the current constant for 15 minutes at each step. When a maximum current of 380 A (necessary to reach 2000°C on the transfer line) is reached, the heating of the target is started, by raising the target current with step of 50 A, up to 1100 A, and keeping it for 15 minutes. The imposed load steps are shown in Figure 2.35.

The temperatures reached at each load step are then investigated for the components of main interest. In particular, the maximum temperature of the hottest disc is analyzed in order to define the maximum target current for the tests. The Silicon Carbide discs, in fact, must not exceed the limit of 1800°C [8]. As shown in Figure 2.36, at the end of the 800 A load step the limit temperature is reached. For this reason, a maximum target current of 800 A is defined for the tests.

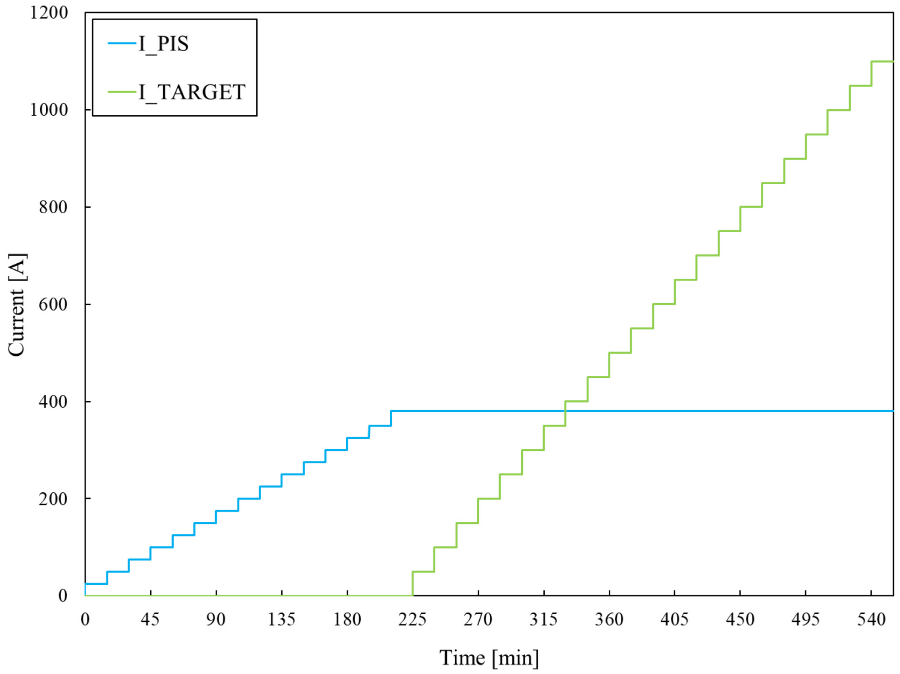

Figure 2.35 Current load steps implemented in the thermal-electrical simulations.

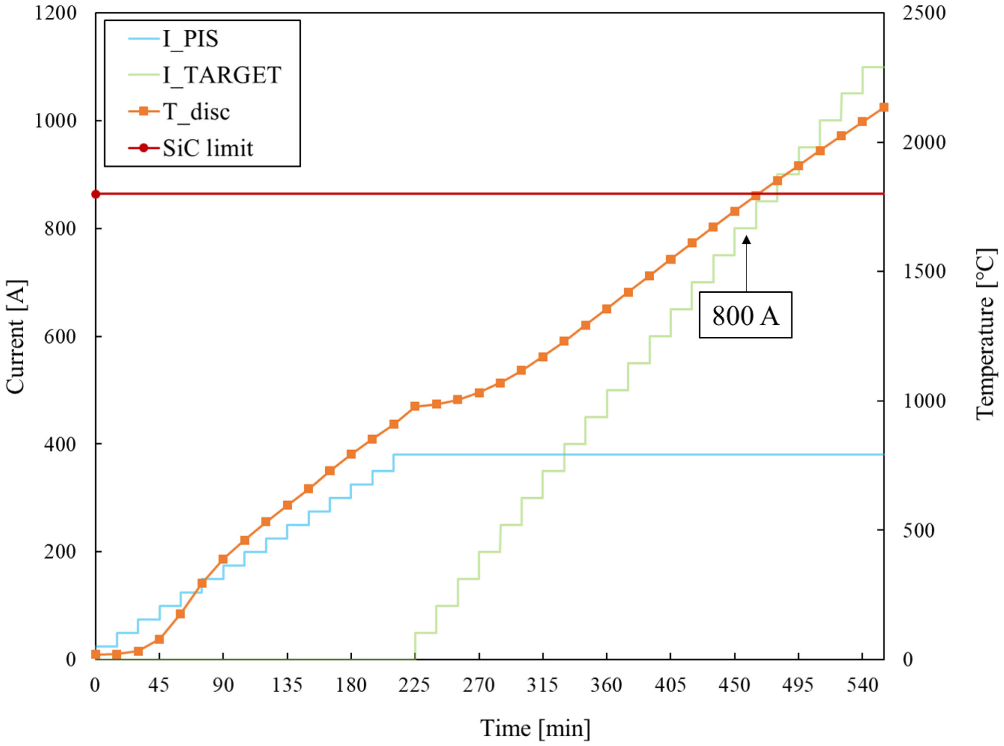

Figure 2.36 Maximum temperature reached by the hottest disc at each load step.

Moreover, the temperatures on the final dump, the first window and the collimator are also analyzed (Figure 2.37). The temperature measurements are in fact carried out on these components during the tests. In order to estimate the discs' temperature, the relationship between the temperature of the window and the discs' maximum temperature is shown in Figure 2.38. The comparison with the experimental data will be present in the following paragraphs. In Figure 2.39, the FE model temperature distribution for I_{PIS}=380 A and I_{TARGET}=800 A is shown.

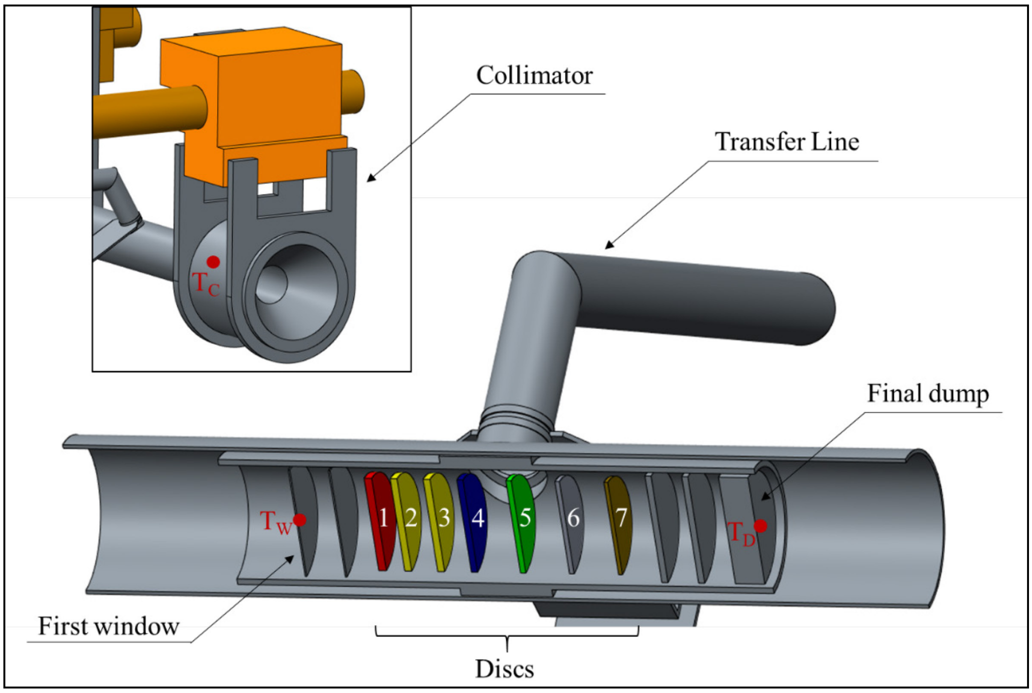

Figure 2.37 Main components of the target block. T_C, T_W, T_D represent the points on which the temperature measurements were carried out during tests.

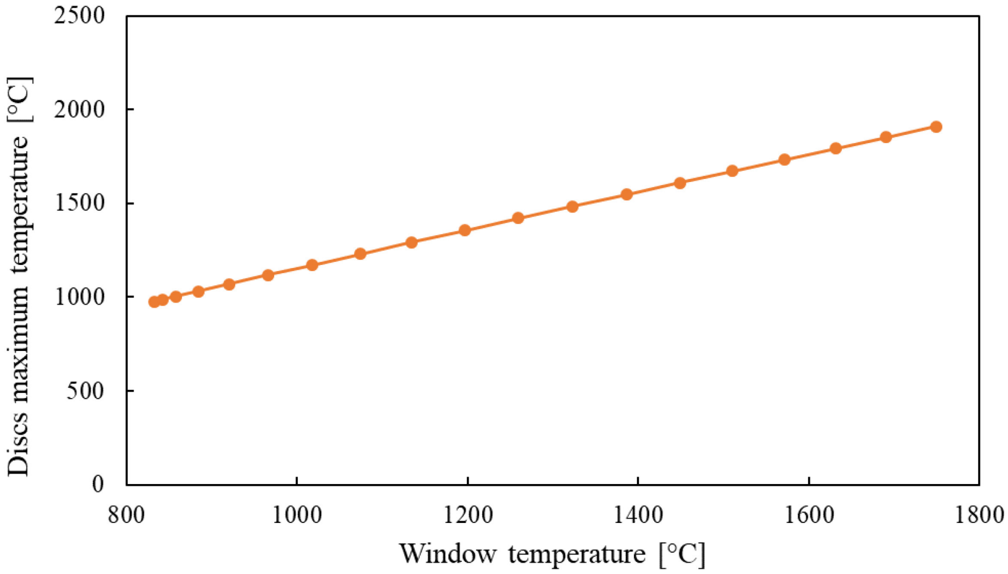

Figure 2.38 Relationship between the temperature of the window and the maximum temperature of the discs, according to the FE simulation.

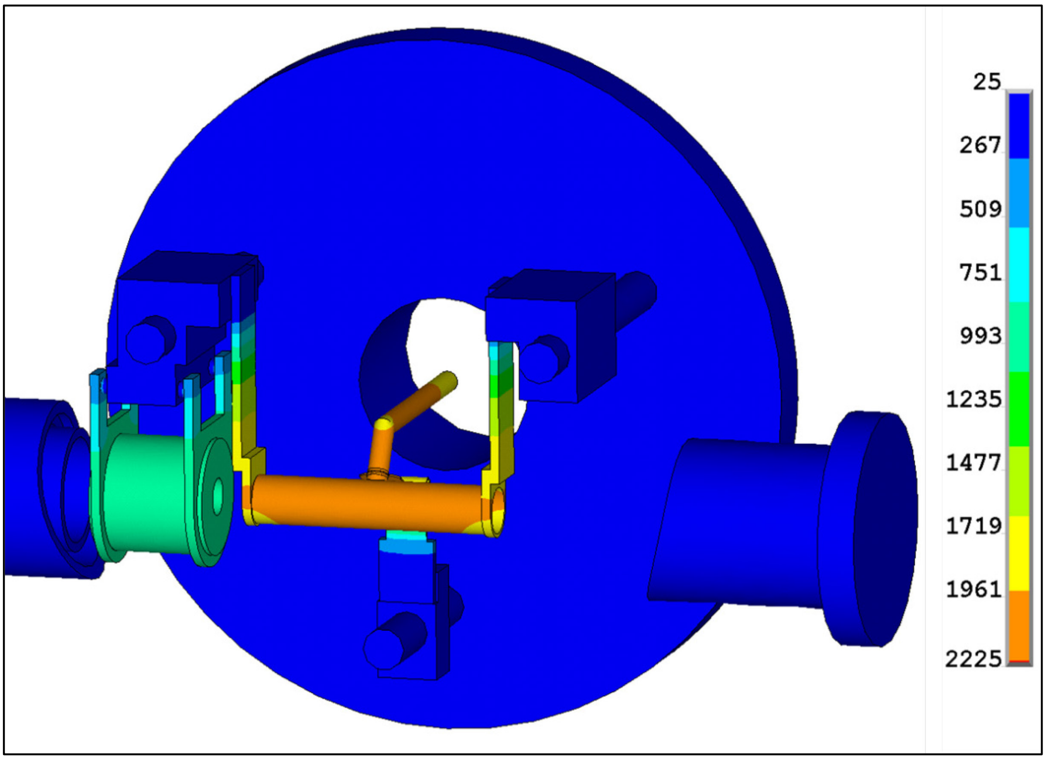

Figure 2.39 FE model temperature distribution for I_{PIS}*=380 A and* I_{TARGET}*=800 A.*

2.5.2 Experimental set up

The components of the experimental set up are prepared and cleaned with an ultrasonic washing machine. The Plasma Ion Source is then installed on the chamber plate. The heater is connected with the copper clamps and installed with the collimator (Figure 2.40). The copper clamps are tightened in order to support the high electrical current flux foreseen to heat the target at the desired temperature. Tantalum screws and molybdenum nuts are preferred to inox bolts: during online tests, in fact, possible iron contamination must be avoided to prevent a loss of efficiency of the Plasma Ion Source. The assembly is then aligned with respect to the protonic VAT valve, using the BOSCH GCL 2-15 Professional laser (Figure 2.41).

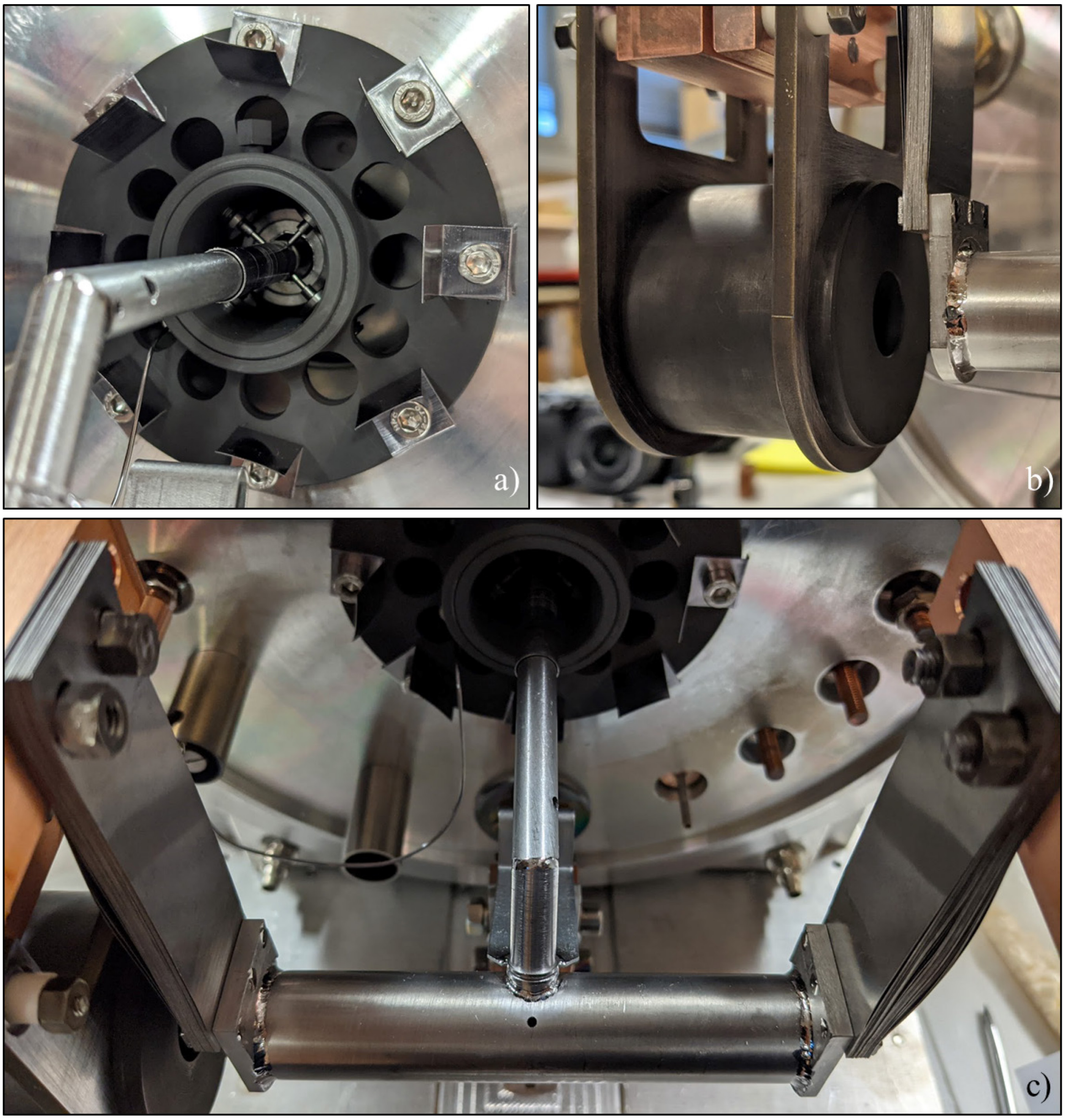

Figure 2.40 The Plasma Ion Source (a), the collimator (b) and the tantalum heater (c) installed on the chamber plate.

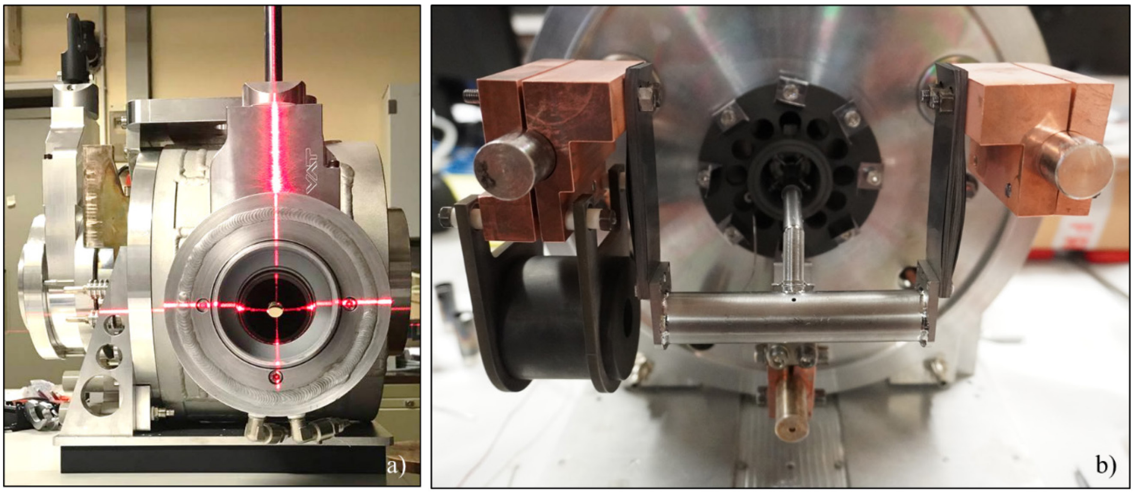

Figure 2.41. Laser alignment (a) of the target assembly (b).

The SiC discs are carefully measured, in weight and dimension, and inserted in the graphite box (Figure 2.42). The whole assembly (discs and box) is finally housed inside the heater and fixed by means of a tantalum pin. The suppressor is then installed on the chamber flange, together with its aluminum oxide supports and a fastening O-Ring.

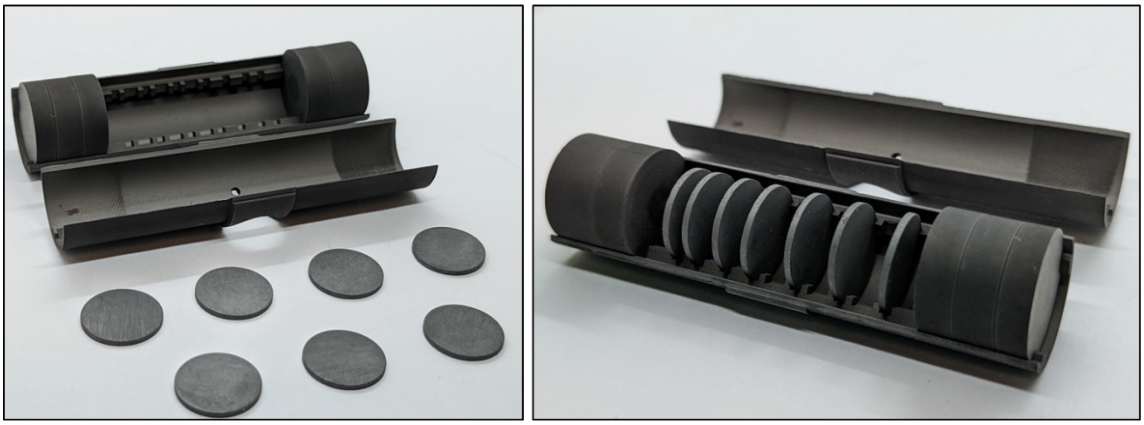

Figure 2.42 The graphite box and the SiC discs used for the test.

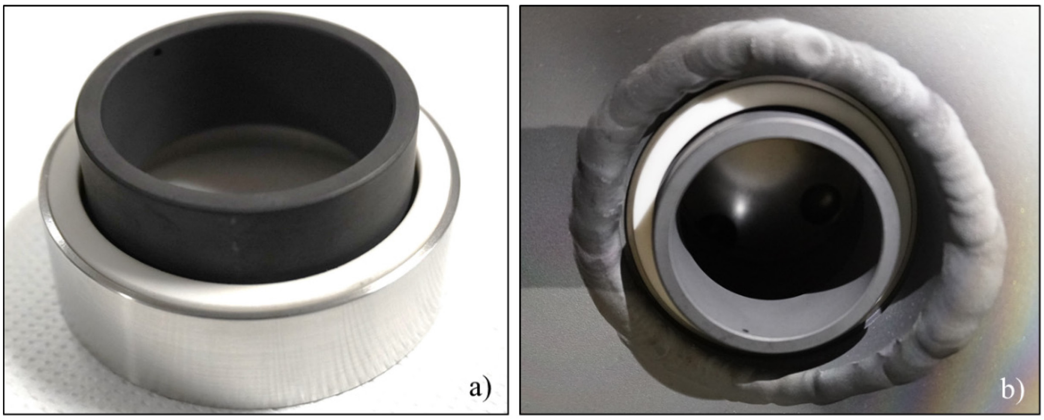

Figure 2.43. The suppressor block (a) and its installation on the chamber flange (b).

Temperature measurements are obtained by means of high temperature type C thermocouples and infrared pyrometers. The type C thermocouples are high temperature sensors built with 95%

Tungsten 5% Rhenium versus 74% Tungsten 26% Rhenium wires. This model of thermocouple offers a temperature range from 426°C to 2315°C [34]. In the customized version used during the test, a tantalum sheath and a platinum sleeve are foreseen. Insulation is provided inside the sheath by HfO_2 powder and by Alumina cylinders around the wires (Figure 2.44).

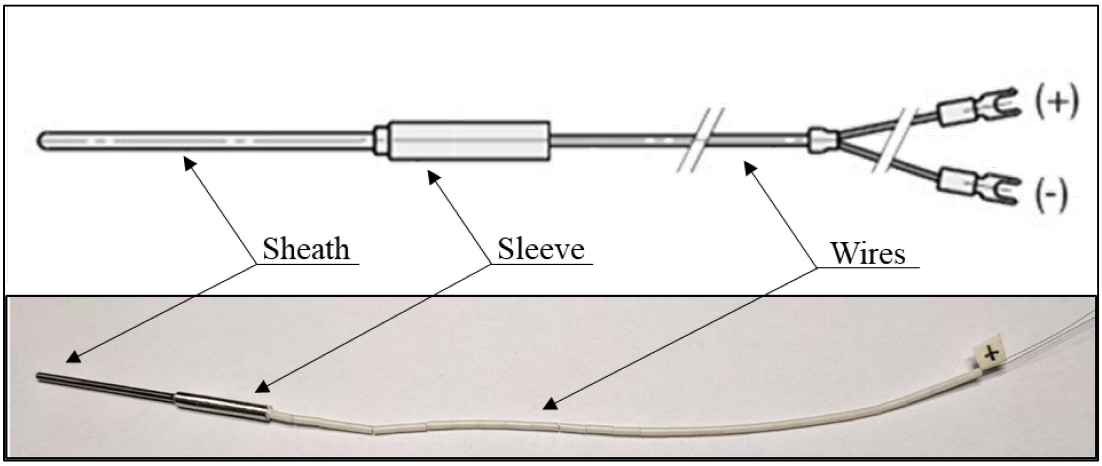

Figure 2.44 Type C thermocouple used during the tests.

The thermocouples are electrically connected to a signal recorder, the Eurotherm Nanodac™, through a vacuum multi pin feedthrough. One thermocouple measures the collimator temperature, while, for the target final dump, two sensors are foreseen. The final target assembly with the connected thermocouples is shown in Figure 2.45.

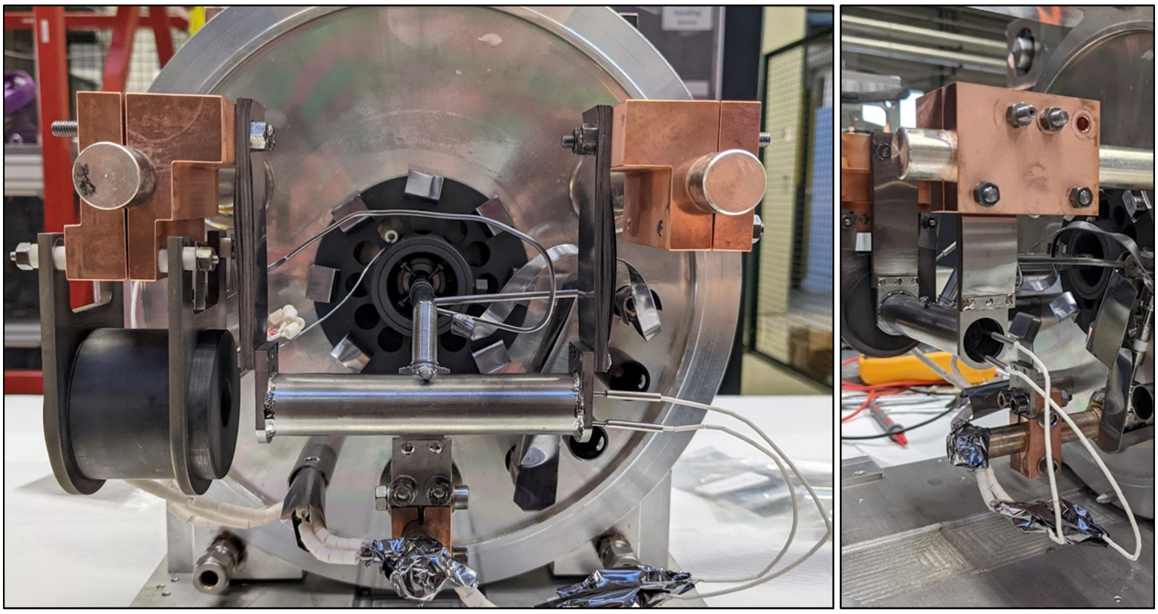

Figure 2.45 Final assembly of the target block after the connection of the thermocouples.

Three different infrared pyrometers are used:

- Low Temperature pyrometer LT (temperature range 600-1400°C)
- Medium Temperature pyrometer MT (temperature range 600-1800°C)

- High Temperature pyrometer HT (temperature range 1000-3000°C)

The LT and HT pyrometers are exchanged during the test to measure the temperature at the center of the first graphite window (Figure 2.46), while the MT pyrometer is maintained fixed to measure the temperature of the final graphite dump (Figure 2.47). To allow for the measurements with the pyrometers, two boro-silicate glass view ports are installed.

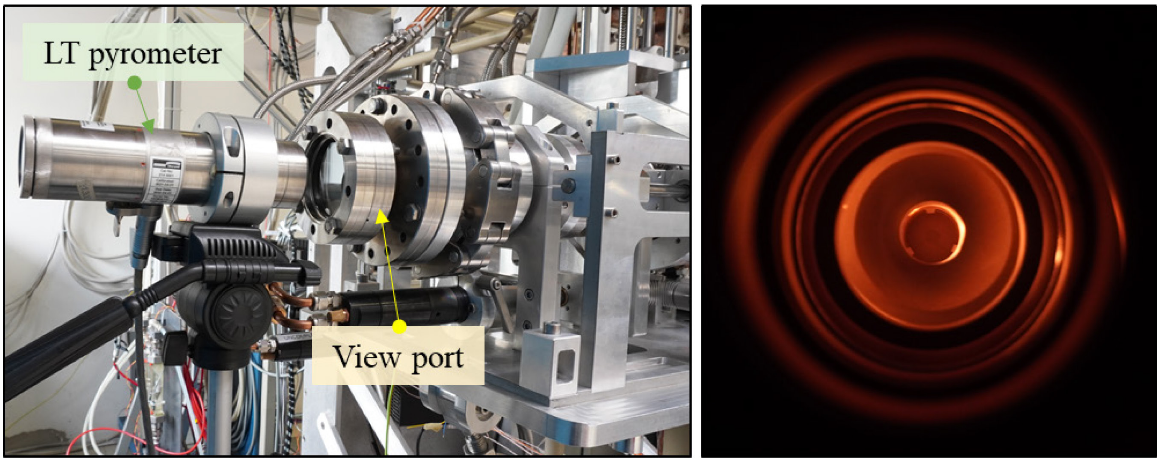

Figure 2.46 Low temperature pyrometer used to measure the temperature of the first graphite window.

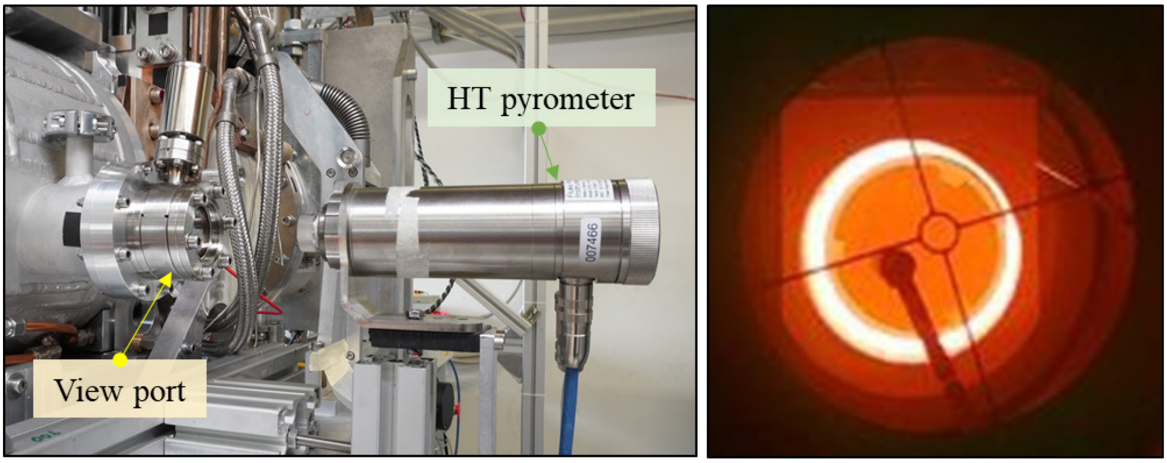

Figure 2.47 Medium temperature pyrometer used to measure the temperature on the final graphite dump.

A power supply unit is connected to the tantalum heater, through the copper clamps, and to the Plasma Ion Source circuit. A rotary and a turbomolecular pumps provide a vacuum level of 10^{-6} mbar inside the target chamber. The system is water cooled for the duration of the test, in order to avoid over-temperature problems and damages.

The final experimental apparatus installed on the SPES Front End is shown in Figure 2.48.

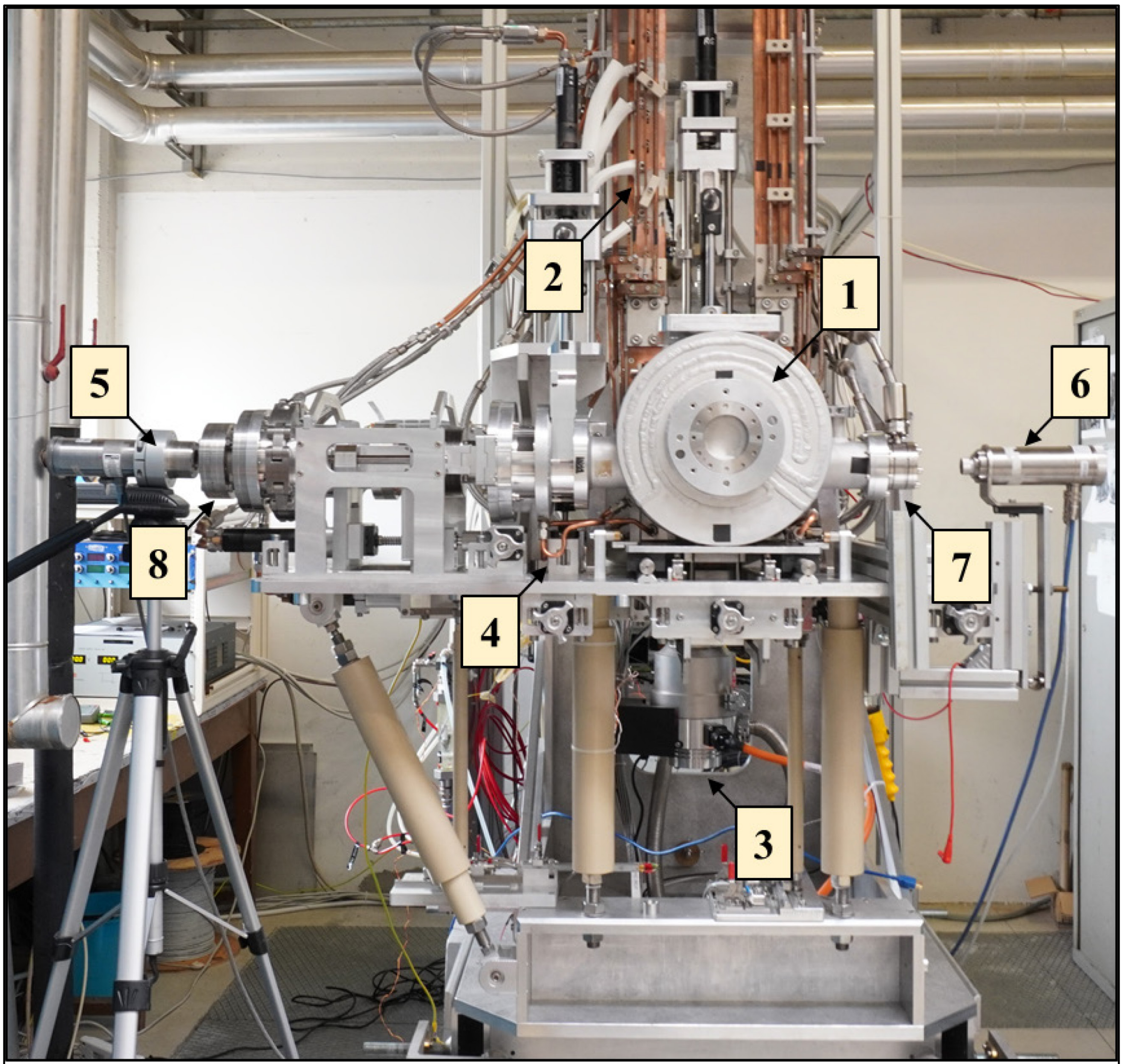

1. Target vacuum chamber
2. Power supply connection
3. Vacuum turbomolecular pump
4. Cooling water line
5. LT/HT pyrometer
6. MT pyrometer
7. Viewport (final dump)
8. Viewport (first window)

Figure 2.48 The experimental apparatus installed on the SPES Front End used for the pre-commissioning tests.

2.5.3 First experimental campaign

During tests, ramp loadings were preferred to step loadings. First, the PIS current was raised up to 380 A, with ramps of 25 A in 8 minutes and then waiting 7 minutes before the next increment. Then, maintaining the PIS current at 380 A, the target current was raised with similar ramps of 50 A up to 800 A. Three complete load ramps were performed, in order to check the repeatability of the collected data. After reaching the maximum currents, the third ramp was then maintained at full capacity for

10 days, before shutting down. Temperature and potential differences were measured and compared with the corresponding FE model results.

The electric potential values measured between the external tips of the target copper clamps are reported in Figure 2.49. The difference between the FE model and the experimental data is probably due to the fact that ideal contacts between the tantalum wings and the copper clamps were implemented in the simulation. Actually, small electric contact resistances are expected due to the real physical connections. The maximum difference with respect to the experimental data is 0.4 V registered at 800 A.

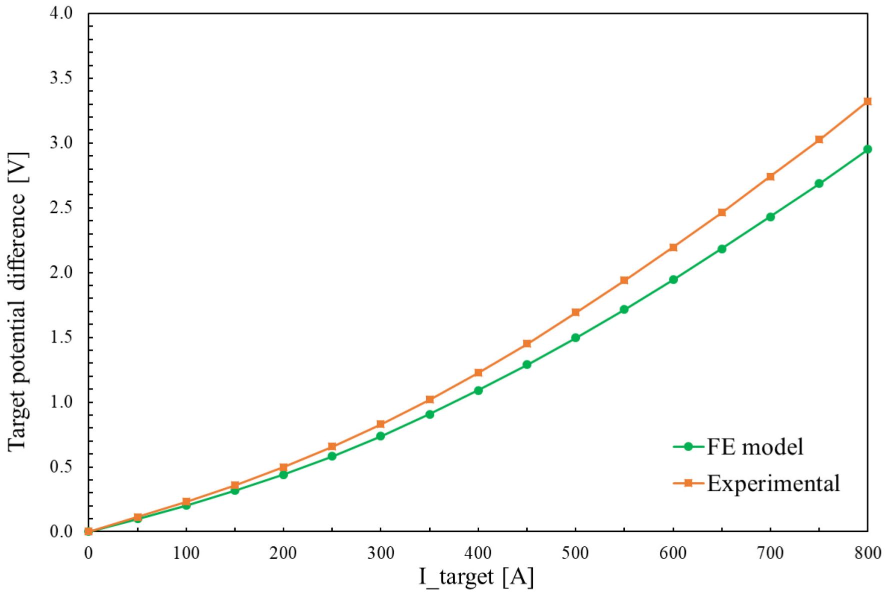

Figure 2.49 Comparison between theoretical and experimental potential difference values in the target heating system.

The electric potential values measured at the external tip of the source copper clamp are reported in Figure 2.50. Also in this case, the difference between the FE model and the experimental data can be attributed in part to the ideal contacts implemented in the simulation. In addition, the transfer line used during the tests was significantly different with respect to the simulated one. In the test assembly, in fact, a transfer line for the Surface Ion Source (SIS) was used, because no PIS transfer line was available. The SIS component is characterized by a smaller external diameter of 8.8 mm, instead of 9 mm, and a length of 65 mm, instead of 100 mm. A junction was thus added to the SIS transfer line, to reach the desired length. The maximum difference with respect to the experimental data is 4.5 V registered at 380 A.

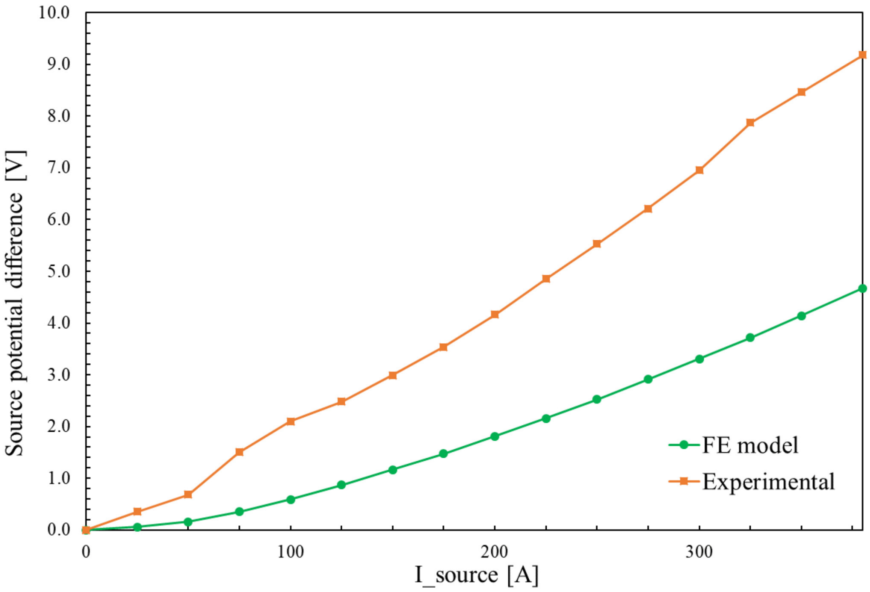

Figure 2.50 Comparison between theoretical and experimental potential difference values of the source copper clamp.

Figure 2.51 shows the comparison between the theoretical and experimental temperature, measured with the pyrometers, for the graphite window of the target. The reported experimental temperatures are the mean of three repeated measurements, taken in three different days. The difference between one single measurement and the mean value is always below 1%, showing a very stable behavior of the system. As shown in Figure 2.51, the experimental temperatures are always lower than the theoretical ones: in particular, at 800 A on the target circuit, a difference between the experimental and theoretical values of about 140°C is recorded.

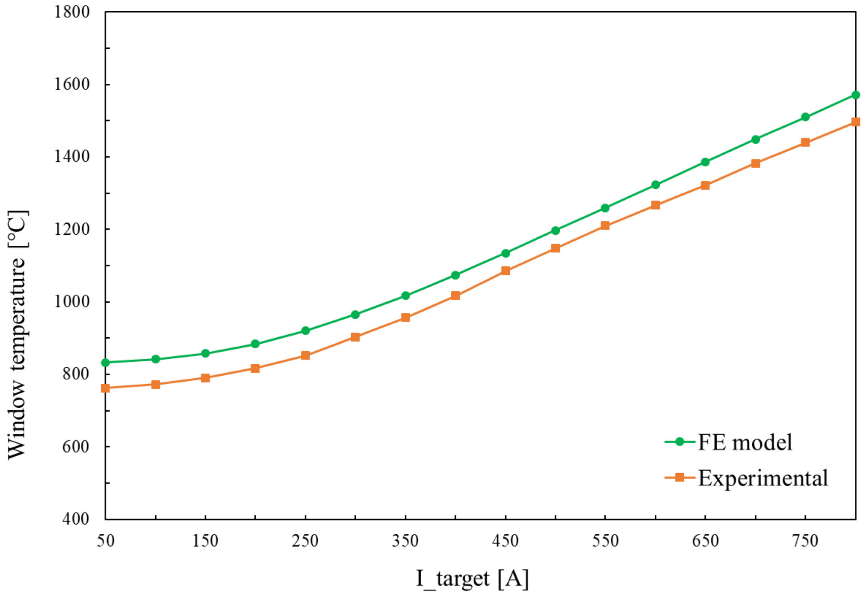

Figure 2.51 Comparison between theoretical and experimental window temperatures.

This discrepancy can be explained with the occurrence of a parallel electric circuit in the experimental assembly: indeed, the deformations due to the thermal expansion causes, especially in proximity of the final dump, a contact point between the graphite box and the target heather, through which part of the heating current flows. In this way, the global electrical resistance decreases and, consequently, for the same heating current, the power dissipation decreases too. Photos taken during and after the tests seem to validate the thesis, as shown in Figure 2.52.

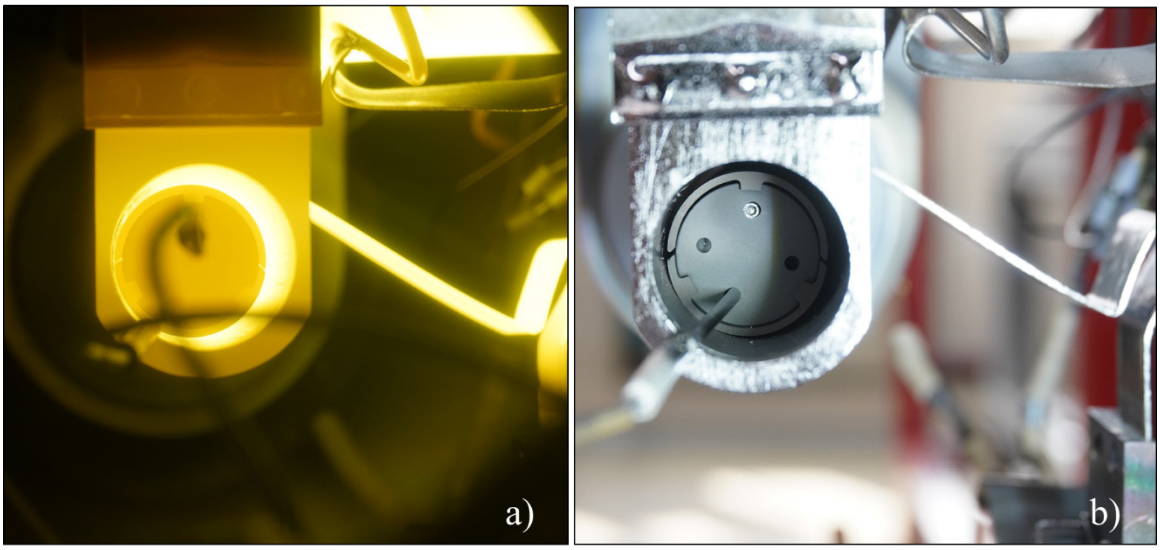

Figure 2.52 Photo of the target block, from the dump side, taken during the heating (a) and after the chamber opening (b). A contact between the graphite box and the tantalum heater in the lower left side can be observed.

No useful temperature data were registered for the collimator and the final dump: several problems arose, in fact, with the thermocouple measurements. For the collimator, different temperatures were registered during the tests, with lower and lower values at each ramp. In particular, at 800 A on the target circuit, temperatures of 650°C, 620°C, 590°C were respectively registered in the first, second and third ramp. It is important to remark that the temperatures measured with the pyrometer on the first window of the target were very similar for the three ramps, with differences lower than 1%. The differences between the collimator measurements have therefore to be ascribed to problems with the thermocouples. Even more serious problems observed with the dump's thermocouples seem to strengthen the thesis. In this case, after reaching about 1100°C during the first ramp, the sensors registered decreasing values even if the target current was increasing. During the second and the third ramp, both the dump's thermocouples registered unrealistic values, ranged between 50°C and 6000°C. For these reasons, these temperature measurements were considered unreliable and discarded.

Unfortunately, it was not possible to measure the temperature with the MT pyrometer, because the presence of the thermocouples obstructed the measurement. Moreover, towards the end of the experimental campaign, a dark layer deposited on the view port at the right side of the target chamber, as shown in Figure 2.53. Later analysis with a Scanning Electron Microscope identified the layer as deposited silicon.

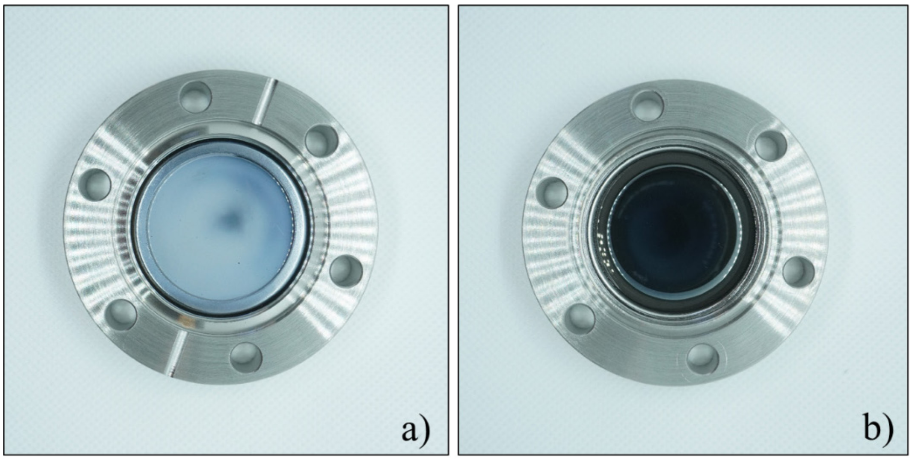

Figure 2.53 Internal (a) and external (b) views of the view port on the right side of the target chamber, with the SiC layer clearly visible.

At the opening of the target chamber at the end of the test campaign, the discs were accurately weighted, and a significant weight loss was observed especially for the central discs, as shown in Table 2.6. In later SEM analyses, it was observed a well-defined silicon loss in the outer layer of the disc, as shown in Figure 2.52. A linear path can be appreciated due to the concentration gradient. Two different explanations are possible for this phenomenon:

- The system has reached an equilibrium: even keeping the discs at the same temperature for a longer time, no difference would have been noticed in the outer layer of the disc.
- The diffusive process of silicon is characterized by different speeds as the diffusion medium changes. In particular, it is slower in silicon carbide, which is very dense, and it is faster in the carbon layer, that can be even more porous due to the passage of silicon. In this case, a target heating for a longer time would have increased the carbon layer thickness.

In any case, these evidence suggest a maximum operating temperature for the silicon carbide lower than the previously hypothesized 1800°C, in order to avoid silicon losses. On the other hand, the silicon carbide resistance at high temperature could also be related to how long temperature is maintained. Further long-duration test on this material could verify these two hypothesis.

Table 2.6 Weight measurements on the seven discs of the target, before and after the tests.

Disc number	Weight before test [g]	Weight after test [g]	Weight loss [%]
Disc 1	0.410	0.342	-16.6
Disc 2	0.407	0.309	-24.1
Disc 3	0.408	0.273	-33.0
Disc 4	0.404	0.256	-36.5
Disc 5	0.407	0.251	-38.3
Disc 6	0.412	0.296	-28.1
Disc 7	0.406	0.326	-19.8

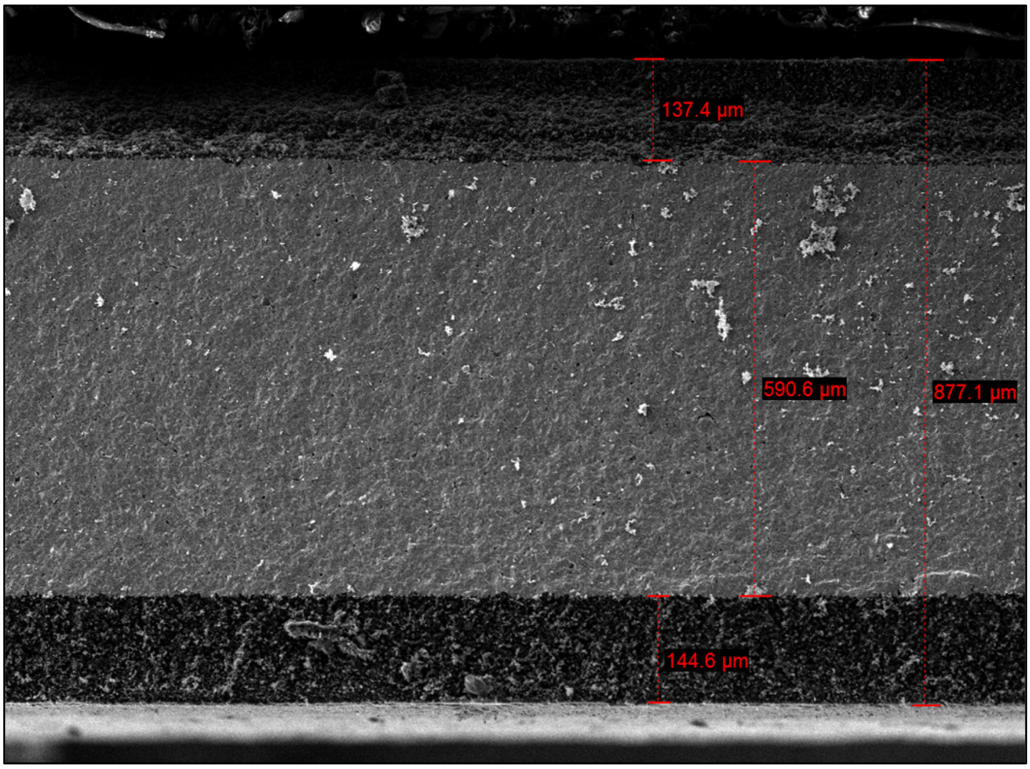

Figure 2.54 Scanning Electron Microscope imagine (200x) of the section of the 5th disc after the first experimental campaign. It can be observed a central zone composed by Silicon Carbide (light grey) and two external bands of graphite (dark grey).

During the survey of the components, carried out at the end of the tests, the problems with the dump's thermocouples were also confirmed, highlighting the melting of the tip of the sheath for both sensors, as shown in Figure 2.55 (b). Moreover, the massive silicon effusion inside the whole target chamber and over the thermocouple's wires (Figure 2.55 (d)), caused the loss of insulation of the wires. This might explain the problems registered with the thermocouple of the collimator: with this sensor, in fact, the tip of the sheath did not melt but no reliable measurements were anyway collected.

During this first experimental campaign it was also possible to evaluate the target's and the collimator's displacements due to the thermal expansion. A photographic comparison between different phases of the heating was used for the evaluation. A camera was installed in front of the view port on the right side of the chamber and held in this fixed position during the whole experimental campaign. The photos have been then compared, as shown in Figure 2.56 and Figure 2.57. The known dimensions of the cold components were taken has references to evaluate the displacements. No significant displacement could be observed for the collimator, while for the target block a displacement of about 0.8 mm was estimated. With the aim to solve the aforementioned problems, a new experimental campaign was planned, as described in the following paragraph.

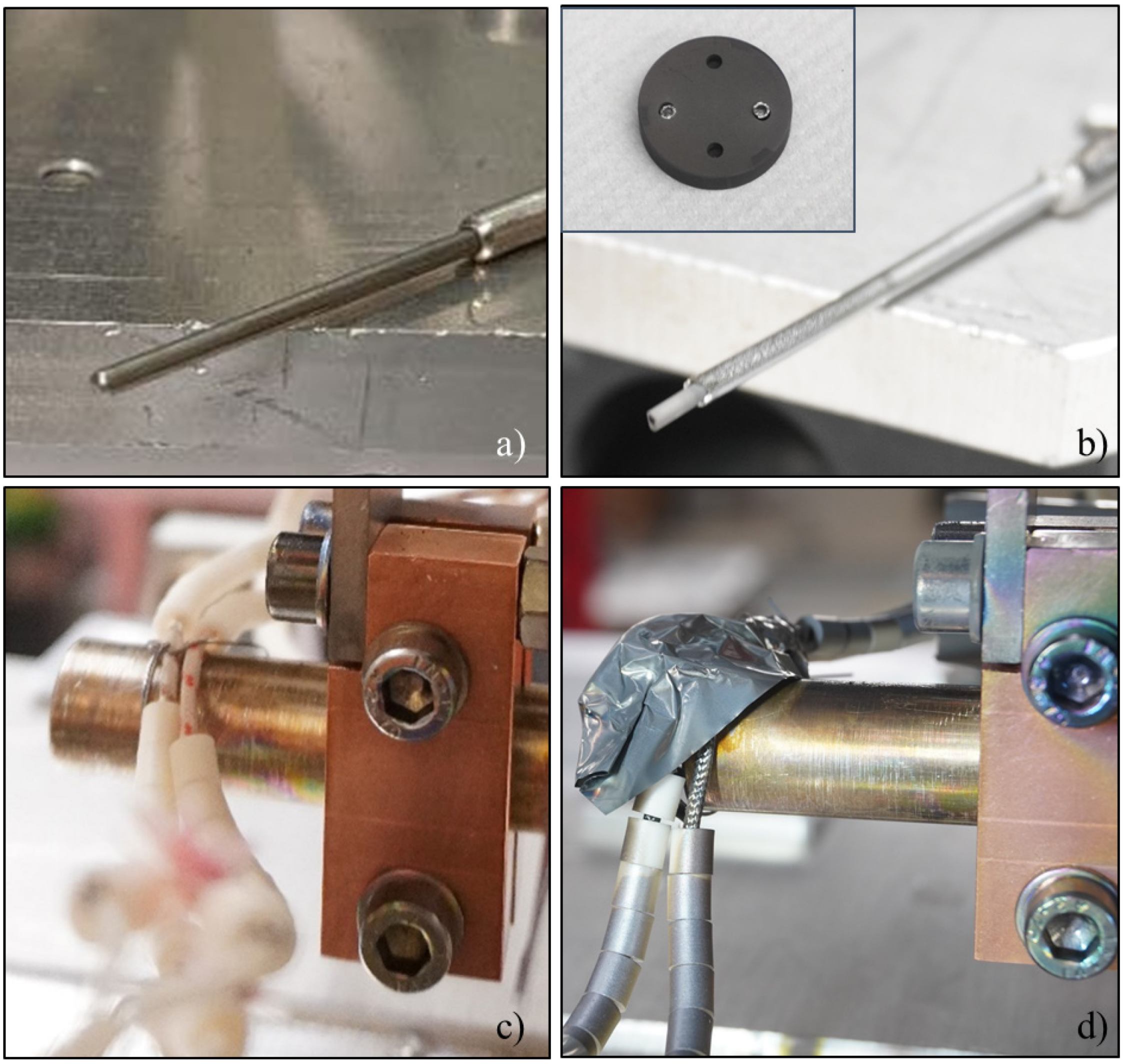

Figure 2.55 The tip of the sheath and the wires of the thermocouple before (a,c) and after (b,d) the test.

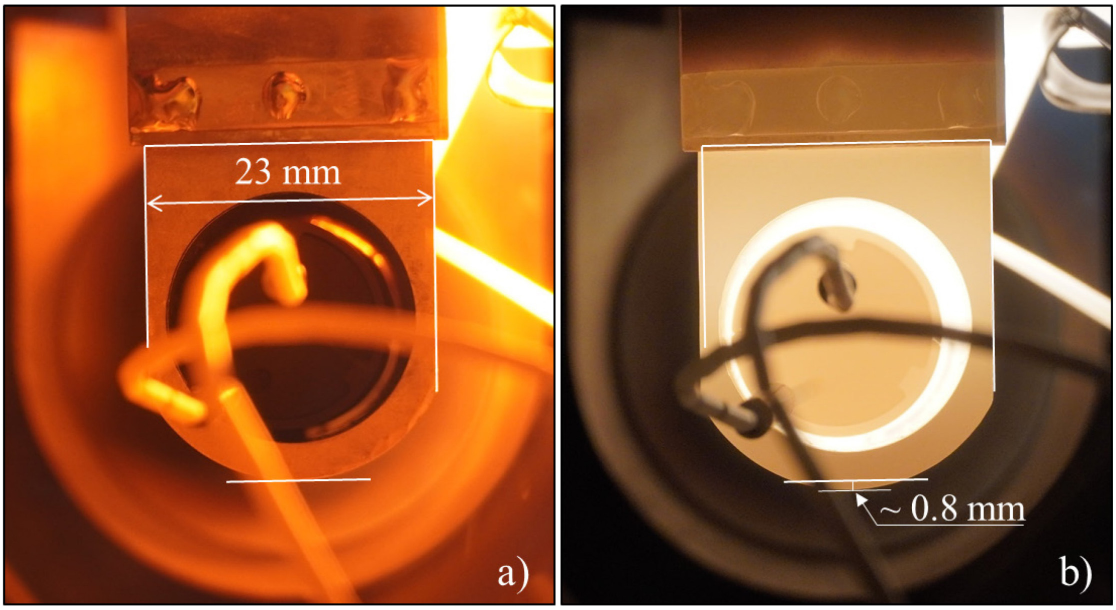

Figure 2.56 The target block at the beginning (a) and at the end (b) of the heating.

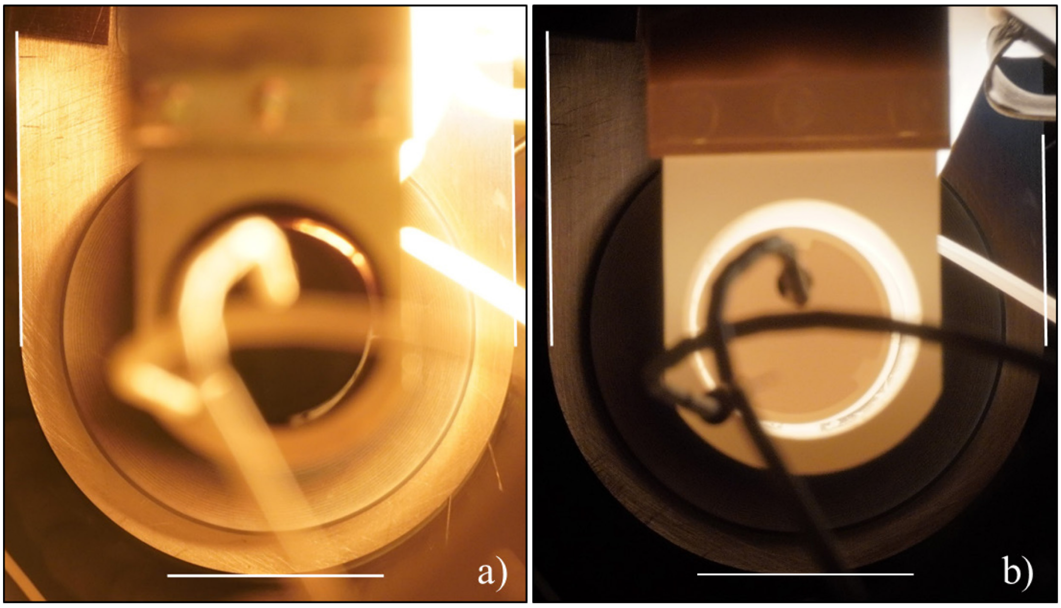

Figure 2.57 The collimator at the beginning (a) and at the end (b) of the heating.

2.5.4 Second experimental campaign

In view of the problems observed during the first experimental campaign, some changes were made, and a new campaign was planned. In particular, two small pieces of tantalum wire were rolled up around the center of the graphite box to help its centering and fixing, as shown in Figure 2.58.

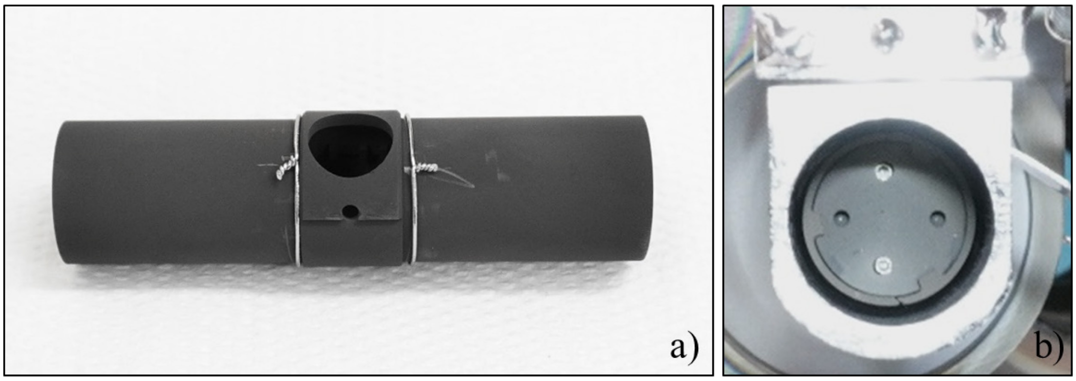

Figure 2.58 The two tantalum wires rolled up around the center of the box (a) to help its centering on the heater (b).

Moreover, the discs were removed from the box. In order to check if the parallel circuit problem was solved, in fact, the new tests had to be carried out with the same load conditions: removing the discs would avoid new problems with the silicon effusion. The view ports were replaced with new ones and the dump's thermocouples were removed in order to allow for the measurements with the MT pyrometer. The experimental data obtained during this second campaign are presented in this paragraph as *Test 2* and are compared with the previous ones, presented as *Test 1*. As in *Test 1,* first the PIS current was raised with ramps of 25 A up to 380 A. Then the target current was raised with ramps of 50 A up to 800 A.

The target and the source electric potential values are reported in Figure 2.59 and Figure 2.60, respectively. As shown in Figure 2.59, a slight increase of the target potential difference was observed: this behavior seems to suggest that the parallel circuit problem was at least in part fixed. No significant differences are observed between *Test 1* and *Test 2* for the source potential.

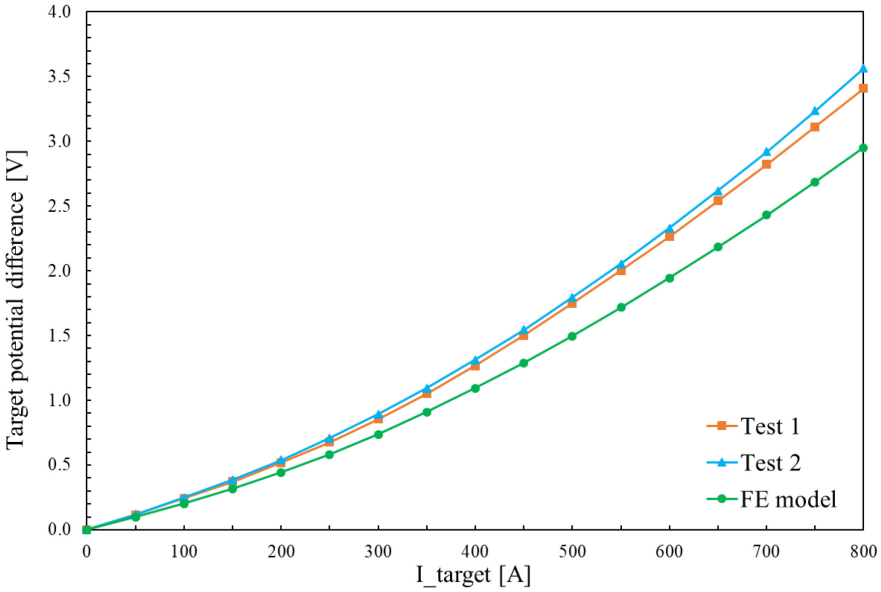

Figure 2.59 Comparison between FE model and experimental target potential difference measured during the first experimental campaign (Test 1) and the second experimental campaign (Test 2).

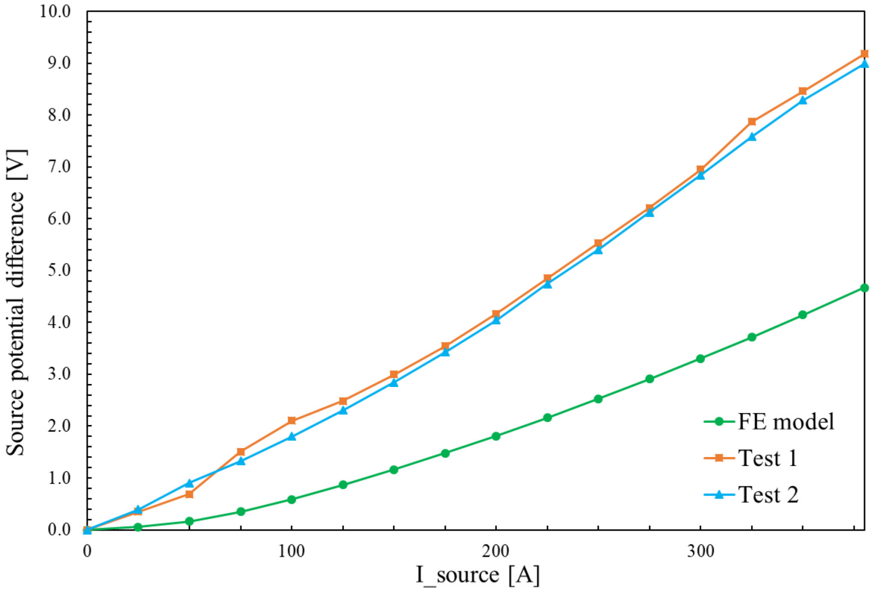

Figure 2.60 Comparison between FE model and experimental source potential difference measured during the first experimental campaign (Test 1) and the second experimental campaign (Test 2).

In Figure 2.61 and Figure 2.62 the window and the dump temperatures, measured by means of the HT and MT pyrometers respectively, are reported. A clear improvement can be observed in Figure 2.61 for the window temperature: at 800 A on the target, 1585°C were measured, with an increase of almost 100°C with respect to *Test 1* and only 50°C less than the FE model. On the other hand, a bigger discrepancy can be seen in Figure 2.62 for the dump temperature. At 800 A, only 1500°C were measured, 120°C less than the FE model. This is probably due to the parallel circuit problem, not completely fixed. No useful measurements were collected for the collimator: also in this case the thermocouple registered unrealistic values, ranged between 1°C and 6000°C.

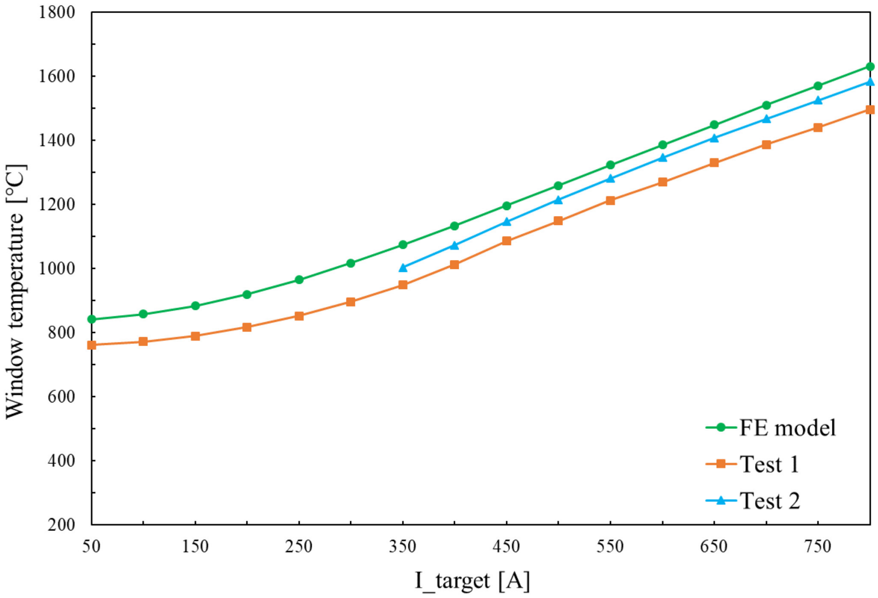

Figure 2.61 Comparison between FE model and experimental window temperature measured during the first experimental campaign (Test 1) and the second experimental campaign (Test 2).

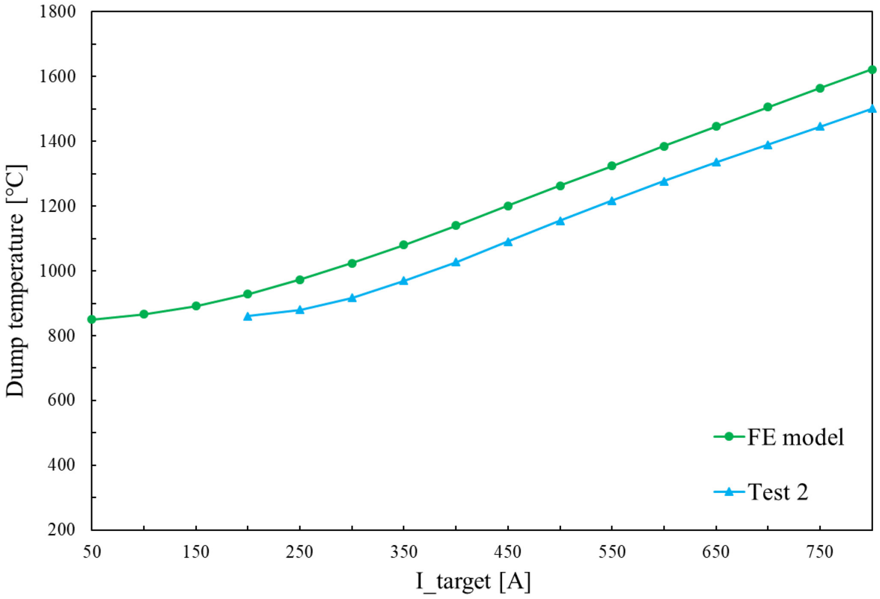

Figure 2.62 Comparison between FE model and experimental dump temperature measured during the second experimental campaign (Test 2).

With the aim of completely clarify the parallel circuit problem, the target chamber was opened, and two tantalum wires were fixed at the extremities of the target heater, as shown in Figure 2.63. The wires were then connected to two connectors installed on the chamber plate, to be able to measure the exact potential difference of the heater, bypassing the clamps connections.

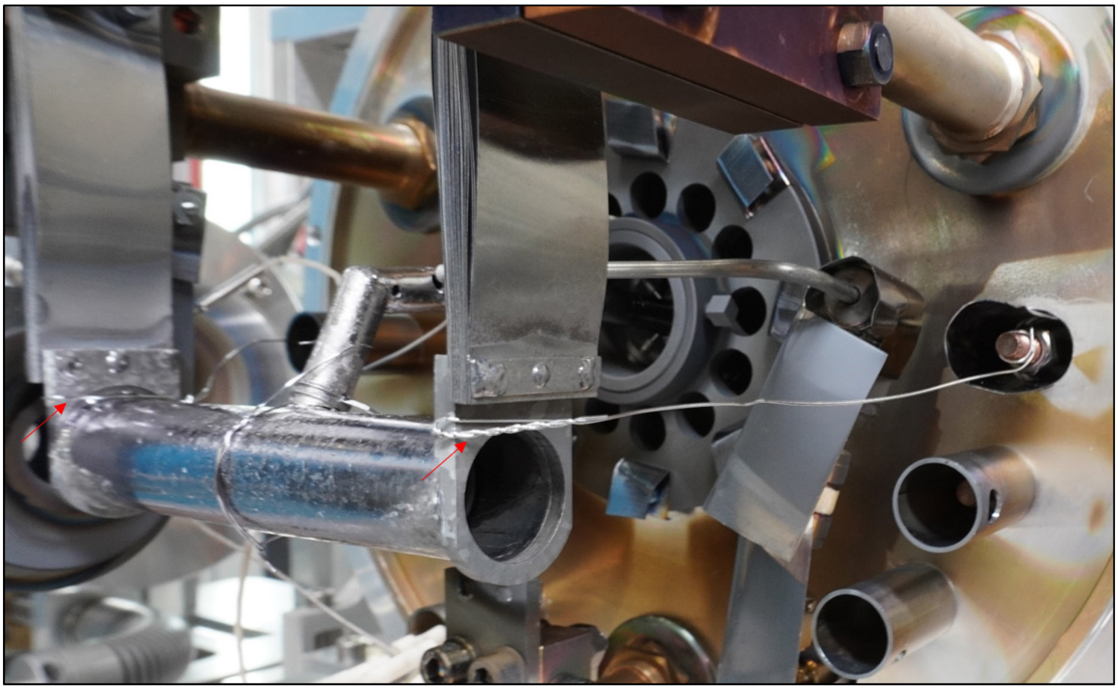

Figure 2.63 The tantalum wires fixed at the extremities of the heater and connected to the chamber plate to measure the potential difference of the heater.

Then, only the target circuit was heated up to 800 A, with ramps of 50 A. Electrical potential difference values were measured during the test in different positions of the circuit, as shown in Figure 2.64 and Figure 2.65.

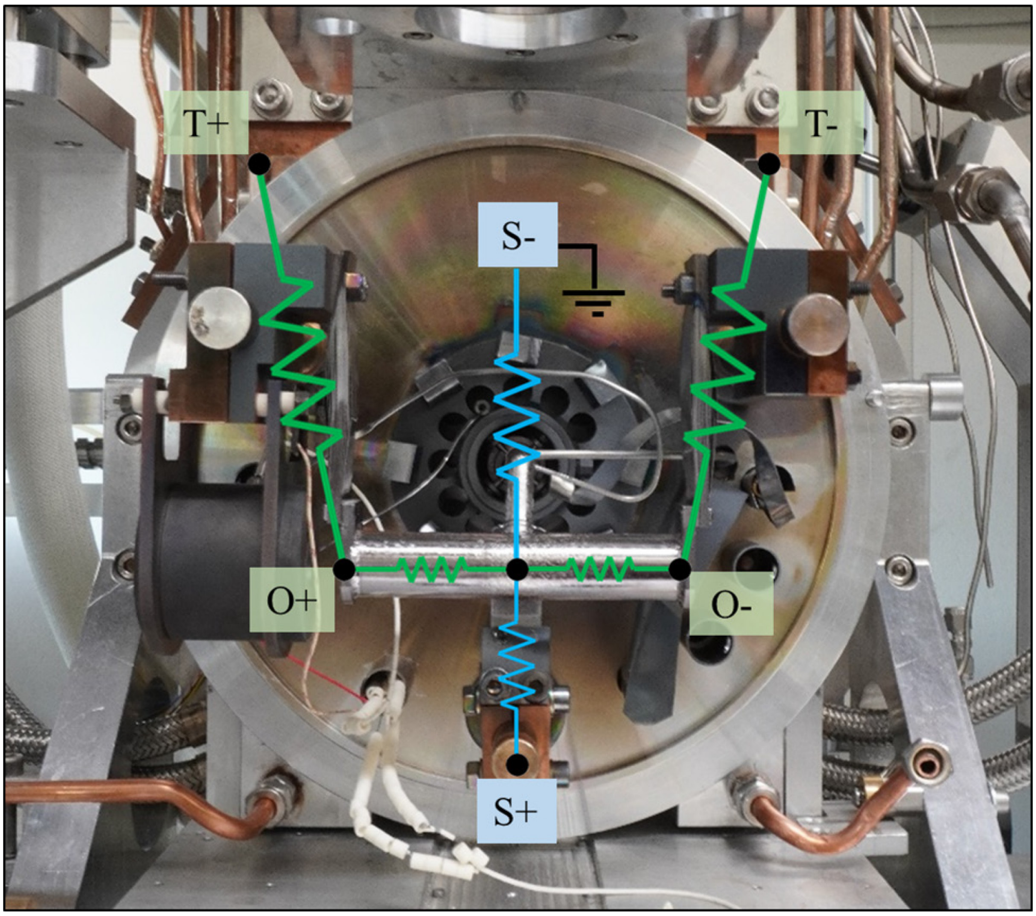

Figure 2.64 Measuring points of the potential difference values. In particular: T+ and T- were collected at the external tip of the target clamps; O+ and O- were collected at the extremities of the heater (thanks to the tantalum wires, through the chamber plate's connectors); S+ was measured at the external tip of the source clamp and S- is the grounded pole.

The window and the dump temperatures (measured with the pyrometers) and the collimator temperature (measured with the thermocouple) are shown in Figure 2.66, Figure 2.67 and Figure 2.68, respectively. As shown in Figure 2.66, the window experimental temperatures are perfectly in accordance with the FE model. On the other hand, a temperature difference of about 125°C can be observed for the dump, as shown in Figure 2.67. It was also possible to measure for the first time the collimator temperature: as shown in Figure 2.68, the experimental results are always slightly higher: at 800 A on the target, a difference of 25°C is observed with respect to the FE model.

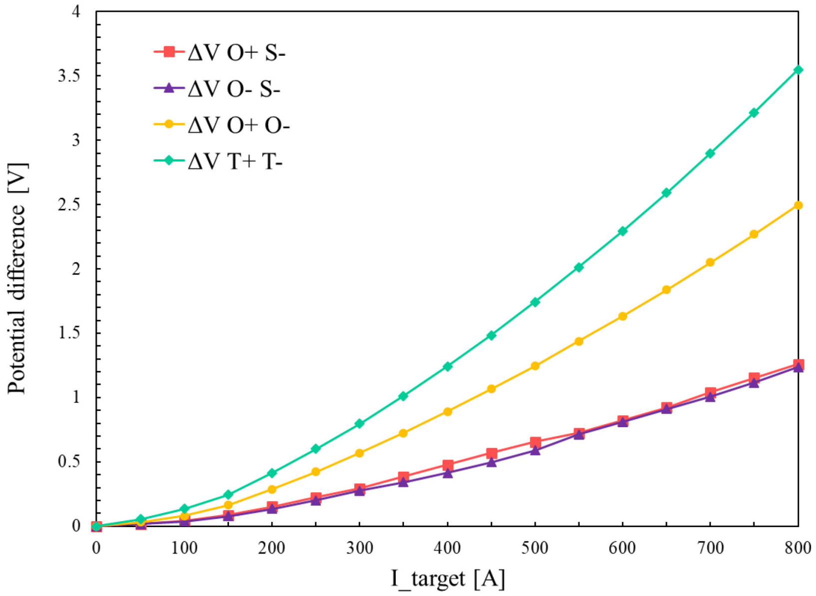

Figure 2.65 Potential differences in different positions of the target assembly.

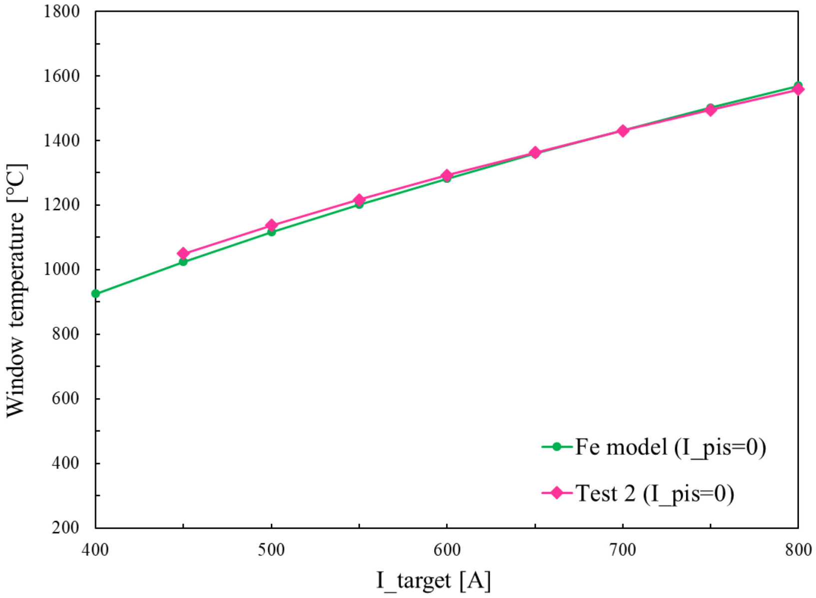

Figure 2.66 Comparison between FE model and experimental window temperature measured during Test 2, with I_{PIS}*=0*

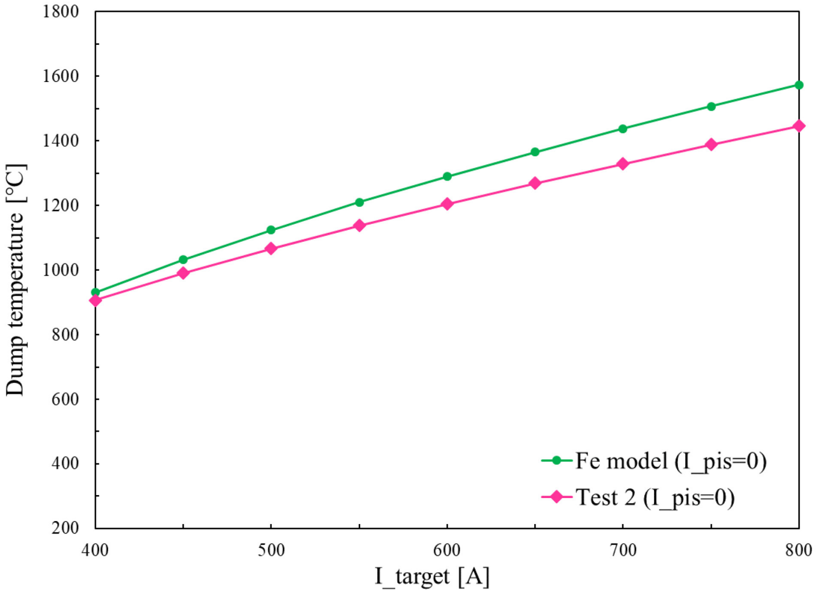

Figure 2.67 Comparison between FE model and experimental dump temperature measured during Test 2, with I_{PIS}=0

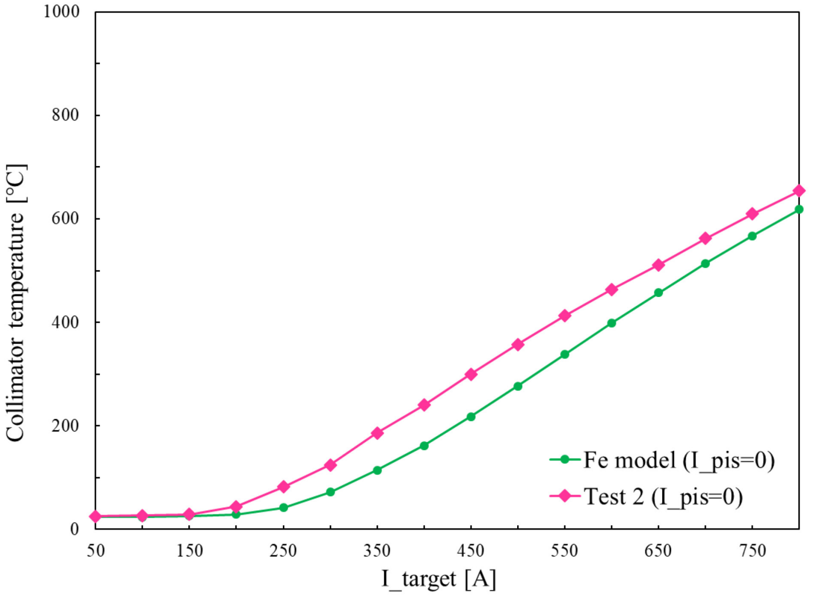

Figure 2.68 Comparison between FE model and experimental collimator temperature measured during Test 2, with I_{PIS}=0

It was possible to plot the temperatures reached on the window and on the dump with respect to the calculated electrical power dissipated through the two halves of the target. As shown in Figure 2.69, with the same power, different temperatures are reached. Therefore, the measurement of the dissipated electrical power in the two halves of the target does not seem useful to detect a parallel circuit. Probably, the parallel circuit problem was partially solved for the first half of the target, as evidenced by the temperatures reached on the window, but local problems could have arisen in the second half of the target, thus explaining the lower temperatures on the dump.

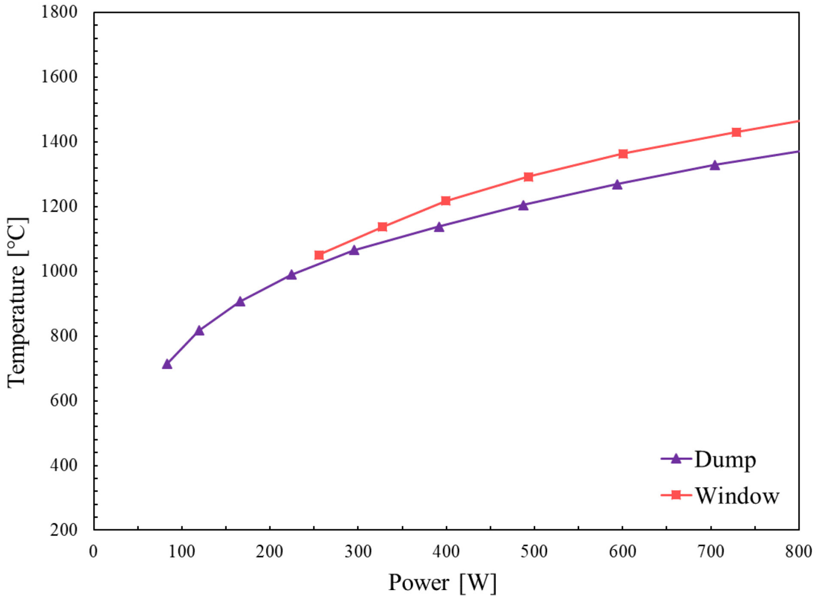

Figure 2.69 Temperatures reached on the window and on the dump of the target, with respect to the electrical power dissipated through the two halves of the target.

2.5.5 Conclusions

In the first experimental campaign, three complete load ramps were performed, in order to check the repeatability of the collected data. The system shown a very stable behavior with difference between the temperature measurements always below 1%. However, a parallel electric circuit occurred in the target assembly, between the graphite box and tantalum heather. This led to lower experimental temperatures with respect to the FE model values, of about 10% at 800 A. During this campaign, the displacement of the target assembly was also evaluated, with a maximum displacement of 0.8 mm at 800 A. The silicon losses and deposition registered at the end of the experimental campaign suggests for SiC a maximum operating temperature lower than the previously hypothesized 1800°C. Another possibility is that the maximum temperature is strongly affected by how long the material is maintained in temperature. Further long duration tests at high temperatures can clarified the behavior of this material.

In the second experimental campaign, some changes were made to solve the parallel circuit problem. A clear improvement was seen for the graphite window, with an increase of the maximum temperature of 100°C at 800 A with respect to the first campaign. This led to a difference with the FE model value of less than 5%. Unfortunately, the problem of the box's parallel circuit was not completely solved in the dump side, with difference with respect to the FE value of 120°C at 800 A, equal to 8%. A new box design must therefore be developed in order to completely solve this problem.

In any case, the comparison between the experimental data and the FE models are in general in quite good agreement, confirming the reliability of the numerical model.

CHAPTER 3

The Proton Beam Line upgrade

3.1 Introduction

As presented in Sec. 1.4.1, along the proton beam line and before the beam impinges the target, several devices have the task of controlling the beam characteristics. The main parameters of a beam are [8]:

- Intensity, defined as the number of particles per second;
- Profile, i.e. the distribution of the beam intensity in the space;
- Position;
- Energy and energy spread;
- Charge state and number of mass;
- Emittance (dimension of the phase space);

The working principle of most of these devices is based on current measurements. The Faraday Cup, for example, is an insulated cup designed to catch and completely stop the beam. The signal, read by an ammeter, is the beam current. In a similar way, the Collimators are used to monitor some beam properties like its size and axial alignment, by measuring the beam current dropped on them. For these components, it is fundamental to suppress the emission of secondary electrons, which are emitted when a particle with enough energy strikes a metal or a conductive surface. The most common method used to prevent the loss of charged secondary particles is to place a suppression electrode in front of the device and to apply a voltage which will establish an electric field to repel the charges and keep them in the surface. It has been proved that a suppressor voltage of about -90 V is enough in order to reach stable values of the current measurements from the device [35].

It seems clear that the design of such devices intercepting the beam is strongly influenced by the energy and the intensity of the beam. For this reason, some of the device currently installed in the 40 MeV proton beam line must be redesigned in view of the energy upgrade foreseen for SPES-2. In the present chapter, the designs of the Collimators (Sec.3.2), the Faraday Cup (Sec.3.3) and the Target Window (Sec. 3.4) are presented. It is important to remark that the redesign process is carried out considering also the 40 MeV solutions: if the actual 40 MeV device is improvable (as for the Collimators) or missing (as for the Target Window), the new design will be carried out with the most critical beam energy so the new device can be installed both in SPES (40 MeV beam energy) and in SPES-2 (70 MeV beam energy).

3.2 Collimators

Before hitting the target, the proton beam delivered by the cyclotron travels along the proton beam line. However, a fraction of the particles can acquire enough transverse momentum by the repulsive space-charge forces within the beam to form a halo. Halo particles can be lost on the walls of the beam line structures and cause beam losses which cannot be neglected. Beam collimation is therefore important to protect components against excessive irradiation, to maintain operational reliability over the whole lifetime of the machine, to provide acceptable maintenance conditions and to reduce the impact of radiation on the environment [36]. The most direct way of collimating a beam of particles is to define a physical aperture (hole) within a solid block made of an absorbing material. The collimator's material must therefore withstand a predefined fraction of the hitting beam and survive for a time long enough to avoid costly replacements. The collimator can also be used to monitor some beam properties like its size and alignment.

3.2.1 Boundary conditions

In ideal conditions, before hitting the target discs, the beam particles follow a trajectory parallel to the target axis. In this situation, a collimator with an inner diameter equal to the target disc diameter would avoid particle dispersion along the beam line and inside the target chamber. Actually, the protons diverge also travelling along the beam line. To avoid an excessive proton dispersion, a collimator with an inner radius smaller than the discs' diameter must be foreseen. Using a collimator with a smaller internal radius, in fact, it is possible to 'cut' the external halo particles of the beam which, in any case, would not have impinged the target. The farther the collimator from the target, the smaller the radius should be, to limit the proton dispersion along the line. However, if the collimator inner radius is too small, less particles reach the edge of the target discs, with a consequent non uniform power deposition. In this case, in fact, the discs would be characterized by a higher deposition around the center and a lower deposition at their edge. In Figure 3.1, the power deposition in the first disc of the 40 MeV high power target (Sec. 1.4.2) is presented, when a collimator is installed at 1.5 m from the target, for different internal radii. The blue curve, called 'REF' represents the ideal power deposition, obtained for parallel trajectories of the particles. As the internal radius decreases, the power deposition at the edge of the disc decreases too. This would cause significant temperature gradients and consequent high stresses. The closer to the target the collimator is installed, the higher is the control on the cut particles and consequently on the particles reaching the target. A higher internal radius can be set for a collimator installed close to the target.

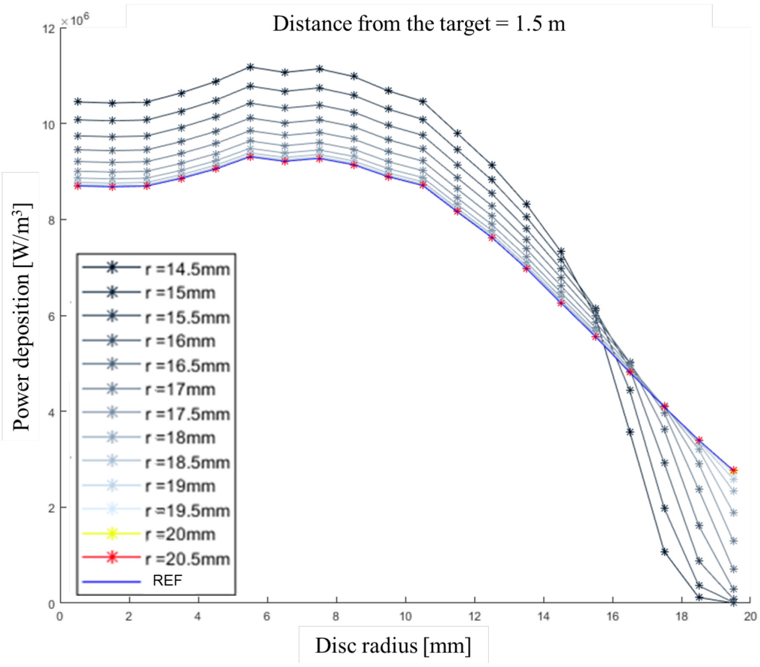

Figure 3.1 Radial power deposition on the first disc of the target, obtained with a collimator installed at 1.5 m from the target, for different internal radii.

In the present SPES beam line, designed for a 40 MeV beam energy, a collimator has been foreseen at about 1.6 m from the target, as shown in Figure 3.2. For this device, an inner radius equal to 16 mm has been chosen.

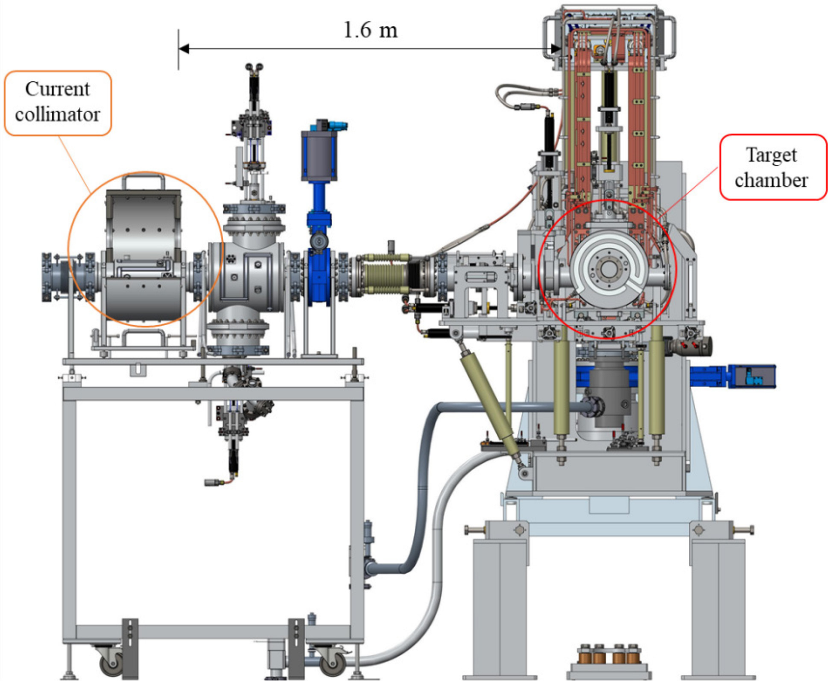

Figure 3.2 Present position of the collimator in the 40 MeV SPES proton beam line.

The small radius, required due to the distance from the target, avoids particle dispersion but, as explained, leads to excessive stresses on the discs, as shown in Figure 3.3. For Uranium Carbide, in fact, a maximum stress of 200 MPa is foreseen, greatly exceeded in the first discs. This is due to a low power deposition at the edge of the disc, caused by the small inner radius.

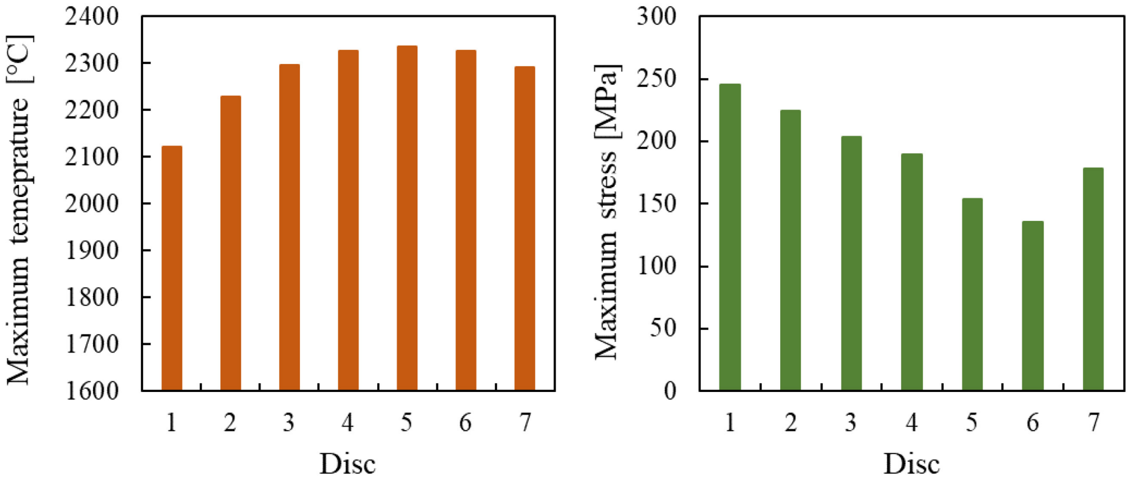

Figure 3.3 Maximum temperatures and stresses reached in the target's discs obtained with the current collimator that has been installed at 1.6 m from the target.

Therefore, to improve the performance of the current collimator, two interventions are needed:

- A new collimator should be added closer to the target: then, it would be possible to foresee higher internal radii and, consequently, more uniform power deposition on the target discs.
- The collimator should be redesigned to be able to work with a higher beam energy: the current device, in fact, is not able to fully stop the external particles with an initial energy of 70 MeV.

To solve these issues, the design of a new modular collimator is proposed. The idea is to design a collimator that can be used in different positions in the line and able to work with both 40 MeV and 70 MeV beam energy. Therefore, it will be possible to add a new collimator to the current 40 MeV beam line, closer to the target, and to replace the old collimator in the future 70 MeV beam line. Graphite is often chosen as absorbing material due to its low activation, high resistance at high temperatures and good workability. Approximately 10 mm of graphite is needed to stop a proton beam at 40 MeV energy, while the minimum thickness is increased up to 27 mm for a 70 MeV energy beam. The collimator can also be used to control the size and the alignment of the beam, measuring the current hitting the absorbing material. For this purpose, graphite must be sustained by an insulated material able to support high temperatures. Boron nitride is chosen since it is an insulating material that presents also a good thermal conductivity and a stability without deterioration up to 1400°C [37]. Finally, if a significant amount of power is dropped on the collimator, a cooling circuit must be foreseen, to properly dissipate the beam power deposition. Thanks to its high thermal conductivity, the cooling circuit is machined in a ETP copper element. A schematic representation of the collimator is shown in Figure 3.4.

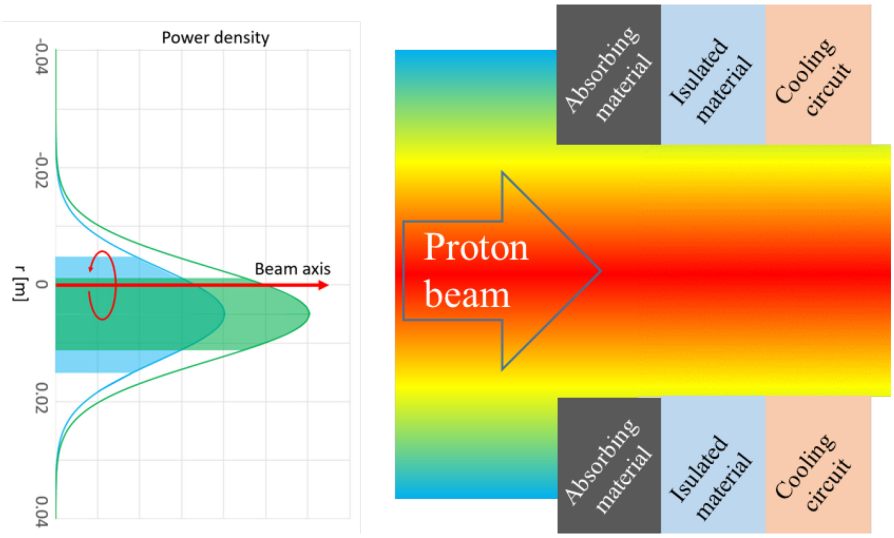

Figure 3.4 Schematic representation of the elements composing a collimator.

The maximum power that can be dropped on the collimator is fixed at 15% of the total power reaching the target [8]. The design has been carried out considering a high-power target since, when a low power target is installed, a smaller centered beam is used. In that case, the beam collimation is entrusted to the small collimator housed inside the target chamber and presented in Sec. 2.3. The SPES high power targets are designed to work with a power of 8000 W (as shown in Sec.1.4.2), therefore a maximum power deposition of about 1200 W is expected on the collimator. To be in safer conditions, the new collimator will be designed for a beam power deposition of 2000 W. Since only the tails of the Gaussian function describing the beam (see Sec. 1.4.2) will impinge the absorbing material, the beam profile does not significantly influence the collimator design. Moreover, it has been proved that in this range of deposited power and in stable conditions, the longitudinal Bragg energy loss profile does not significantly influence the maximum temperatures and stresses reached in graphite [38]. The power deposition is therefore modelled as a homogeneous heat generation inside the 'deposition volume' (Figure 3.5). This volume is defined by the internal radius of the collimator, R_{int}, the maximum radius reached by the beam particles, R_{ext}, and the thickness of graphite needed to fully stop the beam, s. The internal radius of the collimator will be set in the next sections; the maximum radius reached by the particles is set at 25 mm [8], due to other collimation elements placed upstream along the beam line; the deposition thickness is equal to about 10 mm for a 40 MeV energy beam, and to about 27 mm for a 70 MeV beam. With the same internal and external radius, imposing a power deposition of 2000 W, a higher power density is registered in the 40 MeV case, characterized by a smaller deposition volume. For this reason, the design of the new collimator will be carried out considering a 40 MeV beam energy.

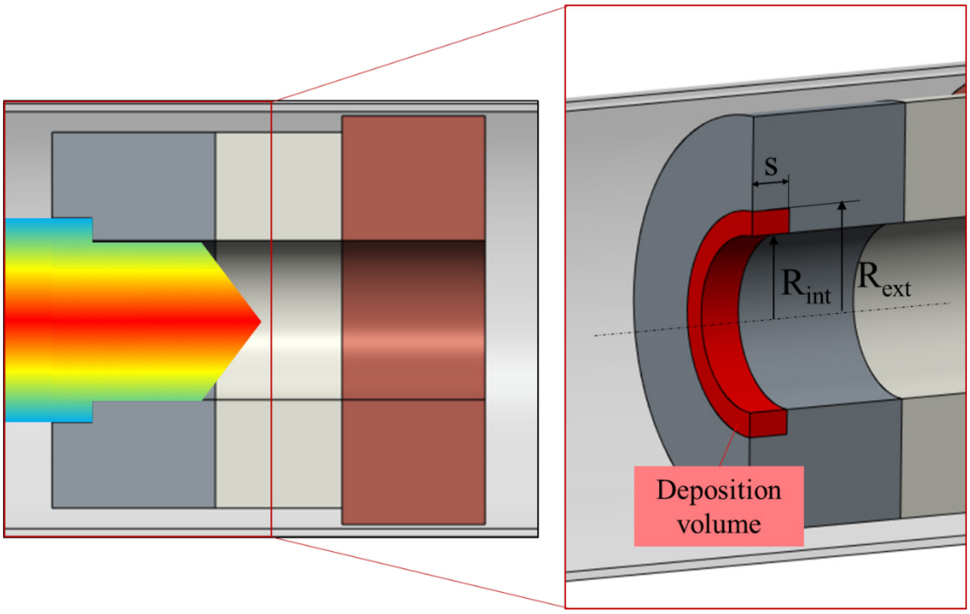

Figure 3.5 Deposition volume in the absorbing material in which the beam power is deposited.

The design boundary conditions can be summarized as follows:

- Graphite as absorbing material, Boron nitride as insulator and ETP Copper for the cooling element.
- Beam characteristics: 40 MeV energy, 7 mm RMS radius and 11 mm wobbling radius.
- 8000 W beam power deposited on the target (high power target).
- 2000 W beam power deposited on the collimator.
- External deposition radius equal to 25 mm.
- Maximum deposition thickness equal to 9.75 mm.

Once designed the modular collimator, it will be necessary to define the proper inner radii and positions along the beam line.

3.2.2 Preliminary design and thermal analyses

As shown in the previous section, the collimator is composed of an assembly of three different materials: an absorbing material (graphite), an electrical insulator (boron nitride) and a third material in which a cooling circuit is foreseen (ETP copper). To control the maximum temperatures reached in the collimator, several thermal simulations are implemented in ANSYS Mechanical [27], imposing a power deposition of 2000 W. The three elements are simulated suspended in vacuum inside an aluminum tube representing the proton channel. A 2D and a 3D models are used, as shown in Figure 3.6. In the bi-dimensional model the cooling is simulated imposing a constant temperature of 50 °C on the external surface of the copper element. In the three-dimensional model a real cooling circuit, properly sized and designed, is implemented and a convective flow is imposed. The thicknesses for the boron nitride and the copper are set respectively equal to 31 mm and 35 mm, while an internal radius of 19.5 mm is chosen for the collimator. This value is set from considerations that will be presented in the following sections. For graphite a thickness of 40 mm is chosen. As better explained in Sec. 3.2.5, the absorbing material will be in fact divided in four separated sectors, diagonally cut, in order to distinguish the part of the beam impinging on each sector. An additional thickness is therefore needed, over the necessary 30 mm to stop completely the beam, to ensure that a particle passing through the separation between two sectors cannot reach the insulating material.

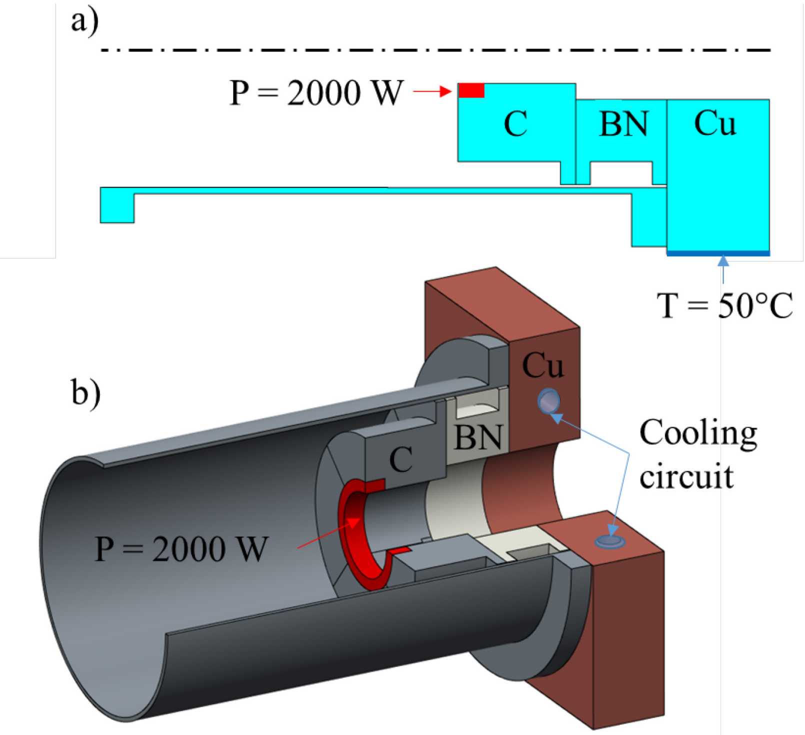

Figure 3.6 2D (a) and 3D (b) models used for the preliminary design of the collimator.

Three different simulations are then implemented:

- Case A: 2D simulation with perfect contact between the elements, simplified cooling.
- Case B: 3D simulation with perfect contact between the elements, real cooling circuit.
- Case C: 2D simulation with real contact between the elements, simplified cooling.

The aim is to validate the bi-dimensional simulations and to verify the influence of the thermal contact resistance between materials. This phenomenon, preliminary described in [39], leads in fact to temperature variations at the interfaces between materials, with consequent higher temperatures reached in the collimator’s elements. The contact thermal resistances, and consequently the temperature change, depend on some materials characteristics, such as micro hardness and thermal conductivity, and on the joint pressure of the mating surfaces. In particular, by increasing the contact pressure, a lower thermal resistance and a lower temperature variation is registered. Even though several analytical models are available to calculate the thermal resistance between two material, such as the Yovanovich model [40], experimental data remain the most reliable reference. Experimental tests of thermal resistance between graphite and boron nitride and between boron nitride and copper have been already carried out [39]. Imposing a reasonable contact pressure of 2 MPa between the surfaces, the resulting experimental specific thermal resistances are:

$$R_{c,s\,C-NB} = R_{c\,C-NB} \cdot A = 1.28 \cdot 10^{-4} \quad m^2KW^{-1} \qquad 3.1$$

$$R_{c,s\,Cu-NB} = R_{c\,Cu-NB} \cdot A = 2.94 \cdot 10^{-4} \quad m^2KW^{-1} \qquad 3.2$$

where $R_{c,s}$ is the specific thermal resistance, R_c is the thermal resistance, and A is the contact area (m^2).

The results of the simulations are presented in Table 3.1. By comparing the 2D and 3D ideal contact models (Case A and Case B), it can be observed that lower temperatures are obtained simulating the real cooling circuit. On the other hand, a significant influence of the real contact between the surfaces can be noted by comparing Case A and Case C, especially for the maximum temperature of the graphite element. Considering these results, further analyses will be implemented using a 2D geometry with simplified cooling, to be on the safe side, and considering the real contact between the surfaces. Higher temperatures are in fact expected with a 2D model, with respect to the more realistic 3D model, and the effect of the thermal contact resistance is not negligible.

Table 3.1 Thermal results of the simplified models of the collimator, imposing a deposited power of 2000 W, for an internal radius of the collimator equal to 19.5 mm.

Maximum temperature:	**Case A** **2D ideal contact** **50°C on copper**	**Case B** **3D ideal contact** **Cooling circuit**	**Case C** **2D real contact (2 MPa)** **50°C on copper**
Graphite	696°C	639°C	815°C
Boron nitride	454°C	416°C	516°C
Copper	64°C	58°C	62°C

3.2.3 Potential distribution for the secondary electron suppression

As presented in Sec. 3.1, the suppression of the secondary electrons is fundamental to evaluate the beam impinging on a target. As seen, a -90 V potential is enough to furnish a sufficient potential shield. For the collimator it is necessary to foresee two suppressors able to stop the emitted electrons, one in the front part (front suppressor) and one in the back part of the graphite element (back suppressor). These elements will present a ring geometry and graphite is chosen as material for their realization. Simple axial symmetric simulations of the potential distribution are needed to properly design the suppressors. By applying a potential of -1 V on the rings, it is possible to calculate the suppression efficiency along the collimator axis. From the simulations the following dimensions are defined:

- Back suppressor: inner radius of 25 mm, external radius of 30 mm and thickness of 5 mm.
- Front suppressor: inner radius of 40 mm, external radius of 54 mm and thickness of 6 mm.

The corresponding potential distribution is presented in Figure 3.7: the shielding efficiency of the secondary electrons is 0.35 for the back suppressor and 0.21 for the front suppressor. Consequently, by applying to the suppressors a potential of -500 V, the minimum potential of -90 V, necessary to stop the electrons emission, is ensured.

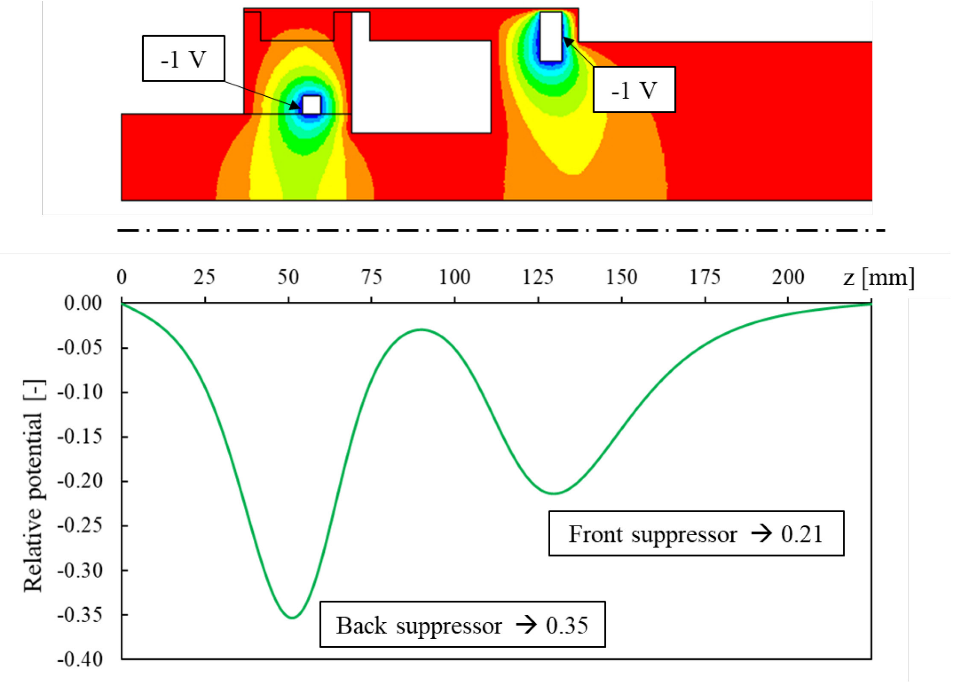

Figure 3.7 Potential distribution of the collimators space, along the axis.

3.2.4 Sensitivity analyses

3.2.4.1 Internal radius

As explained in the previous sections, it should be possible to install the collimator in different positions along the line. However, different positions require different internal radii, to obtain a proper power deposition on the target's discs. Therefore, the design presented in Sec. 3.2.2 must be validated for different internal radii. A sensitivity analysis is therefore performed, in order to control the maximum temperatures reached in the collimator's elements. The bi-dimensional model shown in Figure 3.6 (a) is used, considering the real contact between surfaces. A contact pressure of 2 MPa is maintained, therefore the experimental specific thermal resistances presented in Eq. 3.1 and Eq. 3.2 are still valid. The total deposited power of 2000 W and the external deposition radius of 25 mm are also maintained. However, by varying the collimator internal radius, the deposition volume will vary accordingly. The resulting power depositions and maximum temperatures calculated in the different cases are reported in Table 3.2 and Figure 3.8. It can be noted that the maximum temperatures of graphite and boron nitride increase with higher internal radii. On the other hand, no significant variation is observed in the copper element. Even in the most critical case, with an internal radius equal to 24 mm, the maximum temperatures do not exceed the limit temperature of the materials. In particular, graphite operative temperature is more than 2000°C [41][42], boron nitride presents in vacuum a stable behavior up to 1400°C [37], and the ETP copper guarantees thermal mechanical stability up to 150°C [43]. Moreover, the temperatures reached in the copper element are far from the boiling temperature of water. No erosion effects are therefore expected in the real cooling circuit.

Table 3.2 Power deposition and maximum temperatures by varying the collimator's internal radius, with a total deposited power of 2000 W and a contact pressure of 2 MPa. T_{max} C, T_{max} NB, and T_{max} Cu are the maximum temperatures reached in graphite, boron nitride, and copper respectively.

Internal radius [mm]	**Deposition Volume [m^3]**	**Power deposition [W/m^3]**	**T max C [°C]**	**T max NB [°C]**	**T max Cu [°C]**
8	$1.72 \cdot 10^{-5}$	$1.16 \cdot 10^{-8}$	704	442	65
10	$1.61 \cdot 10^{-5}$	$1.24 \cdot 10^{-8}$	715	450	65
12	$1.47 \cdot 10^{-5}$	$1.36 \cdot 10^{-8}$	733	462	64
14	$1.31 \cdot 10^{-5}$	$1.52 \cdot 10^{-8}$	747	473	64
16	$1.13 \cdot 10^{-5}$	$1.77 \cdot 10^{-8}$	770	488	63
18	$9.22 \cdot 10^{-6}$	$2.17 \cdot 10^{-8}$	795	503	63
19.5	$7.5 \cdot 10^{-6}$	$2.67 \cdot 10^{-8}$	815	516	62
20	$6.89 \cdot 10^{-6}$	$2.9 \cdot 10^{-8}$	823	521	62
22	$4.32 \cdot 10^{-6}$	$4.63 \cdot 10^{-8}$	858	541	62
24	$1.5 \cdot 10^{-6}$	$13.3 \cdot 10^{-8}$	896	563	61

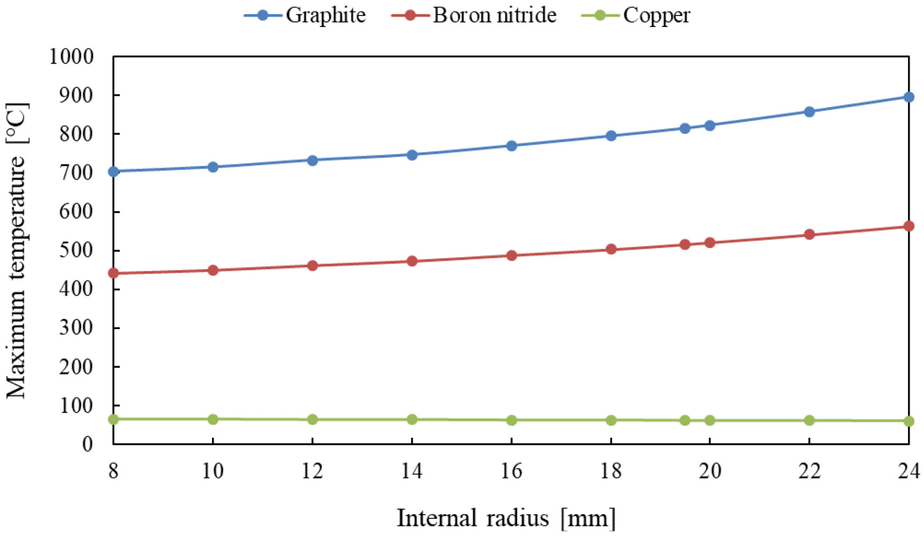

Figure 3.8 Maximum temperatures by varying the collimator's internal radius, with a total deposited power of 2000 W and a contact pressure of 2 MPa.

3.2.4.2 Contact pressure

The previous analyses are carried out imposing a 2 MPa contact pressure. However, by varying this parameter also the thermal resistances vary, and consequently the maximum temperatures. In particular, as the pressure decreases, the thermal resistance increases. It is therefore necessary to validate the collimator's design also when a lower contact pressure is imposed. At this purpose, a bi-dimensional simulation is implemented using the same model presented in the previous section. As shown in Sec. 3.2.4.1, the maximum temperatures are reached when the collimator has an internal radius equal to 24 mm. To validate the design in the most critical conditions, an internal radius equal to 24 mm and a contact pressure of 0.5 MPa are therefore imposed in the simulation. The correspondent experimental specific thermal resistances, measured in [39], are:

$$R_{c,s\,C-NB} = R_{c\,C-NB} \cdot A = 4.640 \cdot 10^{-4} \quad m^2KW^{-1} \tag{3.3}$$

$$R_{c,s\,Cu-NB} = R_{c\,Cu-NB} \cdot A = 4.645 \cdot 10^{-4} \quad m^2KW^{-1} \tag{3.4}$$

The resulting temperature distribution is reported in Figure 3.9. In this case too, no critical temperatures are reached in the materials. The preliminary design is therefore validated.

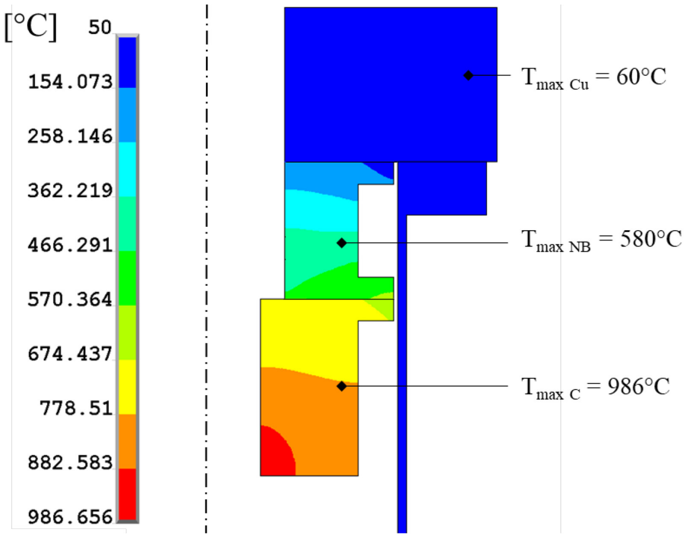

Figure 3.9 Temperature distribution and maximum temperatures reached in the collimator's elements. 2000 W total power deposited; 24 mm inner radius; 0.5 MPa contact pressure.

3.2.4.3 Electron suppression

By varying the inner radius of the collimator, also the shielding potential along the collimator's axis can vary. It is therefore necessary to assure a proper shielding potential also when a different inner radius is chosen. The front suppressor presents the lower shielding efficiency: this value can decrease by decreasing the inner radius of the collimator. The most critical case is therefore verified, imposing a collimator's radius of 8 mm. The same simulation presented in Sec. 3.2.3 is implemented. The resulting potential distribution are shown in Figure 3.10, obtaining an efficiency value of 0.2 for the front suppressor. This value ensures the minimum potential of -90 V to repel the secondary electrons, when a potential of -500 V is applied to the suppressor.

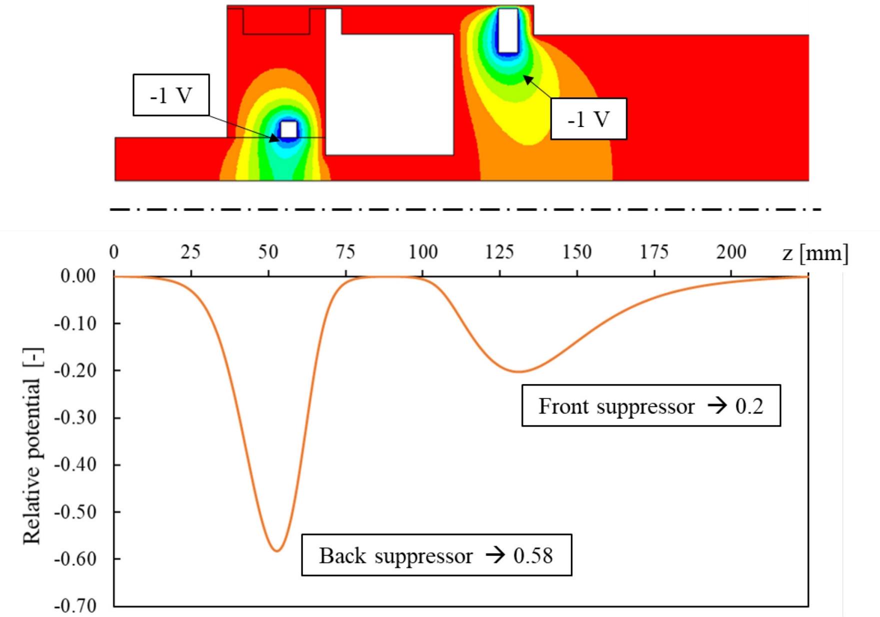

Figure 3.10 Potential distribution of the collimators space, along the axis, with 8 mm internal radius.

3.2.5 Mechanical design [39]

As explained in the previous sections, it is possible to install the modular collimator in different positions along the proton beam line. However, it has been highlighted the need to foresee a new collimator closer to the target also in the current case of a 40 MeV energy beam line. In Sec. 3.2.6 a 0.5 m distance from the target will be fixed for this collimator. A 3D model, presented in Figure 3.11, is therefore implemented in CREO Parametrics [30] in order to define its installation inside the proton beam line.

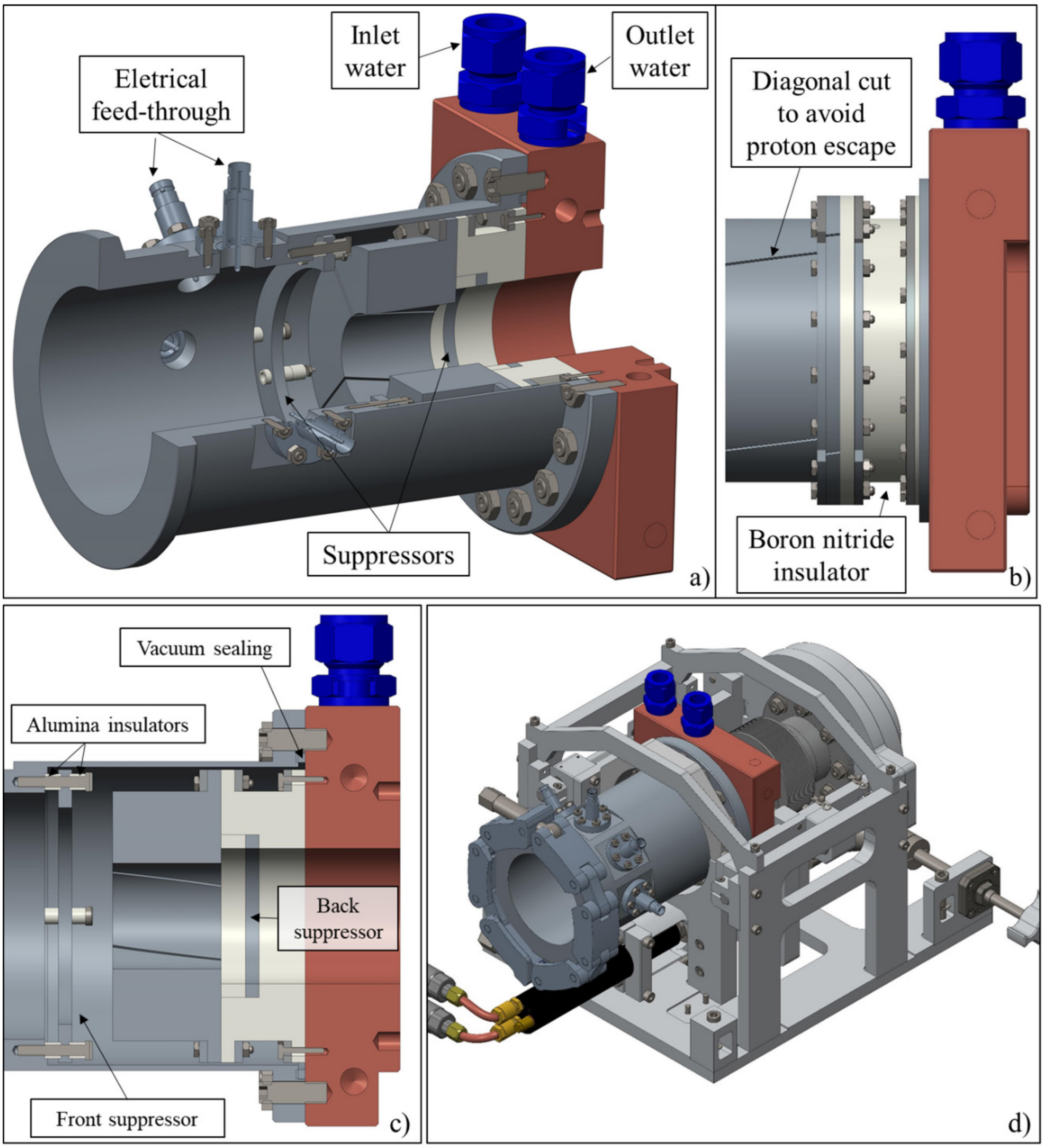

Figure 3.11 Partial section of the complete CAD model (a); lateral particular with the studied diagonal cut to avoid proton escape (b); section of the collimator and suppressors (c); installation of the assembly on the protonic line.

As shown in Figure 3.11, the graphite element has been divided in four sectors in order to detect the beam impinging on each part and to be able to control the beam alignment. Thanks to an opportune diagonal cut at a certain angle, there is no space between the sectors where protons could escape, maintaining the total thickness higher than the proton projectile range. Each sector is electrically insulated by the boron nitride element: the proton beam current dropped on them is collected out by tantalum wires and brought out of the beam line by means of standard BNC feed-throughs. The front and the back suppressors prevent the emission of secondary electrons.

3.2.6 Collimators' sizing and positioning

The collimator designed in the previous sections ensures non-critical temperatures for different internal radius when a power of 2000 W is deposited on it. It is therefore possible to install the device in different position of the line, choosing different inner radii. The proper position and radius will avoid proton dispersion along the beam line and the target chamber and will allow a uniform power distribution in the target discs to be obtained. As shown in Sec. 3.2.1, a new collimator must be installed close to the target, in order to obtain a better control on the particles reaching the discs.

A Matlab [44] code, developed in the framework of the SPES target group, is used to quickly define the optimal dimension of the new collimator, to be placed close to the target. The code allows, setting the beam characteristics, the beam particles trajectories to be calculated and followed and, by defining the dimensions and the positions of one or more collimators, the radial power deposition on the first disc of the target to be calculated. As shown in [8], in the SPES high power targets, the maximum stresses are reached on the first disc. It is therefore possible to use the Matlab code to quickly vary the collimator configuration to find the optimal conditions that allow a uniform power deposition and consequently low stresses to be obtained. The sizing procedure is summarized as follows:

1. An ideal beam (parallel trajectories) is simulated with the FLUKA Montecarlo code [22][23], and the power deposition on the target elements is calculated.
2. The power deposition on the first disc is calculated with the Matlab code, by varying the size and the position of the collimator.
3. Thermal-mechanical simulations are then implemented, imposing the Matlab power deposition in the first disc and the FLUKA power depositions on the other elements.
4. The stresses reached in the first disc (which presents the higher stresses [8]) are analyzed varying the collimator parameters.
5. The optimal collimator configuration is chosen, to obtain the lowest possible stresses on the first disc.

6. A realistic beam is then simulated in FLUKA, implementing the target and the new collimator just defined. The power deposition on the target elements is calculated and a thermal-mechanical simulation is implemented in ANSYS to validate the configuration.

The sizing of the new collimator will be carried out on the 40 MeV high power target, since it will be the first installed on the SPES line. The same procedure can be followed also for the 70 MeV high power target. The Matlab code is executed, by varying the internal radius between 14.5 mm and 20.5 mm, and the distance from the target between 0.1 m and 1.7 m. The correspondent thermal structural simulations are then carried out in ANSYS and the maximum stresses are analyzed. In Figure 3.12, for each distance of the collimator from the target, the minimum radius to avoid excessive stresses on the discs is reported.

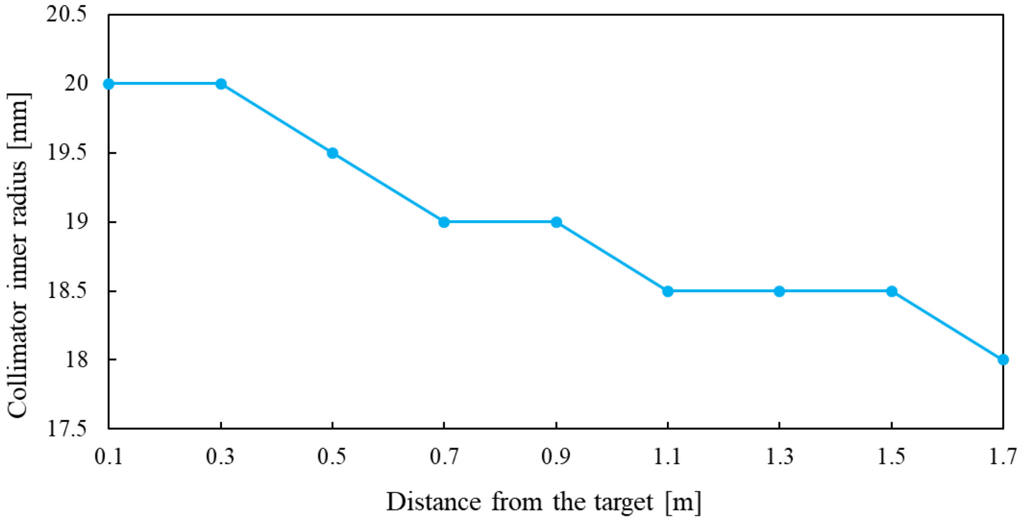

Figure 3.12Minimum collimator's inner radius to avoid excessive stresses on the discs, by varying the distance of the collimator from the target.

The maximum stresses and temperatures obtained in the first disc of the target for different configurations are reported in Table 3.3. Considering a maximum stress of about 200 MPa for Uranium Carbide [18], it can be observed that, when the collimator is installed closer to the target, it is possible to foresee a higher internal radius with respect to farther collimators. Moreover, for closer devices, a better control of the particles is obtained with consequent lower power dispersion out of the target even for higher radii.

Considering the dimensions of the target chamber and other necessary elements of the line, a 0.5 m distance from the target is considered acceptable. The resulting power deposition curves by varying the internal radius are presented in Figure 3.13.

Table 3.3 Maximum temperature (Tmax), temperature difference (dT) and Von Mises stress (σ_{VM}) for different combinations of distance (d) and internal radius (r) of the collimator. P_{out_target} represents the power deposition out of the target, due to particles not impinging the target.

d [m]	**r [mm]**	**Tmax [°C]**	**dT**	**σ_{VM} [MPa]**	**P_{out_target} [W/m^2]**
1.7	17.5	2130	208	244	
	18	**2122**	**183**	**206**	**$1.2 \cdot 10^6$**
1.5	16	2132	213	252	
	17.5	2123	188	215	
	18.5	**2122**	**181**	**204**	**$1.3 \cdot 10^6$**
1.3	18	2122	185	211	
	18.5	**2121**	**182**	**205**	**$1.1 \cdot 10^6$**
1.1	**18.5**	**2122**	**183**	**206**	**$7.8 \cdot 10^5$**
0.7	16.5	2138	227	269	
	17.5	2130	209	249	
	19	**2121**	**182**	**205**	**$4.2 \cdot 10^5$**
0.5	19	2122	184	210	
	19.5	**2121**	**180**	**202**	**$6.1 \cdot 10^5$**

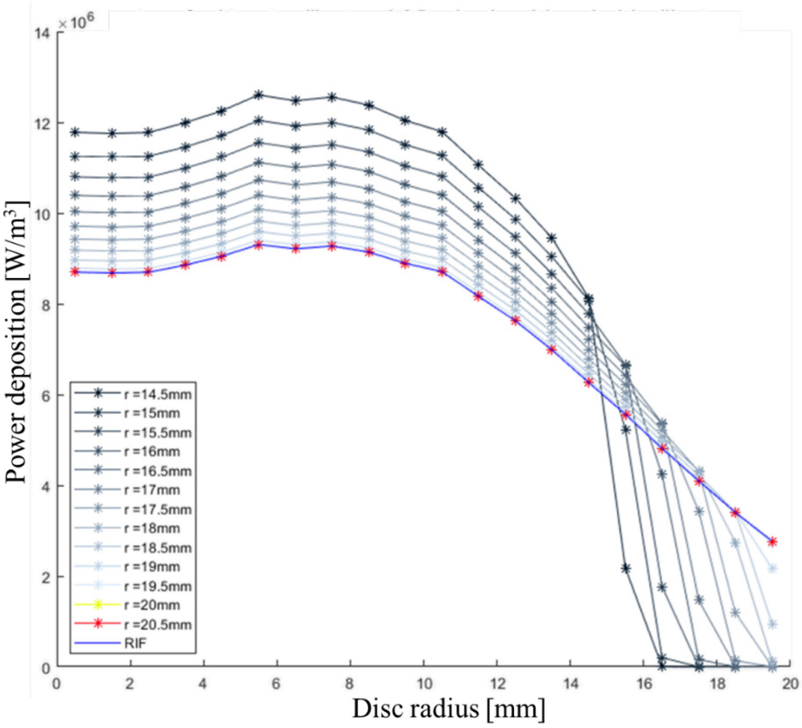

Figure 3.13 Radial power deposition on the first disc of the target, by varying the collimator inner radius r, for a fixed distance of the collimator from the target equal to 0.5 m. 'REF' represents the reference power deposition obtained simulating an ideal parallel beam.

The *REF* curve reported in the graph represents the power deposition obtained with an ideal parallel beam. As shown in the figure, for smaller inner radii a less uniform beam is obtained. A higher deposition is obtained in the central part of the disc with smaller radii because the code adjusts the initial beam current to provide a total power of 8000 W deposited on the target. Considering the thermal structural results, a distance of 0.5 m and an inner radius equal to 19.5 mm are therefore chosen for the new collimator.

It is important to remark that a collimator installed at 1.6 m from the target is also maintained. In fact, when all the external particles are stopped in a single collimator, a significant activation is generated, and shielding must be provided. Since there is not enough space close to the target to install a shielded collimator, the idea is to split the deposition on two different devices. The first collimator, installed far from the target, should stop most of the particles. This device is highly activated and properly shielded. Then, a second collimator will be placed closer to the target: only a small fraction of the particles will be stopped on it, but it will guarantee a good control on the particles reaching the target. The old collimator is then added in the Matlab code, to define the proper inner radius to avoid an excessive power deposition on the new collimator. The radius is varied between 16 mm and 18 mm and the total power depositions on the two collimators, on the target and out of the target (inside the target chamber) are analyzed. Thermo-structural simulations are also implemented in order to control the maximum temperatures and stresses reached on the target. The results are reported in Table 3.4. It is important to remark that in all cases the total power deposited in the target is fixed at 8000 W, because the Matlab code sets the initial current in order to maintain constant this value. As shown in Table 3.4, by increasing the internal radius of the collimator installed far from the target, the power deposition on this device and the maximum stresses on the first disc of the target decrease. On the other hand, a higher power is deposited on the new collimator and a higher power is lost out of the target. However, choosing an internal radius of 18 mm, the power deposited on the new collimator is about 106 W, while on the farther collimator a total power of 1150 W is foreseen. Considering that the new design has been carried out for a total deposited power of 2000 W, the new designed collimator can be used in both positions simply varying the internal radius.

Table 3.4 Maximum temperature (T_{max}), temperature difference (dT) and Von Mises stress (σ_{VM}) reached on the first disc of the target by varying the internal radius of the old collimator installed at 1.6 m from the target, considering also the new collimator installed at 0.5 m with an internal radius of 19.5 mm.

d = 1.6 m	**Temperature and stresses**			**Powers [W]**			
r [mm]	**Tmax [°C]**	**dT**	**σ_{VM} [MPa]**	**Power on the far collimator**	**Power on the close collimator**	**Power out of the target**	**Power on the target**
16	2132	211	247	2005.7	0	4.8	8000
16.5	2128	202	235	1744.2	0.9	17.8	8000
17	2125	193	223	1516.4	8.0	43.3	8000
17.5	2123	187	213	1319.8	38.0	74.5	8000
18	**222**	**183**	**206**	**1149.8**	**105.9**	**94.4**	**8000**

Using the Matlab code, it has been possible to define a new collimator placed at 0.5 m from the target with an internal radius equal to 19.5 mm and a second collimator installed at 1.6 m with an internal radius equal to 18 mm. These positions and dimensions should assure acceptable maximum stresses on the target, comparable with those obtained simulating an ideal beam. In order to validate these results, a final simulation is implemented in FLUKA, considering a real beam (with particles' divergence), the two collimators and the high-power target. The obtained power depositions are then imposed as input in ANSYS for thermal structural simulations to control the maximum stresses and temperatures reached in the target. The results are then compared with:

- the results obtained by imposing the Matlab power deposition on the first disc. On the other elements, the FLUKA power depositions obtained simulating an ideal beam with parallel trajectories of the particles are imposed.
- the results obtained imposing the FLUKA ideal depositions on all the target's elements, including the first disc.

For simplicity, the results obtained with the final FLUKA simulation are referred to as 'FLUKA real beam'; the results obtained with the Matlab deposition on the first disc are referred to as 'Matlab'; the results obtained with the FLUKA ideal beam are referred to as 'FLUKA ideal beam'. The comparison of the maximum stresses and temperatures obtained in the three cases are shown in Figure 3.14, while the radial power deposition on the first disc is reported in Figure 3.15.

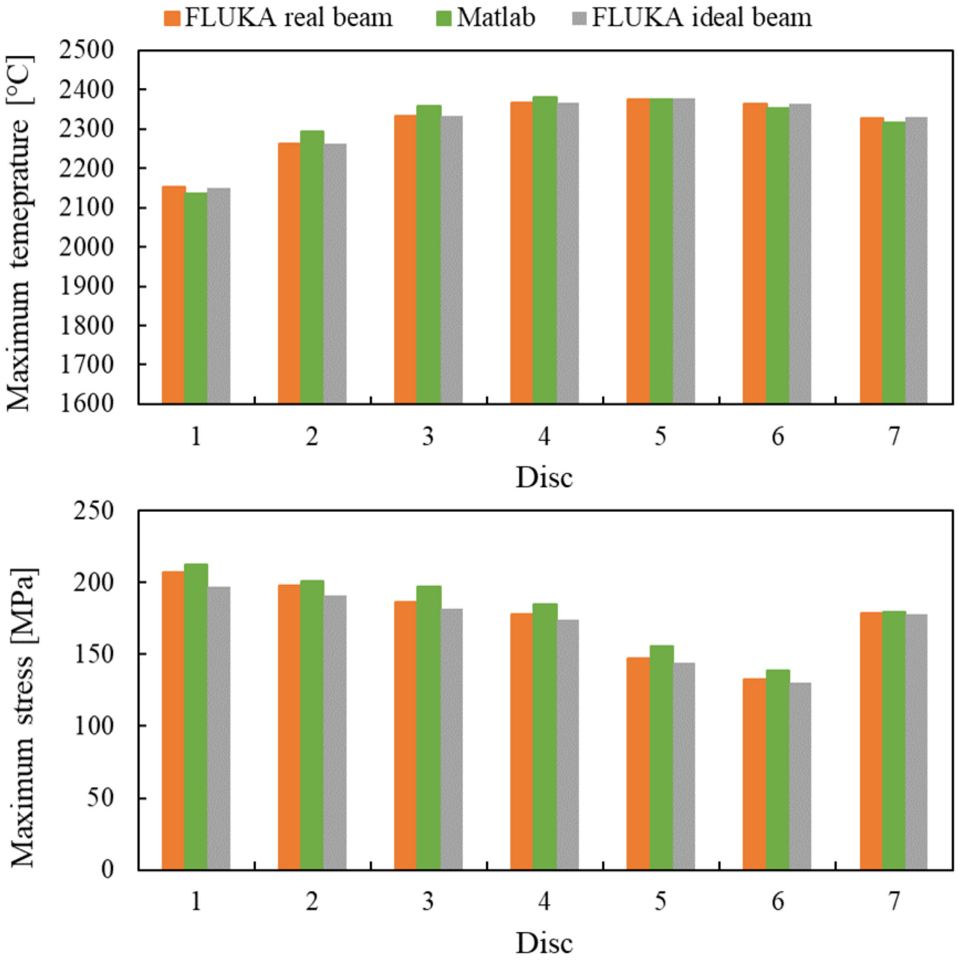

Figure 3.14 Maximum temperatures and stresses reached in the target's discs obtained with the Matlab code and with the FLUKA (realistic and ideal beam) power depositions.

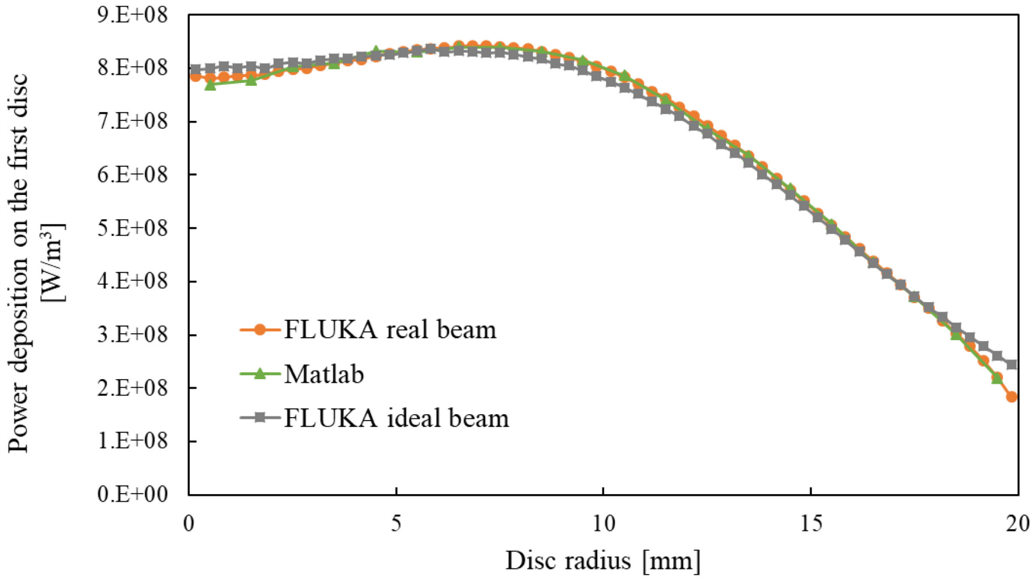

Figure 3.15 Radial power deposition on the first disc of the target, obtained with the Matlab code and with FLUKA (realistic and ideal beam).

No significant differences are highlighted for the maximum temperatures in the three cases. Moreover, the maximum temperature is reached on the 5th disc of the target, in which the differences between the simulations are practically nil, lower than 0.1%. The maximum stress is always reached on the first disc: in this case, the higher value is the one calculated with the Matlab power deposition with a variation of about 7% over the FLUKA ideal beam, but less than 3% over the FLUKA real beam. These discrepancies with respect to the ideal beam can be explained by analyzing the power depositions of Figure 3.15. As expected, a higher power is deposited at the edge of the disc in the real case. This allows the temperature gradient to be limited and, consequently, the thermal stresses. However, as explained in Sec. 3.2.1, in real conditions, a collimator with a smaller internal radius with respect to the disc radius is necessary, to avoid particle dispersion along the line and inside the target chamber. This leads to lower power deposition at the edge and higher stresses. In any case, if the Matlab power deposition is considered for the sizing procedure, the design is in favor of safety. The proposed sizing and positioning process by means of the Matlab code is therefore validated. This allows fast parametric analyses to be performed and a more time-consuming FLUKA simulation to be carried out only as final step of the process.

3.2.7 Beam misalignment diagnosis

As shown in Sec. 3.2.1, the collimator's absorbing material has been separated in four sectors in order to detect the impinging beam on each part and, therefore, to be able to control the beam alignment.

In the previous sections two collimators have been designed:

- First collimator installed at 1.6 m from the target, with internal radius equal to 18 mm;
- Second collimator installed at 0.5 m from the target, with internal radius equal to 19.5 mm.

It is important to verify that this configuration allows a beam misalignment to be detected. Both collimators are separated in four sectors: this ensures a double check on the beam alignment before reaching the target.

The control is carried out both with a low beam current equals to 1 μA, and with a higher current equal to 235 μA. As previously explained, the high-power target is designed in order to work with 8000 W deposited power, corresponding to a current of 200 μA impinging on the target. However, a power loss of about 15% is expected on the collimators: an increased initial current has therefore to be used, in order to obtain the proper amount of current on the target. FLUKA simulations are implemented, considering a real 40 MeV energy beam impinging on the two collimators. First, an aligned beam is simulated, as shown in Figure 3.16, and the currents reaching each collimator's sector are calculated. The results are reported in Table 3.5. Then a vertical misalignment of 5 mm is imposed and the current calculation is repeated, as shown in Table 3.6.

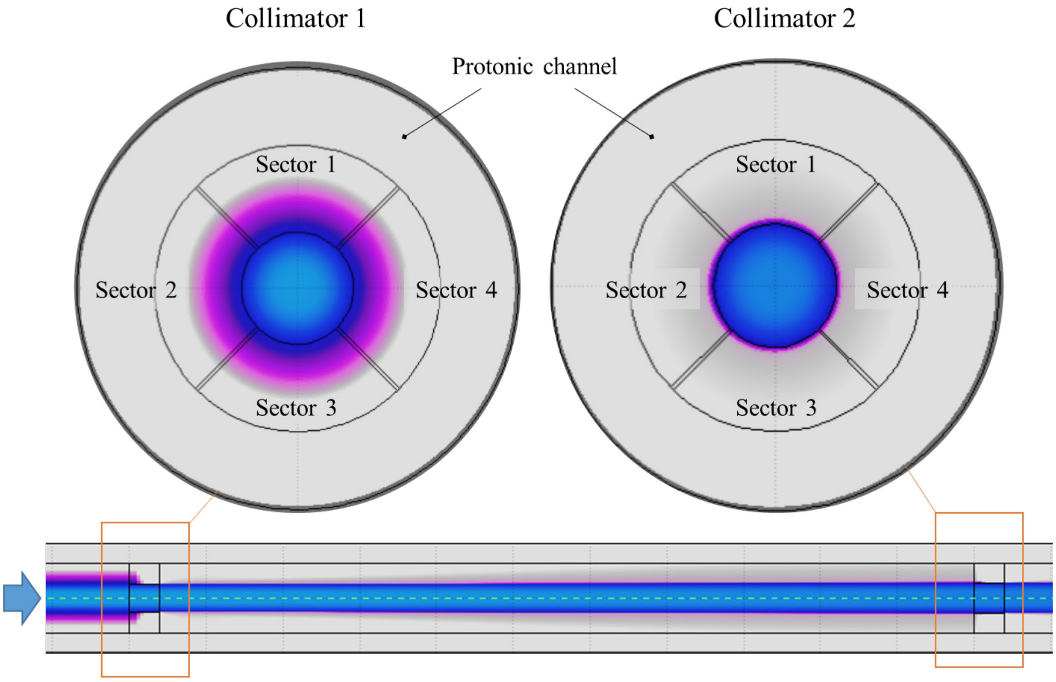

Figure 3.16 Proton distribution along the protonic beam line, for a 40 MeV energy aligned beam.

Table 3.5 Power depositions and beam currents on the collimators' sectors, for 1 μA and 235 μA beam current, with a 40 MeV aligned proton beam.

First collimator **d = 1.6 m** **r = 18 mm**	**For 1 μA beam current**		**For 235 μA beam current**	
	Power [W]	**Current [nA]**	**Power [W]**	**Current [μA]**
On each sector	1.2	29.9	280.8	7.02
Second collimator **d = 0.5 m** **r = 19.5 mm**	**For 1 μA beam current**		**For 235 μA beam current**	
	Power [W]	**Current [nA]**	**Power [W]**	**Current [μA]**
On each sector	0.11	2.6	24.8	0.62

Table 3.6 Power depositions and beam currents on the collimators' sectors, for 1 μA and 235 μA beam current, with a 40 MeV proton beam misaligned with respect to the target axis of 5 mm.

First collimator **d = 1.6 m** **r = 18 mm**	**For 1 μA beam current**		**For 235 μA beam current**	
	Power [W]	**Current [nA]**	**Power [W]**	**Current [μA]**
Sector 1	1.4	34.3	322.3	8.06
Sector 2	1.2	29.6	278.0	6.95
Sector 3	1.0	25.9	243.6	6.09
Sector 4	1.2	30.2	283.8	7.09
Second collimator **d = 0.5 m** **r = 19.5 mm**	**For 1 μA beam current**		**For 235 μA beam current**	
	Power [W]	**Current [nA]**	**Power [W]**	**Current [μA]**
Sector 1	0.11	2.9	26.9	0.673
Sector 2	0.10	2.6	24.5	0.613
Sector 3	0.10	2.4	22.7	0.567
Sector 4	0.11	2.7	24.9	0.623

A sensitivity of 0.1 nA on the current reading should theoretically allow a beam misalignment to be detected, also with only 1 μA initial current. However, this study does not consider the instability of the beam current, which could lead to an incorrect assessment of misalignment, especially for low currents. In any case, the design in separated sectors for both devices is useful to control the beam alignment, even if the first collimator will provide the most significant measurement.

The study is then repeated simulating a 70 MeV energy beam. As shown in the previous section, in fact, the modular collimator has been designed to work with both beam energies foreseen for the SPES line. Even if the positioning process has been carried out considering a 40 MeV high power target, no differences are expected for the 70 MeV energy version. The results obtained with an aligned beam are reported in Table 3.7 while for a vertical misalignment of 5 mm the values are shown in Table 3.8. In this case too, with a sensitivity of 0.1 nA on the current reading, the collimators configuration allows a beam misalignment in both collimators to be detected. The design is therefore validated also for a 70 MeV energy beam.

It is important to remark that these studies consider the target and the collimators perfectly aligned. Actually, typical misalignments of about 0.5 – 1 mm are expected between the target and these devices. The internal radius of the collimators here defined represents therefore the minimum value that must be guaranteed. Slightly higher radius should however be foreseen for the collimators, in order to deposit the beam power along all the disc's radius even in case of target misalignment. As seen so far, this will lead also to higher power deposited on the target.

Table 3.7 Power depositions and beam currents on the collimators' sectors, for 1 µA and 235 µA beam current, with a 70 MeV aligned proton beam.

First collimator **d = 1.6 m** **r = 18 mm**	**For 1 µA beam current**		**For 235 µA beam current**	
	Power [W]	**Current [nA]**	**Power [W]**	**Current [µA]**
On each sector	2.01	28.7	472.9	6.76
Second collimator **d = 0.5 m** **r = 19.5 mm**	**For 1 µA beam current**		**For 235 µA beam current**	
	Power [W]	**Current [nA]**	**Power [W]**	**Current [µA]**
On each sector	0.18	2.5	41.8	0.60

Table 3.8 Power depositions and beam currents on the collimators' sectors, for 1 µA and 235 µA beam current, with a 70 MeV proton beam misaligned with respect to the target axis of 5 mm.

First collimator **d = 1.6 m** **r = 18 mm**	**For 1 µA beam current**		**For 235 µA beam current**	
	Power [W]	**Current [nA]**	**Power [W]**	**Current [µA]**
Sector 1	2.31	33.0	542.4	7.75
Sector 2	1.97	28.1	462.7	6.61
Sector 3	1.75	24.9	410.4	5.86
Sector 4	2.06	29.4	483.4	6.91
Second collimator **d = 0.5 m** **r = 19.5 mm**	**For 1 µA beam current**		**For 235 µA beam current**	
	Power [W]	**Current [nA]**	**Power [W]**	**Current [µA]**
Sector 1	0.19	2.7	45.0	0.64
Sector 2	0.18	2.5	41.3	0.59
Sector 3	0.16	2.4	38.8	0.55
Sector 4	0.18	2.6	42.3	0.60

3.3 High power Faraday Cup

The Faraday Cup is an insulated cup designed to catch and completely stop the beam. It is connected to an ammeter through an electrical connection: in this way the beam current can be measured, determining the number of particles hitting the cup. One of these devices is installed in the SPES bunker along the proton beam line. However, the actual Faraday Cup has been designed to work with a maximum beam energy of 40 MeV. The energy upgrade planned for SPES-2 leads to new operative conditions and, consequently, to the need for a redesign of this component.

3.3.1 Boundary conditions

Beam – Depending on the type of target installed inside the target chamber, different beam characteristics are foreseen, as shown in Sec 1.4.2:

- With the *low power* 70 MeV target, a centered beam with RMS radius equal to 4 mm is used. In Sec. 2.3, a current of 7.5 μA has been set for this target, leading to a total power of 525 W. However, a conservative higher power will be considered for the design of the Faraday Cup, equal to 1400 W.
- With the *high power* 70 MeV target, a wobbled beam is used. For this target, the beam characteristics have not been uniquely defined yet. The RMS radius is expected to be between 5 mm and 7 mm, while the wobbling radius around 10 mm or 11 mm. For this study, an RMS radius equal to 7 mm and a wobbler radius equal to 11 mm will be considered, as for the *high power* 40 MeV target. A maximum power of 9100 W is considered.

Geometry – The geometry of the Faraday Cup will be that of a reversal cone (Figure 3.17): the angle of the cone, in fact, increases the surface where the power is dissipated, allowing for lower temperatures. Moreover, with this shape, the main part of the secondary electrons (see Sec.3.1) are emitted toward the other face. A minimum thickness able to completely stop the 70 MeV beam must be guaranteed. The beam diameter is assumed approximately the same of the last collimator, equal to 36 mm as shown in Sec. 3.2.6. To be on the safe side, the entrance diameter of the cup is set at 45 mm. An insulator material in form of a disc is used to sustain and insulate the cup and a water-cooled shell is used to dissipate the power deposited in the cone.

Materials - The POCO EDM-3 graphite is chosen for the Faraday Cup: as explained in Chapter 4, this material offers high resistance at high temperatures, low thermal expansion and high thermal conductivity, translating into an excellent thermal shock resistance. Its maximum operative temperature is around 2500°C [45]. SHAPAL™ Hi M-soft is chosen as insulating material. This aluminum nitride ceramic exhibits excellent machinability and strength, low thermal expansion, high thermal conductivity and excellent electrical insulation. Its maximum operative temperature in nonoxidizing atmosphere is around 1900°C [46]. Copper ETP [43] is used for the water cooled element. This material exhibits a yield strength of 70 MPa and an ultimate stress of 220 MPa at room temperature: however, as the temperature increases, the strength slightly decreases: at 300°C an ultimate strength of about 180 MPa is registered for this type of copper.

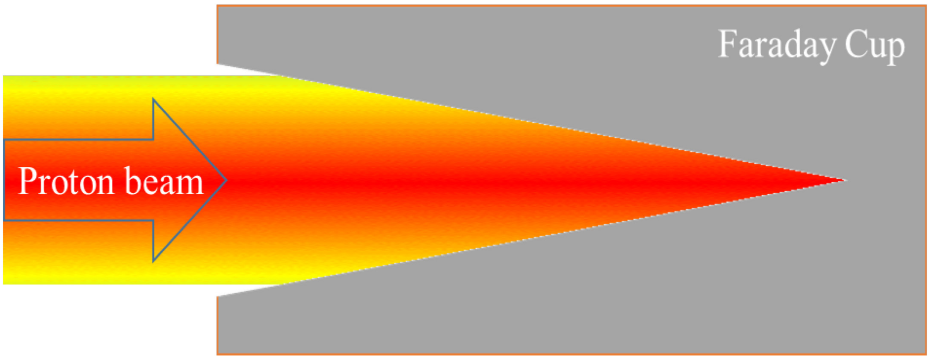

Figure 3.17 Simplified scheme of the Faraday Cup.

3.3.2 Preliminary design and thermal analyses

Bi-dimensional axisymmetric thermal analyses are performed for the preliminary sizing of the Faraday Cup. As explained in the previous section, two different beam load conditions are foreseen:

- Centered beam with RMS radius equal to 4 mm, and a total power of 1400 W;
- Wobbled beam with RMS radius equal to 7 mm, wobbler radius equal to 11 mm and a total power of 9100 W.

In this first stage, the power deposition is modelled as a Gaussian distribution, deposited uniformly in a 30 mm thick area. As shown in [38], in fact, higher temperatures and stresses are expected imposing a Gaussian power deposition with respect to a more realistic deposition obtained with the Monte Carlo FLUKA code. When a fast charged particle moves through matter it ionizes the atoms of the material and deposits a dose along its path. A peak, called the Bragg peak, occurs because the interaction cross section increases as the charged particle's energy decreases. In the Faraday Cup the Bragg peak concentrates the power deposition in a more backward zone than the Gaussian distribution. The heat can be therefore removed more easily from the insulating discs and can be dissipated by means of the water circuit.

In order to avoid the over-heating in the surrounding vacuum chamber and in the other elements installed near the Faraday Cup, this device will be housed inside a water-cooled copper shell. In order to maintain the insulation, SHAPAL™ [46] rings are interposed between the graphite cup and the copper shell, as shown in Figure 3.18.

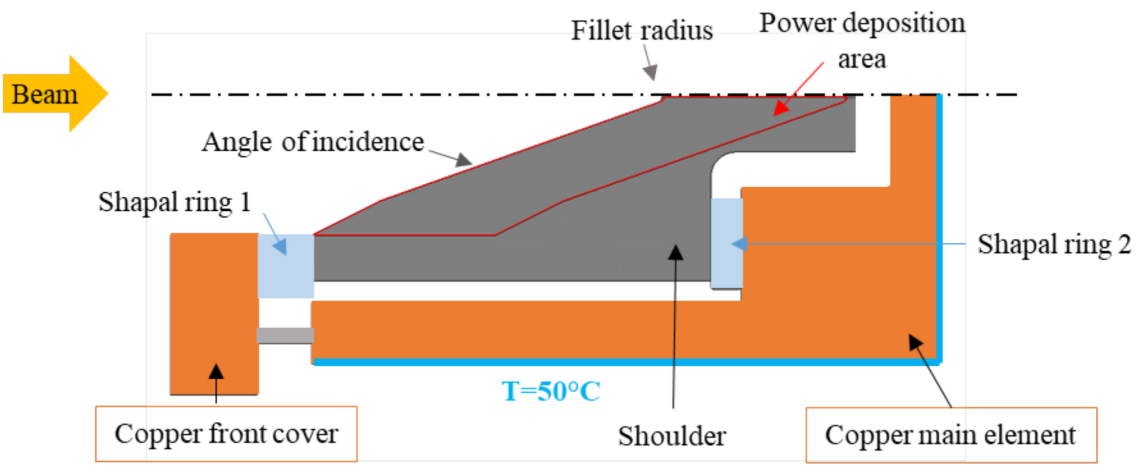

Figure 3.18 2D model used for the preliminary design of the Faraday Cup.

The Faraday Cup will dissipate the beam power mainly by conduction through the Shapal rings, to the water cooled copper main element. Thermal contact resistances are therefore implemented between the materials, as they strongly influence the maximum temperatures, as already shown for the collimators in Sec. 3.2.2. Since no experimental data on thermal conductivity are available between SHAPAL™ and the other two materials, the Yovanovich analytical model [40] is used to calculate the thermal resistances, imposing a reasonable contact pressure of 5 MPa between the surfaces. The water cooling in the copper main element is simulated imposing a constant temperature of 50 °C on the external surface. This allows fast bi-dimensional simulations to be performed, by quickly varying the geometrical parameters of the Faraday Cup, especially the angle of incidence of the cone, the fillet radius and the position and dimension of the shoulder. After several iterations, the geometry presented in Figure 3.18 is chosen: the corresponding temperature distributions for the two different load conditions are shown in Figure 3.19. The highest temperatures are obtained with a wobbled beam and the higher power. For this reason, this load condition is considered for the following analyses. It is important to remark that these temperatures are obtained assuming a contact pressure of 5 MPa between the surfaces. It is therefore necessary to verify that during operations this pressure is maintained. In operation, in fact, the Faraday Cup will warm up and expand and a good contact could not be guaranteed. This phenomenon is studied by means of thermal-structural analyses, presented in the following section.

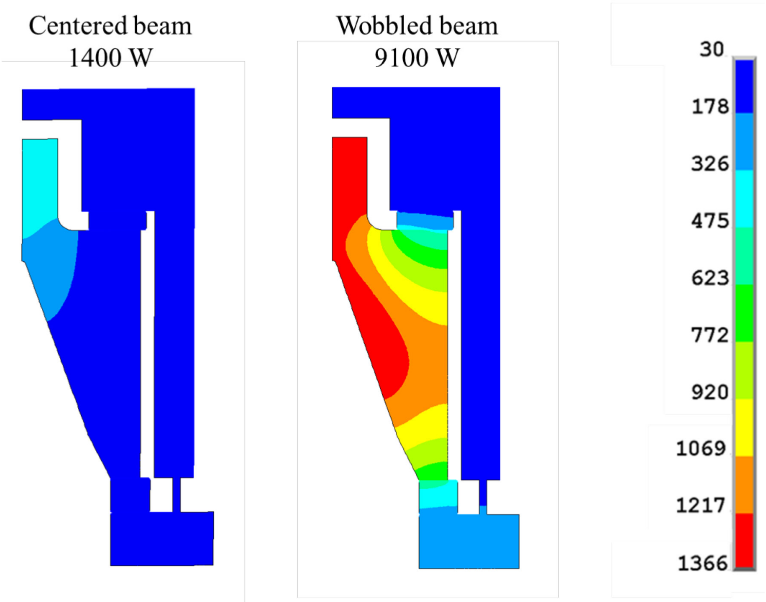

Figure 3.19 Temperature distribution on the Faraday cup assembly with two different load conditions, assuming a gaussian distribution of the power deposition.

3.3.3 Thermal-structural analyses [47]

As shown in the previous Section, it is necessary to guarantee a minimum contact pressure of 5 MPa between the surfaces in order to obtain acceptable temperatures in the Faraday Cup. A compression has therefore to be applied on the copper front cover. To evaluate the proper compression, thermal-structural analyses with structural contact elements between the surfaces are implemented in ANSYS Mechanical [27], using a bi-dimensional model as presented in Sec. 3.3.2. With an iterative process, an arbitrary compression is initially applied on the front cover. Simultaneously, the beam power deposition, calculated with the FLUKA Monte Carlo code, is applied on the Faraday Cup as heat generation. The contact between the surfaces is then checked: if a pressure lower than 5 MPa is obtained, the compression is increased and a new simulation is implemented. When an adequate pressure is ensured, it is then necessary to verify that no critical stresses are reached in the components.

Unfortunately, with a total power of 9100 W no solution is obtained: in fact, two opposite phenomena take place during operation. If on one side the Faraday Cup expands, loosing contact with the other materials if no compression is applied, on the other hand, when a compression is applied, high thermal stresses arise inside the component, due to the restrained expansion. With these dimensions and configuration, in which heat is mainly exchanged by conduction, not enough heat is dissipated through the Shapal rings surfaces in order to avoid excessive expansion of the Faraday Cup. For this reason, the maximum beam power is lowered to 7000 W, which is considered acceptable. With a total beam power of 7000 W, a contact pressure of 5 MPa between the contact surfaces is ensured when 29000 N are applied on the copper front cover.

As shown in the next section, a fixing system composed by Bellaville washers is chosen to apply the necessary 29000 N. The stiffness of the Bellaville washers and their preload are verified by means of new thermal-structural analyses, using the same bi-dimensional model of the previous simulations. In this case, the thermal and the structural loads are applied in two different steps. In the first load step, a reasonable preload is applied to the front cover. In the second load step, the beam power deposition is applied, together with the force exerted by the Bellaville washers when compressed of a quantity equal to the expansion of the Faraday Cup, calculated in the previous simulations and equal to 0.4 mm. Using 24 Bellaville washers, each of them characterized by a stiffness of 2617 Nmm^{-1}, and applying a preload of 6000 N, a compressive force of about 28300 N is calculated, which guarantees a good contact. In particular, as presented in Figure 3.20 and in Table 3.9, a mean contact pressure of at least 10 MPa is ensured in each contact surface. Moreover, no critical stresses are reached in the graphite cup due to the restrained expansion, with a maximum Von Mises stress equal to 44 MPa in a compression state, far below the failure stress of 140 MPa measured for this material (see Chapter 4).

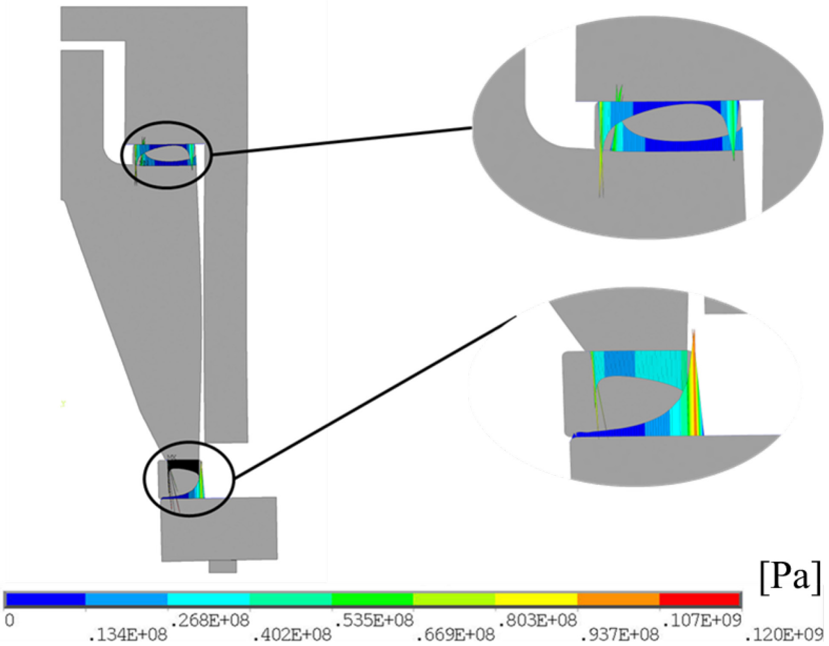

Figure 3.20 Contact pressure distributions between the Shapal rings and the other materials.

Table 3.9 Mean contact pressure between the Shapal rings and the other materials, applying 29000 N on the front cover, with a 7000 W wobbled beam.

	Mean contact pressure
Shapal ring 2 – Copper main element	$10.1\ MPa$
Shapal ring 2 - Graphite	$13.8\ MPa$
Shapal ring 1 – Copper front cover	$14.7\ MPa$
Shapal ring 1 - Graphite	$23.5\ MPa$

3.3.4 Mechanical design and validation

To apply the proper compression but, simultaneously, to guarantee also enough compliance to the assembly, a fixing system composed by 24 Belleville washers divided between 8 M10 grub screws is chosen, as shown in the 3D model presented in Figure 3.21. A water circuit is obtained in the copper main element, to dissipate the heat exchanged through the Shapal rings. Copper braids are added to the copper front cover to help the cooling of this component, avoiding excessive temperatures.

In order to validate the design, a 3D thermal simulation is implemented in ANSYS: the power deposition of a 7000 W wobbled beam (RMS radius equals to 7 mm, wobbler radius equals to 11 mm) is calculated with the FLUKA Monte Carlo code and applied as heat generation to the Faraday Cup. In the three-dimensional model, the real cooling circuit, properly sized and designed, is implemented and a convective flow is imposed. As shown in Figure 3.22, the Faraday Cup reaches a maximum temperature of about 1000°C, well below its maximum operative temperature. The Shapal rings are heated up to about 500°C, especially the first ring in contact with the front cover. However, this value is not critical since Shapal can operate in vacuum up to 1900°C. On the other hand, particular attention must be paid to the copper components. The main element reaches a maximum temperature of 140°C at the contact with the second Shapal ring. However, the cooling channel surfaces do not reach 100°C, avoiding boiling water problems. The front cover reaches a maximum temperature of more than 200°C, with an average value of about 160°C. Given the limited duration of the thermal cycle, if a low stress state arises in the component, these temperatures can be considered acceptable.

A 3D structural analysis on the front cover is therefore implemented to properly evaluate the copper stress state. Exploiting the system's symmetries, a quarter of the front cover is modelled, as shown in Figure 3.23. Structural contact elements are interposed between the materials, and a constant pressure is imposed at the base of the Bellaville washers, for a total compressive force of 29000 N. The cup is only partially modeled, and isostatically blocked. The maximum Von Mises stress reached in the front cover is about 60 MPa. Given the limited duration of the thermal cycle and the low stress state, the temperature foreseen for this component is therefore considered acceptable.

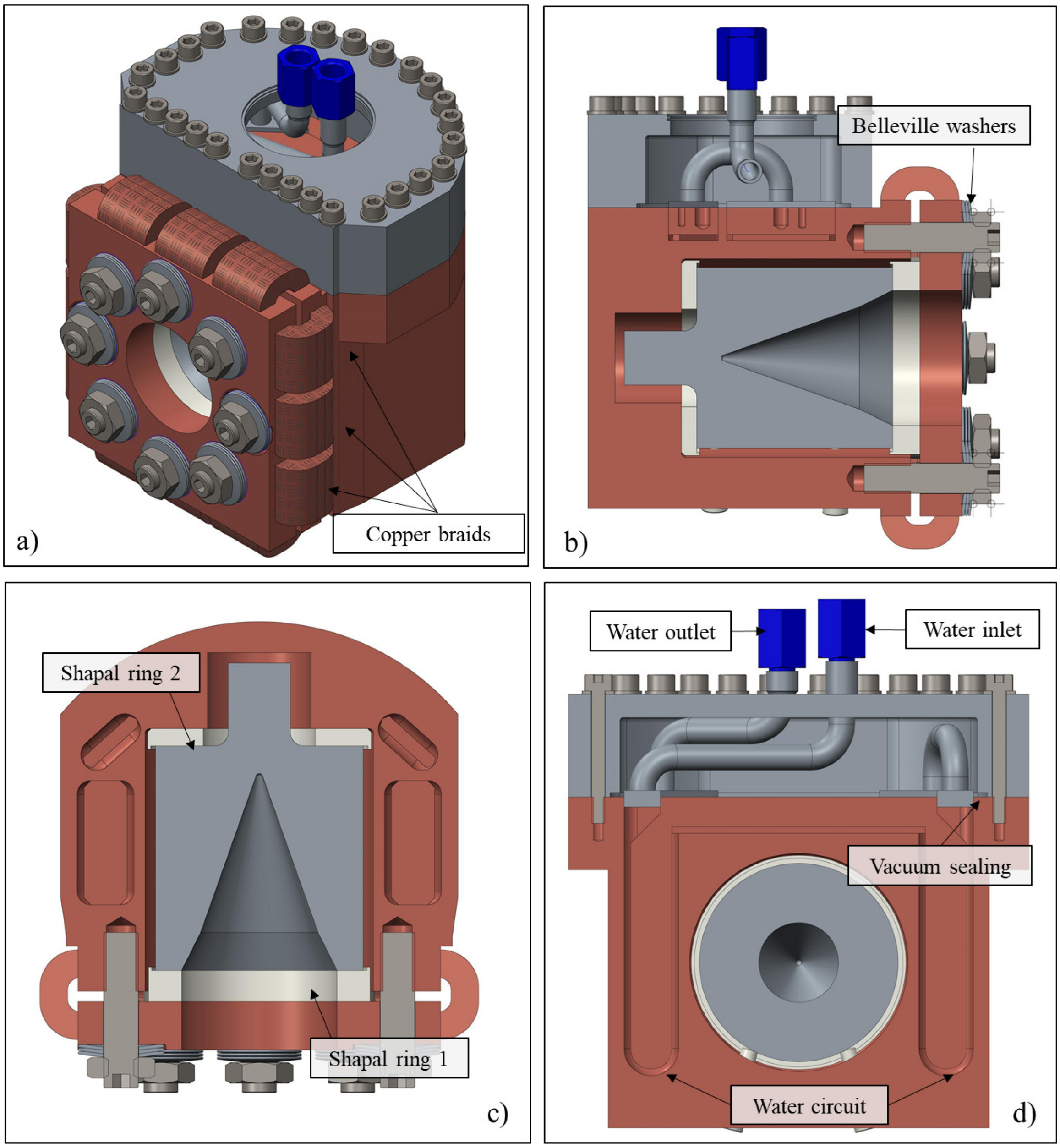

Figure 3.21 3D model of the final assembly (a) and three different sections (b,c,d) highlighting the main elements of the final mechanical design.

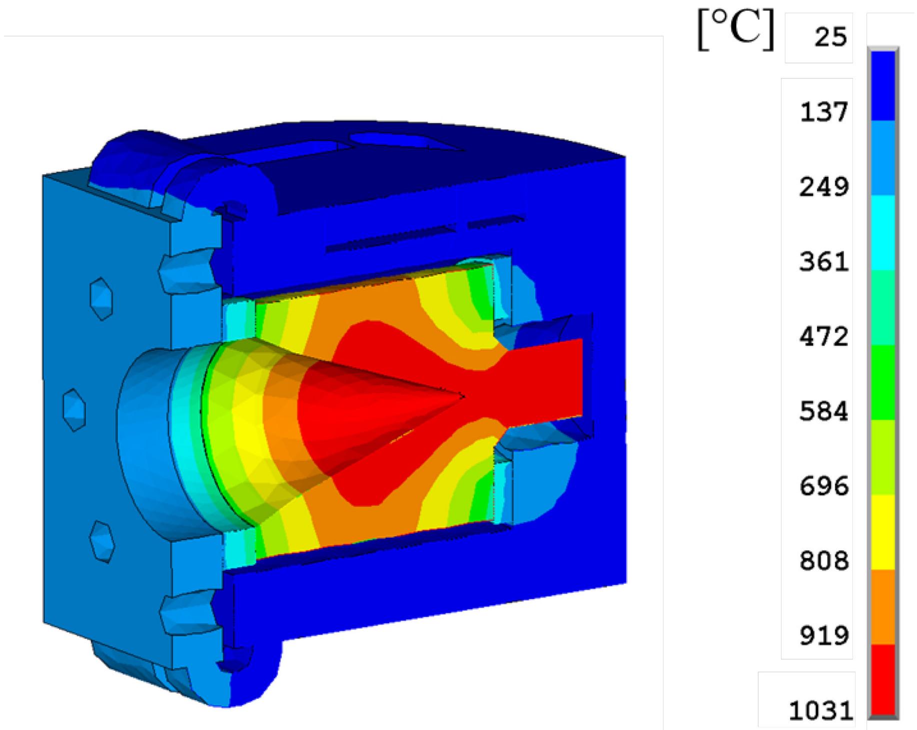

Figure 3.22 Temperature distribution in the Faraday Cup assembly due to a 7000 W wobbled beam (RMS radius = 7 mm, wobbler radius = 11 mm).

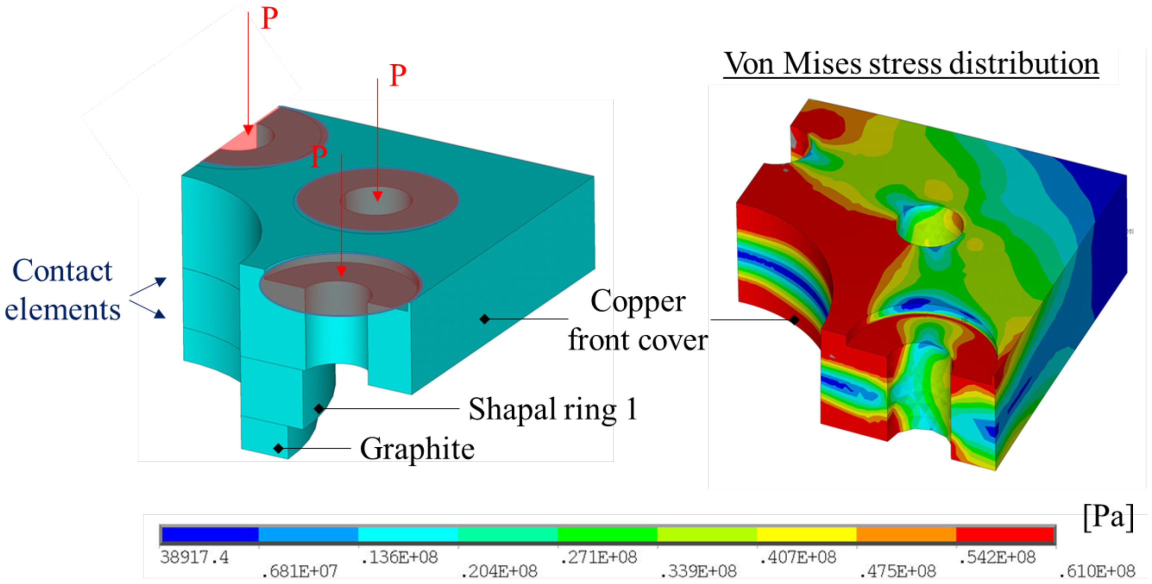

Figure 3.23 Von Mises equivalent stress distribution on the copper front cover, due to the compressive force exerted by the Bellaville washers.

3.3.1 Potential distribution for the secondary electron suppression

To properly measure the beam current impinging on the Faraday Cup, it is fundamental to suppress the secondary electrons. As seen in Sec. 3.1, a potential shield of at least -90 V is needed. In this case, the front copper plate is exploited as suppressor: if properly insulated, it is possible to apply a shielding potential directly to the copper plate. Since its dimensions have been defined in Sec 3.3.3 by the thermal-structural simulations, an axial symmetric simulation of the potential distribution is implemented to verify that a proper shielding potential is reached. By applying a potential of -1 V on the copper front, it is possible to calculate the suppression efficiency along the Faraday Cup axis. The corresponding potential distribution is presented in Figure 3.24: the shielding efficiency of the secondary electrons is 0.75. Consequently, by applying to the copper front a potential of -500 V, the minimum potential of -90 V, necessary to stop the electrons emission, is abundantly ensured.

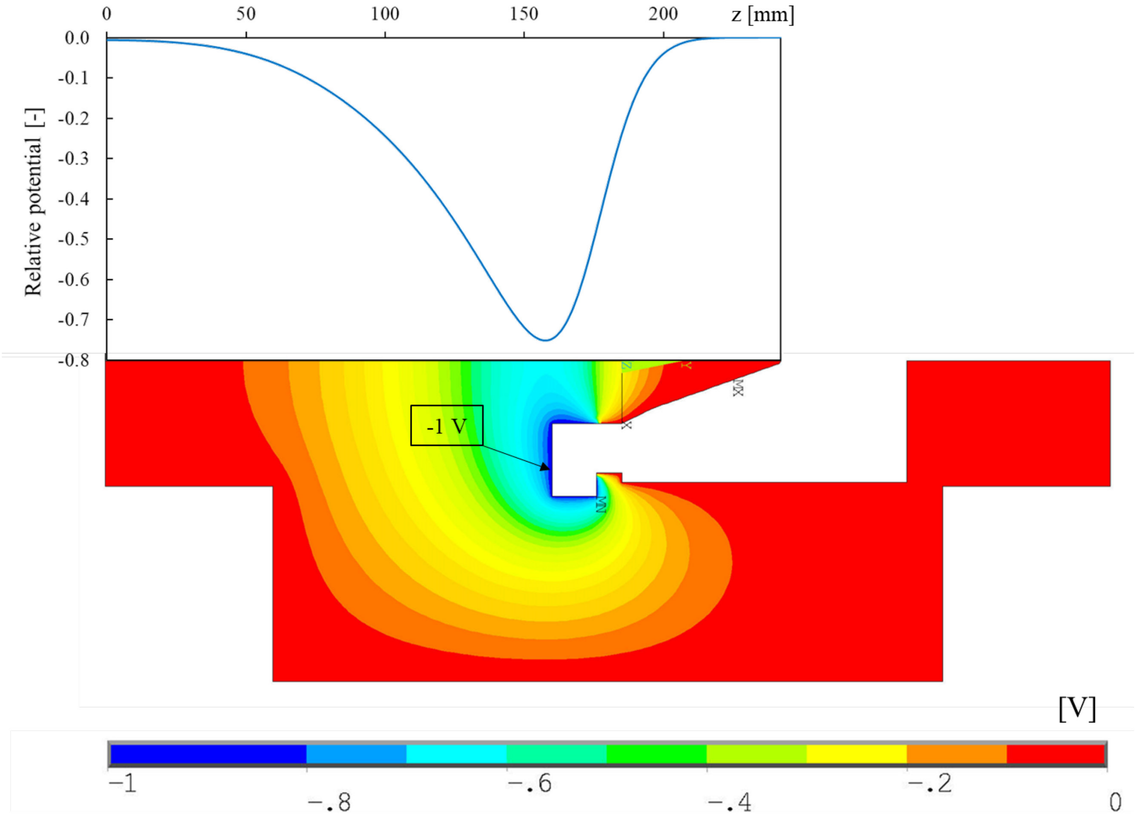

Figure 3.24 Potential distribution of the Faraday Cup space, along the axis.

3.4 Target Window

The fissions products generated inside the material constituting the target diffuse towards the surface of the discs and, once there, they move towards the ion source by random transport in vacuum. However, the radioactive isotopes that have not been ionized could exit the target chamber and contaminate the primary beam line. Moreover, in case of vacuum loss, the radioactive isotopes could reach the cyclotron, causing severe contamination problems. In order to avoid this scenario, an appropriate target window is needed and has to be designed. In accordance with various realizations, a target window is a thin disc or a plurality of foil members in a stacked arrangement, located between a high energy particle entrance side and a target material side. In the SPES line, it will be a thin disc placed at the entrance of the target chamber with the aim to separate the vacuum between the target chamber and the proton beam line. The target window has to be as transparent as possible to the beam and must support both the deposited beam power and the atmospheric pressure.

3.4.1 Boundary conditions

The window will be housed at the entrance of the target chamber (Figure 3.25): for this reason, its external diameter is initially fixed at 70 mm, as the internal diameter of the chamber entrance tube. A flat geometry with a constant thickness is chosen, for ease of modelling and realization. The thickness will be determined during this study. Being the chamber water cooled, a temperature of 70°C is fixed at the edge of the target window.

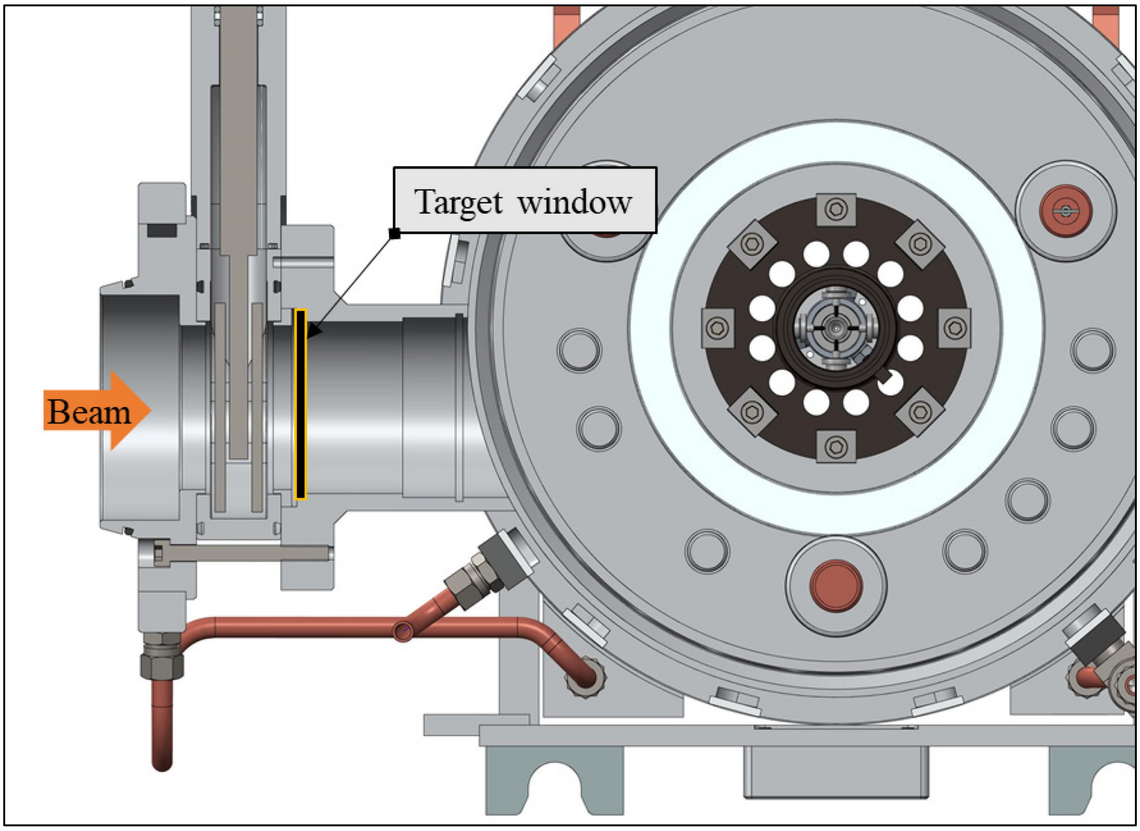

Figure 3.25 The positioning of the target window, at the entrance of the target chamber.

As shown in Sec.1.4.2, the proton beam is modeled with a Gaussian function:

$$p(r) = \frac{P}{2\pi\sigma^2} \cdot e^{-\frac{r^2}{2\sigma^2}} \qquad 3.5$$

where P is the maximum power (W), σ is the RMS radius (mm) and r is the radial coordinate of the window (mm). In order to properly design the window, the most critical conditions of the beam must be chosen. Since currently no target window has been designed, neither for a 40 MeV beam energy nor for a 70 MeV beam energy, this study will be carried out imposing a 40 MeV beam energy. As shown in Sec. 0, in fact, in the same material thickness, a higher power deposition occurs when protons have lower energy. Higher temperatures and stresses will be therefore reached on the target window with a 40 MeV beam. As explained in Sec. 1.4.2, two different targets can be used with a 40 MeV proton beam: a high-power target, designed to work at 8000 W of beam power, and a low-power target, designed to work at a lower power of about 800 W. Since the design must consider the most critical conditions, the higher power configuration is chosen. In this case, a wobbled beam is foreseen, with an RMS radius equal to 7 mm and a wobbler radius of 11 mm. However, as explained in [8], the stresses and temperatures obtained with these beam characteristics are comparable with the stresses and temperatures obtained with a centered beam with RMS radius equal to 10.2 mm. In order to simplify the analytical design procedure, in this study a centered beam is considered. The beam characteristics can therefore be summarized as follow:

- 40 MeV beam energy
- 8000 W beam power
- 10.2 mm RMS radius
- Centered beam

3.4.2 Target window materials

There are several important parameters in the choice of the window material. Often, the best choice with regards to one parameter is not the first choice with regard to another parameter. The main properties to be considered in order to choose the best material are:

- The thermal conductivity;
- The tensile and compressive strength;
- The maximum operative temperature;
- The transparency to the beam (expressed by the stopping power).

The stopping power will determine the amount of power deposited in the window while the thermal conductivity will determine the rate at which the heat will be removed from the foil. Therefore, stopping power and thermal conductivity will set the temperature reached in the component. The temperature will have an effect on the strength of the material. Materials used for making target windows need to be very strong in thin sheets and maintain their strength at elevated temperature. Due to their properties, five materials are taken into account in this study: the aluminum alloy Al6082-T6 (low activation), the POCO EDM-3 graphite (low activation and high resistance at high temperatures), the ETP copper (high thermal conductivity), the Silicon Carbide (high resistance at high temperature) and the Tantalum (high resistance at high temperature). Some properties of interest for these materials are reported in Table 3.10, Figure 3.26 and Figure 3.27. Another important characteristic is the strength of the material as a function of the temperature. Aluminum yield strength decreases between 200-350°C of about 60% with respect to the room temperature value [48]. Also the ETP Copper registers a resistance decrease with temperature. Moreover, this effect worsens if the material is maintained at high temperature for a long time [43]. Since up to 150°C this copper exhibits a stable yield strength of 70 MPa, this temperature and this strength are considered as limit values in this study. Also tantalum yield strength decreases with temperature: at 1700°C a reduction of about 50% is registered [49]. On the other hand, graphite exhibits an increase of resistance with temperature. In particular, at 2000°C, the POCO EDM-3 graphite shows an average increase of 20% over its room temperature value [42]. Finally, silicon carbide maintains its strength to very high temperatures, approaching 1800°C with no significant strength loss.

Table 3.10 Some properties of interest for five different materials considered in the design of the target window.

Material	**Poisson's ratio**	**Elastic modulus at 20°C**	**Density at 20°C**	**Maximum operative temperature**	**Maximum stress**	**Ref.**
	[-]	**[GPa]**	**[g/cm^3]**	**[°C]**	**[MPa]**	
Al6082-T6	0.33	69	2.67	300	110 (yield) At maximum operative temperature	[50]
POCO EDM-3	0.3	10.3	1.81	2500	-140 MPa (compressive) 60 MPa (tensile) at room temperature	[51] [45]
ETP Copper	0.33	126	8.96	150	70 (yield) at maximum operative temperature	[43] [50]
Silicon Carbide Hexology SA®	0.16	380	3.16	1800	-330 (compressive) 330 (tensile)	[31] [52]
Tantalum	0.278	180	16.6	1700	150 (yield) at maximum operative temperature	[49] [50]

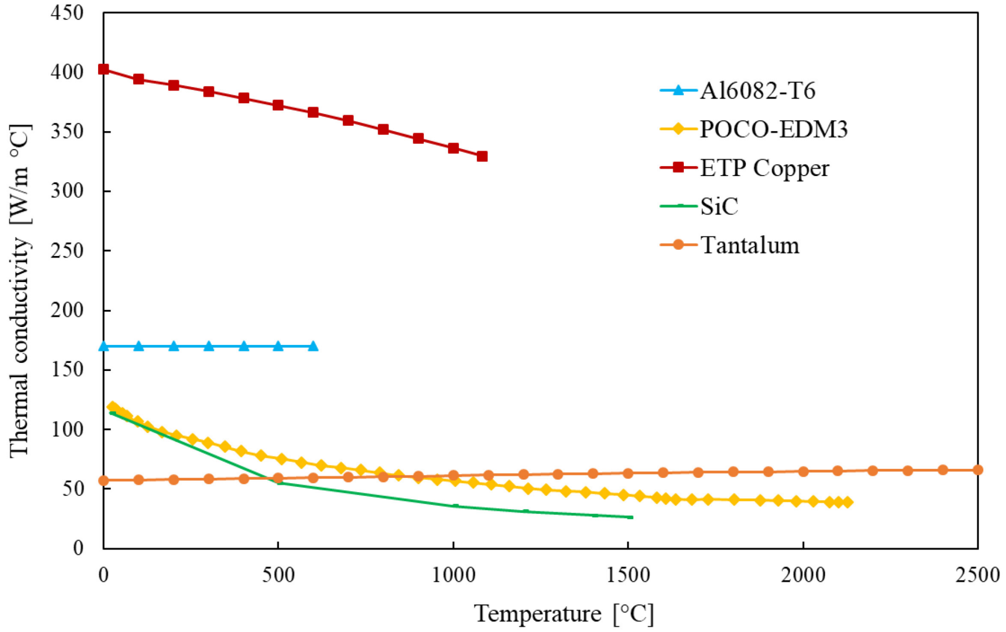

Figure 3.26 Thermal conductivity for five different materials, as a function of temperature.

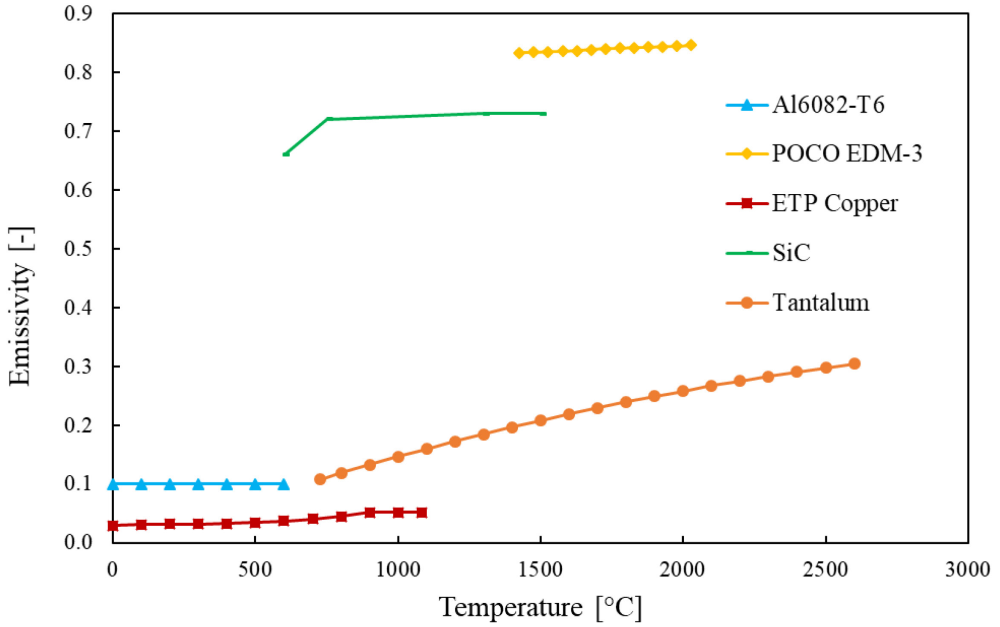

Figure 3.27 Emissivity for five different materials, as a function of temperature.

3.4.3 Structural analysis: the atmospheric pressure

Depending on how the target window will be installed and fixed at the entrance of the target chamber, it can be modeled as a thin disc completely constrained or free to expand, as shown in Figure 3.28. In the first case, both the rotation and the radial and axial displacements at the edge of the disc are prevented. In the second case, only the rotation and the axial displacements are constrained, and the disc is free to expand sliding along the radial direction. In both cases, the atmospheric pressure due to a hypothetical vacuum loss is modeled as a uniform load, q, on one side of the disc.

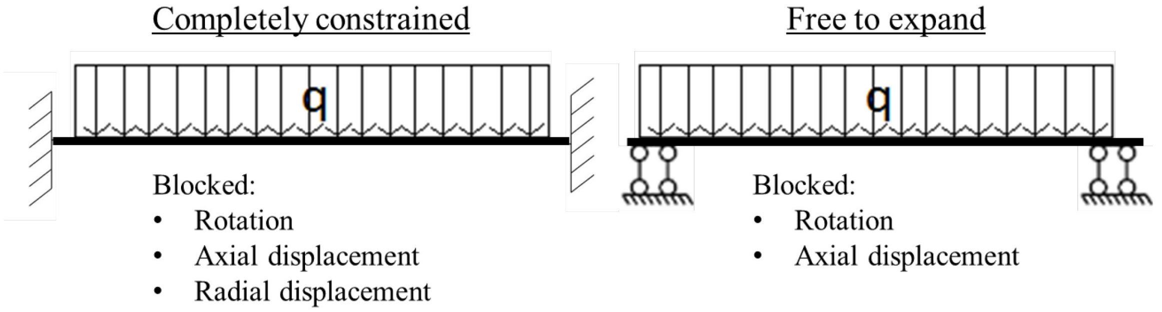

Figure 3.28 Schematic representations of the target window different installations.

Having the disc a small thickness, it is possible to use a two-dimensional model to calculate the maximum stress due to the atmospheric pressure. Using the formulas reported in [53], for both the configurations, the maximum bending moment at the center of a flat disc subject to a uniformly distributed pressure can be calculated as:

$$M_c = \frac{qa^2(1+v)}{16} \tag{3.6}$$

where q is the load per unit area (MPa), a is the outer radius of the disc (mm), and v is the Poisson's ratio. The reaction moment at the edge of the disc, M_{ra}, due to the constrained rotation can be calculated as:

$$M_{ra} = \frac{qa^2}{8} \tag{3.7}$$

The corresponding bending stresses can be found from the moments M_c and M_{ra} by the expression:

$$\sigma = \frac{6M}{t^2} \tag{3.8}$$

where M is the moment and t is the thickness of the disc. For all the five materials considered in this study, the Poisson's ratio is always lower than 0.5. By comparing the equations 3.6 and 3.7, it is clear that the moment at the edge of the disc will be always higher than the bending moment at the center. It is therefore possible to express the maximum bending stress as:

$$\sigma_{ra} = \frac{6M_{ra}}{t^2} = \frac{3}{4}\frac{qa^2}{t^2} \tag{3.9}$$

From equation 3.9 it is possible to express the disc thickness t as:

$$t = a\sqrt{\frac{3}{4}\frac{q}{\sigma_{ra}}} \quad 3.10$$

By substituting to σ_{ra} the admissible stress of the materials, σ_{adm}, it is possible to calculate for each material the minimum thickness needed in order to withstand the atmospheric pressure *q,* equal to about 0.1 MPa. Assuming a safety factor equal to 1.3, the corresponding admissible stresses and the calculated minimum thicknesses are reported in Table 3.11.

Table 3.11 The admissible stress and the minimum thickness calculated for each material, assuming: safety factor 1.3; q, load per unit area, 0.1 MPa; a, external radius of the disc, 35 mm.

	Al6082T6	**POCO EDM-3**	**ETP Copper**	**Silicon Carbide Hexology SA®**	**Tantalum**
σ_{max} [MPa]	110	60	70	330	150
σ_{adm} [MPa]	85	46	54	254	115
t_{min} [mm]	1.0	1.4	1.3	0.6	0.9

These thicknesses ensure a structural resistance of the target window when subject to a constant load equal to the atmospheric pressure. However, future experimental tests can definitely validate the structural integrity of the window due to a vacuum loss, taking into account also the dynamics of a sudden vacuum loss in the beam line or in the chamber side.

In any case, it has to be verified that these thicknesses do not cause an excessive degradation of the proton beam energy with energy deposition and, consequently, excessive temperatures in the material.

3.4.4 Analysis of the interaction with the beam

When the beam passes through a material, it deposits an amount of energy that depends on the initial energy of the beam, on the density and the atomic composition of the material, and on the crossed thickness of the material. The lighter the constituent atoms are, the more transparent a material is to the beam, i.e. less energy will be released. An excessive energy deposition inside the target window can lead to a lower efficiency of the target isotope production and, moreover, to a higher power deposition and higher temperatures in the target window. The amount of energy deposited in the material when the beam passes through it can be expresses as:

$$\Delta E = E_0 - E_F = E_0 \cdot f(t) \quad 3.11$$

where E_0 is the initial energy of the beam, E_F is the mean energy of the exiting beam, and $f(t)$ is the energy deposition factor, that is a function of the thickness t crossed by the beam. With the code SRIM [26] it is possible to calculate the deposition factor for each material by varying the thickness t, simulating an incident proton beam with 40 MeV initial energy and calculating the mean energy of the particles exiting the geometry. The resulting deposition factors for the five materials considered in this study are shown in Figure 3.29.

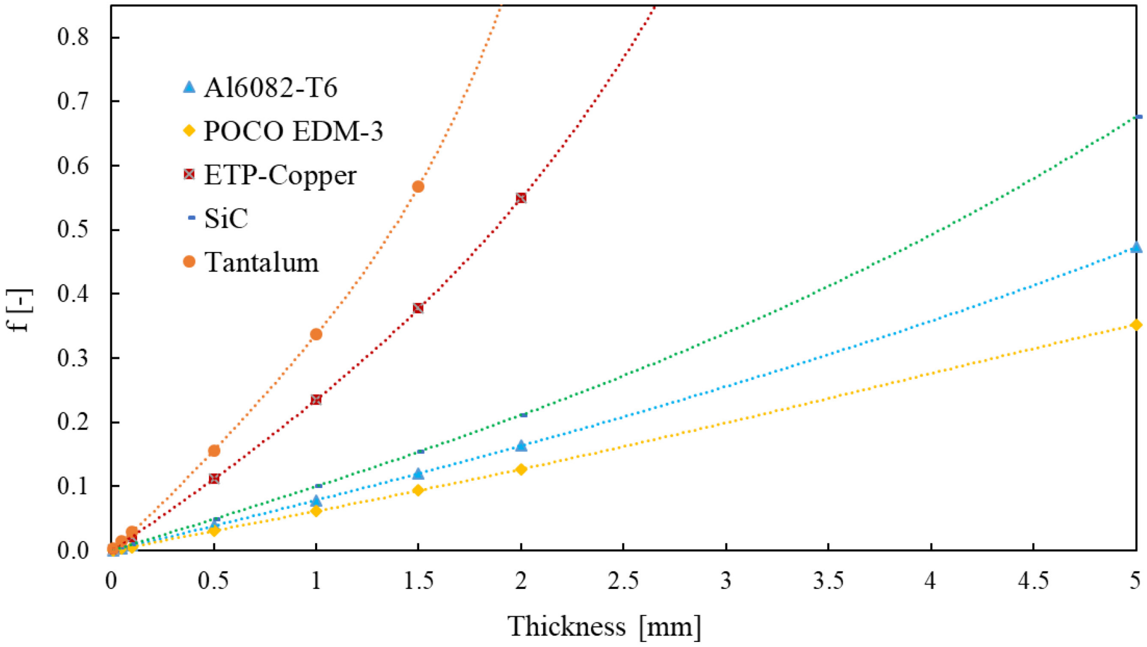

Figure 3.29 Energy deposition factors as a function of the thickness of the material crossed by the beam, for the five materials considered in this study.

Using Equation 3.11, it is therefore possible to calculate the amount of energy deposited on the minimum thicknesses obtained for each material and reported in Table 3.11. The resulting energy depositions are shown in Table 3.12.

Table 3.12 The amount of energy ΔE deposited by a 40 MeV proton beam on different thickness t_{min} of different materials, and the corresponding deposition factor f(t).

	Al6082T6	**POCO EDM-3**	**ETP Copper**	**Silicon Carbide Hexology SA®**	**Tantalum**
t_{min} [mm]	1.0	1.4	1.3	0.6	0.9
f(t)	0.083	0.088	0.323	0.058	0.276
ΔE [MeV]	3.4	3.5	12.8	2.3	10.8

The results confirm that a higher energy is deposited on the heavier materials. Using a tantalum disc, for example, an energy three times higher than that of graphite is deposited, even if graphite needs a higher thickness to withstand the atmospheric pressure. It seems that the aluminum alloy, the graphite and the silicon carbide are the most suitable design materials for what concerns the interaction with the beam. However, a thermal analysis is carried out before excluding definitely tantalum and copper.

3.4.5 Thermal analysis

A thermal analysis is needed in order to calculate the temperature reached on the target window, due to the beam power deposition. A centered 40 MeV proton beam with an RMS radius of 10.2 mm is deposited on the target window, with a maximum power of 8000 W. The target window is characterized by a maximum radius, *a,* equal to 35 mm and a small thickness *t,* which varies according to the considered material. The disc will present an axisymmetric temperature distribution with the maximum value at the center and the minimum one at the periphery. The temperature gradient in the axial direction is considered negligible. No convective heat exchange is foreseen, since the system will work in vacuum. A temperature of 70°C is set on the edge of the target window, simulating the presence of the water cooled chamber. Applying the First Law of Thermodynamic, a heat balance equation can be written in steady-state condition:

$$E_{in} - E_{out} + E_{gen} = 0 \tag{3.12}$$

where E_{in} and E_{out} are the energy entering and leaving the control volume respectively, and E_{gen} is the thermal energy generation. Thanks to the axisymmetric geometry, the problem can be simplified considering a target window's infinitesimal volume at the radial coordinate *r*, with height and thickness equal to *dr* and *t* respectively, as shown in Figure 3.30. The quantities involved in the heat balance are:

- The conductive heat flux entering the infinitesimal volume in the radial direction, q_r
- The conductive heat flux exiting the infinitesimal volume in the radial direction, q_{r+dr}
- The radiative heat flux exiting the infinitesimal volume from the lateral surface, q_{rad}
- The proton beam power deposition, q_p

Equation 3.12 can therefore be expressed as:

$$q_r - q_{r+dr} - q_{rad} + q_p = 0 \tag{3.13}$$

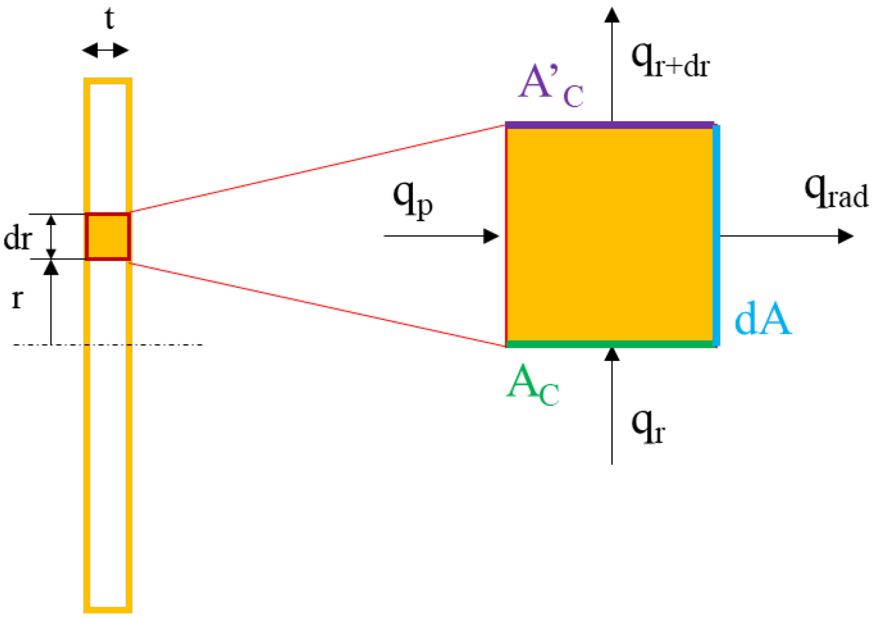

Figure 3.30 Target window's control volume and the involved heat fluxes.

In particular, the conductive heat flux entering the infinitesimal volume can be calculated with the Fourier Law as:

$$q_r = -\lambda A_c \frac{dT}{dr} \tag{3.14}$$

where λ is the material's thermal conductivity (Wm^{-1}K^{-1}), A_C (m^2) is the radial area of the infinitesimal volume at the radial coordinate r, and dT/dr is the space derivative of the temperature along the radial coordinate. Similarly, the conductive heat flux exiting the infinitesimal volume can be expressed as:

$$q_{r+dr} = q_r + q_{dr} = -\lambda A_c \frac{dT}{dr} + \frac{d}{dr}\left(-\lambda A_c{}' \frac{dT}{dr}\right) dr \tag{3.15}$$

where $A_C{}'$ is the radial area at the radial coordinate $r+dr$. In particular, the two radial areas A_C and $A_C{}'$ are expressed respectively as:

$$A_C = 2\pi r t \tag{3.16}$$

$$A_C{}' = 2\pi(r + dr)t \tag{3.17}$$

where t is the target window thickness. For each material, the minimum thickness calculated with the structural analysis presented in Sec. 3.4.3 is considered. By substituting Eq. 3.17 in Eq. 3.15, the conductive heat flux exiting the infinitesimal volume results:

$$\begin{aligned}\frac{d}{dr}\left(-\lambda A_c' \frac{dT}{dr}\right) dr &= -\lambda \frac{d}{dr}\left((2\pi r\cdot t + 2\pi dr\cdot t)\frac{dT}{dr}\right)\\ &= -\lambda\left(\frac{d}{dr}\left(2\pi r\cdot t\frac{dT}{dr}\right) + \frac{d}{dr}\left(2\pi dr\cdot t\,\frac{dT}{dr}\right)\right)\\ &\approx -\lambda\frac{d}{dr}\left(2\pi r\cdot t\frac{dT}{dr}\right) = -\lambda\frac{d}{dr}\left(A_C\frac{dT}{dr}\right)\end{aligned} \tag{3.18}$$

Since A_C' generates a higher order term, in the following dissertation A_C and A_C' will be considered equal and referred to as A_C.

The radiative heat flux exiting one side of the infinitesimal volume can be expressed as:

$$q_{rad} = \varepsilon\sigma_{SB}(T^4 - T_0^4)dA \tag{3.19}$$

where ε is the material emissivity, σ_{SB} is the Stefan-Boltzmann constant ($\mathrm{Wm^{-2}K^{-4}}$), T is the temperature of the infinitesimal volume surface (K), T_0 is the surroundings temperature (K), and dA is the lateral annular area of the infinitesimal volume. It is important to remark that the target window will be placed not far from the target, that in operations will work at high temperature of about 2000-2300°C. A significantly lower temperature is expected on the target window: it is therefore assumed that no radiative heat transfer will take place on the target side. The lateral annular area is calculated as:

$$dA = \pi(r + dr)^2 - \pi r^2 \approx 2\pi r\cdot dr \tag{3.20}$$

The beam power deposition on the infinitesimal volume can be expressed as:

$$q_p = p(r)\cdot dA = \frac{f(t)\,P_{tot}}{2\pi{\sigma_{RMS}}^2}e^{-\frac{r^2}{2{\sigma_{RMS}}^2}}\cdot dA \tag{3.21}$$

where $f(t)$ is the power deposition factor, P_{tot} is the total power deposition (W), and σ_{RMS} is the beam RMS radius.

The heat balance can therefore be expressed as:

$$-\lambda A_C\frac{dT}{dr} - \left(-\lambda A_C\frac{dT}{dr} + \frac{d}{dr}\left(-\lambda A_C\frac{dT}{dr}\right)dr\right) - \sigma_{SB}\varepsilon\, dA\,(T^4 - T_0^4) + p(r)\,dA = 0 \tag{3.22}$$

Remembering that the thermal conductivity is a function of temperature and that the temperature varies with the radius, Eq. 3.22 can be written as:

$$\frac{d\lambda}{dr}A_c\frac{dT}{dr}dr + \lambda\frac{dA_C}{dr}\frac{dT}{dr}dr + \lambda\,A_c\,\frac{d^2T}{dr^2}dr - \sigma_{SB}\varepsilon\,dA\,(T^4 - T_0^4) + p(r)\,dA = 0 \tag{3.23}$$

By dividing both members of Eq. 3.23 by the thermal conductivity λ, for the radial variation dr, and for the radial area A_C it results:

$$\frac{d\lambda}{dT}\frac{dT}{dr}\frac{1}{\lambda}\frac{dT}{dr}+\frac{dA_C}{dr}\frac{1}{A_C}\frac{dT}{dr}+\frac{d^2T}{dr^2}-\frac{\sigma_{SB}}{\lambda A_C}\varepsilon\frac{dA}{dr}(T^4-T_0^4)+\frac{p(r)}{\lambda A_C}\frac{dA}{dr}=0 \qquad 3.24$$

Finally, substituting the expressions for areas and the radial power deposition, the following second order differential equation can be obtained:

$$\frac{d^2T}{dr^2}+\frac{d\lambda}{dT}\frac{1}{\lambda}\left(\frac{dT}{dr}\right)^2+\frac{1}{r}\frac{dT}{dr}-\frac{\sigma_{SB}}{\lambda t}\varepsilon\,(T^4-T_0^4)+\frac{fP_{TOT}}{2\pi\sigma_{RMS}^2\lambda t}e^{-\frac{r^2}{2\sigma_{RMS}^2}}=0 \qquad 3.25$$

In order to numerically solve the differential equation, the following boundary conditions are imposed:

1) $\left.\frac{dT}{dr}\right|_{r=0}=0$ due to the axisymmetric geometry of the target window;
2) $T|_{r=a}=70°C$ due to the water cooled chamber walls.

Moreover, the temperature dependence of the material properties is considered. An iterative process is therefore implemented in a Microsoft Excel spreadsheet [54] in order to solve the differential equation. A first-attempt temperature is imposed at the center of the disc and a discretization along the radial coordinate is performed. This allows the temperature second derivative to be calculated and, consequently, the first derivative and the temperature itself at each radial coordinate. The temperature obtained at the edge of the window is then compared with the second boundary condition. This iterative process is implemented in the spreadsheet until the temperature at the edge of the disc is equal to 70°C. The maximum temperature at the center of the target window can then be calculated for each material, as reported in Table 3.13.

Table 3.13 Maximum temperature at the center of the target window (T_c) compared with the maximum operative temperature (T_{adm}), for different materials.

	Al6082T6	**POCO EDM-3**	**ETP Copper**	**Silicon Carbide Hexology SA®**	**Tantalum**
t_{min} [mm]	1.0	1.4	1.3	0.6	0.89
T_C [°C]	762	1156	1070	1574	3184
T_{adm} [°C]	300	2500	150	1800	1700

By analyzing the results of Table 3.13, it is clear how the aluminum alloy, the ETP copper and the tantalum reach excessive temperatures due to the beam power deposition. This result is in accordance with the analysis of the interaction with the beam reported in Sec. 3.4.4, in which tantalum and copper revealed to be critical due to a high energy deposition. For these reasons, only the graphite and the silicon carbide are taken into account in the further analyses.

3.4.6 Structural analysis: the thermal stresses

Using the same two-dimensional model described in Sec. 3.4.5, it is possible to obtain indications on the stress state induced by thermal gradients [55]. In these conditions the hypothesis of plane stress can be applied, according to which only the radial and the hoop stresses are different from zero. It is also supposed that the stress and strain components do not vary across the thickness. A small portion of the disc is taken into consideration: the small element is closed among two cylindrical surfaces characterized by the radius *r* and *r+dr* and two radial planes spaced by the angle *dθ,* as shown in Figure 3.31.

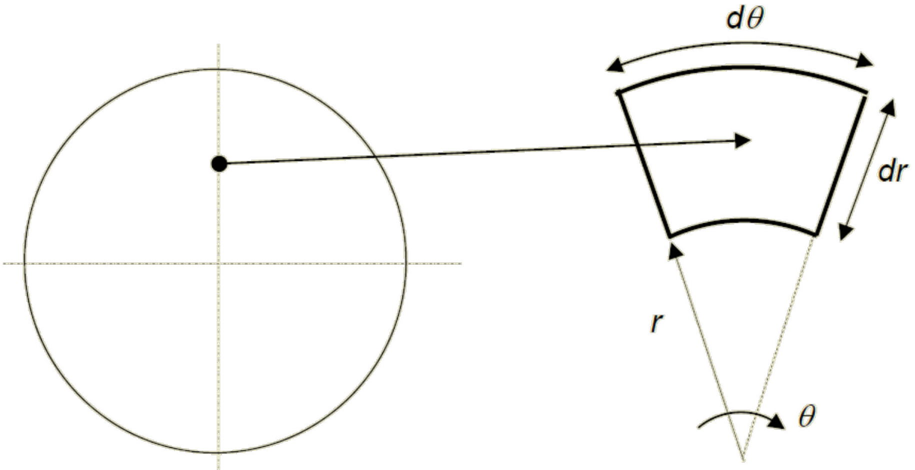

Figure 3.31 The small element considered for the calculation of the thermal stresses [29].

If ε_r and ε_θ are the strain components due to both stress and thermal expansion, it is possible to write the Hooke's law as:

$$\varepsilon_r = \frac{1}{E} \cdot (\sigma_r - \nu\sigma_\theta) + \alpha T \quad 3.26$$

$$\varepsilon_\theta = \frac{1}{E} \cdot (\sigma_\theta - \nu\sigma_r) + \alpha T \quad 3.27$$

where E is the elastic modulus (Pa), ν is the Poisson's ratio, α is the coefficient of thermal expansion (°C^{-1}) and T is the element temperature (°C).

As shown in Figure 3.32, choosing two arbitrary points along the radial direction, the strain components can be expresses as function of the radial displacement, *u,* as:

$$\varepsilon_r = \frac{(r_2+u_2)-(r_1+u_1)-(r_2-r_1)}{r_2-r_1} = \frac{u_2-u_1}{r_2-r_1} = \frac{du}{dr} \qquad 3.28$$

$$\varepsilon_\theta = \frac{2\pi\cdot(r+u)-2\pi\cdot r}{2\pi\cdot r} = \frac{u}{r} \qquad 3.29$$

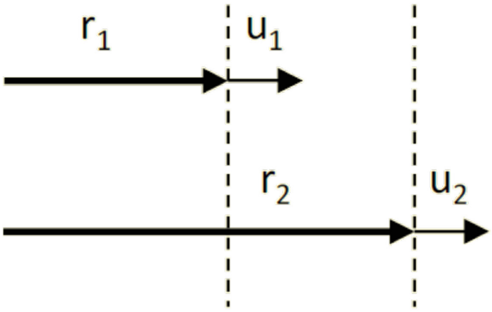

Figure 3.32 Two arbitrary points along the radial direction [18].

Finally, the equilibrium equation written in polar coordinates can be expressed as:

$$\frac{d\sigma_r}{dr} + \frac{\sigma_r-\sigma_\theta}{r} = 0 \qquad 3.30$$

Substituting the previous equations in Eq. 3.30, the equilibrium can be written as a function of the radial displacement *u* as:

$$\frac{d^2u}{dr^2} + \frac{1}{r}\cdot\frac{du}{dr} - \frac{1}{r^2}\cdot u = (1+\nu)\cdot\alpha\cdot\frac{dT}{dr} \qquad 3.31$$

Once performed the integration, the function *u* allows the stress and the strain components to be defined. Without describing the steps needed to obtain them, reported in [29], the radial and the hoop stresses, σ_r and σ_θ, can be expressed as:

$$\sigma_r = -\alpha\cdot E\cdot\frac{1}{r^2}\cdot\int_0^r T\cdot r\cdot dr + \frac{E}{1-\nu^2}\cdot\left[C_1(1+\nu) - C_2(1-\nu)\cdot\frac{1}{r^2}\right] \qquad 3.32$$

$$\sigma_\theta = \alpha\cdot E\cdot\frac{1}{r^2}\cdot\int_0^r T\cdot r\cdot dr - \alpha\cdot E\cdot T + \frac{E}{1-\nu^2}\cdot\left[C_1(1+\nu) - C_2(1-\nu)\cdot\frac{1}{r^2}\right] \qquad 3.33$$

where C_1 and C_2 are the constants of integration, that can be obtained imposing the proper boundary conditions. In particular, for a disc free to expand:

1) $u|_{r=0} = 0$ for the axisymmetry
2) $\sigma_r|_{r=a} = 0$ for the structural constraints (free to expand)

where *a* is the external radius of the disc. In this case, Eq. 3.26 and 3.27 become:

$$\sigma_r = \alpha \cdot E \cdot \left[\frac{1}{a^2}\int_0^a Trdr - \frac{1}{r^2}\int_0^r Trdr\right] \tag{3.34}$$

$$\sigma_\theta = \alpha \cdot E \cdot \left[-T + \frac{1}{a^2}\int_0^a Trdr + \frac{1}{r^2}\int_0^r Trdr\right] \tag{3.35}$$

On the contrary, if the disc is completely constrained, the following boundary conditions are imposed:

1) $u|_{r=0} = 0$ for the axisymmetry
2) $u|_{r=a} = 0$ for the structural constraints (completely constrained)

In this case, Eq. 3.26 and 3.27 become:

$$\sigma_r = -\alpha \cdot E \cdot \left[\frac{1+\nu}{1-\nu} \cdot \frac{1}{a^2}\int_0^a Trdr + \frac{1}{r^2}\int_0^r Trdr\right] \tag{3.36}$$

$$\sigma_\theta = -\alpha \cdot E \cdot \left[T + \frac{1+\nu}{1-\nu} \cdot \frac{1}{a^2}\int_0^a Trdr - \frac{1}{r^2}\int_0^r Trdr\right] \tag{3.37}$$

At this point, the temperature radial distribution calculated in Sec. 3.4.5 for graphite and silicon carbide can be described by the related polynomial interpolating curve. In particular, for the POCO EDM-3 graphite, the radial temperature distribution is shown in Figure 3.33 and the interpolating polynomial results:

$$T(r) = -1.54 \cdot 10^9 r^4 + 1.43 \cdot 10^8 r^3 - 4.12 \cdot 10^6 r^2 + 3.46 \cdot 10^3 r + 1.15 \cdot 10^3 \tag{3.38}$$

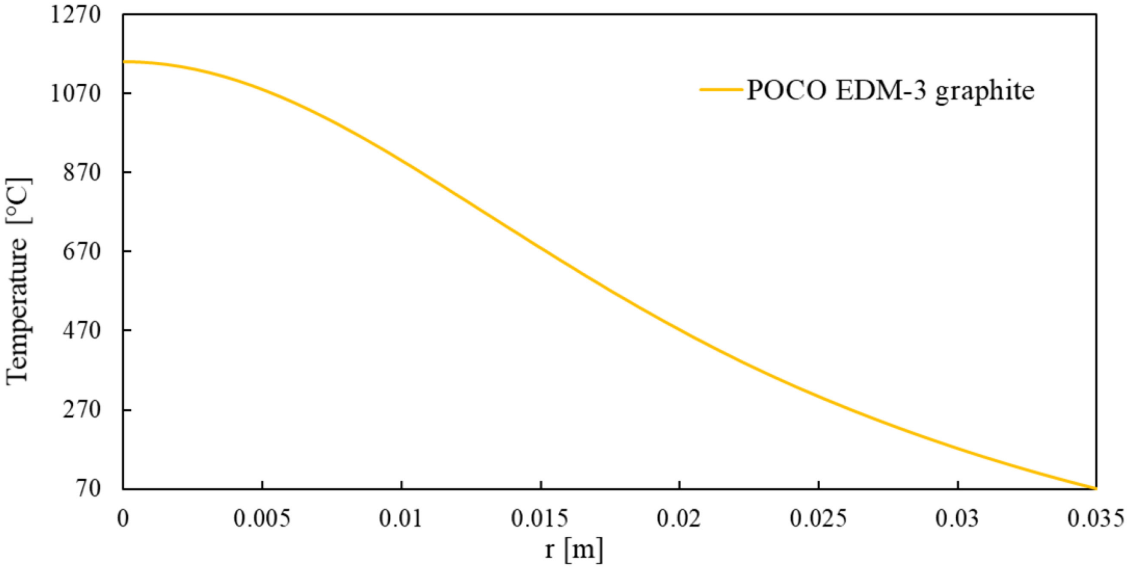

Figure 3.33 Radial temperature distribution for the POCO EDM-3 graphite, with a thickness t equal to 1.4 mm.

The term $\int_0^r Trdr$ in Eq.3.36 and 3.37 can therefore be written as:

$$\int_0^r Trdr = \int_0^r [-1.54 \cdot 10^9 r^5 + 1.43 \cdot 10^8 r^4 - 4.12 \cdot 10^6 r^3 + 3.46 \cdot 10^3 r^2 + 1.15 \cdot 10^3 r]\, dr \tag{3.39}$$

The integral can be solved without approximation, leading to the following expression:

$$\int_0^r Trdr = -1.54 \cdot 10^9 \frac{r^6}{6} + 1.43 \cdot 10^8 \frac{r^5}{5} - 4.12 \cdot 10^6 \frac{r^4}{4} + 3.46 \cdot 10^3 \frac{r^3}{3} + 1.15 \cdot 10^3 \frac{r^2}{2} \tag{3.40}$$

Similarly, considering the radial temperature distribution obtained for silicon carbide and shown in Figure 3.34, the interpolating polynomial results:

$$T(r) = -2.78 \cdot 10^9 r^4 + 2.61 \cdot 10^8 r^3 - 7.45 \cdot 10^6 r^2 + 1.71 \cdot 10^4 r + 1.57 \cdot 10^3 \tag{3.41}$$

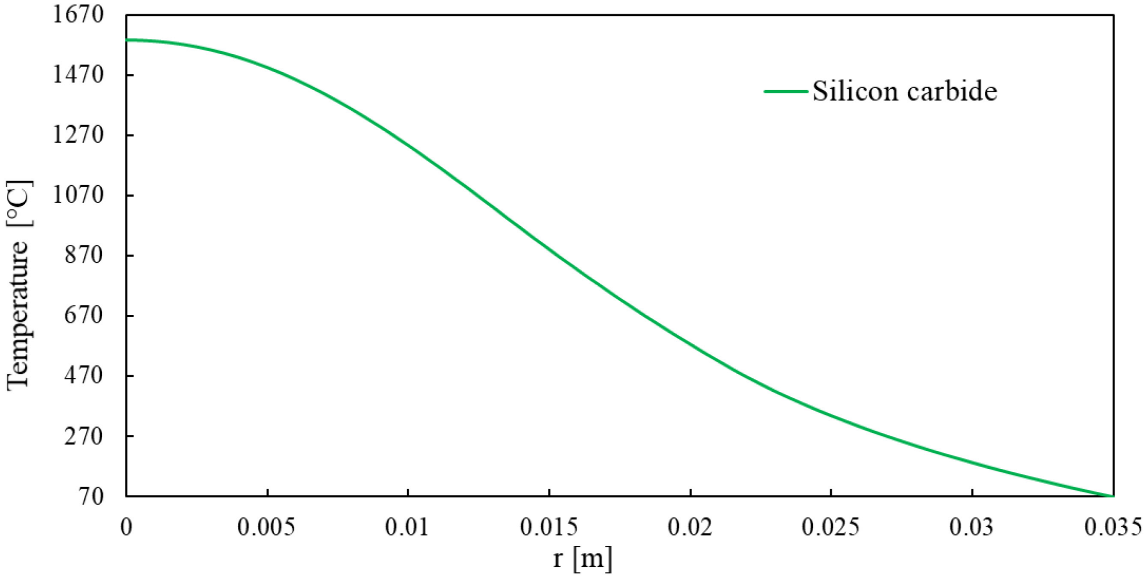

Figure 3.34 Radial temperature distribution for the Hexoloy SA silicon carbide, with a thickness t equal to 2.4 mm.

Following the same procedure shown for graphite, the integral $\int_0^r Trdr$ in Eq. 3.36 and Eq. 3.37 can be written for the silicon carbide as:

$$\int_0^r Trdr = -2.78 \cdot 10^9 \frac{r^6}{6} + 2.61 \cdot 10^8 \frac{r^5}{5} - 7.45 \cdot 10^6 \frac{r^4}{4} + 1.71 \cdot 10^4 \frac{r^3}{3} + 1.57 \cdot 10^3 \frac{r^2}{2} \tag{3.42}$$

At this point, the radial distribution of the stress component σ_r and σ_θ can be obtained for graphite and silicon carbide, for both the constraint configurations. In case of a disc free to expand, Eq. 3.40 and Eq. 3.42 will be substituted in Eq. 3.34 and Eq. 3.35; in case of a completely constrained disc, they will be substituted in Eq. 3.36 and Eq. 3.37. The resulting radial distributions are shown in Figure 3.35 for graphite and in Figure 3.36 for silicon carbide.

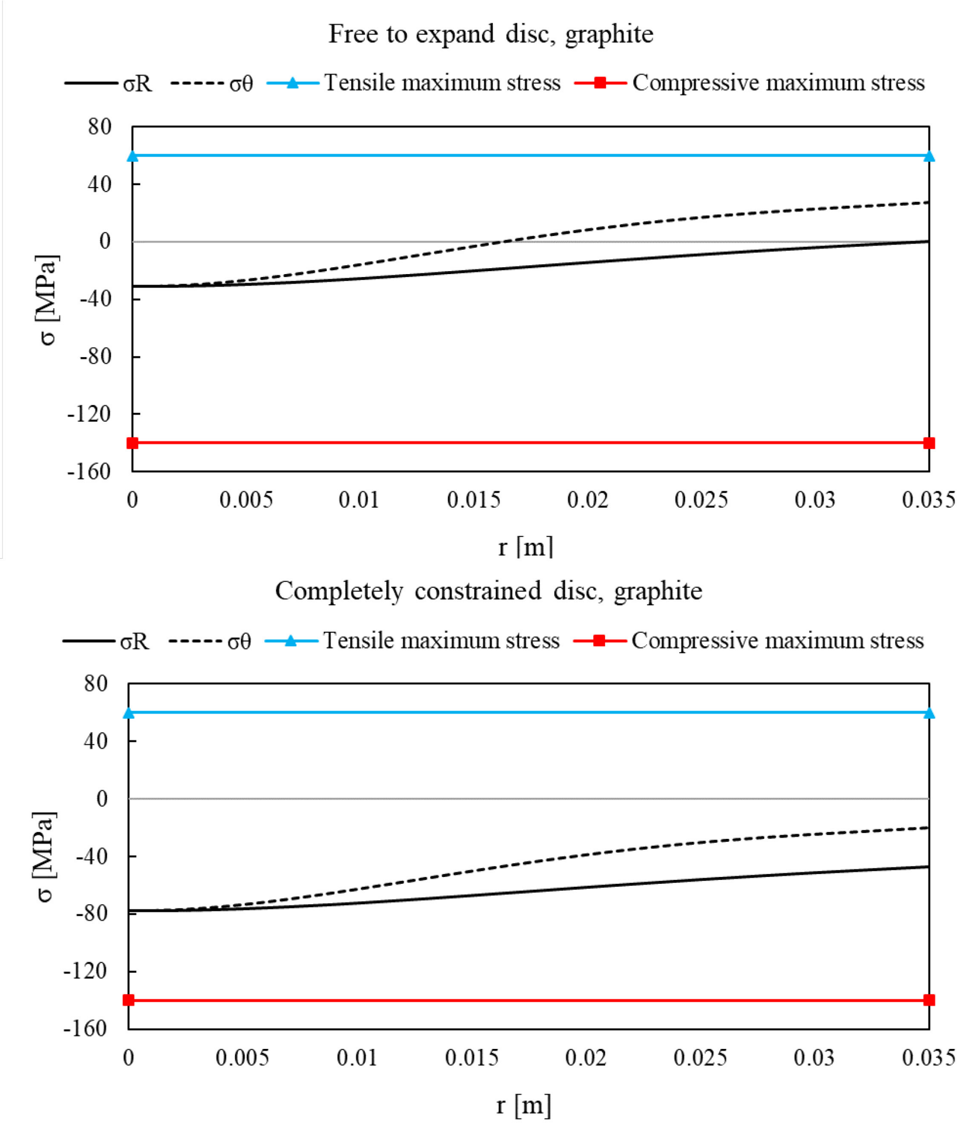

Figure 3.35 The radial distribution of the stress components σ_r *and* σ_θ *on a graphite target window with thickness equal to 1.4 mm, calculated by means of the analytical model in the two different constraint configurations.*

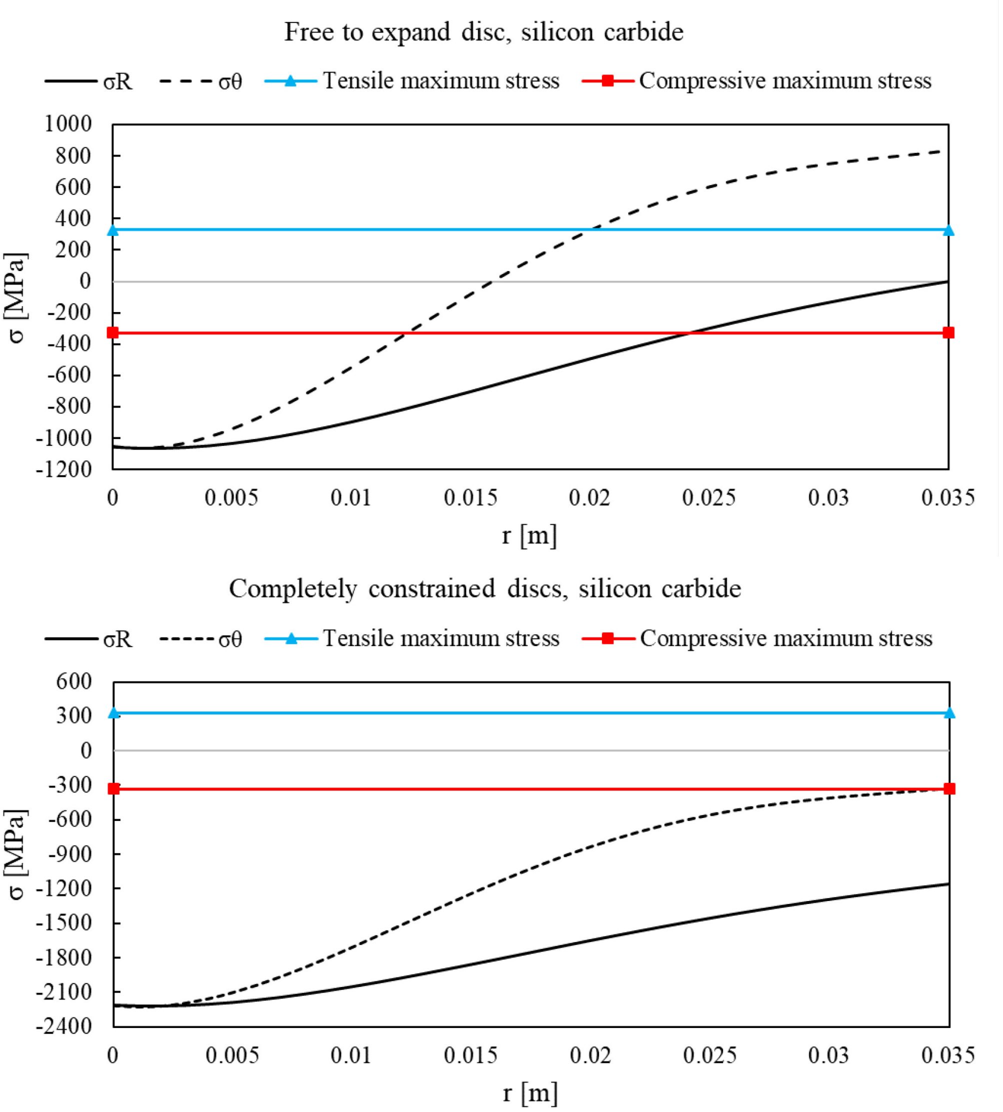

Figure 3.36 The radial distribution of the stress components σ_r *and* σ_θ *on a silicon carbide target window with thickness equal to 0.6 mm, calculated by means of the analytical model in two different constraint configurations.*

It can be observed how the stresses reached in the silicon carbide target window exceed the maximum stress values foreseen for this material. On the contrary, the graphite target window presents low stresses, ensuring a good resistance. This marked difference between the two materials can be explained analyzing the materials' elastic modulus. The silicon carbide is characterized by a high elastic modulus, about forty times higher than graphite. Being the thermal stresses directly proportional to this property, higher stresses are generated in the silicon carbide. Graphite is therefore chosen as design material for the target window.

3.4.7 Stability analysis

As shown in the previous Section, the thermal stresses generated in a graphite target window of thickness *t* equal to 1.4 mm are always lower than the maximum stresses foreseen for this material. However, it is necessary to carry out a stability analysis in order to check whether the radial compressive stresses generated at the edge of the disc can lead the target window to instability. In fact, if a slender structure is subject to a compressive load, when the load reaches a critical level, the structure collapses. This phenomenon is called buckling and may occur even though the stresses developed in the side structure are well below those needed to cause failure. For a flat circular plate under uniform radial edge compression, the critical load can be calculated as [53]:

$$\sigma' = 1.22\frac{E}{1-\nu^2}\left(\frac{t}{a}\right)^2 \qquad 3.43$$

where *E* is the elastic modulus (MPa), *ν* is the Poisson's ratio, *t* is the plate thickness (mm) and *a* is the plate external radius (mm). Considering a disc thickness of 1.4 mm, the external radius equal to 35 mm and the POCO EDM-3 properties reported in Table 3.10, the critical compressive load for the graphite target window results:

$$\sigma' = -1.22\frac{10300}{1-0.3^2}\left(\frac{1.4}{35}\right)^2 = -22.1\,MPa \qquad 3.44$$

As shown in Figure 3.37, when the disc is completely fixed, an excessive radial stress is reached at the edge of the window. For this reason, the free-to-expand configuration is chosen, in order to avoid instability problems due to constrained thermal expansion along the radial direction, that can generate excessive radial stresses at the edge.

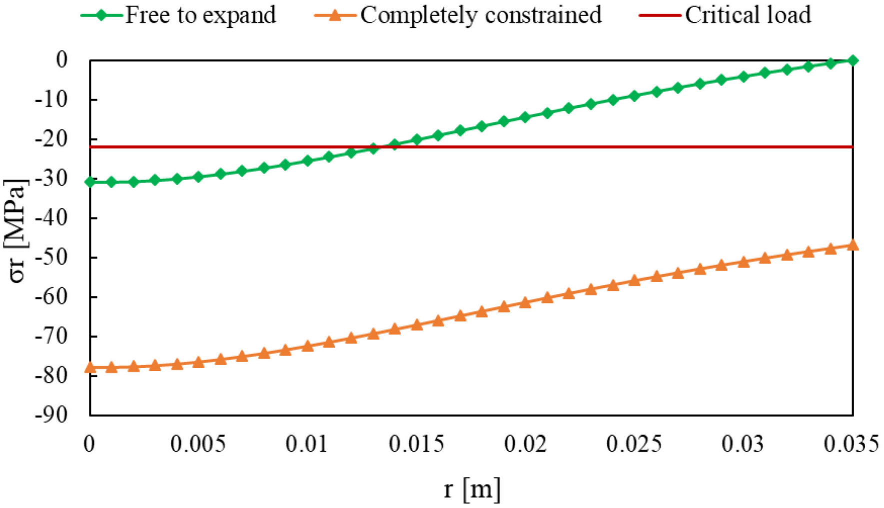

Figure 3.37 Radial distribution of the radial thermal stresses generated in the graphite target window.

3.4.8 Mechanical design and validation

As shown in the previous analyses, a graphite target window with a thickness *t* equal to 1.4 mm is adopted as final design. An installation able to allow for the radial expansion of the disc has to be guaranteed, in order to avoid instability problems. A 3D model is therefore implemented in CREO Parametrics [30] in order to define the target window installation inside the target chamber. As shown in Figure 3.38, the target window will be installed at the entrance flange of the chamber. An O-ring will guarantee the vacuum sealing. A shoulder fillet is also introduced on the target window, to avoid dangerous contact points at the flange internal edge or at the fastening ring internal radius. However, this change of section, due to the shoulder fillet, will cause an internal stress concentration.

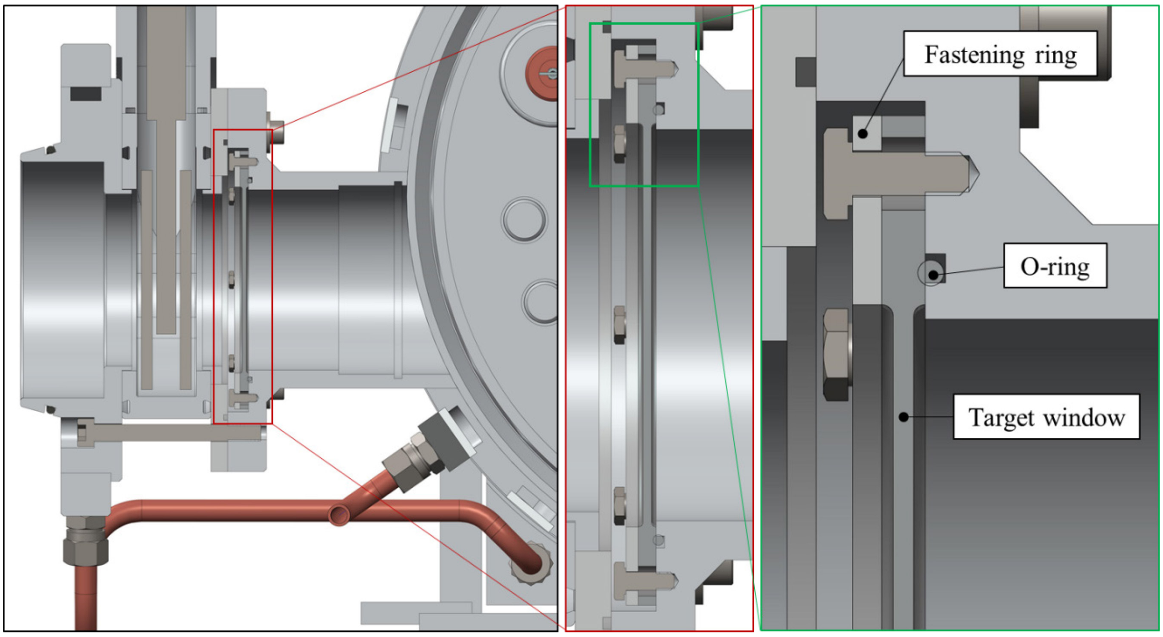

Figure 3.38 3D model of the target window installation at the entrance of the target chamber.

In order to validate this new design, a bi-dimensional axisymmetric simulation is implemented in ANSYS Mechanical [27]. First a thermal simulation allows the temperature gradient due to the beam power deposition to be calculated. Then, the thermal results are imposed as boundary conditions for the structural simulation, together with a uniform pressure of 0.1 MPa on one side of the disc, simulating the atmospheric pressure in case of vacuum loss. The applied constrains allow for the radial displacement of the target window, as requested to avoid instability problems. In Figure 3.39, the comparison between the radial temperature distribution obtained with the simplified analytical model and the bi-dimensional simulation with the final design is reported. As shown, the temperature distributions in the two cases are in very good agreement.

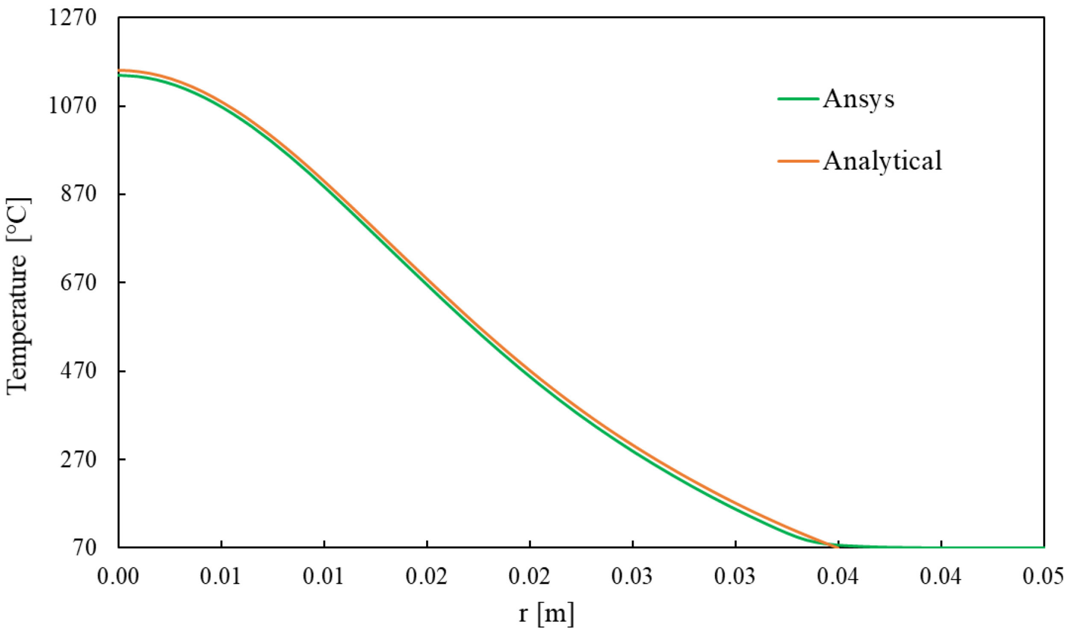

Figure 3.39 Radial temperature distribution obtained with the simplified analytical model and the bi-dimensional simulation on the final design.

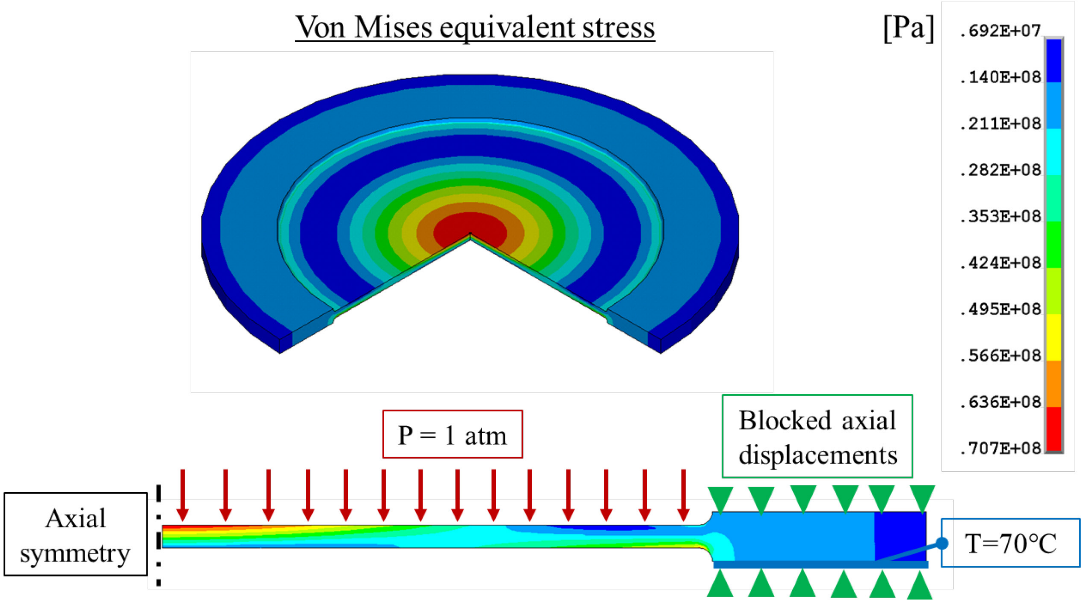

Figure 3.40 Von Mises equivalent stress distribution on the graphite target window, due to atmospheric pressure and thermal stresses.

The resulting Von Mises stress distribution is shown in Figure 3.40, together with the applied loads and boundary conditions. In Figure 3.41 the principal stresses in different points of the target window are reported. It can be noted how biaxial stresses originate in the disc, in compression-compression, compression-tension or tension-tension stress states.

A	
σ1	0
σ2	-70.8
σ3	-70.8
σVM	70.8

B	
σ1	31.3
σ2	26.7
σ3	0
σVM	28.9

C	
σ1	21
σ2	11.4
σ3	0
σVM	18.3

D	
σ1	19
σ2	4.5
σ3	0
σVM	17.4

E	
σ1	11.8
σ2	0
σ3	-1.7
σVM	12.7

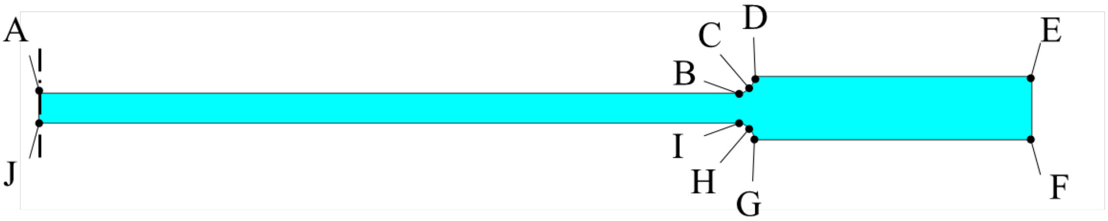

J	
σ1	0
σ2	-14.7
σ3	-14.7
σVM	14.7

I	
σ1	0
σ2	0
σ3	-65
σVM	64.7

H	
σ1	10.2
σ2	0
σ3	-29.6
σVM	35.9

G	
σ1	15.9
σ2	0
σ3	-12.5
σVM	24.6

F	
σ1	11.8
σ2	0
σ3	-1.7
σVM	12.8

Figure 3.41 Principal stresses and Von Mises equivalent stress in different points of the Target Window. Stress values are expressed in MPa.

As shown in Chapter 3, when graphite is loaded by a complex or non-uniform system of stresses, the choice of a failure criterion becomes important. When graphite is subject to a compression-compression biaxial stress, the Von Mises criterion can be applied [51]. On the other hand, in case of tension-compression or tension-tension biaxial stresses, the modified maximum strain energy theory and the Modified Coulomb Mohr theory are preferred [56] [57] [51]. The correspondent failure envelopes and the calculated stress points are shown in Figure 3.42. All the biaxial points lie inside the failure envelopes; this means that no critical stress state is generated inside the target window. The final design is therefore validated.

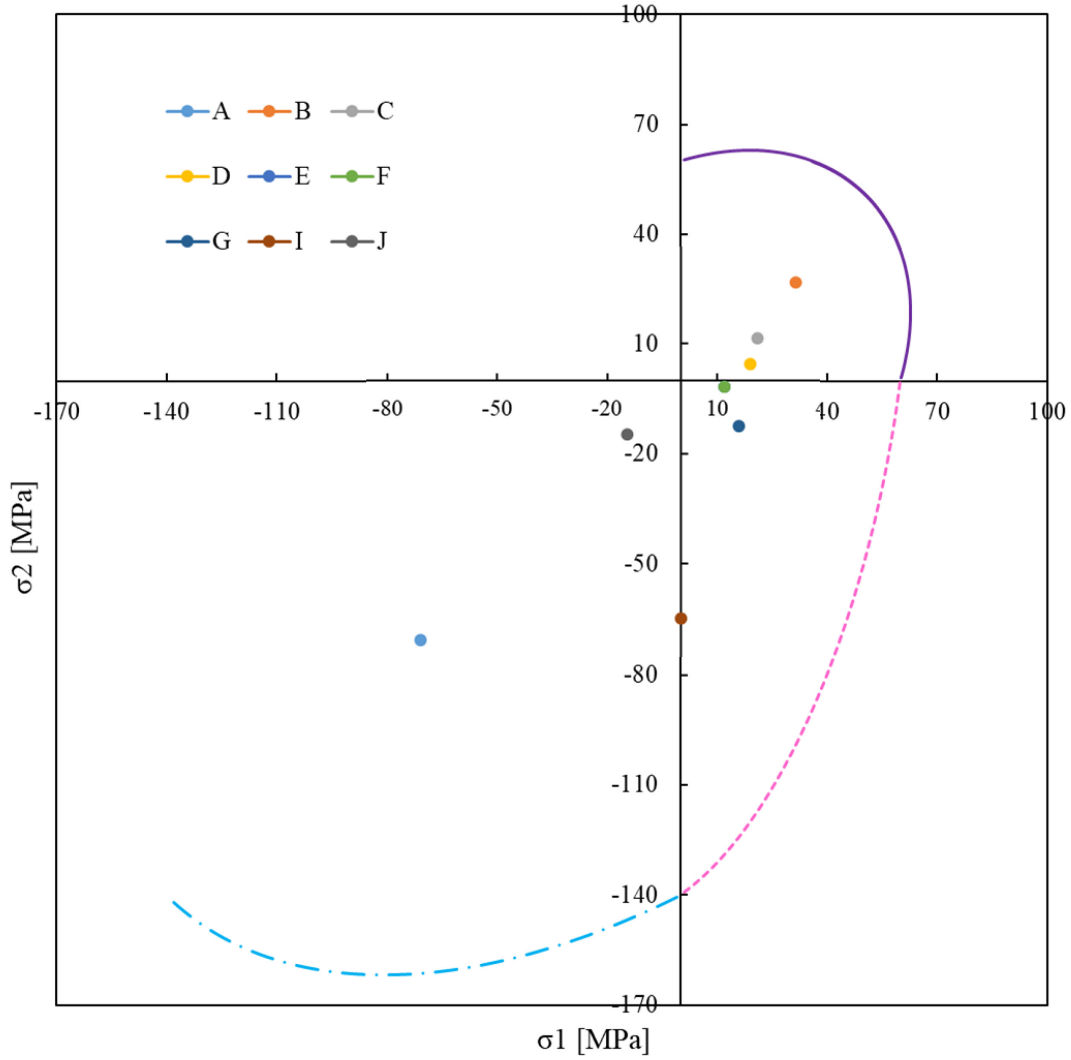

Figure 3.42 Biaxial failure envelopes predicted by the Von Mises criterion (compression-compression quadrant), the Modified maximum strain energy theory and the Modified Coulomb Mohr theory (tension-tension and tension-compression quadrants), for the POCO EDM-3 graphite. The biaxial stresses calculated with the thermal-structural analysis are also reported.

CHAPTER 4

Mechanical properties of graphite at high temperatures

4.1 Introduction

Graphite is used in a wide field of industrial applications, thanks to its high resistance at high temperatures, low thermal expansion and high thermal conductivity, translating into an excellent thermal shock resistance. For its properties, it is also chosen for the design of several devices in the SPES bunker. Therefore, knowing the mechanical strength of graphite at high temperatures is an important issue for structural design.

Numerous investigations on high temperature mechanical and thermal properties have been conducted on different types of graphite. Greenstreet [58], Price [56] and Green [59] presented reviews about published mechanical properties data; Malmstrom [60] and Wagner [61] analyzed some mechanical properties at high temperature; Smith [62], Martens [63], Green [64] and Gillin [65] performed uniaxial tensile or compressive tests over 2000°C. Biaxial mechanical properties at room temperature have been presented by Broutman [66], Ely [57], Weng [67], Ho [68] and Eto [69], while Babock [70] and Jortner [71] performed also high temperature biaxial tests, over 2000°C. In these studies, different types of graphite have been analyzed, as reported in Table 4.1. However, the following general conclusions are supported by all results:

- Resistance increases with temperature up to 2500°C where the highest strength value can be up to twice its room temperature. At higher temperatures, a significant decrease is observed;
- Resistance increases with density;
- Elastic modulus increases with temperature.

Table 4.1 Designation and characteristics of graphite analyzed in previous studies.

Author	Material Designation	Manufacturer	Description
Malmstrom et al. [60]	AGX	National Carbon Company	Extruded and graphitized at 2600°C; anisotropic; ρ=1.58 g/cm^3
	C-18	National Carbon Company	Molded and graphitized at 2600°C; anisotropic; ρ=1.60 g/cm^3
	SA-25	National Carbon Company	Molded and graphitized at 3000°C; isotropic with small crystallites; ρ=1.55 g/cm^3
	AUF	National Carbon Company	Extruded and graphitized at 3000°C; anisotropic; ρ=1.67 g/cm^3

	AWG	National Carbon Company	Molded and graphitized at 3000°C; anisotropic; ρ=1.76 g/cm^3
Wagner et al. [61]	H4LM	Great Lake Carbon Company	Extruded; maximum particle size 838.2 μm; ρ=1.72 g/cm^3
	CK	Los Alamos Scientific Laboratories	Molded; ρ=1.71 g/cm^3
	LDH	Los Alamos Scientific Laboratories	Molded; Uranium content 125 mg/ cm^3 carbon; ρ=1.73 g/cm^3
	LDC	Los Alamos Scientific Laboratories	Molded; Uranium content 250 mg/ cm^3 carbon; ρ=1.66 g/cm^3
Smith [62]	H4LM	Great Lake Carbon Company	Extruded; maximum particle size 838.2 μm; ρ=1.72 g/cm^3
Martens [63]	3499	Speer Carbon Company	Molded and graphitized above 2260°C; maximum particle size 127 μm; ρ=1.57 g/cm^3
	H3LM	Great Lake Carbon Company	Extruded; maximum particle size 838.2 μm; ρ=1.68 g/cm^3
Green [64]	AUF	National Carbon Company	Extruded and graphitized at 3000°C; anisotropic; ρ=1.67 g/cm^3
Gillin [65]	"Type A"	UKAEA, Harwell	Extruded and graphitized at 2700°C; anisotropic; ρ=1.74 g/cm^3
	"Isotropic"	Berkeley Nuclear Laboratories	Extruded and graphitized at 2700°C; less anisotropic than "Type A"; ρ=1.70 g/cm^3
Broutman et al. [66]	AXF-5Q	POCO	Particle size 5 μm; pore size 0.8 μm; apparent density 1.78 g/cm^3; declared compressive strength 138 MPa; Isotropic.
Ely [57]	Graph-I-Tite "G"	Carborundum Co.	Maximum grain size 0.840mm; bulk density 1.908 g/cm^3;
Weng [67]	ATJ	National Carbon Company	Fine-grained; molded; bulk density 1.73 g/cm^3; transversely isotropic.
Ho [68]	PGX	Union Carbide Corp	Conventional molded; medium-grained semi-isotropic; bulk density 1.78 g/cm^3; maximum particle size 0.76mm; high ash and other impurities content
	2020	Stackpole Carbon Company	Isostatic molded; medium-grained graphite; bulk density 1.79 g/cm^3
Eto [69]	IG-11	TANSO	Fine-grained isotropic; bulk density 1.77 g/cm^3; declared compressive strength 78MPa
	PGX	Union Carbide Corp	Medium-grained semi-isotropic; bulk density 1.78 g/cm^3; maximum particle size 0.76mm; high ash and other impurities content
Babcock [70]	ATJ-S	Union Carbide Corp	Polycristalline, molded, anysotropic; maximum grain size 0.15mm; bulk density 1.83 g/cm^3
Jortner [71]	AXF-5Q	POCO	Particle size 5 μm; pore size 0.8 μm; apparent density 1.78 g/cm^3; declared compressive strength 138 MPa; isotropic

Nevertheless, some aspects are not completely clarified: graphite is generally considered as a brittle material ([45], [72], [73], [74]) and therefore an elastic behaviour can be expected. Moreover, in biaxial strength studies, failure criteria suitable for brittle materials have been often chosen, such as the Coulomb-Mohr theory, as the best interpolation with the experimental data ([68], [75], [76]). However, some authors highlighted a plastic deformation during compressive tests, also at room temperature ([65], [70], [71]). Moreover, Christensen [77] states that, relative to failure, all materials can behave either in a ductile or a brittle manner, depending upon the state of stress and other environmental influences. In addition, graphite physical properties and characteristics may vary depending on the raw materials, the process, the microstructure and the particle size ([45],[72]). For these reasons, it is necessary to perform a dedicated characterization of any given graphite.

In the present work, the POCO EDM-3 isotropic ultrafine grain graphite used for the devices of the SPES bunker is studied. These devices are often subject to compressive stresses, due to restrained thermal expansions. Therefore, uniaxial compressive tests are performed, to obtain the stress-strain curve at room temperature. Then, in order to evaluate the biaxial resistance, hourglass-shaped specimens, characterized by different hourglass radius, are tested in compression both at room temperature and at 1000°C. One geometry is finally chosen to be tested also at 2000°C.

4.2 Materials and methods

4.2.1 Tested material

The EDM-3 grade offers a uniform ultrafine microstructure: the particles are all the same small size, less than 5 μm. The pores are also small, typically less than 1 μm. This graphite has no preferred grain orientation, and it is therefore isotropic. Density influences the strength of the graphite: a higher density leads in fact to a higher strength [42]. However, also in the same graphite billet, a density variation can be found. For this reason, each sample is carefully measured by means of a Sartorius hydrostatic balance. Even though the graphite is porous, the intrusion of water into the porosity is slow and the accuracy with this method is acceptable if the submerged weight is taken quickly. A density of 1.73 ± 0.01 g/cm^3 is considered acceptable for this study. The Poisson' ratio of the material is assumed to remain constant with respect to temperature, in accordance with other similar studies ([78],[79]).

4.2.2 Testing equipment

Two different testing equipments are used in this study. The uniaxial compressive tests are performed using the commercial MTS 858 Mini Bionix II servohydraulic testing system. For the biaxial strength tests, a previously designed equipment, housed inside an aluminum chamber, has been modified, and it is shown in Figure 4.1. This apparatus has been designed to operate in a vacuum chamber and permits high temperature tests. The specimen lies on the fixed punch, and it is compressed by the movable punch. Tantalum end blocks, foreseen for each punch, allow the high temperature reached during the tests to be withstood. Heating is obtained by Joule effect, through tantalum foils attached to copper clamps. The temperature on the specimen cross section surface is measured by means of an optical pyrometer and a disappearing filament pyrometer, aligned with the observation windows. A bellows maintains the vacuum, of the order of 10-5 mbar inside the chamber to avoid materials oxidation. An HBM-U9C 10 kN tension-compression load cell, installed thanks to two threaded connections, measures the compressive force. The load is applied manually: a joint allows the rotation of a screw, which is brazed to a steel component that loads two axial bearings. Four bushes are fixed on a plate and allow the screw rotary motion to be converted to a linear motion. The axial load is then transferred to the force sensor and to the specimen, by means of a cylindrical nut.

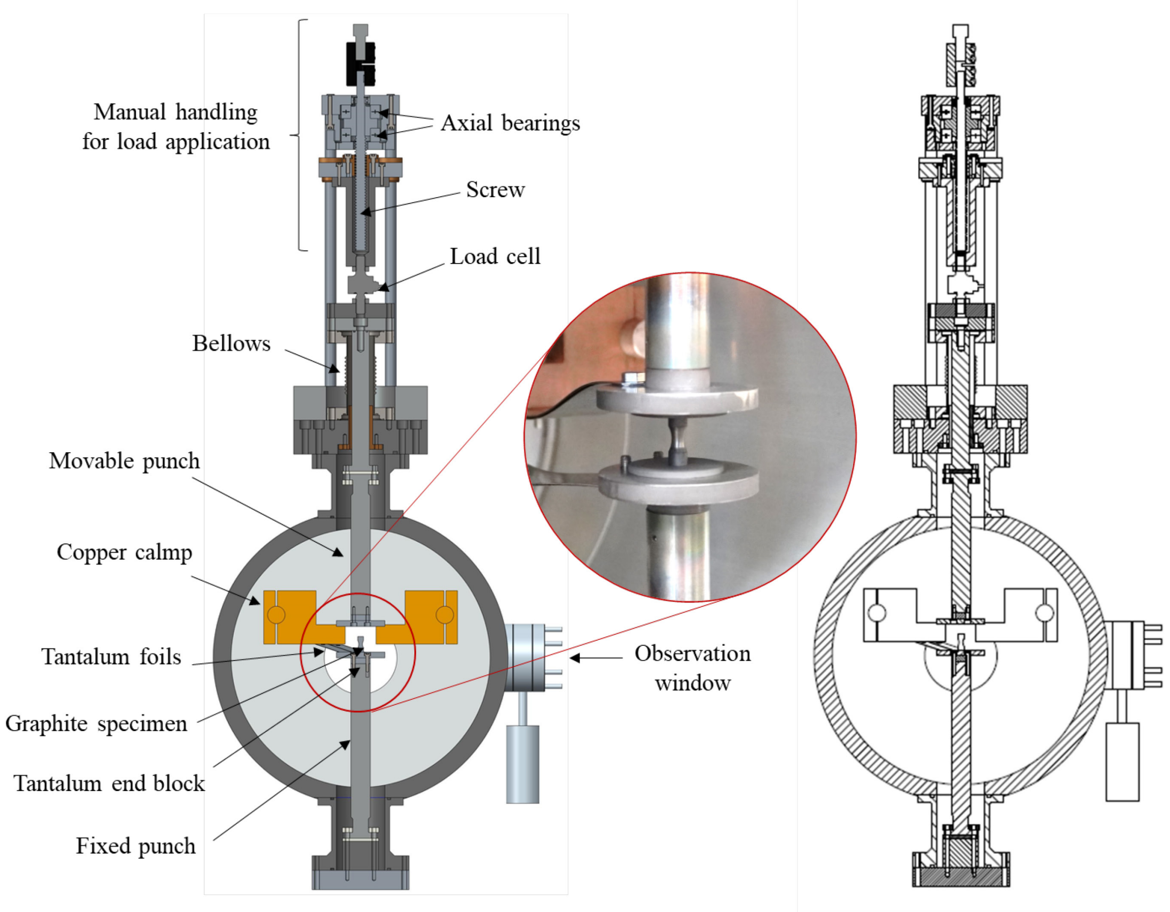

Figure 4.1 Experimental apparatus used during the biaxial strength tests. [51]

4.2.3 Specimen design

Several studies have been made to clarify graphite behavior under multiaxial stress, but few definitive conclusions have been reached. Usually, tubular specimens were tested to failure under a combination of internal pressure and axial tension or compression. The failure points were then compared with the predictions of various theories for failure under multiaxial stress (see Table 4.2). Most studies were conducted at room temperature, while only Babcock [70] and Jortner [71] performed also high temperatures biaxial tests.

Table 4.2 Comparison between different criteria analyzed in previous biaxial studies.

	Maximum test temperature	**Biaxial stress state**	**Suitable criteria**
Broutman [66]	RT	Tension-tension	Modified maximum strain energy theory
		Tension-compression	Coulomb-Mohr theory
Ely [57]	RT	Tension-tension	Modified maximum strain energy theory
		Tension-compression	Modified maximum strain energy theory
Weng [67]	RT	Tension-tension	Hoffman's theory
		Tension-compression	Modified maximum strain energy theory
		Compression-compression	*Buckling problems*
		Compression-tension	Modified maximum strain energy theory
Ho [68]	RT	Tension-tension	Modified Coulomb-Mohr theory
		Tension-compression	Modified Coulomb-Mohr theory
		Compression-compression	Modified Coulomb-Mohr theory
Eto [80]	RT	Tension-tension	Modified maximum strain energy theory
		Tension-compression	Modified maximum strain energy theory
Babcock [70]	2760°C	Tension-tension	Coulomb-Mohr theory
		Tension-compression	Coulomb-Mohr theory
		Compression-compression	*Buckling problems*
Jortner [71]	2200°C	Tension-tension	Weibull's criterion
		Tension-compression	Maximum shear stress theory

In most cases, the tension-tension and the tension-compression quadrants in the biaxial stress plane were analyzed. In fact, in the compression-compression quadrant, buckling problems often arose during tests, preventing valid data to be obtained ([67], [70]). It seems that the biaxial compressive stress state cannot be measured accurately with thin-walled cylindrical specimens, that is the method adopted in the aforementioned studies.

For these reasons, in the present study, a different approach is adopted. The idea is to obtain a biaxial compressive state, by axially compressing hourglass specimens. Due to the hourglass radius, also a second principal stress (the hoop stress) originates in the sample. By varying the geometrical parameters of the specimen, it is then possible to obtain different biaxial ratios (axial stress over hoop stress), translating in different points in the compression-compression quadrant of the biaxial stress plane. This approach is also suitable for high temperatures tests. Several notched geometries are considered, characterized by different parameters such as the net section diameter and the hourglass radius. At the end, four geometries are selected for the study, as shown in Figure 4.2 and Table 4.3. Thermo-electrical simulations are performed in order to assess the temperature distribution along the specimens, by means of the FE code ANSYS Mechanical [27]. Axisymmetric constraints are defined and the sample, the tantalum end block and the steel punch are modelled. An input fixed current is imposed and, by taking advantage of the symmetry of the sample, a voltage constraint of 0V is imposed at the center. Radiation heat transfer is applied on specimen lateral surface to the surrounding space, at a fixed temperature of 25°C. An example of simulation results is reported in Figure 4.3 for the Hourglass I geometry, relevant to a current of 150 A. These analyses allow also the temperature reached by the tantalum end blocks and by the steel punches to be assessed. To ensure the structural integrity of these components, a maximum temperature of 1980°C for tantalum [81] and 925°C for AISI316 [82] is considered.

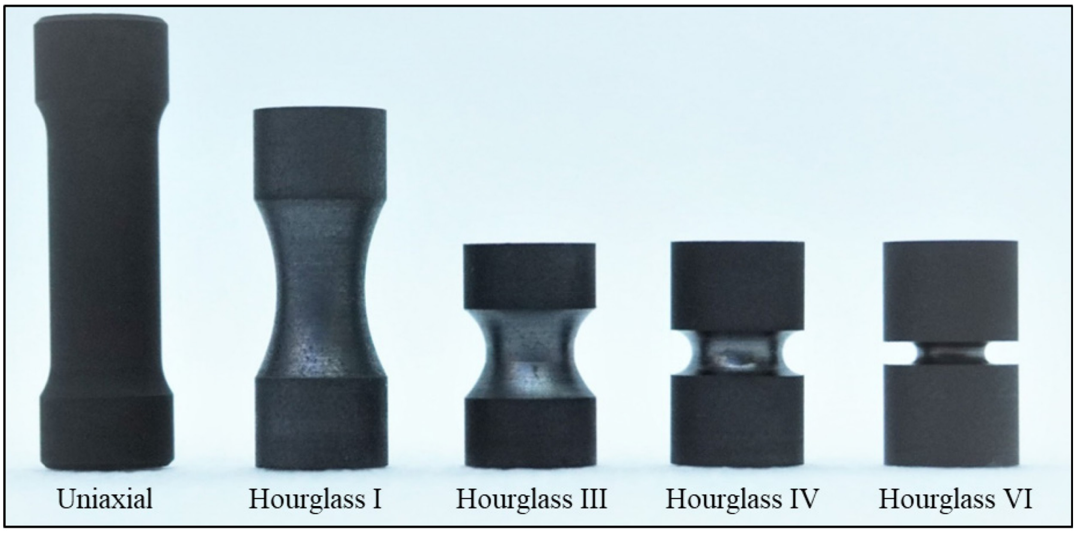

Figure 4.2 Plane and notched specimens.

Table 4.3 Geometrical parameters of uniaxial and biaxial specimens.

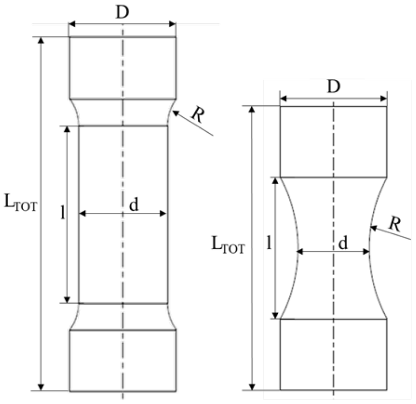

Geometry	D [mm]	d [mm]	L_{TOT} [mm]	l [mm]	R [mm]
Uniaxial	6	5	20	10	2.5
Hourglass I	6	4	16	8	8.5
Hourglass III	6	4	10	4	2.5
Hourglass IV	6	4	10	2	1
Hourglass VI	6	3	10	1	0.5

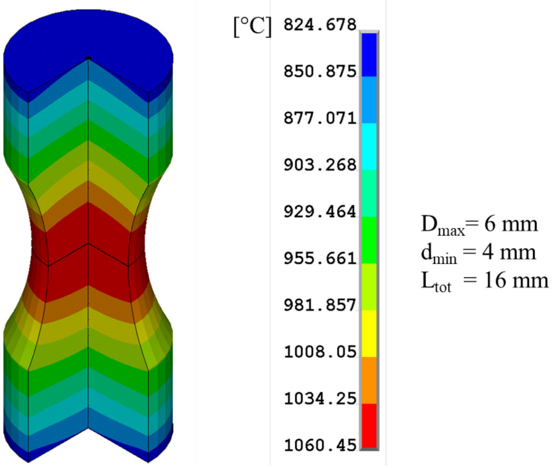

D_{max}= 6 mm
d_{min} = 4 mm
L_{tot} = 16 mm

Figure 4.3 Temperature distribution in the Hourglass I geometry for a current I = 150 A.

4.2.4 Testing procedure

The uniaxial tests are performed with the MTS servo hydraulic testing system. The strain is measured by means of a MTS axial contact extensometer, with a gage length of 5mm. During the test a strain rate of 0.02 min-1 is imposed. To evaluate the biaxial strength, the experimental apparatus described in Sec. 4.2.2 is used. The specimen is placed inside the aluminum chamber, on the tantalum end block of the fix punch. For the high temperature tests, tungsten or graphite discs are interposed between the specimen and the tantalum end blocks, to avoid material deterioration. No influence of the contact material is expected for hourglass specimens [27]. When a vacuum of 10^{-5} mbar is reached, a pressure is applied to the sample, in order to decrease the electrical resistivity of the surfaces in contact and facilitate the current flow. The applied compressive load is approximately 20 MPa on the reduced section. The desired heat power is then gradually reached, while the temperature is checked by means of two pyrometers. It is then possible to start the compressive test, by manually applying the load up to failure.

4.3 Uniaxial compression strength at room temperature

Analyzing the available data in the literature, it is not clear whether a linear elastic model can be adopted for this type of graphite in compression states. For this reason, uniaxial compression tests are performed in order to shed light on the mechanical behavior of this material. Unnotched samples, presented in Figure 4.2 and Table 4.3 named “uniaxial”, are therefore tested in compression, while strain is measured by means of an extensometer. The resulting stress strain curves are reported in Figure 4.4. The POCO EDM-3 graphite shows a significant plastic deformation at room temperature.

For a lot with density equal to 1.73 ± 0.01 g/cm^3, the average stress at failure is approximately 140 MPa with approximately 4.5% of strain. A yield strength around 100 MPa can be defined using the 0.2% offset method. These results are in line with other data presented by Gillin [65], Babock [70] and Jortner [71].

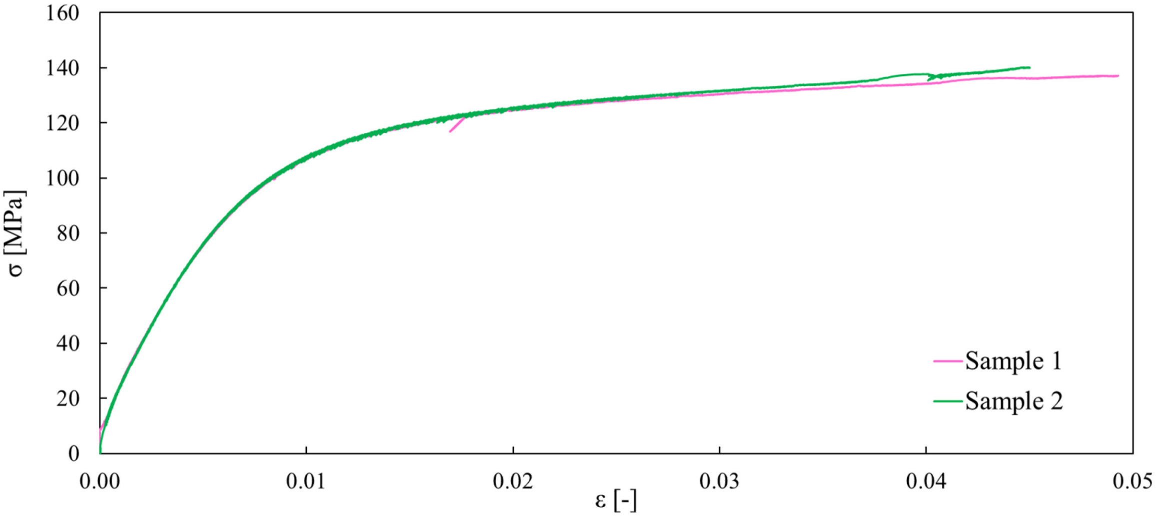

Figure 4.4 Experimental stress-strain curves obtained at room temperature for EDM-3 graphite.

4.4 Biaxial compression strength at room temperature

Hourglass specimens are tested at room temperature. In the light of uniaxial test results, elastic-plastic simulations are performed to evaluate the stress field at failure. The experimental stress-strain curve is implemented in structural simulations and the suitability of the Von Mises yield criterion is evaluated: the registered loads at failure are imposed and the equivalent Von Mises stresses are compared. In the simulations, axisymmetric constraints are defined and the horizontal displacements on the upper edge of the sample are coupled. In Figure 4.5, an example of Von Mises stress distribution for each geometry is reported, while Figure 4.6 presents the corresponding failure points on the stress-strain curve. The experimental curve has been extended in ANSYS, following the same slope, to allow for extrapolations. All geometries show a Von Mises stress of approximately 140 MPa, in accordance with the uniaxial tests. This seems to validate the choice of this yield criterion. Moreover, the Von Mises total mechanical strain is not too different if compared with 4.5% uniaxial strain. Therefore, no significant extrapolations of the stress-strain curve are performed in the simulations. Assessed the suitability of the Von Mises yield criterion, it is then possible to analyze the biaxial stress state at failure for the different geometries. As shown in Figure 4.7, it seems that resistance increases as the stress state approach the equibiaxial stress state, where the ratio between the axial and the hoop stresses approaches the unit value.

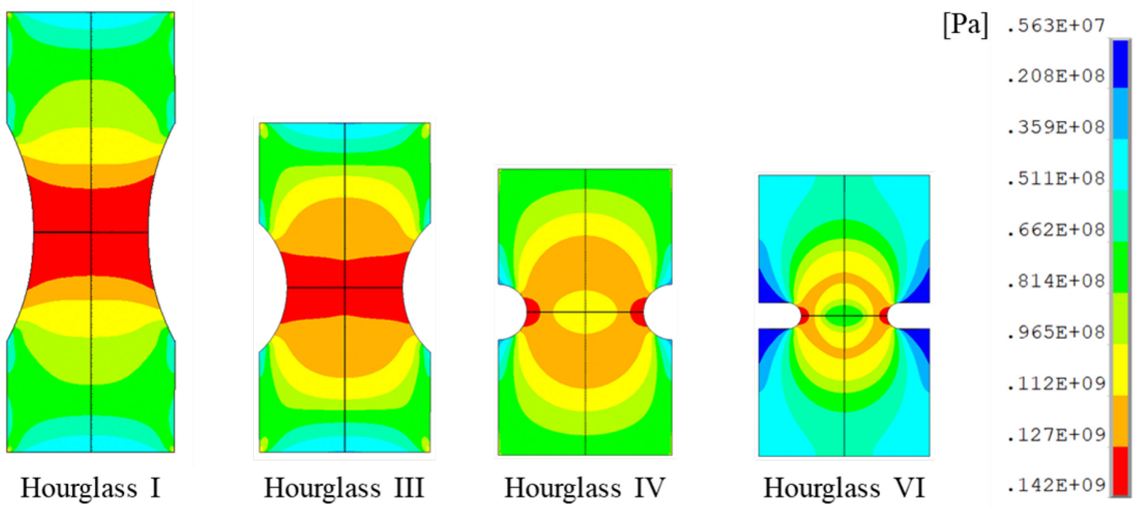

Figure 4.5 Example of equivalent Von Mises stress distribution at failure load for each hourglass geometry.

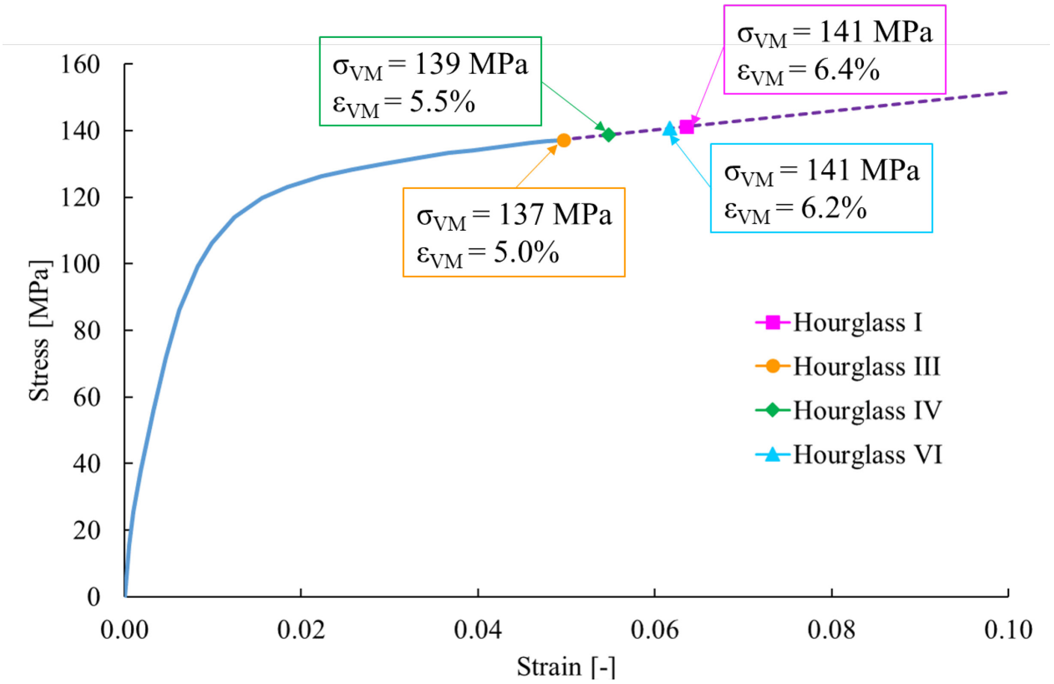

Figure 4.6 Failure points on the stress-strain curve. The experimental curve (solid line) has been extended following the same slope (dashed line).

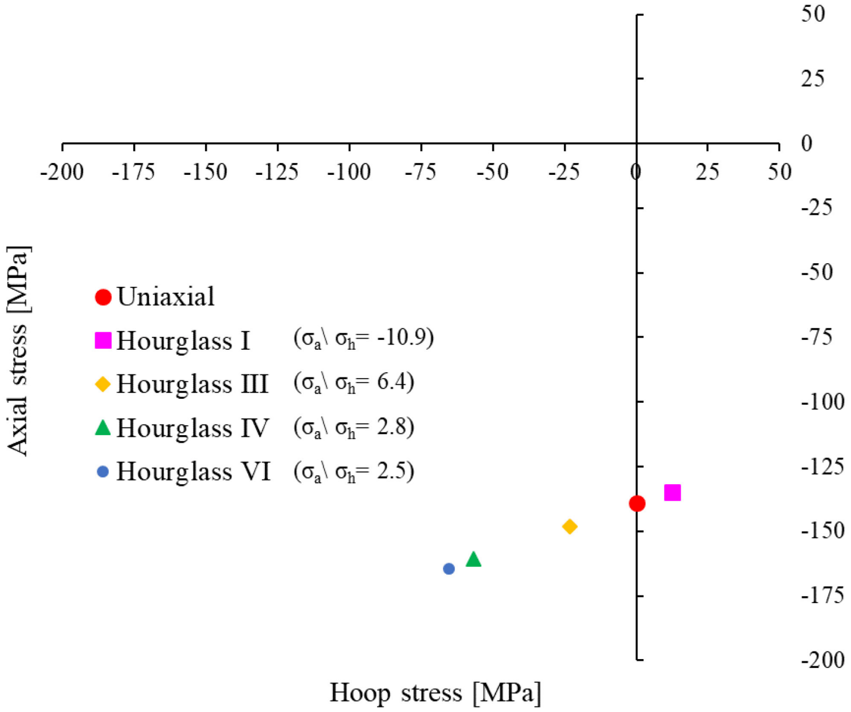

Figure 4.7 Biaxial fracture stresses at room temperature for POCO EDM-3 graphite specimens.

4.5 Biaxial compression strength at high temperature

Hourglass specimens are tested also at high temperature. Graphite increases its elastic modulus and its resistance with temperature. Therefore, the stress-strain curve obtained at room temperature are no longer valid: it is not possible to determine the equivalent stress at failure by means of an elastic-plastic simulation. However, it is possible to compare the load at failure, in order to highlight an increase of strength with temperature. First, all the geometries are tested up to 1000°C: the experimental apparatus used during the high temperature tests is reported in Figure 4.8. Figure 4.9 presents the average trend of the compressive load with temperature. The data are presented as nominal pressure on net section in order to decrease variability due to different dimensions of samples. No data at high temperature are obtained for Hourglass VI, due to problems in determining the failure load without a clear view of the sample. Then, the Hourglass I geometry is chosen to be tested up to 2000°C. This geometry presents in fact the more homogenous temperature distribution on the net section, allowing for more precise temperature measurements by means of the optical pyrometer. The nominal failure pressure on the net section up to 2000°C is presented in Figure 4.10. The tests demonstrated that, as the temperature increases, the compressive failure load increases: at 1000°C, Hourglass I shows an average increase of 16%, Hourglass III of 18% while Hourglass IV of 8.5% with respect to room temperature values. Moreover, at 2000°C, an average increase of 24.5%

over the room temperature value is noted for Hourglass I. This behavior is consistent with POCO indications [45] and it is in agreement with data in the literature [64][65][42]. However, in order to properly define the stress state at failure by dedicated elastic-plastic simulations as for room temperature, it would be necessary to obtain the stress-strain curve at 1000°C.

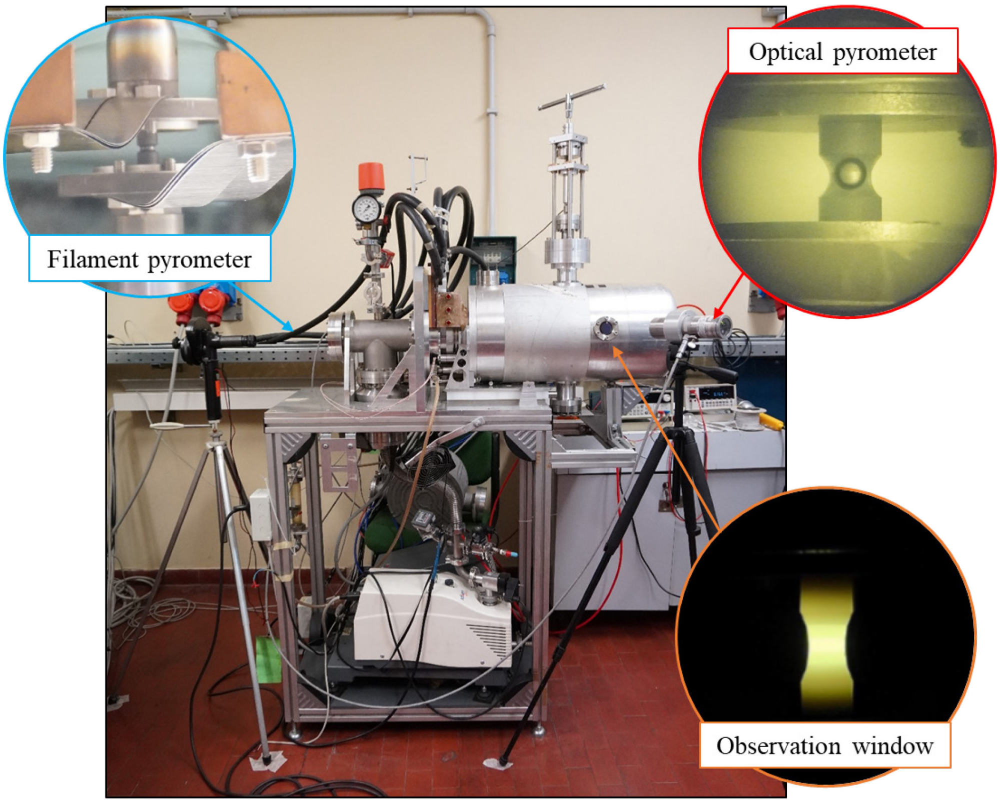

Figure 4.8 Experimental apparatus used for the high temperature tests and the different observation positions.

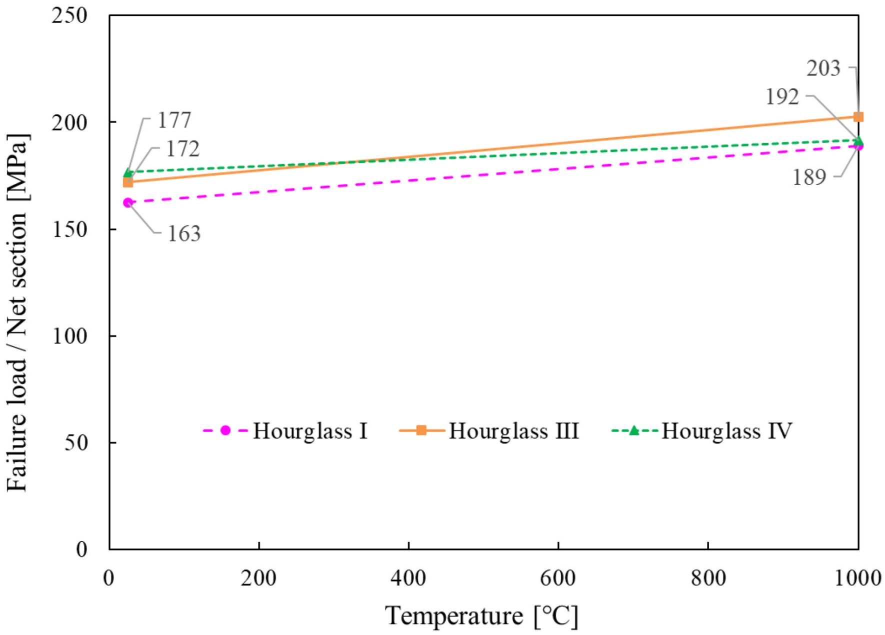

Figure 4.9 Average nominal pressure on net section up to 1000°C for all the tested biaxial geometries.

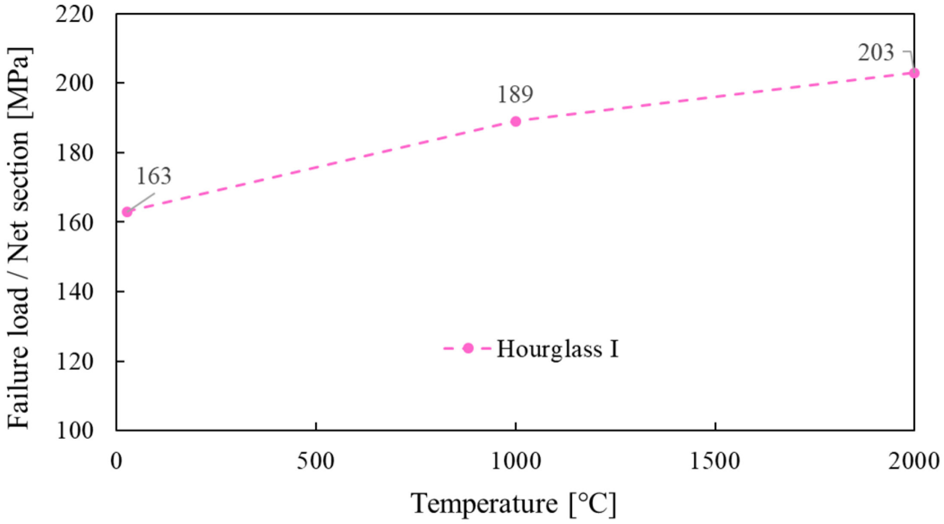

Figure 4.10 Average nominal pressure on net section up to 2000°C for the Hourglass I geometry.

Failure modes - In hourglass specimens, failure always started at the reduced cross section and exhibited two different modes. In the first one, the fracture plane was oriented at a 45° plane with respect to the load direction (*shear plane*). The second mode consisted in interacting shear planes with a co-axial fracture plane starting from the re-entrant corner (*interacting plane*).

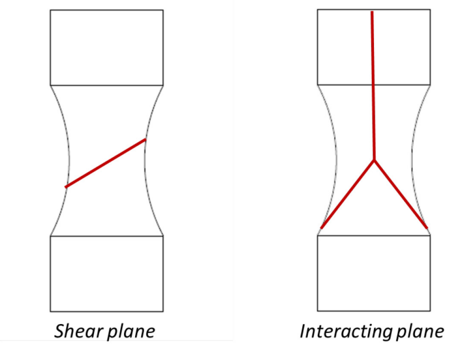

Figure 4.11 Failure modes observed in the hourglass specimens, both at room temperature and high temperature.

Fracture surfaces have been analyzed by means of a Scanning Electron Microscope. Two hourglass I specimens, tested at room temperature and at 2000°C, respectively, have been compared. The scans have been performed in different positions along the surfaces of the samples. Both at room temperature and at high temperature, two different fracture surface morphologies can be observed. The first one is characterized by indented surfaces, while in the second one smooth platelets can be recognized, as reported in Figure 4.12 and Figure 4.13. Neither the indented surfaces nor the platelets-like morphology seem to be definitely attributable to a specific type of failure.

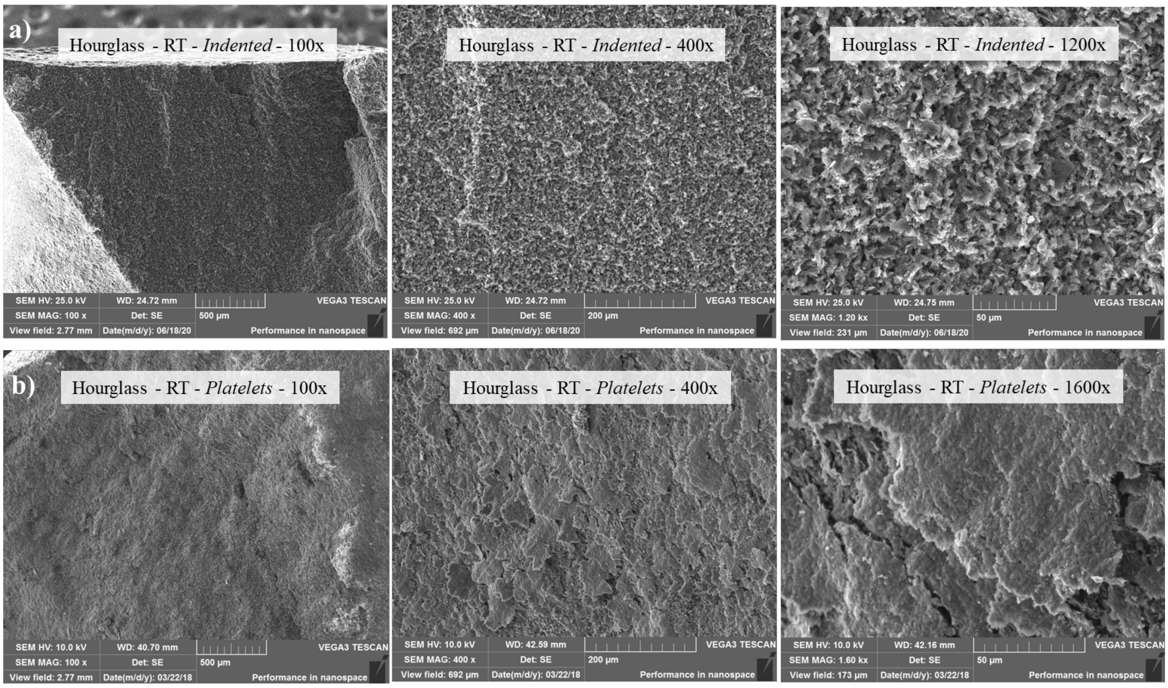

Figure 4.12 SEM micrographs of fracture surface of an hourglass specimen tested at room temperature (RT). Two different fracture surface morphologies can be observed: Indented (a) and Platelets (b).

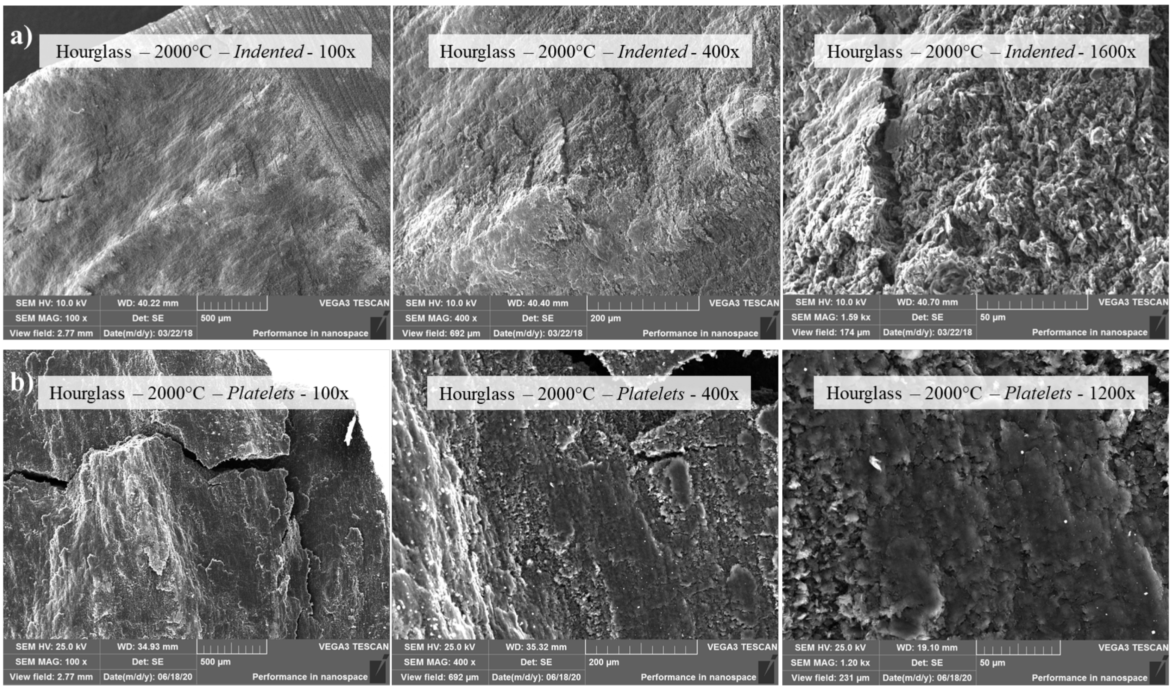

Figure 4.13 SEM micrographs of fracture surface of an hourglass specimen tested at 2000°C. Two different fracture surface morphologies can be observed: Indented (a) and Platelets (b).

4.6 Biaxial failure criteria

When graphite is loaded by a complex or non-uniform system of stresses, the choice of a failure criterion becomes important. Different failure criteria have been suggested in literature, but none has been generally adopted as applicable to graphite under all loading conditions. The experimental tests reported in the previous sections show how the Von Mises criterion can be applied for the POCO EDM-3 graphite in the compression-compression quadrant. No experimental data are available for tension-tension and tension-compression biaxial stresses for this type of graphite. However, it is possible to apply the criteria proposed in the literature for similar isotropic, fine grained graphite. In particular, in both these quadrants, several studies ([66],[57],[67],[69] [83]) show that the Modified maximum strain energy theory [57] is usually in accordance with the experimental data. The correspondent failure envelopes for the POCO EDM-3 are shown in Figure 4.14, and will be used for the design of SPES devices.

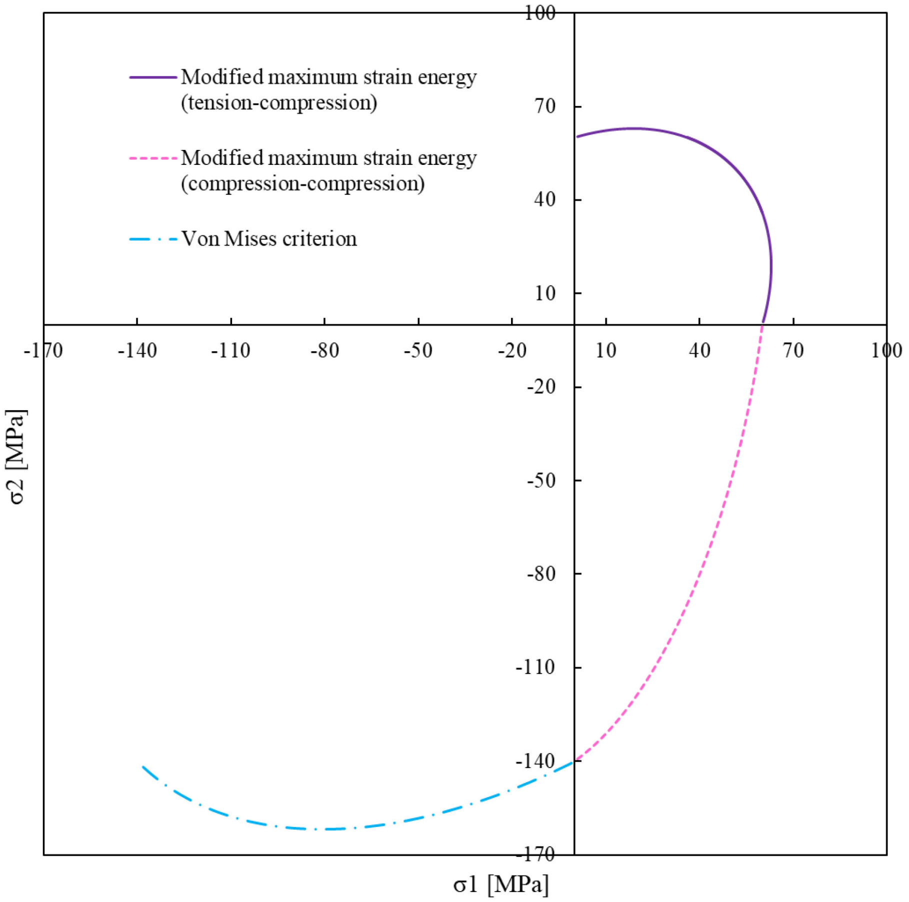

Figure 4.14 Biaxial failure envelopes for the isotropic graphite POCO EDM-3 with Poisson's ratio = 0.3, ultimate compressive strength = 140 MPa [51] *and ultimate tensile strength = 60 MPa* [45].

CHAPTER 5

Maintenance inside the SPES bunker

5.1 Introduction

In the SPES facility, the proton beam produced by a commercial cyclotron enters in the production bunker along the Primary Proton Beam (PPB) line and interacts with the UC_x target, inducing fission of the ^{238}U nuclei [16]. Mechanical components of the Front-End system are expected to be irradiated by intense fluxes of both primary protons and neutrons generated by fission in the target. A mixed radiation field of protons, neutrons and photons is generated during the irradiation. Consequently, the materials are subject to the nuclear activation process. The level of residual activation and the ion deposition on the RIB (Radioactive Ion Beam) line of the Front-End system have been assessed at different times during the life cycle of the facility, predicting the level of radiological hazard in different areas surrounding the SPES Front-End [84]. This allows strategies for the protection of personnel involved in the operations of ordinary and extraordinary maintenance and final dismantling to be defined and implemented. Inspection and maintenance operations on the main elements of the protonic and radioactive beam lines become, in fact, a fundamental aspect of the life cycle of the facility. Due to the hazardous environment where these operations will be performed, the design of the devices must be human engineered to promote safe, reliable and error-free maintenance performance. In fact, maintenance tasks that might appear quite reasonable and manageable under normal work circumstances or environments, may prove highly unwieldy and error-prone under less-than-optimal conditions. Performance degrading circumstances that can be encountered in the SPES bunker include:

- Low light conditions: no fixed lightening is foreseen inside the bunker;
- Stress condition associated with the hazardous environment;
- Clothing for protection against radioactive contamination such as a double pair of gloves;
- Respiratory protective equipment, usually including a full-face mask supplied with air or oxygen from compressed gas cylinders carried by the operator.

It follows that, in addition to the radiological risks, other hazards arise in the area. The personal protective equipment can create other problems and exacerbate hazards. For example, a worker's field of vision may be reduced while wearing respiratory protection; the gloves can reduce the operator's manual skills, while the gas cylinders can limit his movements. The stress condition to which the operator is subjected can lead to a drop of attention and concentration. Moreover, operators know that they need to minimize the time they stay in the SPES bunker, in order to minimize their exposure to radiations. Such conditions increase the worker's vulnerability to normal hazards and necessitate increased awareness and care [85]. The mechanical solutions adopted for the devices inside the SPES bunker should therefore require operations as simple as possible to minimize the time needed, to reduce the stress conditions of the operators and, consequently, the possibility of errors. For these reasons, a deep analysis of the actual beam line is carried out. First, a complete mapping of the elements installed inside the SPES bunker is performed. They are then summarized in a table, together with useful characteristics and information. The table aims to highlight critical maintenance operations related to safety aspects for the operator, in particular those aspects which can lead to an increase of the exposure time for him. Critical aspects of the current procedures are highlighted and possible human-centered redesign solutions are proposed. General design guidelines for maintainability are then proposed, to adapt the design of future lines since the early stage. This table will also represent a precious tool to plan maintenance interventions during operations and to monitor the state and the criticality of the mechanical solutions adopted inside the SPES bunker.

5.2 Radiological hazard inside the SPES bunker

For the SPES apparatus, 30-day operation cycles are foreseen: during the first 15 days the target is continually irradiated, in the following 15 days the proton beam is switched off. At the end of the 30-day long operation cycle, the TIS (Target Ion Source) unit is removed from the Front-End and replaced with a new one. Ten production cycles per year are foreseen in operation and longer shutdown periods are planned at least once per year. The radiation dose generated inside the SPES bunker is due to different contributions:

- The activation of the materials of the Front-End, caused by the protons of the primary beam and by the neutrons generated by fission in the target.
- The deposition of radioactive ions along the RIB line electromagnetic elements. In particular, the most critical components are those where the produced radioisotopes other than the selected ones stop: i.e., the ion extraction electrode and the "Wien Filter" (a velocity selector able to perform a first mass separation stage).

The assessment of the external exposure of personnel inside the bunker due to both these contributions has been already performed for different positions along the beam lines and for different times of cooling [84], by means of Monte Carlo simulations with the FLUKA code [22][23]. These data are a fundamental tool to properly plan inspection and maintenance work during the operation of the facility, in compliance with the Italian legal dose limits and within the agreements of the radiation protection recommendations. Following the ALARA principle, in fact, the exposure of personnel to ionizing radiation has to be kept “As Low As Reasonably Achievable”. The main methods for improving radiation protection are the increase of the distance from the source, the use of radiation shielding and the limitation of the exposure time [86]. When personnel must intervene for maintenance operations on the beam line components, keeping sufficient distance is quite often impossible. Some operations can be performed by robots or by manipulators operated by remote control, however the increased complexity and the high financial cost make this solution rarely feasible. Shielding is foreseen in some critical points of the line, such as the protonic beam line collimators. However, this leads to higher weights and, therefore, to a difficult handling of the components during maintenance operations. Given the difficulties to apply distance and shielding methods, the reduction of exposure time is often the most effective method to reduce the personal dose during maintenance operations.

5.3 Table contents

The reduction of exposure time during maintenance interventions can be achieved by well-trained personnel but also by adopting design solutions that simplify the procedures, reducing the possibility of human errors. With this in mind, the actual beam line is deeply analyzed, in order to highlight critical designs that can lead to an increase of the exposure time. A brief description of the main components installed inside the SPES bunker is reported in Sec. 1.4, while a comprehensive presentation of the devices is available in Appendix A. Six main **apparatus** are identified, as shown in Figure 5.1:

- The protonic diagnostic;
- The Front End;
- The first radioactive diagnostic;
- The Wien Filter;
- The second radioactive diagnostic;
- The triplet.

Each apparatus is divided into several **modules**: for each module, the components that can be individually replaced are highlighted. Each row of the table contains therefore an element (a component or a module) that can be replaced during a maintenance operation. A small representation of the first rows of the table is reported in Figure 5.2, while in Figure 5.3 the corresponding elements are shown.

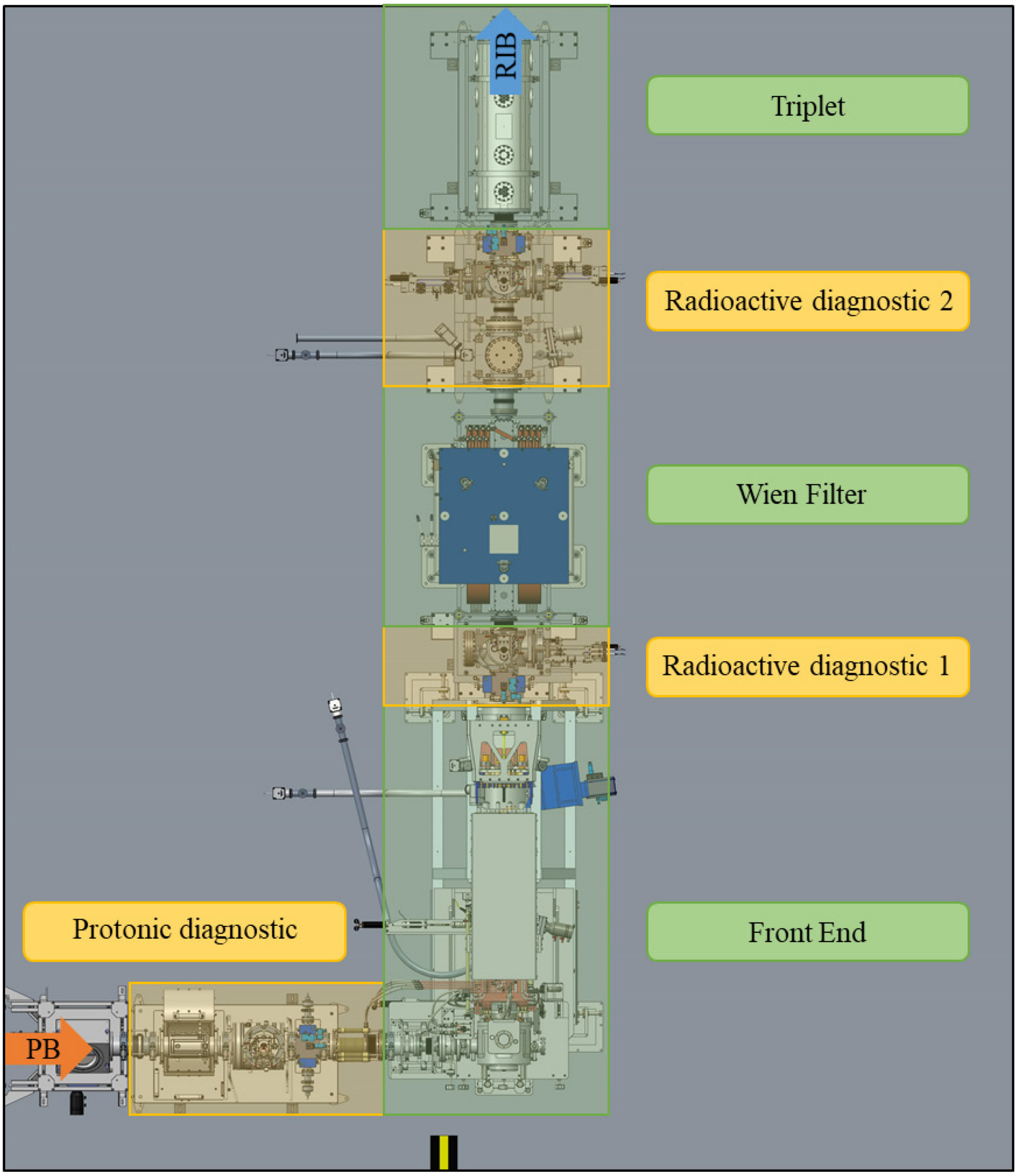

Figure 5.1. The six main apparatus identified in the SPES bunker beam line.

APPARATUS	MODULE	COMPONENT
Protonic diagnostic		
	Bellow	
	Collimators	
	Vertical diagnostic (up)	
		Limit switch (up)
		Limit switch (down)
		Potentiometer (left)
		Potentiometer (right)
		Pneumatic motor
	Vertical diagnostic (down)	
		Limit switch (up)
		Limit switch (down)
		Potentiometer (left)
		Potentiometer (right)
		Pneumatic motor
	Diagnostic cross	
	Gate valve ALL METAL in line	
		High vacuum Gauge
		High vacuum Gauge Fast Valve
	Protonic insulator	

Figure 5.2. An extract of the first rows of the table.

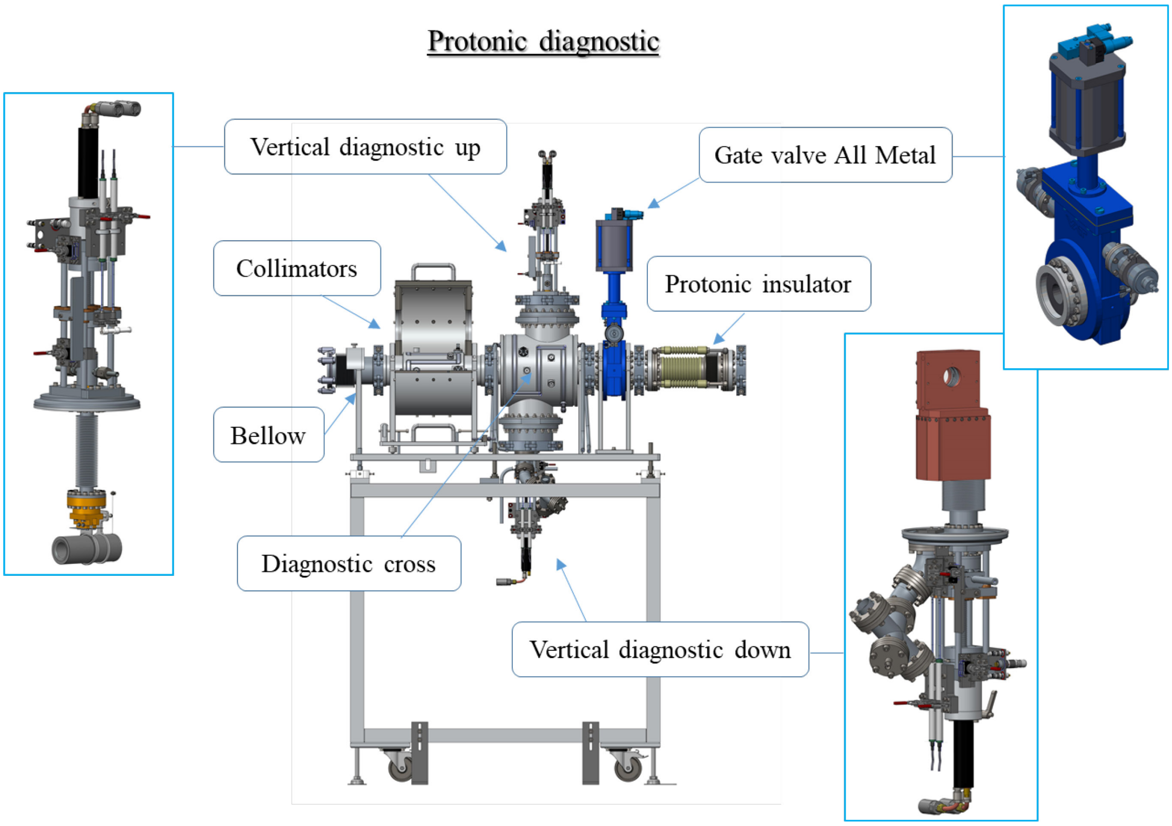

Figure 5.3 The ‘protonic diagnostic’ apparatus and its modules, as reported in Figure 5.2.

The columns of the table summarize the aspects that can influence the equivalent ambient dose absorbed by the operator, with a particular attention to those which may lead to an increase in the exposure time during maintenance.

Five main categories of columns have been identified:

1. *References*
2. *Component characteristics*
3. *Intervention features*
4. *Intervention criticalities*
5. *Final analysis*

In ***References*** the information related to the component's cataloguing are contained:

- Reference document: if available, the name of the document describing the component or the device is indicated.
- CAD model code: identification code of the 3D model of the component in the software CREO Parametrics [30]. This software is a 3D modelling computer code employed for the design of the beam line.
- Unique code: Identification code of a single component. If available, the code follows the nomenclature indicated in the official floor plan of the SPES building (Figure 5.3). For a greater level of details, an arbitrary nomenclature is added to the code to uniquely identify a component.
- Commercial code: In the case of commercial components, it indicates the identification code in the catalogue of the company.

This information will be useful for the training and preparation of the operator that will carry out the intervention, in the knowledge and recognition of the element to be replaced. In the Reference document the element is described in detail, with particular attention also to its integration and interfaces. With the code of the CAD model, the operator is able to visualize the module or component and to have a familiarization with it. The unique code allows for the precise individualization of the component to be substituted, even in the case of the redundant elements. The commercial code consents the operator to choose the right component to replace the faulty one. A small representation of the *References* columns is shown in Figure 5.5, for the first rows of the table.

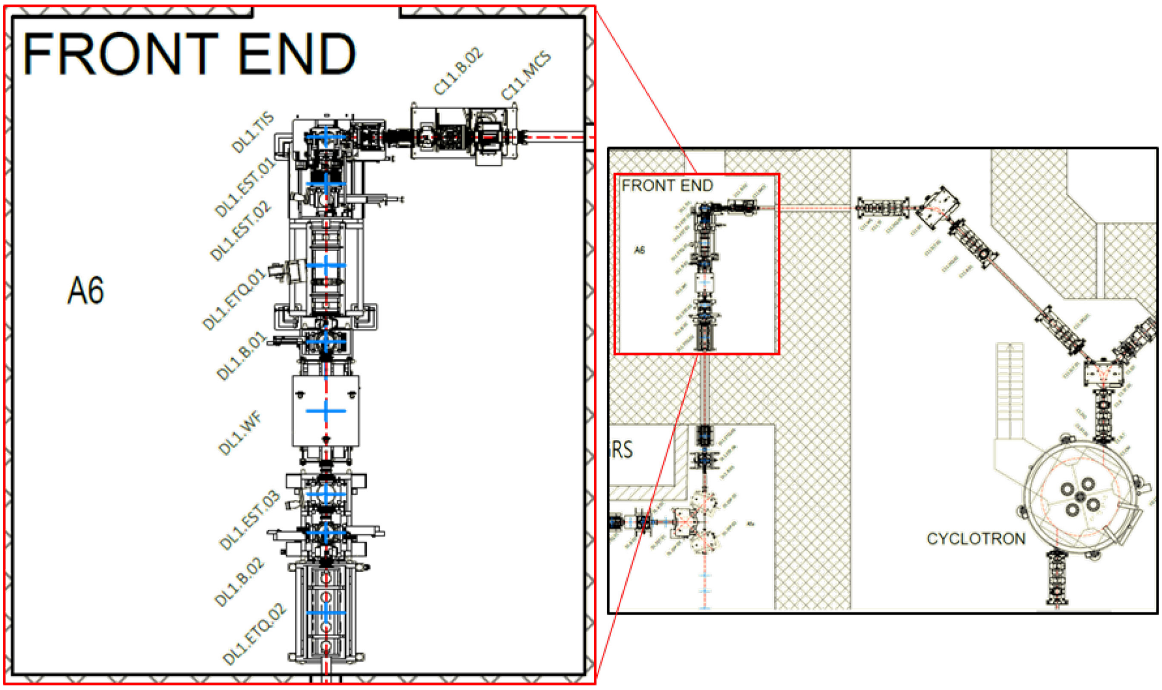

Figure 5.4 Floor plan of the cyclotron area and, in particular, of the SPES bunker.

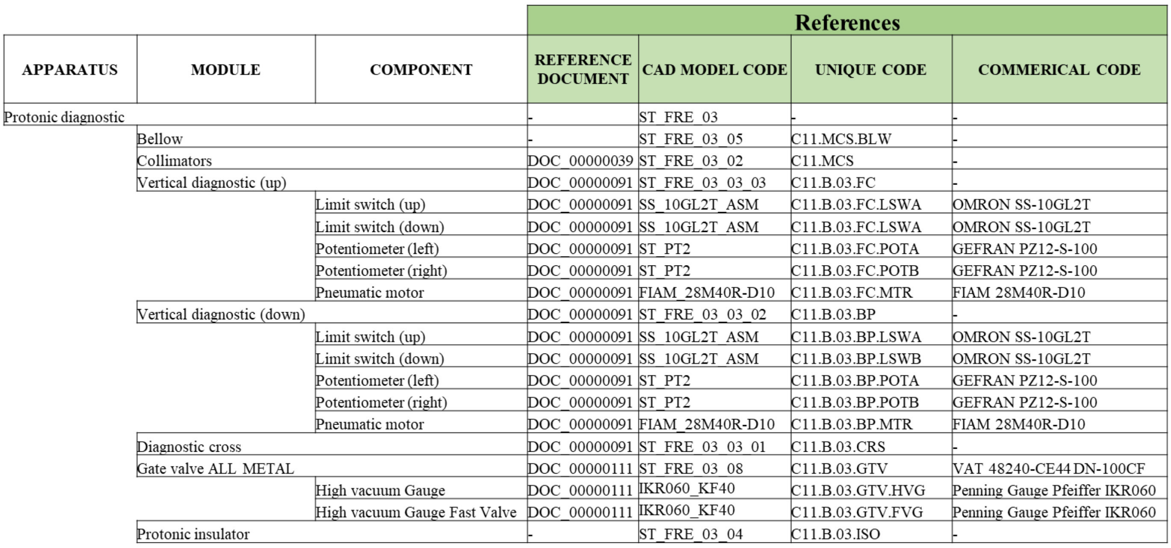

			References			
APPARATUS	**MODULE**	**COMPONENT**	**REFERENCE DOCUMENT**	**CAD MODEL CODE**	**UNIQUE CODE**	**COMMERICAL CODE**
Protonic diagnostic			-	ST_FRE_03	-	-
	Bellow		-	ST_FRE_03_05	C11.MCS.BLW	-
	Collimators		DOC_00000039	ST_FRE_03_02	C11.MCS	-
	Vertical diagnostic (up)		DOC_00000091	ST_FRE_03_03_03	C11.B.03.FC	-
		Limit switch (up)	DOC_00000091	SS_10GL2T_ASM	C11.B.03.FC.LSWA	OMRON SS-10GL2T
		Limit switch (down)	DOC_00000091	SS_10GL2T_ASM	C11.B.03.FC.LSWA	OMRON SS-10GL2T
		Potentiometer (left)	DOC_00000091	ST_PT2	C11.B.03.FC.POTA	GEFRAN PZ12-S-100
		Potentiometer (right)	DOC_00000091	ST_PT2	C11.B.03.FC.POTB	GEFRAN PZ12-S-100
		Pneumatic motor	DOC_00000091	FIAM_28M40R-D10	C11.B.03.FC.MTR	FIAM 28M40R-D10
	Vertical diagnostic (down)		DOC_00000091	ST_FRE_03_03_02	C11.B.03.BP	-
		Limit switch (up)	DOC_00000091	SS_10GL2T_ASM	C11.B.03.BP.LSWA	OMRON SS-10GL2T
		Limit switch (down)	DOC_00000091	SS_10GL2T_ASM	C11.B.03.BP.LSWB	OMRON SS-10GL2T
		Potentiometer (left)	DOC_00000091	ST_PT2	C11.B.03.BP.POTA	GEFRAN PZ12-S-100
		Potentiometer (right)	DOC_00000091	ST_PT2	C11.B.03.BP.POTB	GEFRAN PZ12-S-100
		Pneumatic motor	DOC_00000091	FIAM_28M40R-D10	C11.B.03.BP.MTR	FIAM 28M40R-D10
	Diagnostic cross		DOC_00000091	ST_FRE_03_03_01	C11.B.03.CRS	-
	Gate valve ALL_METAL		DOC_00000111	ST_FRE_03_08	C11.B.03.GTV	VAT 48240-CE44 DN-100CF
		High vacuum Gauge	DOC_00000111	IKR060_KF40	C11.B.03.GTV.HVG	Penning Gauge Pfeiffer IKR060
		High vacuum Gauge Fast Valve	DOC_00000111	IKR060_KF40	C11.B.03.GTV.FVG	Penning Gauge Pfeiffer IKR060
	Protonic insulator		-	ST_FRE_03_04	C11.B.03.ISO	-

Figure 5.5 An extract of the References columns, for the first rows of the table.

The ***Component characteristics*** contains the main properties of the component, which are useful to define the characteristics of the intervention:

- Electrical connections: Indicates whether there are (Y) or not (N) electrical connectors to be disconnected in order to carry out the replacement operation.
- Water circuit connections: Indicates whether the component / module is water cooled and, therefore, if there are (Y) or not (N) connectors for the cooling channel that the operator must disconnect in order to make the replacement.

- Compressed air connections: Indicates whether there are (Y) or not (N) compressed air connections (for valves or pneumatic motors), with connectors that the operator must disconnect in order to make the replacement.
- Relationship with other components: Indicates whether to replace the component / module it is also necessary to intervene on the adjacent elements (Y) or if the operation involves only the element subject to maintenance (N).
- Weight: Expresses the weight in kg of the component / module to be replaced.
- Height: Expresses the maximum height in cm that the operator's hands must reach in order to complete the replacement intervention.
- Installed in other positions: Indicates whether the same component is also present in other part of the beam line. This allows the replacement of similar components during the same maintenance operation to be considered.

Intervention features contains the information regarding the maintenance operation:

- Preventive maintenance frequency: Provides a rough indication of the expected lifetime of a component, before its replacement is necessary. This field will be gradually updated based on the experience gained during the operation of the system.
- Number of operators: Identifies the number of operators required to complete the maintenance operation.
- Level of training: In this stage, a qualitative classification of the required training level of the operator for the specific maintenance operation is provided. Training procedures are not yet defined for the operators of the SPES project: this first evaluation is based on the intuitiveness of the operation and on how much training the operator needs before being able to complete the replacement. More quantitative and objective evaluations will be done when a training plan is defined.
- Required tools: Provides a list of the necessary tools that the operator must bring with him in order to carry out the maintenance operation.
- Required time: Expresses the time required, in seconds, for the assembly or disassembly maintenance operation. If different, the operation that requires a longer time is considered. The data will be collected with practical tests to be carried out.
- Integrated dose: Based on the times calculated in the previous point, an indication of the equivalent dose absorbed (expressed in μSv) is provided. The equivalent ambient dose inside the SPES bunker has been already calculated with Monte Carlo simulations [84].

In ***Intervention criticalities*,** the aspects considered critical are summarized, as they are linked to a possible increase in the radiological risk for the operator in terms of the time required to complete the maintenance operation and therefore of the dose absorbed by the operator. The criticalities are divided into three main groups: ergonomics, complexity and radiological issues.

As ergonomics issues, the following aspects are considered:

- Internal position: It highlights whether, in order to carry out the maintenance operation, the operator must pass under the beam line to reach the internal part.
- Height: Highlights if the operation must be performed at a height greater than 150 cm or lower than 70 cm. Following the Italian legislation (D. Leg 81/08), it is preferable to handle load in the area between the height of the shoulders and the height of the knuckles.
- Weight: It highlights if the involved weight exceeds 3 kg. Following the Italian legislation (D. Leg 81/08), in fact, the manual handling of a load exceeding this value could lead to a potential physical damage.
- Handling of small components: Highlights whether during the maintenance the operator must work with small screws or elements

As complexity issues, the following aspects are considered:

- Component relationship: Indicates whether to replace the component / module it is also necessary to intervene on adjacent elements.
- Need for settings: Indicates if the maintenance operation does not end with the installation of the component / module but a subsequent setting is also required in order to make it operational.
- Involved resources: Indicates if the operator needs to bring different tools to complete the operation, or if more than one operator is required.

Regarding the radiological issue, a reasonable dose constraint for one single intervention must be defined. This choice is based on the annual dose limits established for radiation exposed workers by the Italian legislation (D. Leg. 101/20) [87], equal to 20 mSv/year, and on the more restrictive limits set by the LNL-INFN radiation protection service, equal to 5 mSv/year [88]. A dose of 200 μSv for a single maintenance operation has been assumed as a reasonable limit. However, this indication should not be considered as a radiation protection assessment but only to highlight a possible criticality related to the dose that the operator could absorb during that specific maintenance operation. In the table this aspect is taken into account as follows:

- Radiological risk: Indicates if an expected equivalent dose higher than 200 μSv is foreseen, based on the requested time of the intervention.

The ***Final analysis*** provides a summary assessment of the current design solution, based on the critical issues highlighted above. Three different levels are identified: critical, improvable and good. A replacement is defined as critical if one of the following conditions is met:

- It involves both ergonomics, complexity and radiological issues;
- It involves the radiological risk and at least one other issue.
- It involves more than one ergonomic issue, in addition to at least one complexity issue;
- It involves more than one complexity issue, in addition to at least one ergonomic issue;
- It involves more than two ergonomic issues;
- It involves more than two complexity issues;

An operation is defined as improvable if one of the following conditions is met:

- It involves only the radiological risk;
- It involves only one ergonomic issue in addition to one complexity issue;
- It involves only two ergonomic issues;
- It involves only two complexity issues.

Finally, the current solution is considered good if one of the following conditions is met:

- It involves only one ergonomic issue but no complexity or radiological issues;
- It involves only one complexity issue but no ergonomic or radiological issues;
- It does not involve any issue.

The complete table can be consulted at the following link:
http://www4.lnl.infn.it/~spes_target/index.php/download/spes-bunker-maintenance/

5.4 Table analysis and discussion

This table represents an important tool for several reasons: it can be useful to plan and monitor the maintenance interventions during the operation of the facility (as will be better explained in Sec.5.6), but it can also help to highlight critical elements that can be modified before starting operations. If significant modifications are required, they can be foreseen for the design of the future SPES-2 line.

By highlighting the interventions classified as critical or improvable in the table, it emerges that many criticalities are related to few components, repeated in different positions of the line. For example, the potentiometers are installed in many points of the line, as shown in the extract of the table reported in Figure 5.6. These position transducers are in fact used in both the protonic and the radioactive diagnostics and also in all the Front-End handling systems. The maintenance of these elements is made difficult since small screws must be handled and different tools are needed, namely a hexagonal key and a spanner. By simply modifying the fixing system of this component, it is possible to eliminate this criticality in many points of the line, reducing the complexity of the operation and consequently, the possibility of errors.

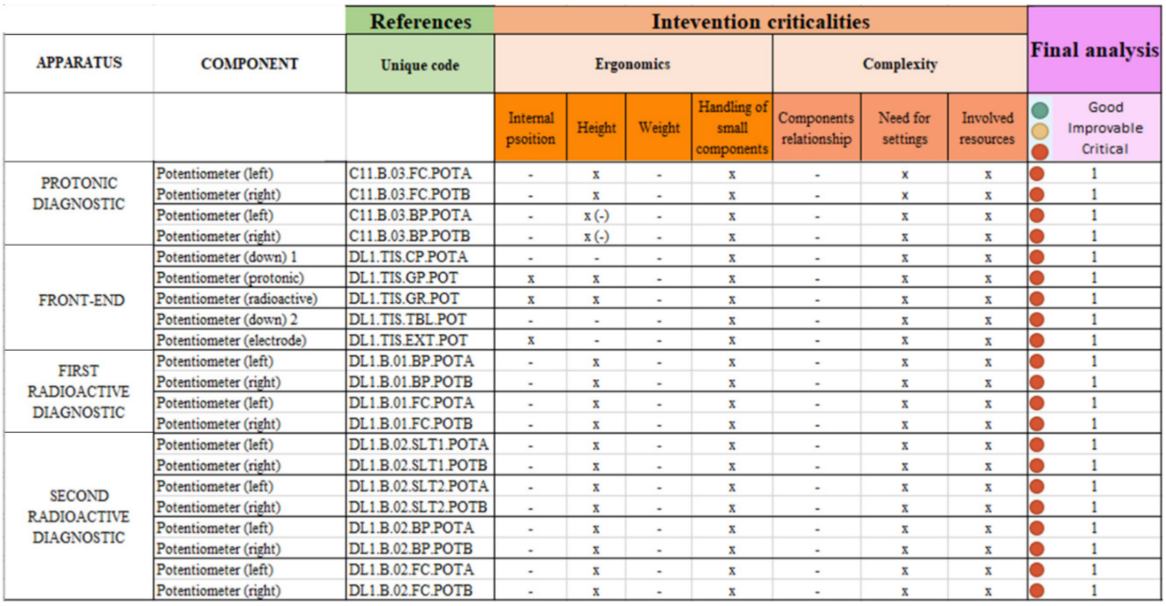

		References	Intevention criticalities							Final analysis	
APPARATUS	COMPONENT	Unique code	Ergonomics				Complexity				
			Internal psoition	Height	Weight	Handling of small components	Components relationship	Need for settings	Involved resources	🟢 🟡 🔴	Good Improvable Critical
PROTONIC DIAGNOSTIC	Potentiometer (left)	C11.B.03.FC.POTA	-	x	-	x	-	x	x	🔴	1
	Potentiometer (right)	C11.B.03.FC.POTB	-	x	-	x	-	x	x	🔴	1
	Potentiometer (left)	C11.B.03.BP.POTA	-	x (-)	-	x	-	x	x	🔴	1
	Potentiometer (right)	C11.B.03.BP.POTB	-	x (-)	-	x	-	x	x	🔴	1
FRONT-END	Potentiometer (down) 1	DL1.TIS.CP.POTA	-	-	-	x	-	x	x	🔴	1
	Potentiometer (protonic)	DL1.TIS.GP.POT	x	x	-	x	-	x	x	🔴	1
	Potentiometer (radioactive)	DL1.TIS.GR.POT	x	x	-	x	-	x	x	🔴	1
	Potentiometer (down) 2	DL1.TIS.TBL.POT	-	-	-	x	-	x	x	🔴	1
	Potentiometer (electrode)	DL1.TIS.EXT.POT	x	-	-	x	-	x	x	🔴	1
FIRST RADIOACTIVE DIAGNOSTIC	Potentiometer (left)	DL1.B.01.BP.POTA	-	x	-	x	-	x	x	🔴	1
	Potentiometer (right)	DL1.B.01.BP.POTB	-	x	-	x	-	x	x	🔴	1
	Potentiometer (left)	DL1.B.01.FC.POTA	-	x	-	x	-	x	x	🔴	1
	Potentiometer (right)	DL1.B.01.FC.POTB	-	x	-	x	-	x	x	🔴	1
SECOND RADIOACTIVE DIAGNOSTIC	Potentiometer (left)	DL1.B.02.SLT1.POTA	-	x	-	x	-	x	x	🔴	1
	Potentiometer (right)	DL1.B.02.SLT1.POTB	-	x	-	x	-	x	x	🔴	1
	Potentiometer (left)	DL1.B.02.SLT2.POTA	-	x	-	x	-	x	x	🔴	1
	Potentiometer (right)	DL1.B.02.SLT2.POTB	-	x	-	x	-	x	x	🔴	1
	Potentiometer (left)	DL1.B.02.BP.POTA	-	x	-	x	-	x	x	🔴	1
	Potentiometer (right)	DL1.B.02.BP.POTB	-	x	-	x	-	x	x	🔴	1
	Potentiometer (left)	DL1.B.02.FC.POTA	-	x	-	x	-	x	x	🔴	1
	Potentiometer (right)	DL1.B.02.FC.POTB	-	x	-	x	-	x	x	🔴	1

Figure 5.6 An extract of the table highlighting all the potentiometers inside the SPES bunker.

Another critical element is represented by the protonic and the radioactive diagnostics, presented in Figure 5.7. These devices are heavy and usually two operators are required to complete the replacement correctly. One operator has in fact to sustain the weight while the other can take care of fixing. The introduction of a support to unload the weight can avoid the need of a second operator and can simplify the procedure, reducing the exposure time.

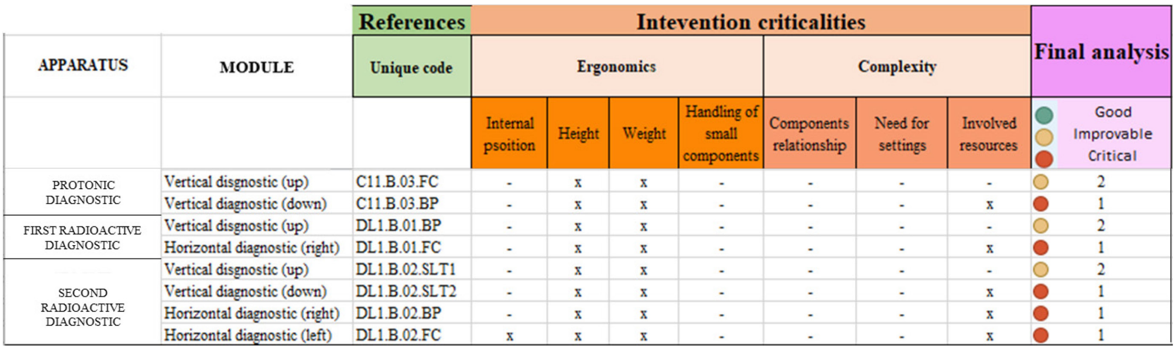

		References	Intevention criticalities							Final analysis	
APPARATUS	MODULE	Unique code	Ergonomics				Complexity				
			Internal psoition	Height	Weight	Handling of small components	Components relationship	Need for settings	Involved resources	🟢 🟡 🔴	Good Improvable Critical
PROTONIC DIAGNOSTIC	Vertical disgnostic (up)	C11.B.03.FC	-	x	x	-	-	-	-	🟡	2
	Vertical diagnostic (down)	C11.B.03.BP	-	x	x	-	-	-	x	🔴	1
FIRST RADIOACTIVE DIAGNOSTIC	Vertical disgnostic (up)	DL1.B.01.BP	-	x	x	-	-	-	-	🟡	2
	Horizontal diagnostic (right)	DL1.B.01.FC	-	x	x	-	-	-	x	🔴	1
SECOND RADIOACTIVE DIAGNOSTIC	Vertical disgnostic (up)	DL1.B.02.SLT1	-	x	x	-	-	-	-	🟡	2
	Vertical diagnostic (down)	DL1.B.02.SLT2	-	x	x	-	-	-	x	🔴	1
	Horizontal diagnostic (right)	DL1.B.02.BP	-	x	x	-	-	-	x	🔴	1
	Horizontal diagnostic (left)	DL1.B.02.FC	x	x	x	-	-	-	x	🔴	1

Figure 5.7 An extract of the table highlighting the protonic and radioactive diagnostics.

The collimator of the protonic line also represents a criticality, in particular for the radiological risk. This device, presented in Sec. 3.2, shapes the beam by absorbing a high percentage of protons in the beam external halo. High activation levels and radiation doses are therefore expected, imposing the positioning of a lead shielding. This increases considerably the weight of the component, which complicates the maintenance operation. The use of a cart able of lifting and transporting the collimator permits, at the same time, to unload the operator and to keep him at a safer distance.

Some of these suggestions will be better developed in the next sections, however it is already clear that the table represents a strong tool for highlighting the criticalities of the beam line. This allows the designers of the SPES group to focus on precise interventions to be carried out before the facility begins operations.

5.5 Maintainability guidelines

Tasks that in normal conditions might appear manageable, can become complex in particular environments as the SPES bunker, characterized by low light conditions, stress associated to the radiological hazard and the cumbersome protective equipment foreseen for the operators. It is therefore important to verify that some general maintainability guidelines are being met. These rules, described below, aim to help the designers to identify possible improvements on the current solutions:

- The operation should be simplified as much as possible: a simple procedure is less prone to errors. Operator stress would be reduced, improving his performance in a performance-degrading environment such as the SPES bunker. Moreover, a simple procedure requires less training, and this allows operators to be quickly trained to complete the maintenance.
- The number of required movements should be reduced, and single-handed operations should be preferred, in order to keep the second hand as support in case of necessity.
- The need of tools should be avoided: if one or more tools are required, they can be a source of troubles. For example, the wrong tool could be taken, or it could hinder the operator’s manual skills during the operation.
- Small screws and nuts should be avoided: during the maintenance, the operator will wear two pairs of gloves in order to avoid contamination. Therefore, his manual skills will be extremely reduced, and the handling of small components could become critical.
- Carts and lifters should be used to manage both the critical weights and heights. In order to reduce the absorbed dose, the operator should stay as far as possible from the component to be replaced. However, if the involved weight is high, the operator will tend to keep the component close to his body. The use of a cart/lifter would unload the worker and would also allow the right distance to be maintained.

- A portable illumination should be foreseen, to allow the operator to properly see the working space, to perform faster maintenances and to avoid accidental hits against obstacles.

Some of these principles are applied in Sec. 5.5.1 to a re-design case study of the current beam line, regarding the fixing system of the potentiometers. However, if a drastic change of the design is required, it is not possible to revolutionize the current beam line, already in advanced installation phase inside the SPES bunker. In view of the new 70 MeV beam line (SPES-2), it is in any case possible to fix some helpful concepts that can be already applied from the conceptual design phase:

- All the maintainable components should be reachable without passing under the line. This is in fact a high-risk operation that should be avoided at any cost. At the same time, cable channels and wirings can be foreseen in the internal part of the beam line, where the operator is not required to access.
- The frames supporting the devices should be unified at the same height and with the same mechanical interface to be coupled with a standard cart or lifter.

5.5.1 Case study: the potentiometer replacement [89]

Description of the current solution: The potentiometers are mounted in several positions inside the SPES bunker. The maintenance of these components is complicated by the handling of small screws and nuts which also requires the use of different tools. The existing holding system, shown in Figure 5.8, is based on a screw clamping ring which holds the body, and a hold on the sliding carriage of the threaded head of the potentiometer's shaft. To assemble the potentiometer, the operator has to align the body to the clamping ring, make it slide through the holding and keep it in position with one hand while the other tightens the screws using a key. The next step is to align the shaft's head to the positioning hole, slide through it and fix it with an M3 nut, tightened with a key.

Criticalities identification: To mount the potentiometer, a sequence of operations is required, two different keys are needed, the nut is hard to handle with two gloves and, also, the aligning and sliding operations are not easy due to the position of potentiometers. The stress condition to which the operator is subjected can worsen his manual skills and increase the exposure time. All these factors can lead to a lack of accuracy in the alignment or to the fall of components or tools during the intervention.

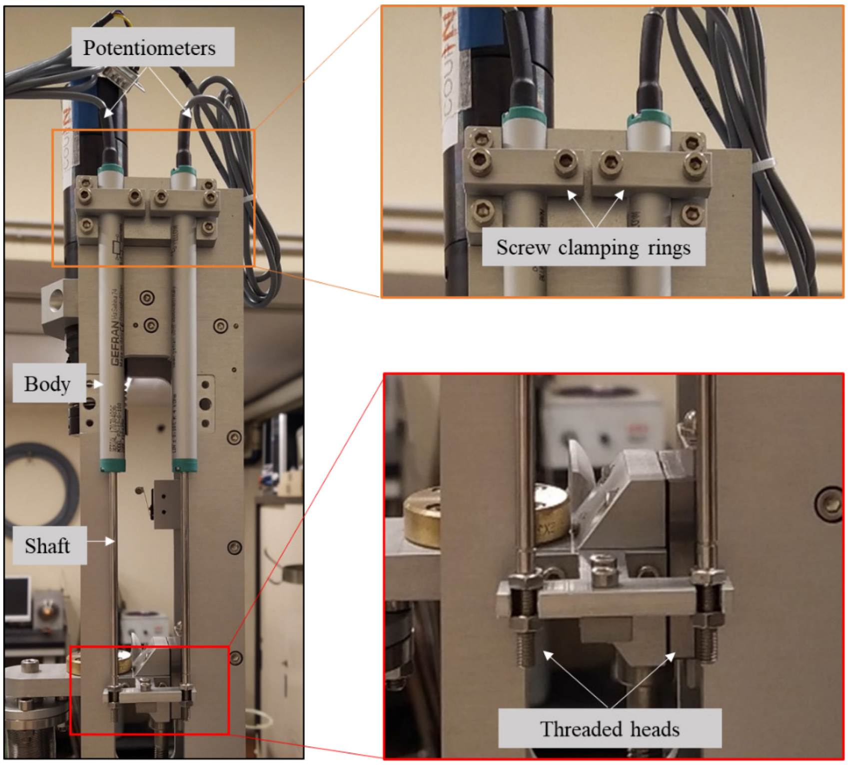

Figure 5.8 The existing holding system for the potentiometers of the SPES bunker.

Guidelines application and new solution proposal: Following the concepts presented in the previous section, no tools will be foreseen in the new solution and the operator's tasks are simplified as much as possible. In particular, screw and nut locks are substituted by spring-based locks and commercial latch clamps. Moreover, the holding system is divided into several parts, each of which guides the operator's movements and blocks one degree of freedom. The proposed solution is shown in Figure 5.9. First, before maintenance operation, a couple of discs held together by a spring is screwed on the threaded head of the potentiometer's shaft. Then, a screw clamping ring is mounted on the potentiometer body. This part will provide exact aligning avoiding operator errors and will also block the longitudinal degree of freedom. It is important to remark that both these operations are carried out before entering the SPES bunker, in the absence of stress conditions. The tasks to be performed inside the bunker are therefore significantly reduced, decreasing the operator exposure time. The only tasks foreseen in the hazardous environment is a preliminary alignment of the potentiometer and then push it on the holding system to reach the correct alignment. The component is then blocked through a commercial clamp.

Comparison between the old and the new solution: The new solution is tools-free and allow the operator to manage the potentiometer with two hands and mount it with only two movements (positioning and blocking). The simplicity of the required tasks leads also to an ease of learning, allowing a fast training. Moreover, part of the tasks can be performed outside the bunker, reducing the operator exposure time. Operative tests have been carried out with the old and the new solution. Time trials have been performed, to quantify the improvement obtained with the redesign. It is important to remark that during the tests the operator did not wear the clothing for protection against contamination, including the two pairs of gloves, and the respiratory protective equipment. Moreover, the operation has been carried out in normal light conditions. However, also in these less critical conditions, a significant impact of the new solution has been observed. In fact, the time required for the mounting operation, around 55 seconds with the old design, has been reduced to 13 seconds with the new solution.

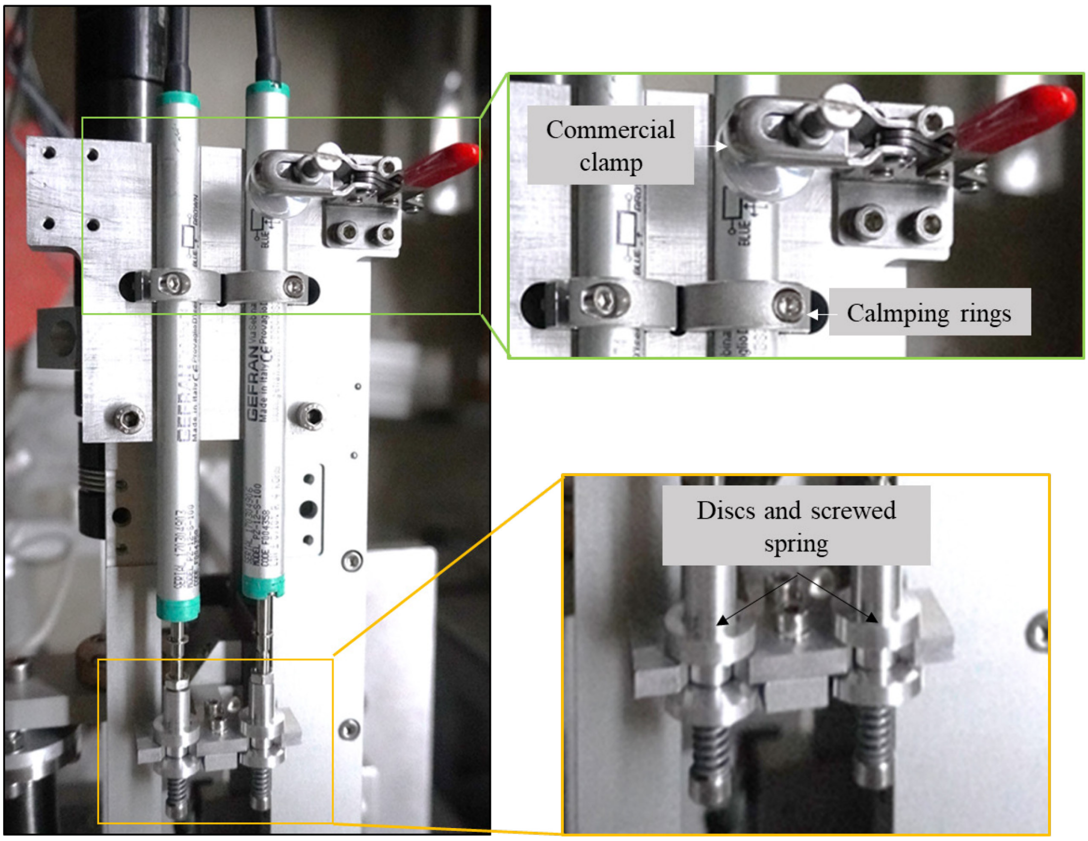

Figure 5.9 The new solution proposed for the holding system of the potentiometers of the SPES bunker.

5.6 Future applications

The table presented in Sec. 5.3 has been used to highlight critical elements of the line, from a maintenance point of view. It allows in fact the specific criticalities of the component to be identified, in order to guide the designer into the re-design phase. However, the table will represent an important tool also during operation, collecting and providing important information about the maintenance operations. For example, it is possible to isolate a specific type of component in order to highlight all the positions where it is installed. This could be helpful to check if the same component presents different substitution frequencies by varying the position in the line where it is installed, due to a different radiation damage. The potentiometers, for example, can be found both in the protonic beam line and in the radioactive beam line diagnostics. A preventive substitution every two years is initially foreseen for this type of component but, once in operations, frequencies can be updated depending on the gained experience.

Moreover, if maintenance instructions are attached to each component, the table could become an important instrument for the training of the operators. The worker could in fact find all the necessary information about the substitution to be performed, becoming familiar with the component, and receiving the instructions necessary to complete the operation. The table could also collect the operator’s feedback, leading to a systematic and iterative optimizing process of the procedure.

CONCLUSIONS

This thesis is inserted in the framework of the SPES project, currently in an advanced construction phase at the National Laboratories of Legnaro. The work aims at the analysis and the revision of the present structure of the Front-End subsystem, of the components and of the used materials, in view of a planned upgrade of the proton beam energy up to 70 MeV. In particular, the study of a new target – ion source unit and of some important devices of the proton beam line is presented. Moreover, high temperature experimental tests performed on graphite are reported, being this material chosen for the design of all the devices. Finally, critical aspects related to maintenance operations are highlighted, in order to guide the designer into the re-design phase.

After a brief overview of the SPES project and its scientific aim and context, summarized in Chapter 1, the revision design of two main components of the Target-Ion Source Unit has been presented in Chapter 2. In particular, the study and the experimental tests of a new 70 MeV target and collimator assembly have been described and discussed in detail. First, a Uranium Carbide low-power target has been designed by means of thermal-structural simulations. 17 discs of 13 mm diameter and 1 mm thickness have been equally spaced inside a graphite box, housed in a tantalum heater heated by Joule effect with 900 W dissipated power. The proper beam properties have been also investigated, setting an RMS radius equal to 4 mm and a maximum beam current on the target of 7.5 μA. Then, a new collimator housed inside the target chamber has been designed, taking into account its influence on the target's temperatures and stresses. An exit diameter of 16 mm has been set, to avoid the beam scattering on the surfaces surrounding the target assembly but, simultaneously, to allow for a proper power deposition on the target also in case of misalignments. The thermal-electrical behavior of the whole assembly was then studied by means of a FE model and validated with experimental tests performed at the National Laboratories of Legnaro. The comparison between the experimental data and the FE models was in general satisfactory, confirming the reliability of the numerical model.

In Chapter 3, the upgrade of three important devices of the proton beam line has been presented. In particular, the design of the Collimators, the Faraday Cup and the Target Window for a 70 MeV beam energy has been developed. These devices, used to monitor the beam characteristics, are essential for a correct functioning and setting of the facility. The design process has been conducted by means of thermal-structural FE models and Monte Carlo simulations of the interaction of particles with matter. First, a modular graphite collimator has been designed, able to work with both 40 MeV and 70 MeV beam energies when a total power of 2000 W is deposited on it. The proper inner radius and distance from the target have been set to obtain a uniform power distribution on the target discs.

A graphite Faraday Cup has been then designed, able to intercept a 70 MeV proton beam for a maximum deposited power of 7000 W. Thermal-structural simulations have been implemented in order to validate the proposed mechanical design. Finally, a Target Window has been designed, able to work with both 40 MeV and 70 MeV beam energy. This thin disc, placed at the entrance of the target chamber, accomplishes the task of separating the vacuum between the target chamber and the proton beam line, avoiding contamination problems in case of vacuum loss. By means of analytical models and thermal-structural simulations, a thickness of 1.4 mm has been set for the Target Window.

High temperature experimental tests on graphite are presented in Chapter 4. This material, widely used in industrial applications thanks to its excellent high temperature resistance, is also used for the design of several devices of the SPES project, like those presented in the previous Chapter. It is therefore important to know the mechanical resistance of this material at high temperature. Uniaxial compressive tests have been first performed, in order to obtain the stress-strain curve at room temperature. The results showed a plastic deformation in compression for this type of graphite. In order to evaluate the biaxial resistance, hourglass-shaped specimens, characterized by different hourglass radius, have been tested in compression both at room temperature and at 2000°C. The validity of Von Mises criterion at room temperature has been verified by means of elastic-plastic simulations, imposing the failure loads registered during the tests. At 2000°C, an increase in strength has been registered for this material, with an average increase of 24.5% over the room temperature value.

Finally, in Chapter 5, a mapping of the elements installed inside the SPES bunker has been performed. They have been summarized in a table, together with useful characteristics and information. The table aims to highlight critical maintenance operations related to safety aspects for the operator, in particular those aspects which can lead to an increase of the exposure time for him. Critical aspects of the current procedures have been highlighted and possible human-centered redesign solutions have been proposed. General design guidelines for maintainability were then proposed, to adapt the design of future lines since the early stage. This table will also represent a precious tool to plan maintenance interventions during operations and to monitor the state and the criticality of the mechanical solutions adopted inside the SPES bunker.

REFERENCES

[1] A. Gottberg, “Target materials for exotic ISOL beams,” *Nucl. Instruments Methods Phys. Res. Sect. B Beam Interact. with Mater. Atoms*, vol. 376, pp. 8–15, Jun. 2016, doi: 10.1016/J.NIMB.2016.01.020.

[2] J. Dilling, R. Krücken, and L. Merminga, “ISAC and ARIEL: The TRIUMF radioactive beam facilities and the scientific program,” *ISAC ARIEL TRIUMF Radioact. Beam Facil. Sci. Progr.*, pp. 1–284, Jan. 2014, doi: 10.1007/978-94-007-7963-1.

[3] D. Pietro, K. Riisager, V. Duppen, A. Herlert, and Y. Kadi, “The HIE-ISOLDE Project,” *J. Phys. Conf. Ser.*, vol. 312, no. 5, p. 052010, Sep. 2011, doi: 10.1088/1742-6596/312/5/052010.

[4] T. Junquera, “THE SPIRAL 2 PROJECT: CONSTRUCTION PROGRESS AND RECENT DEVELOPMENTS ON THE SC LINAC DRIVER,” 2007.

[5] H. J. Woo *et al.*, “Overview of the ISOL facility for the RISP,” *J. Korean Phys. Soc. 2015 663*, vol. 66, no. 3, pp. 443–448, Feb. 2015, doi: 10.3938/JKPS.66.443.

[6] A. Andrighetto *et al.*, “Spes: An intense source of Neutron-Rich Radioactive Beams at Legnaro,” *J. Phys. Conf. Ser.*, vol. 966, no. 1, 2018, doi: 10.1088/1742-6596/966/1/012028.

[7] A. Andrighetto *et al.*, “The ISOLPHARM project: A New ISOL production method of high specific activity beta-emitting radionuclides as radiopharmaceutical precursors,” *Int. J. Mod. Phys. Conf. Ser.*, vol. 48, p. 1860103, Jan. 2018, doi: 10.1142/S2010194518601035.

[8] A. Monetti, “Design and development of the target-ion source system for the SPES project,” University of Padua, Padua, 2017.

[9] M. Manzolaro, F. D’agostini, A. Monetti, and A. Andrighetto, “The SPES surface ionization source; The SPES surface ionization source,” 2017, doi: 10.1063/1.4998246.

[10] M. Manzolaro *et al.*, “Ongoing characterization of the forced electron beam induced arc discharge ion source for the selective production of exotic species facilitya),” *Rev. Sci. Instrum.*, vol. 85, no. 2, p. 02B918, Jan. 2014, doi: 10.1063/1.4857175.

[11] D. Scarpa *et al.*, “Studies for aluminum photoionization in hot cavity for the selective production of exotic species projecta),” *Rev. Sci. Instrum.*, vol. 83, no. 2, p. 02B317, Feb. 2012, doi: 10.1063/1.3673628.

[12] International Atomic Energy Agency, "Cyclotron Produced Radionuclides: Principles and Practice," *IAEA Tech. Rep.*, no. 465, p. 230, 2008, doi: 10.1016/j.jenvrad.2011.12.004.

[13] M. Nastasi and J. W. Mayer, "Ion Range and Range Distribution," *Ion Implant. Synth. Mater.*, pp. 63–76, 2006, doi: 10.1007/978-3-540-45298-0_6.

[14] P. Van Duppen, "Isotope Separation On Line and Post Acceleration," *Lect. Notes Phys.*, vol. 700, pp. 37–77, 2006, doi: 10.1007/3-540-33787-3_2.

[15] L. Biasetto *et al.*, "Developing uranium dicarbide–graphite porous materials for the SPES project," *J. Nucl. Mater.*, vol. 404, no. 1, pp. 68–76, Sep. 2010, doi: 10.1016/J.JNUCMAT.2010.06.032.

[16] A. Monetti *et al.*, "The RIB production target for the SPES project," *Eur. Phys. J. A*, vol. 51, no. 10, 2015, doi: 10.1140/epja/i2015-15128-6.

[17] S. Corradetti *et al.*, "The SPES target production and characterization," *Nucl. Instruments Methods Phys. Res. Sect. B Beam Interact. with Mater. Atoms*, vol. 488, pp. 12–22, Feb. 2021, doi: 10.1016/J.NIMB.2020.12.003.

[18] M. Manzolaro, "Study, design and test of the Target - Ion Source system for the INFN SPES facility," University of Padua, Padua, 2011.

[19] A. Monetti *et al.*, "The RIB production target for the SPES project," *Eur. Phys. J. A*, vol. 51, no. 10, 2015, doi: 10.1140/epja/i2015-15128-6.

[20] "ENDF: Evaluated Nuclear Data File." [Online]. Available: https://www-nds.iaea.org/exfor/endf.htm. [Accessed: 01-Oct-2021].

[21] V. V. Zerkin and B. Pritychenko, "The experimental nuclear reaction data (EXFOR): Extended computer database and Web retrieval system," *Nucl. Instruments Methods Phys. Res. Sect. A Accel. Spectrometers, Detect. Assoc. Equip.*, vol. 888, pp. 31–43, Apr. 2018, doi: 10.1016/J.NIMA.2018.01.045.

[22] A. Ferrari, P. R. Sala, A. Fasso, and J. Ranft, "FLUKA: A Multi-Particle Transport Code," no. January, 2005, doi: 10.2172/877507.

[23] T. T. Böhlen *et al.*, "The FLUKA Code: Developments and Challenges for High Energy and Medical Applications," *Nucl. Data Sheets*, vol. 120, pp. 211–214, Jun. 2014, doi: 10.1016/J.NDS.2014.07.049.

[24] K. Tshoo *et al.*, "Design study of 10 kW direct fission target for RISP project," *EPJ Web Conf.*, vol. 66, p. 11016, 2014, doi: 10.1051/EPJCONF/20146611016.

[25] S. Corradetti, "Study and development of high release refractory materials for the SPES

project," University of Padua, Padua, 2013.

[26] J. F. Ziegler, M. D. Ziegler, and J. P. Biersack, "SRIM – The stopping and range of ions in matter (2010)," *Nucl. Instruments Methods Phys. Res. Sect. B Beam Interact. with Mater. Atoms*, vol. 268, no. 11–12, pp. 1818–1823, Jun. 2010, doi: 10.1016/J.NIMB.2010.02.091.

[27] "ANSYS® Academic Research Mechanical, Release 18.2." .

[28] "Ansys® Academic Research Mechanical, Release 18.1, Help System, Command reference, ANSYS, Inc." .

[29] M. Manzolaro, "Study, design and test of the Target - Ion Source system for the INFN SPES facility," Jan. 2011.

[30] "Software di modellazione 3D Creo Parametric | PTC." [Online]. Available: https://www.ptc.com/it/products/creo/parametric. [Accessed: 11-Dec-2021].

[31] "Hexoloy SA | Alpha Silicon Carbide." [Online]. Available: https://www.ceramicsrefractories.saint-gobain.com/materials/silicon-carbide-sic/hexoloy-silicon-carbide-material/hexoloy-sa-sic-material. [Accessed: 14-Oct-2021].

[32] M. Barbui *et al.*, "Calculations and first results obtained with a SiC prototype of the SPES direct target," *Nucl. Instruments Methods Phys. Res. Sect. B Beam Interact. with Mater. Atoms*, vol. 266, no. 19–20, pp. 4289–4293, 2008, doi: 10.1016/j.nimb.2008.05.049.

[33] M. Manzolaro, S. Corradetti, A. Andrighetto, and L. Ferrari, "A steady-state high-temperature method for measuring thermal conductivity of refractory materials," *Rev. Sci. Instrum.*, vol. 84, no. 5, 2013, doi: 10.1063/1.4804258.

[34] ASTM C695-15, "Standard Test Method for Compressive Strength of Carbon and Graphite," *ASTM B. Stand.*, pp. 1–3, 2015.

[35] D. M. Jamba, "Secondary particle collection in ion implantation dose measurement," *Rev. Sci. Instrum.*, vol. 49, no. 5, pp. 634–638, 1978, doi: 10.1063/1.1135473.

[36] N. V Mokhov, "HIGH-INTENSITY BEAM COLLIMATION AND TARGETRY *."

[37] S. Rathinasabapathy, M. S. Santhosh, and M. Asokan, "Significance of Boron Nitride in Composites and Its Applications," *Recent Adv. Boron-Containing Mater.*, Apr. 2020, doi: 10.5772/INTECHOPEN.81557.

[38] L. Centofante, "Progettazione meccanica, simulazione e test sperimentali dell'integratore di corrente per le prove di accettazione del bersaglio SPES," Università degli Studi di Padova, 2018.

[39] E. Serena, "Progettazione meccanica, simulazione e test sperimentali dei collimatori destinati

alla linea protonica del progetto SPES," Università degli Studi di Padova, 2019.

[40] M. YOVANOVICH, "Thermal contact correlations," in *16th Thermophysics Cofnerence*, 1981, doi: 10.2514/6.1981-1164.

[41] "POCO EDM Graphite Selection Guide."

[42] L. Centofante, A. Monetti, and G. Meneghetti, "High Temperature Compression Tests of A Commercial Isotropic Ultrafine Grain Graphite," *Adv. Mater. Sci. Technol.*, vol. 2, no. 1, pp. 45–49, 2020.

[43] "CuETP." [Online]. Available: http://www.conductivity-app.org/alloy-sheet/33. [Accessed: 19-Oct-2021].

[44] "MATLAB R2019a." The MathWorks Inc., Natick, Massachusetts, 2018.

[45] POCO Graphite, "Properties and characteristics of graphite," 2015.

[46] "Shapal^{TM} Hi-M Analysis - Ceramics - Research Materials - Goodfellow." [Online]. Available: https://www.goodfellow.com/de/en-gb/information/larger-quantities/512/527/ceramics/shapal-hi-m-soft-analysis. [Accessed: 30-Nov-2021].

[47] L. Antoniazzi, "Progettazione meccanica dell'integratore di corrente destinato alla linea protonica del progetto SPES," Università degli Studi di Padova, 2021.

[48] P. T. Summers *et al.*, "Overview of aluminum alloy mechanical properties during and after fires," *Fire Sci. Rev. 2015 41*, vol. 4, no. 1, pp. 1–36, Apr. 2015, doi: 10.1186/S40038-015-0007-5.

[49] G. P. Škoro, J. R. J. Bennett, T. R. Edgecock, and C. N. Booth, "Yield strength of molybdenum, tantalum and tungsten at high strain rates and very high temperatures," *J. Nucl. Mater.*, vol. 426, no. 1–3, pp. 45–51, Jul. 2012, doi: 10.1016/J.JNUCMAT.2012.03.044.

[50] "Matweb." [Online]. Available: http://www.matweb.com/.

[51] L. Centofante, A. Monetti, and G. Meneghetti, "High temperature biaxial compressive strength of a commercial isotropic ultrafine grain graphite," *IOP Conf. Ser. Mater. Sci. Eng.*, vol. 1038, no. 1, p. 012037, Feb. 2021, doi: 10.1088/1757-899X/1038/1/012037.

[52] A. Milanese, "Caratterizzazione termo-strutturale e studio dei meccanismi di frattura di dischi in materiale ceramico per applicazioni nucleari," Università degli Studi di Padova, 2019.

[53] R. J. (Raymond J. Roark, W. C. (Warren C. Young, and R. G. (Richard G. Budynas, *Roark's formulas for stress and strain*. McGraw-Hill, 2002.

[54] Microsoft Corporation, "Microsoft Excel." 2018.

[55] S. Timoshenko, *Theory of elasticity*, 3rd ed. New York: McGraw-Hill, 1970.

[56] R. J. Price, “Mechanical properties of graphite for high-temperature gas-cooled reactors: a review.” 1975.

[57] R. E. Ely, “Sterngth of Magnesium Silicate and Graphite Under Biaxial Stresses,” *Ceram. Bull.*, vol. 47, no. 5, pp. 37–41, 1968.

[58] W. L. Greenstreet, “Mechanical Properties of Artificial Graphites - A Survey Report,” Oak Ridge, Tennessee, 1968.

[59] L. Green, “Observations on the high-temperature elastic and inelastic properties of polycrystalline graphites,” in *Proceedings of the Fourth Carbon Conference*, 1959, pp. 497–509.

[60] C. Malmstrom, R. Keen, and L. Green, “Some mechanical properties of graphite at elevated temperatures,” *J. Appl. Phys.*, vol. 22, no. 5, pp. 593–600, 1951, doi: 10.1063/1.1700013.

[61] P. Wagner and A. R. Driesner, “High-temperature mechanical properties of graphite. I. creep in compression,” *J. Appl. Phys.*, vol. 30, no. 2, pp. 148–151, 1959, doi: 10.1063/1.1735123.

[62] M. C. Smith, “Effects of Temperature and Strain Rate on Transverse Tensile Properties of H4Lm Graphite Tested in Helium and in Vacuum,” *Carbon N. Y.*, vol. 1, pp. 147–153, 1964.

[63] H. E. Martens, D. D. Button, D. B. Fischbach, and L. D. Jaffe, “Tensile and creep behavior of graphites above 3000°F,” in *Proceedings of the Fourth Carbon Conference*, 1960, pp. 511–531.

[64] L. Green, “High temperature compression tests on graphite,” *J. Appl. Mech.*, vol. 20, no. 2, pp. 289–294, 1952.

[65] L. M. Gillin, “Deformation characteristics of nuclear grade graphites,” *J. Nucl. Mater.*, vol. 23, no. 3, pp. 280–288, 1967, doi: 10.1016/0022-3115(67)90160-2.

[66] J. Broutman, S. M. Krishnakumar, and P. K. Mallick, “Effects of Combined Stresses on Fracture of Alumina and Graphite,” *J. Am. Ceram. Soc.*, vol. 53, no. 12, pp. 649–654, 1970, doi: 10.1111/j.1151-2916.1970.tb12034.x.

[67] T. Weng, “Stress-strain properties of grade ATJ graphite under combined stresses.” 1972.

[68] F. H. Ho, R. E. Vollman, H. Yu, and N. R. Adsit, “Biaxial Failure Surfaces of 2020 and PGX Graphites,” 1983.

[69] M. Eto, S. Ishiyama, T. D. Burchell, and G. T. Yahr, “Biaxial Strength and Fracture Criterion for HTGR Graphites,” *J. Nucl. Sci. Technol.*, vol. 34, no. 5, pp. 476–483, 1997, doi: 10.1080/18811248.1997.9733694.

[70] S. G. Babcock, “Dynamic Biaxial and Elevated-Temperature Properties of ATJ-S Graphite,” in *Proceedings of the Conference on Continuum Aspects of Graphite Design*, 1972, p. 50.

[71] J. Jortner, “Biaxial Mechanical Properties of AXF-5Q Graphite to 4000°F,” in *Proceedings of the Conference on Continuum Aspects of Graphite Design*, 1972, pp. 541–532.

[72] H. O. Pierson, V. Nicolosi, M. Chhowalla, M. G. Kanatzidis, M. S. Strano, and J. N. Coleman, “HANDBOOK OF CARBON , GRAPHITE , DIAMOND AND FULLERENES by,” *Science (80-.).*, vol. 340, no. 6139, 2013, doi: 10.1126/science.1226419.

[73] L. G. B. Manhani, L. C. Pardini, and F. L. Neto, “Assessement of tensile strength of graphites by the Iosipescu coupon test,” *Mater. Res.*, vol. 10, no. 3, pp. 233–239, 2007, doi: 10.1590/S1516-14392007000300003.

[74] F. Berto, P. Lazzarin, and M. R. Ayatollahi, “Brittle fracture of sharp and blunt V-notches in isostatic graphite under pure compression loading,” *Carbon N. Y.*, vol. 63, pp. 101–116, 2013, doi: 10.1016/j.carbon.2013.06.045.

[75] T. Iyoku, S. Shiozawa, M. Ishihara, T. Arai, and T. Oku, “Graphite core structures and their structural design criteria in the HTTR,” *Nucl. Eng. Des.*, vol. 132, no. 1, pp. 23–30, Dec. 1991, doi: 10.1016/0029-5493(91)90291-O.

[76] J. L. Pickerling, “Multiaxial graphite test specimen,” General Atomics Co., San Diego, CA (United States), Oak Ridge, TN, Sep. 1988.

[77] R. M. Christensen, “A comprehensive theory of yielding and failure for isotropic materials,” *J. Eng. Mater. Technol. Trans. ASME*, vol. 129, no. 2, pp. 173–181, Apr. 2007, doi: 10.1115/1.2712847.

[78] F. H. Ho, “Graphite Design Handbook,” 1988.

[79] R. J. Price, “Mechanical properties of graphite for high temperature gas cooled reactors: a review,” no. 17.

[80] M. Eto, S. Ishiyama, T. D. Burchell, and G. T. Yahr, “Biaxial strength and fracture criterion for HTGR graphites,” *J. Nucl. Sci. Technol.*, vol. 34, no. 5, pp. 476–483, 1997, doi: 10.1080/18811248.1997.9733694.

[81] AZO Materials, “Properties: Tantalum - An Overview.” [Online]. Available: https://www.azom.com/properties.aspx?ArticleID=1207.

[82] SSINA: Stainless Steel Information Center, “High temperature properties.” [Online]. Available: http://www.ssina.com/composition/temperature.html.

[83] M. Eto and S. Ishiyama, “Biaxial fatigue strength of a fine-grained isotropic graphite for

HTTR," *J. Nucl. Sci. Technol.*, vol. 35, no. 11, pp. 808–815, 1998, doi: 10.1080/18811248.1998.9733948.

[84] Donzella Antonietta, "Containment of Radioactive Hazard and Environmental Impact in a Radioactive ION Beam Facility," University of Brescia, 2021.

[85] "Personal Protective Equipment," *Pratical Radiation Technical Manual* . International Atomic Energy Agency, Vienna, 2004.

[86] T. Otto, *Safety for Particle Accelerators*. Cham: Springer International Publishing, 2021.

[87] "Decreto Legislativo 31 Luglio 2020, n.101. Attuazione della direttiva 2013/59/Euratom." .

[88] D. Zafiropoulos, "Relazione tecnica in materia di radioprotezione relativa al progetto SPES - Fase alfa dei Laboratori Nazionali di Legnaro dell'INFN." 2010.

[89] D. Paderno, I. Bodini, A. Zenoni, A. Donzella, L. Centofante, and V. Villa, "Proof of Concept Experience in the SPES Experiment: First Solutions for Potentiometers Replacement in System Maintenance," *Lect. Notes Mech. Eng.*, pp. 301–306, Jun. 2020, doi: 10.1007/978-3-030-70566-4_48.

APPENDIX A

THE DEVICES INSIDE THE SPES BUNKER

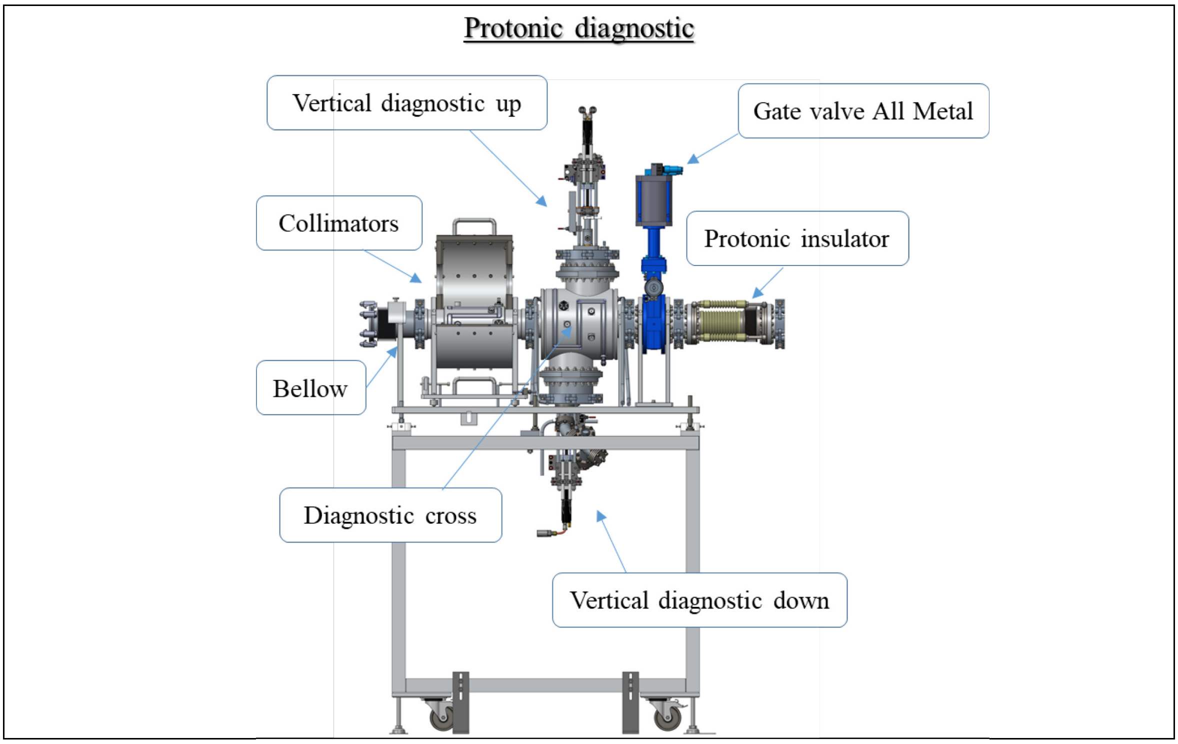

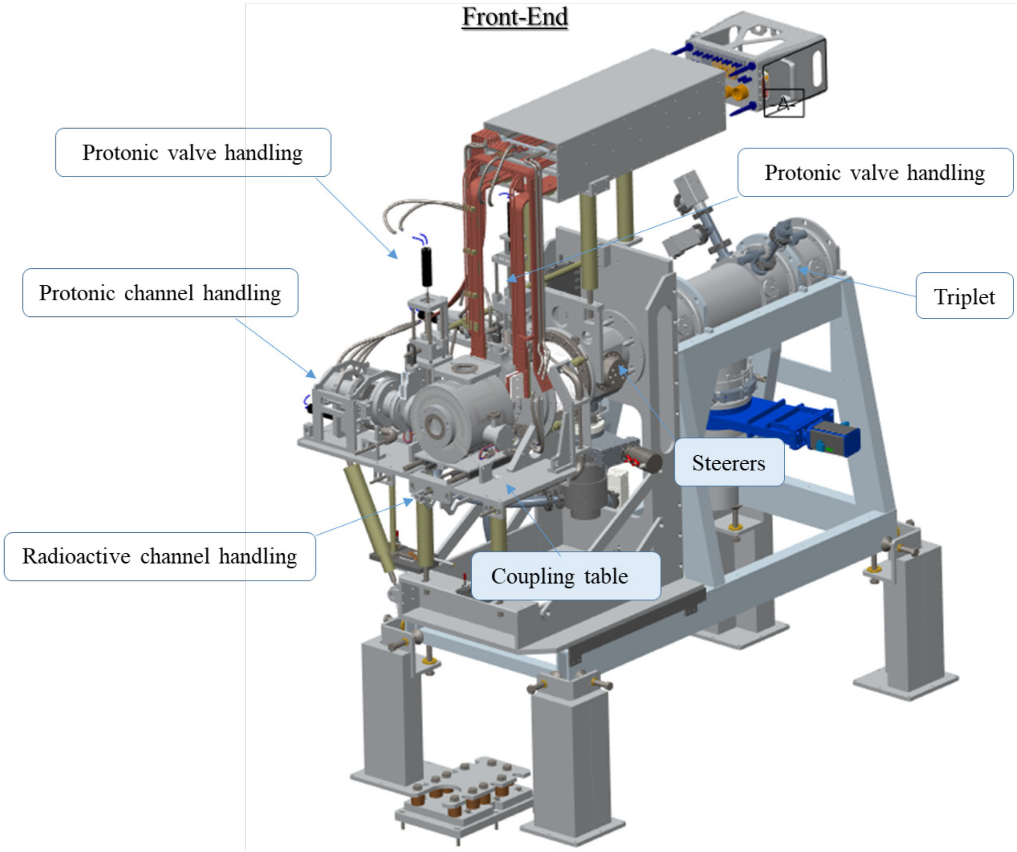
Front-End
Protonic valve handling
Protonic valve handling
Protonic channel handling
Triplet
Steerers
Radioactive channel handling
Coupling table

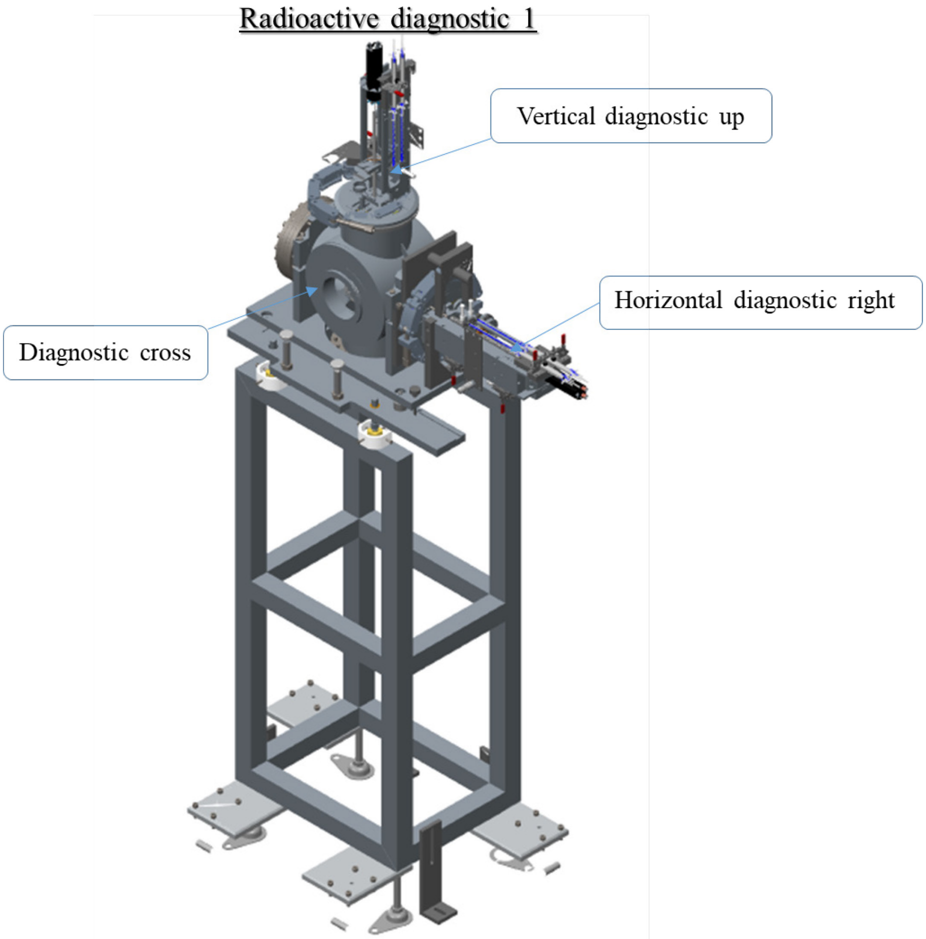
Radioactive diagnostic 1
Vertical diagnostic up
Horizontal diagnostic right
Diagnostic cross

Wien Filter

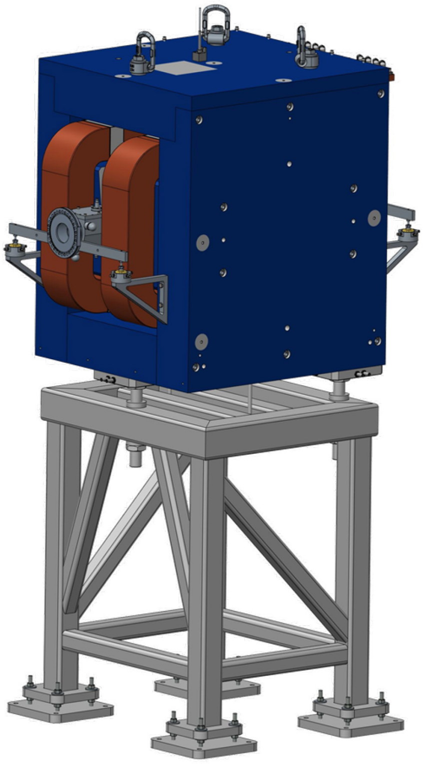

Radiaoctive diagnostic 2

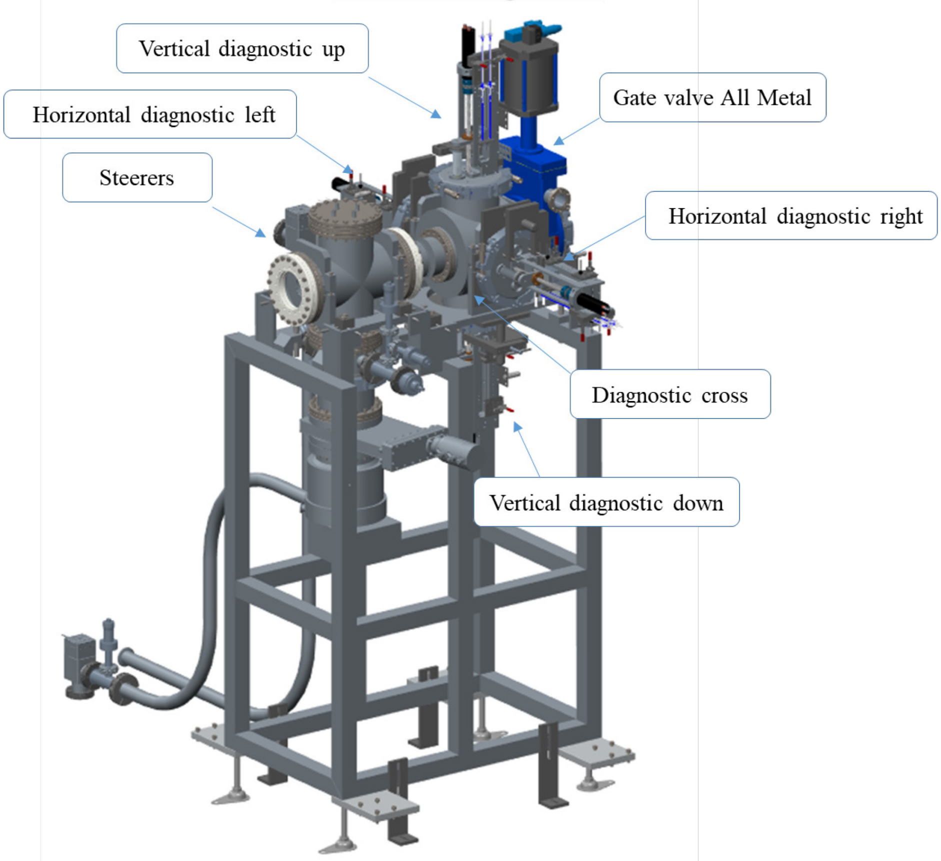

Triplet